

12

AFGL-TR-86-0002

OBJECTIVE ANALYSIS AND PREDICTION TECHNIQUES - 1985

Alan M. Gerlach (ed.)

AD-A169 746

SASC Technologies, Inc.  
4400 Forbes Blvd.  
Lanham, MD 20706

DTIC  
ELECTE  
JUL 24 1986  
S D D

November 30, 1985

Scientific Report No. 10

Approved for public release; distribution unlimited

AIR FORCE GEOPHYSICS LABORATORY  
AIR FORCE SYSTEMS COMMAND  
UNITED STATES AIR FORCE  
HANSCOM AFB, MASSACHUSETTS 01731

DTIC FILE COPY

This technical report has been reviewed and is approved for publication.

*Allan J. Bussey*

ALLAN J. BUSSEY  
Contract Manager

FOR THE COMMANDER

*Robert A. McClatchey*

ROBERT A. McCLATCHEY, Director  
Atmospheric Sciences Division

This report has been reviewed by the ESD Public Affairs Office (PA) and is releasable to the National Technical Information Service (NTIS).

Qualified requestors may obtain additional copies from the Defense Technical Information Center. All others should apply to the National Technical Information Service.

If your address has changed, or if you wish to be removed from the mailing list, or if the addressee is no longer employed by your organization, please notify AFGL/DAA, Hanscom AFB, MA 01731. This will assist us in maintaining a current mailing list.

## REPORT DOCUMENTATION PAGE

1a. REPORT SECURITY CLASSIFICATION UNCLASSIFIED		1b. RESTRICTIVE MARKINGS	
2a. SECURITY CLASSIFICATION AUTHORITY		3. DISTRIBUTION/AVAILABILITY OF REPORT Approved for public release; distribution unlimited	
2b. DECLASSIFICATION/DOWNGRADING SCHEDULE		4. PERFORMING ORGANIZATION REPORT NUMBER(S)	
4. PERFORMING ORGANIZATION REPORT NUMBER(S)		5. MONITORING ORGANIZATION REPORT NUMBER(S) AFGL-TR-86-0002	
6a. NAME OF PERFORMING ORGANIZATION SASC Technologies, Inc.	6b. OFFICE SYMBOL (If applicable)	7a. NAME OF MONITORING ORGANIZATION Air Force Geophysics Laboratory	
6c. ADDRESS (City, State and ZIP Code) 4400 Forbes Blvd. Lanham, MD 20706		7b. ADDRESS (City, State and ZIP Code) Hanscom AFB, MA 01731 Monitor/LY/Allan J. Bussey	
8a. NAME OF FUNDING/SPONSORING ORGANIZATION Air Force Geophysics Laboratory	8b. OFFICE SYMBOL (If applicable) LY	9. PROCUREMENT INSTRUMENT IDENTIFICATION NUMBER Contract No. F19628-82-C-0023	
8c. ADDRESS (City, State and ZIP Code) Hanscom AFB, MA 01731		10. SOURCE OF FUNDING NOS.	
11. TITLE (Include Security Classification) Objective Analysis and Prediction Techniques - 1985		PROGRAM ELEMENT NO. 62101F	PROJECT NO. 6670
12. PERSONAL AUTHOR(S) Gerlach, Alan M. (ed.)		TASK NO. 00	WORK UNIT NO. AC
13a. TYPE OF REPORT Scientific Rpt. No 1	13b. TIME COVERED FROM 84/12/1 TO 85/11/30	14. DATE OF REPORT (Yr., Mo., Day) 85/11/30	15. PAGE COUNT 239
16. SUPPLEMENTARY NOTATION			
17. COSATI CODES		18. SUBJECT TERMS (Continue on reverse if necessary and identify by block number)	
FIELD	GROUP	SUB. GR.	
0401			Objective analysis Interactive forecasting
0402			Initialization Mesocyclone detection/classification
			VAS data processing Satellite cloud analysis
19. ABSTRACT (Continue on reverse if necessary and identify by block number): This report summarizes weather research in several technical areas: in numerical weather prediction, use of supplemental moisture information in global optimum interpolation analysis of humidity, development of a relocatable limited area model; in mesoscale forecasting, FOCUS guidance error study, forecast guidance displays; in boundary layer meteorology, specialized computer programs for studies of atmospheric refractive index, wind-flow model, troposcatter raytrace models; in radar meteorology, detection of synoptic scale wind anomalies, gust front detection, 3-D cloud and precipitation mapping, icing detection, severe storm indicators; in satellite meteorology, development of microprocessor-based satellite data ingest system, system design (hardware, software) for McIDAS upgrade; in climatology, data processing and display studies for statistical properties of cumulus cloud structures, spatial/temporal cloud cover distributions from conventional observations, rainfall rate recurrence statistics, and cumulus cloud vs. satellite brightness values.			
20. DISTRIBUTION/AVAILABILITY OF ABSTRACT UNCLASSIFIED/UNLIMITED <input checked="" type="checkbox"/> SAME AS RPT <input type="checkbox"/> DTIC USERS <input type="checkbox"/>		21. ABSTRACT SECURITY CLASSIFICATION UNCLASSIFIED	
22a. NAME OF RESPONSIBLE INDIVIDUAL Allan J. Bussey		22b. TELEPHONE NUMBER (Include Area Code) (617) 861-2977	22c. OFFICE SYMBOL LY

FOREWORD

This interim scientific report details the results and status of research performed by Systems and Applied Sciences Corporation/SASC Technologies, Inc. under Contract F19628-82-C-0023 with the Atmospheric Sciences Division, Air Force Geophysics Laboratory, for the period December 1, 1984 to November 30, 1985.

Presentations vary in technical detail according to their subject matter, ranging from narrative descriptions of work accomplished to technical papers.

The contract calls for effort in six discrete areas, reported upon in the monthly R&D Status Reports under these headings:

- Numerical Weather Prediction
- Mesoscale Forecasting
- Boundary Layer Meteorology
- Radar Meteorology
- Satellite Meteorology
- Climatology

This report is organized similarly.

Personnel associated with these areas at any time during the reporting period were:

- Numerical Weather Prediction - Donald C. Norquist, M.S.  
Isidore M. Halberstam, Ph.D.  
Shu-Lin Tung, M.S.  
Chris Johnson, B.S.
- Mesoscale Forecasting - Randy Schechter, M.S.
- Boundary Layer Meteorology - Joan M. Ward, B.A.  
Joan-Marie Freni, B.A.  
Clyde L. Lawrence
- Radar Meteorology - F. Ian Harris, Ph.D.  
Glenn R. Smythe, M.S.  
Ralph J. Donaldson, Jr., S.M.  
Frank H. Ruggiero, M.S.  
Paul R. Desrochers, M.S.  
Dagmar Rapp, B.S.  
Donald C. Rich, Jr.  
Neil Day

For	
RA&I	<input checked="" type="checkbox"/>
B	<input type="checkbox"/>
ced	<input type="checkbox"/>
Availability Codes	
Available and/or Special	



DUPLICATE  
A-1

**Satellite Meteorology**

- Gary B. Bustafson, B.S.
- Charles F. Ivaldi, Jr., B.S.
- Robert G. Hallowell, B.S.
- Barry A. Mareiro
- D. Keith Roberts

**Climatology**

- James H. Willand

Principal Investigator was Alan M. Gerlach, Ph.D.

Subcontracts with Harris Corporation Computer Systems Division and Perkin-Elmer Customer Service Division provided on-site maintenance services for the McIDAS and Weather Radar Data Processing System, respectively.

Reports were prepared by the scientists, engineers, and mathematicians identified in the Table of Contents.

## TABLE OF CONTENTS

<b>I. NUMERICAL WEATHER PREDICTION</b>	<b>11</b>
<b>A. Use of Supplemental Moisture Information in the Global Optimum Interpolation Analysis of Humidity - Donald C. Norquist</b>	<b>11</b>
1. Introduction	11
2. Recent Modifications to ASAP Codes	11
3. Investigation of Alternative Sources of Moisture Information	21
a. Satellite Observed Layer Precipitable Water	26
b. Upper Air Relative Humidity Inferred from Surface Weather Observations	27
c. Upper Air Relative Humidity Inferred from Cloud Analyses	35
4. Use of Relative Humidity Observations in the Global Humidity Analysis	41
Appendix A. Conversion of Cloud Amount to Relative Humidity	44
<b>B. Relocatable Limited Area Model - Progress in Development - Isidore M. Halberstam, Chris Johnson, Shu-Lin Tung</b>	<b>50</b>
1. Introduction	50
2. Initial Conditions	50
3. Boundary Conditions	53
4. The Model	68
5. Results	71
6. Outlook	77
Appendix B. Spectral Evaluation at the Poles	82
<b>II. MESOSCALE FORECASTING - Randy Schechter</b>	<b>93</b>
<b>A. Evaluation of the Generalized Exponential Markov (GEM) Technique Using Hourly Observations at Patrick Air Force Base, Florida</b>	<b>93</b>

TABLE OF CONTENTS (Con't.)

B.	FOUS Guidance Error Study	97
C.	Forecast Guidance Displays	118
III.	BOUNDARY LAYER METEOROLOGY	122
A.	Refractive Index Study - Joan M. Ward	122
B.	Surface Layer Windflow Model - Joan M. Ward	123
C.	Troposcatter Raytrace Models - Joan-Marie Freni	125
D.	Raytrace - Joan-Marie Freni	126
E.	Otis Weather Test Facility - Clyde L. Lawrance	126
IV.	RADAR METEOROLOGY	129
A.	Detection of Synoptic Scale Wind Anomalies - Ralph J. Donaldson, Jr.	129
1.	Introduction	129
2.	Terms of the Kinematic Properties	130
3.	A Realistic Difffluence Model	131
4.	Interactions Among the Kinematic Terms	133
5.	Techniques for Distinguishing Curvature and Crosswind Shear	134
a.	Information External to the Doppler VAD Pattern	135
b.	Isolation and Examination of Second Order and Higher Derivatives of the VAD Pattern	135
c.	Comparison of Equivalent Crosswind Shear Parameter $c_0$ with Displacements of the Doppler Velocity Extrema $\delta$	136
d.	Effect of Curvature on the Difffluence Signature	138
6.	Future Work	138
B.	Gust Front Detection - F. Ian Harris and Glenn R. Smythe	139
1.	Introduction	139
2.	Radar Measurements	139

TABLE OF CONTENTS (Con't.)

3. The Technique	140
a. Polar Computations	142
b. Cartesian Computations	142
4. Application	143
a. Gust Fronts	143
b. Mesocyclones and Downbursts	143
5. Area Thresholding	148
6. Future Development	148
7. NEXRAD Documentation	148
C. Three-Dimensional Cloud and Precipitation Mapping - F. Ian Harris, Donald C. Rich, Jr., and Dagmar Rapp	149
1. Introduction	149
2. RAPID System Development	149
3. Precipitation Mapping	151
4. Cloud Mapping	151
5. Detection and Prediction Techniques	152
6. Future Development	153
D. Icing Detection - Frank H. Ruggiero	153
1. Introduction	153
2. Algorithm	153
3. Implementation	156
4. Sensitivity Tests	158
5. Conclusion	161
E. Severe Storm Indicators - Paul R. Desrochers	161
1. Introduction	161
2. Automatic Mesocyclone Detection	162
3. Mesocyclone Discriminators	163



TABLE OF CONTENTS (Con't.)

4. Analysis	165
5. Evaluation	167
6. Summary	172
F. Turbulence Algorithm Implementation - Frank H. Ruggiero	172
V. SATELLITE METEOROLOGY	174
A. Microprocessor-Based Satellite Data Ingest System - Charles F. Ivaldi, Jr.	174
1. Introduction	174
2. Communications Testing	174
3. ODIS Configuration	175
4. Software Development	176
a. Ingest Routines	176
b. Transmission Routine	177
c. Exception Handler	179
d. Clock/Calendar Software	179
5. Software Integration	180
a. Network Manager	180
b. Coordinate Transformation Software	180
6. Summary	181
Appendix C. Data File Structures Description	182
B. AFGL Interactive Meteorological System (AIMS) - Gary B. Gustafson, Charles F. Ivaldi, Jr., and D. Keith Roberts	183
1. Introduction	183
2. System Overview	183
a. Batch Processing	183
b. Real Time Data Ingest	185
c. Image Processing Workstations	185

TABLE OF CONTENTS (Con't.)

3. Implementation Plan	185
4. Database Manager	187
5. Local Area Network	191
6. User Interface	192
a. Keyboard Terminals - Command Line Interpreter	193
b. Keyboard Terminals - Screen Menus	195
c. Graphics Pull Down Menus	195
d. Graphics Tablet Icons Menu	195
7. GOES Ingest	195
C. McIDAS Operations and Maintenance	197
1. McIDAS Operations	197
2. McIDAS Maintenance	197
a. Resident Engineering	197
b. Contract Engineering	198
VI. CLIMATOLOGY - James H. Willand	199
A. An Update to the LANDSAT MSS Data Handling Configuration at AFGL	199
B. Statistical Properties of Cumulus Cloud Structures	199
1. Introduction	199
2. Specifications	202
3. Source Data	202
4. Software Development	203
C. Spatial and Temporal Cloud Cover Distributions from Conventional Observations	212
1. Introduction	212
2. Specifications	214
3. Source Data	214

TABLE OF CONTENTS (Con't.)

4. Software Development	216
D. Rainfall Rate Recurrence Statistics	219
1. Introduction	219
2. Specifications	219
3. Data Sources	223
4. Software Development	223
E. Cumulus Cloud Cover vs. Satellite Brightness Values	227
1. Introduction	227
2. Specifications	227
3. Source Data	227
4. Software Development	228
Appendix D. Program COND80	233

## I. NUMERICAL WEATHER PREDICTION

### A. Use of Supplemental Moisture Information in the Global Optimum Interpolation Analysis of Humidity

#### 1. Introduction

This report details recent modifications made to the global optimum interpolation procedure developed for the Air Force Geophysics Laboratory (AFGL), designated the AFGL Statistical Analysis Programs (ASAP). Also included is a description of a study conducted to investigate the feasibility and effects of using non-conventional humidity information to supplement conventional humidity observations. An experimental set of analysis cycles was designed to test the use of such supplemental humidity information.

Previous reports described the formulation of the original ASAP procedure (Gerlach, 1983)<sup>1</sup> and later modifications and an experimental trial of the modified procedure (Halberstam *et al.*, 1984).<sup>2</sup> This report describes further modifications of the procedure and the use of supplemental moisture information in its application.

#### 2. Recent Modifications to ASAP Codes

Before discussing the modifications made to the series of codes responsible for preparing the global optimum interpolation analysis, a brief description of the codes as they existed in the 1984 assimilation experiment (Halberstam *et al.*, 1984) is in order. The five codes used to prepare the analysis at that time were run in the following sequence:

(1) PRSFPR, which converted the spectral coefficients of the previous forecast fields to physical space values on the 62 X 62 (62 Gaussian latitude, 62 equally spaced longitude) analysis grid;

---

1. Gerlach, A. M., ed., 1983: Objective Analysis and Prediction Techniques - 1983. AFGL-TR-83-0333, Contract F19628-82-C-0023, Systems and Applied Sciences Corporation, ADA142441.

2. Halberstam, I. M., C. Johnson, D. C. Norquist, and S.-L. Tung, 1984: Two Methods of Global Data Assimilation. AFGL-TR-84-0260, Contract F19628-82-C-0023, Systems and Applied Sciences Corporation, ADA155981.

(2) SFPRS, which evaluated first guess (forecast) values of surface pressure ( $p_*$ ) and winds at the observation locations using spectral coefficients, then formed the observation-minus-first guess residuals and performed a multivariate (univariate over land and in the tropics) OI surface pressure analysis;

(3) PRASAP, in which the 62 X 62 X 12 (sigma layer) first guess values of temperature (T), wind components (u, v), and specific humidity (q) were vertically interpolated from sigma layer pressures based on first guess surface pressures to those based on analyzed surface pressures;

(4) ASAP, the upper air analysis of height and winds (multivariate) and specific humidity (univariate) on the 62 X 62 X 12 analysis grid in which observations were interpolated to sigma layers, first guess spectral expansions were evaluated at the observation latitude-longitude locations, and the resulting observation-minus-first guess residuals were used to perform the OI analysis at sigma layers; whereupon height corrections were converted to temperature corrections and T, u, v, q were all updated by adding the calculated corrections to the first guess values;

(5) POASAP, which converted all analyzed fields (T, u, v, q,  $p_*$ ) to spectral coefficient form for input to the Machenhauer non-linear normal mode initialization (NMI) which initialized the analysis before its use as initial conditions for the global spectral model (GSM). The NMI and GSM codes are documented in Gerlach (1982)<sup>3</sup> and Brenner, Yang, and Yee (1982)<sup>4</sup> respectively.

The first major modification to the set of codes was the removal of PRASAP, which performed the vertical interpolation of the first guess fields from the old sigma layer pressures to the new sigma layer pressures. As mentioned in Gerlach (1983), this step is justified if the first guess

---

3. Gerlach, A. M., ed., 1982: Objective Analysis and Prediction Techniques. AFGL-TR-82-0394, Contract F19628-82-C-0023, Systems and Applied Sciences Corporation, ADA131465.

4. Brenner, S., C. H. Yang, and S. Y. K. Yee, 1982: The AFGL Spectral Model of the Moist Global Atmosphere: Documentation of the Baseline Version. AFGL-TR-82-0393, Air Force Geophysics Laboratory, Hanscom AFB, MA, ADA129283.

values are thought of as being associated with a sigma value rather than a pressure value. Since the  $\sigma$  value for each layer does not change in the surface pressure analysis (although the sigma layer pressure does), there is no need for an interpolation. The effect on the upper air analysis of not preceding it by this interpolation was studied by performing a single analysis of surface pressure and sigma layer height and winds with and without the intervening vertical interpolation. The concern was that the subsequent normal mode initialization would have to force a balance between the separately analyzed surface pressure and sigma layer height fields, and in doing so would decrease the amount of slow mode information that would be provided by the analysis to the forecast. Results from this one-time test, based on a 12 h GSM forecast valid 2/4/79 12 Z and using FGGE II-B data in the analysis, are shown in Table 1. Root mean square (RMS) differences between forecast field and initialized forecast field (G-GI, the fast mode due to the forecast), analyzed field and initialized analysis field (A-I, the total fast mode due to both forecast and analysis), and initialized analysis and initialized forecast (I-GI, the slow mode due to the analysis) are given. The latter two RMS differences are shown for the runs that did (\*) and did not include the vertical interpolation.

TABLE 1. COMPARISON OF FIELDS WITH (\*) AND WITHOUT VERTICAL INTERPOLATION OF FIRST GUESS TO NEW SIGMA LAYER PRESSURES AFTER SURFACE PRESSURE ANALYSIS

	(RMS DIFFERENCE)						
	G-GI	(A-I)*	A-I	(I-GI)*	I-GI	R*	R
Z ( $\hat{\sigma}_3$ )(m)	0.41	2.22	2.02	9.76	10.02	0.19	0.16
Z ( $\hat{\sigma}_5$ )	3.25	8.84	7.87	15.31	15.89	0.18	0.15
Z ( $\hat{\sigma}_9$ )	9.69	21.61	19.83	14.56	15.26	0.82	0.66
$\rightarrow$ V ( $\sigma_2$ )(m s <sup>-1</sup> )	0.61	1.44	1.44	2.21	2.19	0.38	0.38
$\rightarrow$ V ( $\sigma_4$ )	0.25	1.36	1.35	1.98	2.02	0.56	0.54
$\rightarrow$ V ( $\sigma_8$ )	1.10	2.32	2.31	3.12	3.21	0.39	0.38
p <sub>*</sub> (mb)	0.41	3.66	3.55	1.49	1.59	2.18	1.91

This table is an exact analog to Table 2 in Halberstam et al. (1984) which showed that these quantities did not vary significantly from cycle to cycle in the assimilation sequence. This fact allows one to draw conclusions from this one-time case that would apply to other untested cases. As in the earlier table, the fast mode/slow mode ratio given by

$$R \equiv \frac{(A-I) - (G-GI)}{I - GI}$$

is included, in this case showing the results both with and without interpolation. In all cases shown in the table, the analysis fast mode/slow mode ratio without interpolation is smaller than or equal to the same ratio for the procedure including interpolation. Thus, the vertical interpolation does not improve mass-motion balance and in fact may worsen it, possibly because interpolation errors could lead to a greater imbalance in the first guess before the upper air analysis is performed.

The results shown in this table and the analogous table in the earlier report indicate that relatively little of the slow mode information from the surface pressure analysis survives the normal mode initialization to be passed on to the subsequent forecast. In fact, the earlier table showed that the fast mode contribution from the analysis (unavailable to the forecast) was 2.33 times greater than the slow mode contribution, where typically for other fields the slow mode was at least as large as the fast mode contribution and generally was larger, as would be desired.

Since little benefit was being gained from the surface pressure analysis in comparison to its cost in time, it (SFPRS) was also dropped from the job sequence. In its place, a routine was added to POASAP that provided an estimate of analyzed surface pressure on the model terrain surface by using the analyzed temperatures at the lowest three sigma layers and the model terrain geopotential at each analysis point to derive hydrostatically the sigma level (interface) geopotential at the three levels above the surface. These sigma level geopotentials and their sigma level pressures were used to extrapolate a pressure value for the model terrain geopotential value, assuming that geopotential varies quadratically in the natural logarithm of pressure. The method used is analogous to the GETPS routine mentioned in Halberstam et al. (1984).

Another major change made in the sequence of codes was to replace the evaluation of the spectral expansions of the first guess fields at the observation location with the bilinear interpolation of first guess grid values on a fine mesh grid. The first code in the sequence, PRANAL (changed from PRSFPR by the removal of the surface pressure analysis), was modified to produce a 360 X 181 (1° longitude X 1° latitude) grid as well as the 62 X 62 grid of first guess values that it previously computed. The 1° interval was chosen after testing the accuracy of the bilinear interpolation against direct spectral evaluation for several resolutions of interpolation grids. Results of the tests showed that for 1° X 1° resolution, maximum T interpolation RMS errors were less than 0.1° K, maximum wind component RMS errors were less than 0.3 m s<sup>-1</sup>, and maximum surface pressure interpolation RMS errors were about 1.0 mb. These were considered satisfactory since they did not exceed generally accepted levels for observation error. However, maximum RMS differences between analyzed fields using the two methods of obtaining the first guess values at the observation sites were somewhat larger for temperature and winds (0.7° K, 1.5 m s<sup>-1</sup>), suggesting that small differences in the residual values between the two methods can be amplified somewhat in the analysis. Most of the increase in difference was found at just a few analysis points rather than spread out throughout the field. Implementation of the bilinear interpolation in ASAP resulted in a 25 percent reduction in CPU time over the spectral method.

To allow for a minimum of storage space and input/output time in bringing the 360 X 181 first guess fields into the OI analysis program ASAP, the program was modified to read in and store only two 360 point latitude bands at each of the sigma layers for each of the analysis variables at any one time. These would necessarily be the two 1° latitude bands that surrounded the observation site for which the first guess value was to be estimated. Implementation of this step required that the observation sites be dealt with in latitudinal order to prevent rewinding and searching the first guess tape for the correct surrounding latitudes. Latitudinal sorting was achieved by subjecting the observation data file to the code F2BSORT obtained from Gutowski (private communication) which produced files of observations sorted from south to north separately for each observation type.

Some general changes were made in the sequence of analysis codes. As will be discussed in more detail later, the use of FGGE II-B



satellite layer precipitable water values was discontinued after comparisons of relative humidity values derived from them with co-located rawinsonde relative humidity observations showed RMS differences as high as 50 percent. The data set used for the computation of statistics as well as for the data assimilation experiment was the Final FGGE Level II-B Data Set which was later upgraded to form the Reprocessed Final Data Set. Lonnberg (private communication) performed a similar co-location study with a period of 1979 data from the reprocessed set and found RMS differences on the order of 10 - 15 percent. The ASAP analysis code was modified to allow switching on the use of this type of data should it be desired.

Another change made to the upper air analysis code was to redefine the topmost sigma level to correspond to a pressure of 10 mb. The former value of 1 mb led to an unnecessarily deep uppermost layer. When the first guess and observation layer temperatures in the uppermost layer were used to derive geopotential height values at 1 mb, the observation-minus-first guess residual values at this level were excessive. Since the value of the uppermost sigma layer was  $\sigma = .02075$ , a surface pressure value less than 482 mb would be required to give an uppermost sigma layer pressure less than 10 mb. Because of the unlikelihood of such a low surface pressure, 10 mb was chosen as the pressure of the top of the analysis atmosphere for computational purposes.

Another change was the use of forecast error standard deviation values for u and v (denoted  $\sigma_u$ ,  $\sigma_v$ ) since they are derived from prescribed values of  $\sigma_z$ , rather than prescribing them separately (Dey and Morone, 1985).<sup>5</sup> Values of  $\sigma_z$  used in the analysis were the same as those used previously (Halberstam et al., 1984, Table 1) but values of  $\sigma_u$ ,  $\sigma_v$  poleward of 25° latitude were evaluated from those using the expression  $\sigma_{u_i} = \sigma_{v_i} = \frac{G_i g}{f_i} \sqrt{2 k_h} \sigma_{z_i}$  where g is the gravitational constant, f is the coriolis parameter,  $k_h = 1.96 \times 10^{-6} \text{ km}^{-2}$ , and G is the coefficient of geostrophy plotted along with the entire function in Fig. 1. The geostrophy coefficient G shown in Fig. 1 is given by

$$G = \begin{cases} 1 - \exp[-0.05|\phi|] & 25^\circ < |\phi| \leq 90^\circ \\ \{1 - \exp[-0.05|25^\circ|\}] \{0.5(\cos[(|\phi|-10)12-180] + 1)\} & 10^\circ < |\phi| \leq 25^\circ \\ 0 & |\phi| \leq 10^\circ \end{cases}$$

5. Dey, C. H., and L. L. Morone, 1985: Evolution of the National Meteorological Center global data assimilation system: January 1982 - December 1983. Mon. Wea. Rev., 113, 304-318.

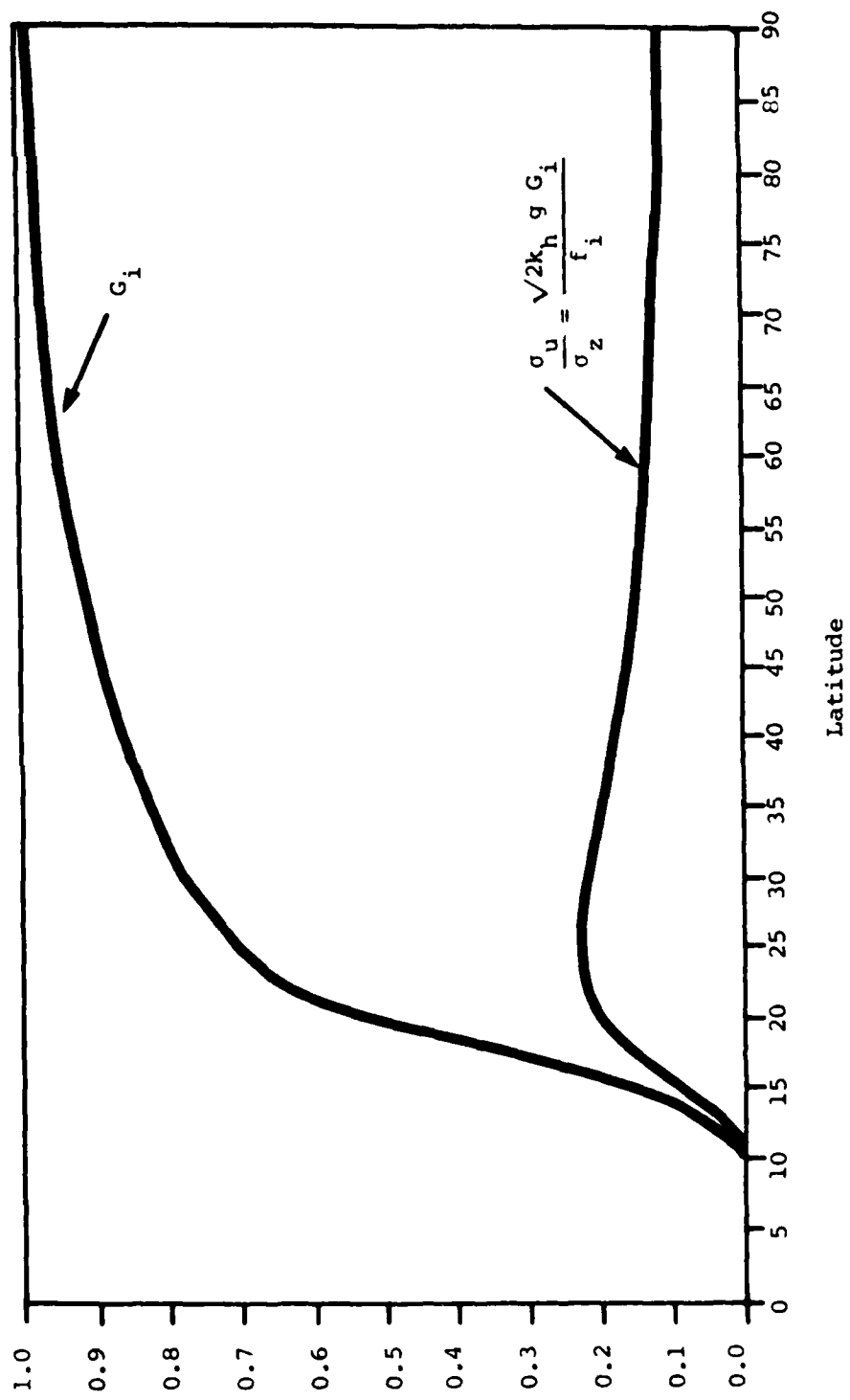


Fig. 1. Coefficient of Geostrophy and Ratio of Wind to Height F. E. S. D.

whereas formerly the expression  $1 - \exp[-0.5|\phi|]$  was used for all latitudes. Equatorward of  $25^\circ$ , a linearly weighted blend of the value obtained in the above expression and tropical values taken from Dey and Morone (1985) interpolated linearly to the proper latitude was assigned to  $\sigma_u$  and  $\sigma_v$ .

Also, the  $q$  vs.  $\ln p$  interpolation of rawinsonde humidity to sigma layers was replaced by a linear  $\ln q$  vs.  $\ln p$  interpolation. Mitchell (1985)<sup>6</sup> showed that the log-log interpolation introduced significantly less bias in the resulting interpolated values. Finally, a tighter control over use of data of questionable quality was imposed. Only data from the FGGE II-B data set with horizontal and vertical consistency check indicators of 0 (no check made) or 1 (value found correct in consistency check) were used in the analysis.

In the earlier study (Halberstam *et al.*, 1984), the results of the 12 h cycle data assimilation experiment showed no significant growth of error and good agreement with FGGE III-A fields for the analyzed height fields. However, as Figs. 3(d) - (f) from that report demonstrate, an appreciable growth of error (difference from observations) was realized in the analyzed wind fields, in contrast to a level, much lower error curve for the FGGE III-A analyses. In the conclusions of that report it was stated that the error growth may be due to the use of a 12 h data assimilation cycle in that experiment. Preliminary results using a 6 h cycle, however, showed the same error trend.

In addition, a steady growth of global mean divergence and vorticity was detected in the preliminary runs using the 6 h cycle. Assuming that the growth of divergence and vorticity is related to the growth of error in the wind fields, the local change of divergence due to the analysis was diagnosed for all grid points on the analysis grid using Gauss' Theorem. Areas of excessive change in divergence due to the analysis were studied in more detail to determine the cause for the drastic change in divergence. It was quickly noticed that using the geostrophy coefficient  $G = 1 - \exp[0.05|\phi|]$  at low latitudes led to an over amplification at low

---

6. Mitchell, K. E., 1985: A comparison of moisture variables in the vertical interpolations of a 4-D data assimilation system. Proceedings, Seventh Conference on Numerical Weather Prediction, Omaha; American Meteorological Society (AMS), Boston, 310-317.

latitudes of height residuals used to correct winds when the derived weights are non-dimensionalized. This was corrected by adopting the new definition for geostrophy given earlier. However, the steep slope of the G curve in Fig. 1 between 10° and 25° sometimes caused excessively large or small values of the factor  $G_{g_j} f_j / G_{j_g} f_g$  which is used to modify the weight for a wind observation at point j used to correct a grid point g wind value. This was corrected by using Bergman's (1979)<sup>7</sup> assumption that the variance of the wind,  $u_i^2$  or  $v_i^2$ , is constant in the vicinity of a particular grid point and level, and thus the weights used for winds at observation sites to correct winds at analysis points are not modified. In other cases, especially at low latitudes, weights with excessive values were being obtained, indicating that the correlation matrix was nearly singular. A test for excessive weights was installed, forcing the recalculation of the weights (by removing one of the two observations most highly correlated with another, then resolving the reduced matrix equation) if any of the weights has a value exceeding 1.1.

It was noticed that, by choosing the ten closest observations to the grid point on the basis of distance alone, many times some of the closest observations had the lowest actual correlation with the grid point. This resulted from the fact that in the selection process, each observation's correlation with the grid point is divided by  $1 + c_i^2$ , where  $c_i$  is the normalized observation error value. In this way an observation's reliability is used as a factor in its selection. The less reliable observations, with their larger value of  $c_i$ , will not have as much influence in the analysis. Thus, the method of selecting the ten observations to be used in the analysis was changed as follows: for each height observation, its correlation with grid point z, u, v (including the  $1 + c_i^2$  factor) was computed, and the sum of the absolute values of the three correlations was stored. For each wind observation, the six correlations uz, vz, uu, vu, uv, vv (where in all cases the second letter in each pair denotes the variable at the grid point) were calculated using the  $1 + c_i^2$  factor, and the sums  $|uz| + |uu| + |uv|$  and  $|vz| + |vu| + |vv|$  were averaged and stored. Then these absolute sums for

7. Bergman, K. H., 1979: Multivariate analysis of temperatures and winds using optimum interpolation. Mon. Wea. Rev., 107, 1423-1444.

all height and wind observations were compared against each other, and the observations with the ten highest values of these quantities (all of which had to be  $\geq 0.1$ ) were the observations chosen for the analysis. This was done in an attempt to choose those observations that would have the maximum overall influence in the analysis of  $z$ ,  $u$ , and  $v$ , since the ASAP analysis uses the same observations to analyze all three at a particular grid point.

Several other modifications were made in an attempt to bring under control the change in divergence due to the analysis. First, since no other type of observation is allowed to impose an error flag on rawinsonde observations in the buddy checking procedure, there were isolated cases of single erroneous rawinsonde observations lying in the same buddy check box as observations of other types (e.g., satellite, aircraft). As a result, the erroneous rawinsonde observations were being allowed into the analysis. To prevent this, the gross error limits for residuals were changed from their previous value of four times the standard deviation to 2.5 times the standard deviation. Secondly, the limits for the height and wind corrections were reset to 250 m and  $25 \text{ m s}^{-1}$  respectively. Thirdly, the previously mentioned co-location study of satellite sounding data with rawinsonde observations showed RMS differences in temperature of a vertically averaged value of  $3.5^\circ \text{ K}$ . Since rawinsonde temperature observations were assigned a value of  $1^\circ \text{ K}$ , the square root of the difference of the squares of these two values (3.35) was used as the factor by which rawinsonde height observation error standard deviations were multiplied to obtain the corresponding values for satellites. Also, in assigning points to the observations for the searching procedure (see Gerlach, 1983), the factor  $1/3.35$  multiplies the points assigned to a satellite height observation to make it less likely to be chosen when observations of other types are available.

As mentioned in Halberstam *et al.* (1984), the Flattery routine used to convert calculated sigma layer height corrections to temperature corrections occasionally produced temperature corrections in the top layer that were not realistic due to an extrapolation. A modification to remedy the problem was sought but no suitable solution was found. Therefore, in the present version of the ASAP analysis, the temperature correction for the highest sigma layer is set to zero, meaning that the first guess temperature field is left unaltered in this layer.

Previously, the analysis of specific humidity for a particular grid point was performed immediately after the height and wind analysis for that same point. Recently, the humidity analysis was converted from analysis of specific humidity to analysis of relative humidity, and was separated from the mass-motion procedure as a separate code. The humidity analysis is now performed at the lower sigma layers only, with the highest sigma layer in this group being the lowest sigma layer having a nominal pressure (i.e., assuming  $p_s = 1000$  mb) less than 300 mb. In the NMC 12 sigma layer structure currently used, the humidity analysis is performed in the lowest seven sigma layers. The horizontal and vertical structure functions given by Dey and Morone (1985) for relative humidity are now used in the moisture analysis, which necessitates the use of the previously analyzed temperature and wind values. Analyzed temperature and relative humidity at each grid point are used to compute specific humidity, which is then converted to spectral form along with the other analyzed variables. The forecast error standard deviations used for relative humidity are given in Table 2.

TABLE 2. FORECAST ERROR STANDARD DEVIATIONS FOR RELATIVE HUMIDITY BASED ON NMC STATISTICS, MARCH 1983

	<u>90S-10S</u>	<u>10S-10N</u>	<u>10N-30N</u>	<u>30N-50N</u>	<u>50N-90N</u>
1000 mb	.19	.18	.15	.16	.21
850	.23	.19	.20	.22	.22
700	.23	.21	.18	.27	.29
500	.20	.19	.17	.26	.30
400	.22	.17	.14	.26	.30
300	.22	.22	.18	.25	.27

### 3. Investigation of Alternative Sources of Moisture Information

An Air Force requirement for improved global cloud distribution forecasts implies a need for more accurate forecasts of global atmospheric

humidity. Current global forecast models tend to generate a "model-preferred" humidity climatology so that after some 24 hours of forecast time, the distinct spatially varying character of the initial humidity distribution is "smeared out" over the model domain. Along with work being done by AFGL scientists on improving the realism with which the global model itself handles humidity, SASC Technologies, Inc. has nearly completed experimentation in testing the use of alternate forms of moisture information in an attempt to prepare a more realistic initial humidity field for the forecast model. This section describes the steps taken in considering alternative types of global atmospheric humidity information to supplement the relatively sparse rawinsonde observations.

Typically, the initial conditions are prepared in a forecast model-analysis data assimilation sequence, in which the short term (6 h) forecast provides the "first guess" for an analysis that uses synoptic observations coinciding with that forecast time. However, in regions where conventional humidity observations are sparse, no observations are available to correct the forecast drift toward its preferred humidity distribution as the assimilation sequence is run to prepare subsequent analyses. In Fig. 2, zonal mean cross sections of analyzed data (FGGE III-A) and observed data (rawinsonde), which were both time averaged over an 18-day period in February 1979, reveal significant differences between an assimilated analysis and observations, especially at upper levels where the analyzed fields are more moist than the observed fields. The current project involves consideration of three other forms of moisture information to "fill in" the otherwise data void areas: (1) satellite observed layer precipitable water, (2) upper air relative humidity inferred from surface weather observations, and (3) upper air relative humidity inferred from global cloud analyses. For each type of supplementary information the following steps were taken in investigating their possible use in the ASAP humidity analysis: (1) identify the source of such data, (2) determine how best to convert the information to estimate upper air relative humidity, (3) estimate an error level associated with the information by comparing it with co-located rawinsonde humidity, then determining whether or not the error level is acceptable, and (4) determine the best way to include the estimated relative humidities in the OI procedure.

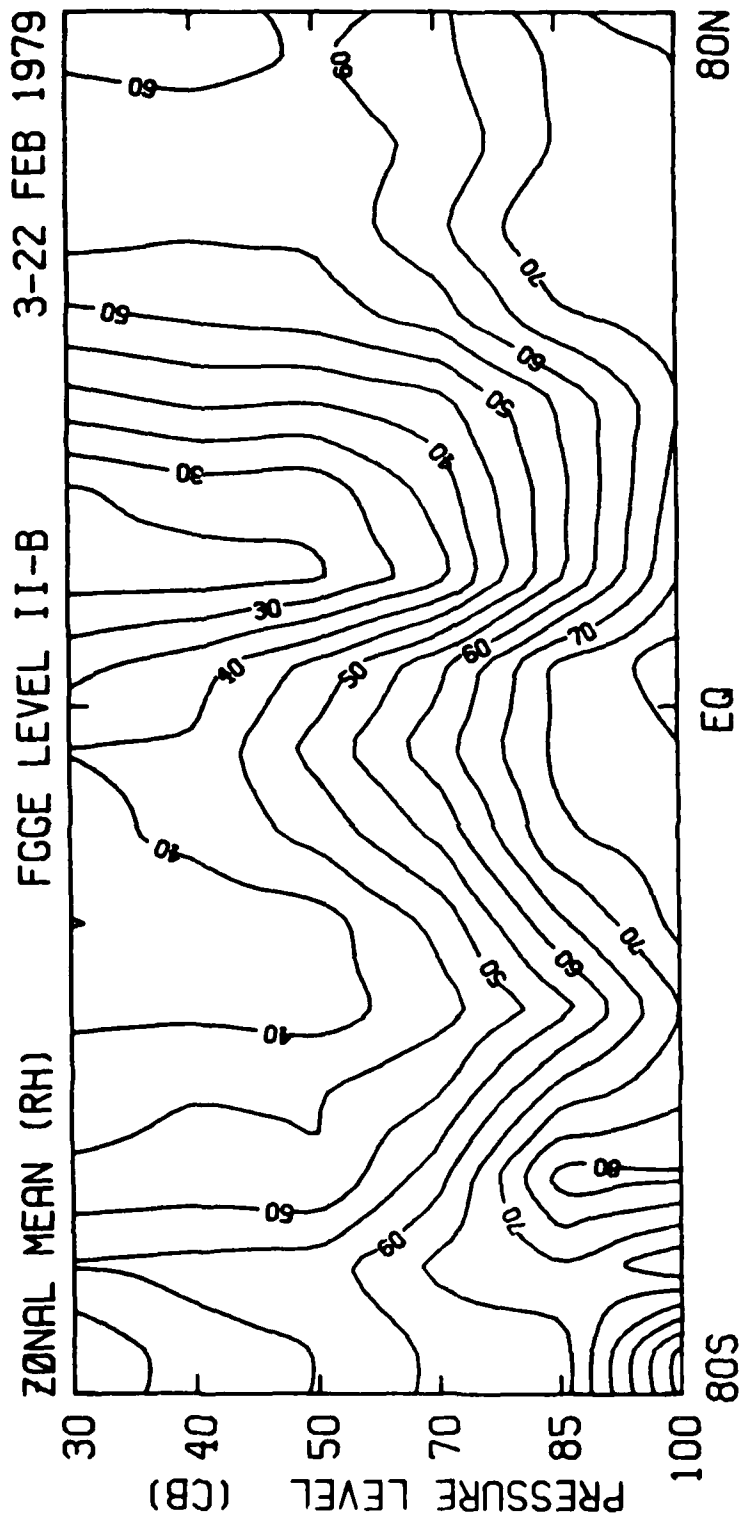


Fig. 2a. Zonal Mean Cross Sections of Relative Humidity from FGGE II-B Observations during the Period 2/3/79 12 GMT - 2/22/79 00 GMT



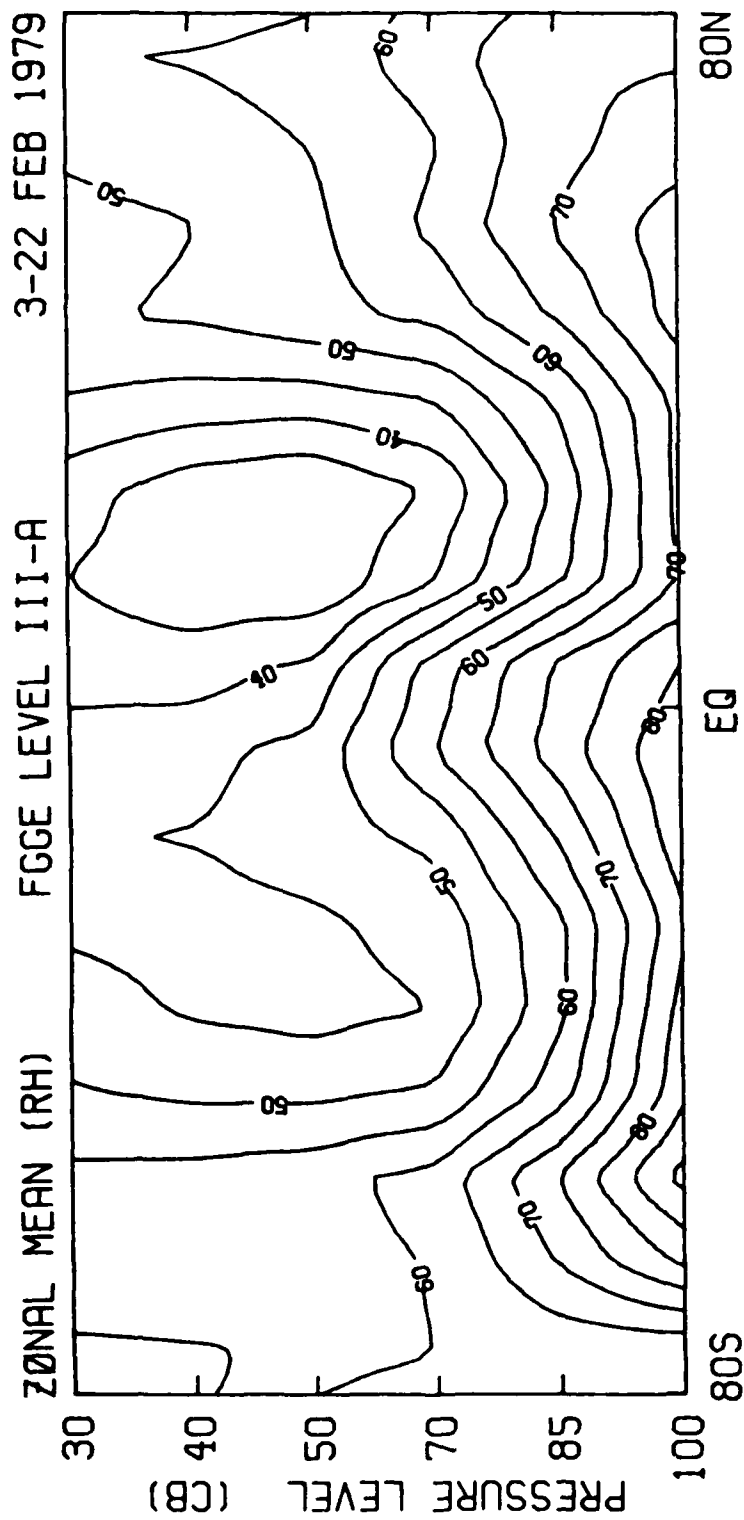


Fig. 2b. Zonal Mean Cross Sections of Relative Humidity from FGGE III-A Analyses during the Period 2/3/79 12 GMT - 2/22/79 00 GMT

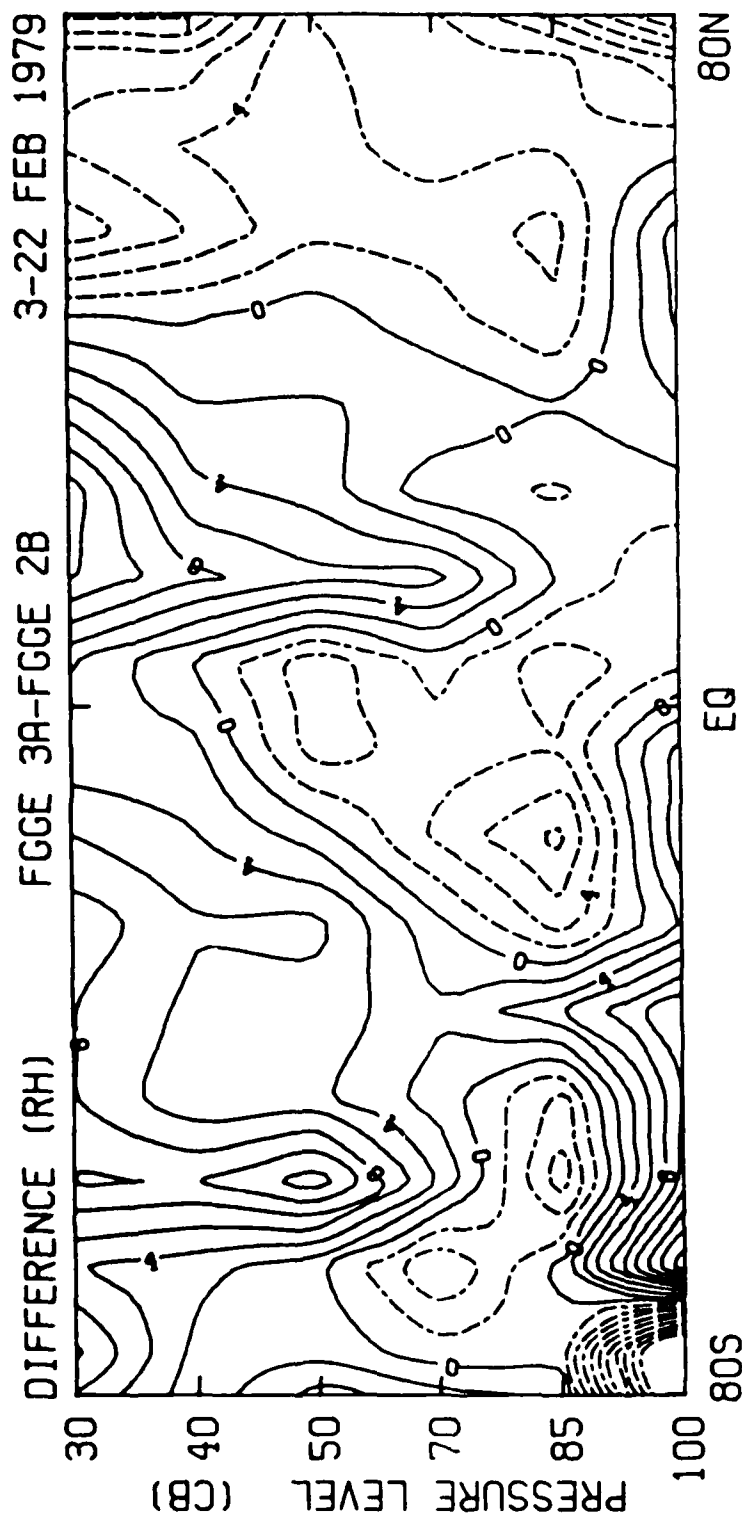


Fig. 2c. Difference between FGGE III-A Zonal Mean Analyses and FGGE II-B Zonal Mean Observations for the Period 2/3/79 12 GMT - 2/22/79 00 GMT

a. Satellite Observed Layer Precipitable Water

Satellite layer precipitable water (LPW) data are available from the special observing periods of the FGGE II-B data set. Values of LPW in mm were given for the layers 1000 mb - 700 mb, 700 mb - 500 mb, and 500 mb - 300 mb. RMS differences between relative humidity obtained from satellite LPW and rawinsonde values that were within 0.5° latitude and longitude of each other were calculated for the period February 3, 1979 12 Z to February 22, 1979 00 Z at 6 h intervals. For each satellite observation that was found to be co-located with a rawinsonde observation for the same date and time, LPW values were converted to mandatory level specific humidity  $q$  using the definition of LPW given by

$$W = \frac{1}{g\rho_0} \int_{p_u}^{p_l} q dp$$

and assuming that specific humidity varies linearly with  $\ln p$  between the two pressure surfaces  $p_l$  and  $p_u$  according to

$$q(p) = \frac{q(p_l) + q(p_u)}{2} + \frac{q(p_l) - q(p_u)}{\ln p_l - \ln p_u} \left[ \ln p - \frac{\ln p_l + \ln p_u}{2} \right].$$

Substituting this expression into the integral definition of  $W$  above, we obtain the following expression for  $q(p_l)$ :

$$q(p_l) = \frac{Wg\rho_0 - q(p_u)[(1/2)(p_l - p_u) + A]}{(1/2)(p_l - p_u) - A}$$

$$\text{where } A(p_l, p_u) = \frac{p_l - p_u}{\ln p_l - \ln p_u} - (1/2)(p_l + p_u).$$

Thus, knowing the layer precipitable water (in  $10^{-1}$  m) and the top and bottom pressures of the layer (in mb), and using  $g = 9.8 \text{ m s}^{-2}$  and the density of water  $\rho_0 = 1 \text{ g cm}^{-3}$ , then  $q$  will have units of  $\text{g g}^{-1}$ .

The rawinsonde value of  $q$  at the top of the uppermost satellite observation reporting layer (usually 500 mb - 300 mb) was used to anchor the  $q$

calculation. In this way, a satellite observation value for  $q$  was derived for 500 mb and 700 mb. The satellite sounding temperature values reported with the LPW values were used to convert  $q$  to relative humidity (RH). Because the reported  $T$  values for the satellite are actually a mean temperature for the observation layer, these were interpolated from the mean layer pressures to the mandatory level pressures in order to perform this conversion. Thus, since no extrapolation was allowed in this  $T$  interpolation and the bottom of the lowest  $T$  layer is 1000 mb, no 1000 mb value of  $T$  was calculated, so that no 1000 mb value of satellite RH was calculated, even though a value of  $q$  was available. RMS differences for 700 mb and 500 mb for the February period were calculated to be 34 percent and 53 percent in relative humidity respectively, and even though the same calculation for a similar period in June 1979 resulted in values of 22 percent and 25 percent, the results were clearly disappointing.

In order to determine if a correction relationship between satellite RH and rawinsonde RH could be derived empirically, scatter plots of the two sets of values were constructed and are shown for the February period in Figs. 3 (a-b). Because of the significant scatter observed, no attempt was made to try to develop a correction function for satellite RH. Comparisons of rawinsonde RH converted to LPW with satellite LPW were just as disappointing, with RMS differences in LPW ranging from 50 to 70 percent of the averaged rawinsonde values. It was decided not to use the Final FGGE II-B satellite moisture values because of their large, rather random differences with rawinsonde values. However, it is possible that at some later date a similar study may be conducted using the satellite LPW from the reprocessed data set to see if those data offer more promise, as suggested by Lonnborg.

b. Upper Air Relative Humidity Inferred from Surface Weather Observations

Surface weather observations (SWO) included in the FGGE II-B data set were used in a similar co-location study to see how well upper air RH inferred from them would agree with nearby rawinsonde RH. The algorithm described by Tibaldi (1982),<sup>8</sup> modified slightly from a method first

8. Tibaldi, S., 1982: The ECMWF humidity analysis and its general impact on global forecasts and on the forecasts in the Mediterranean area in particular. Rivista di Meteorologia Aeronautica, 42, 309-328.

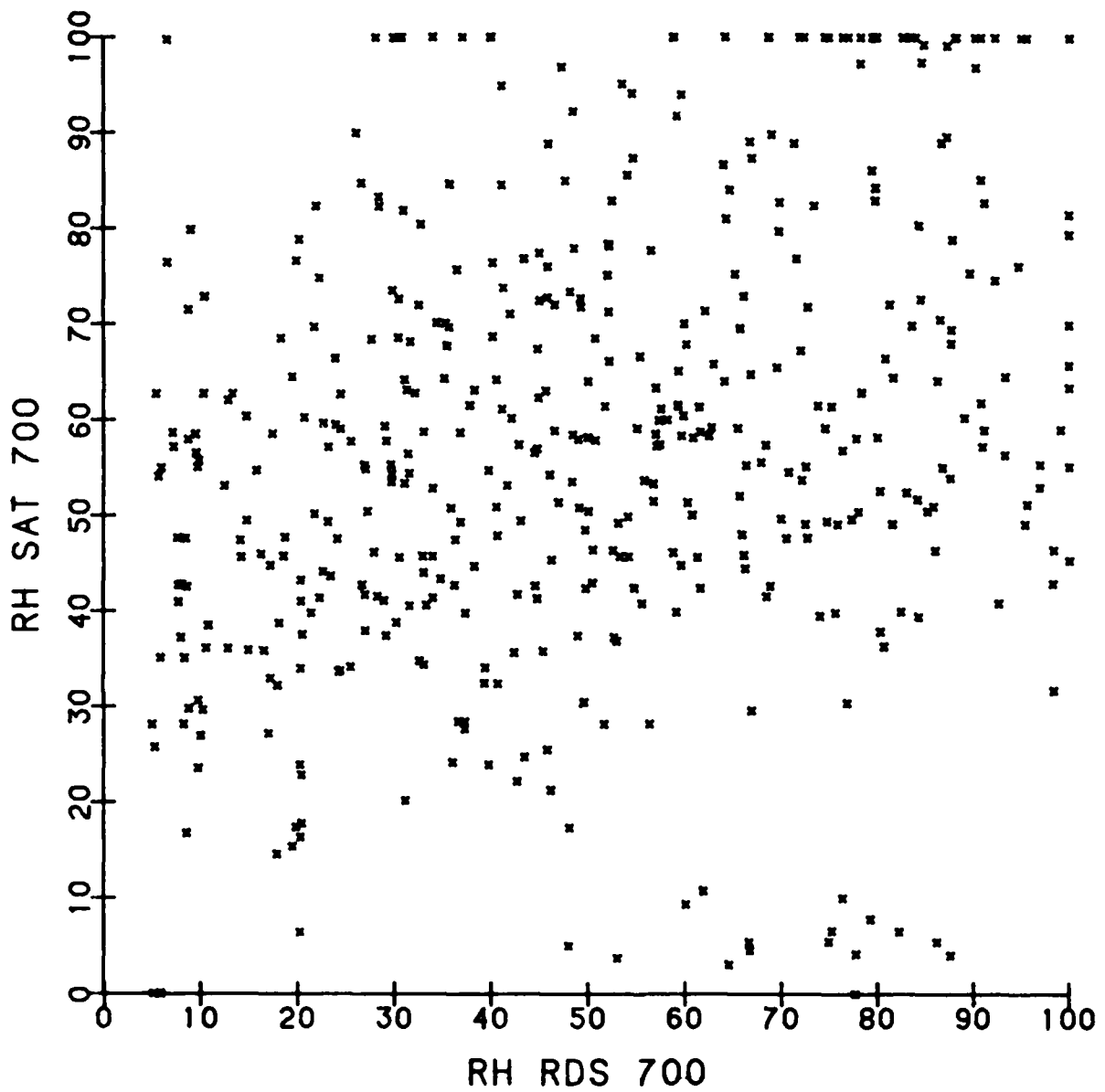


Fig. 3a. Satellite LPW Estimates of 700 mb RH vs. Rawinsonde 700 mb RH for 2/3/79 12 GMT - 2/22/79 00 GMT

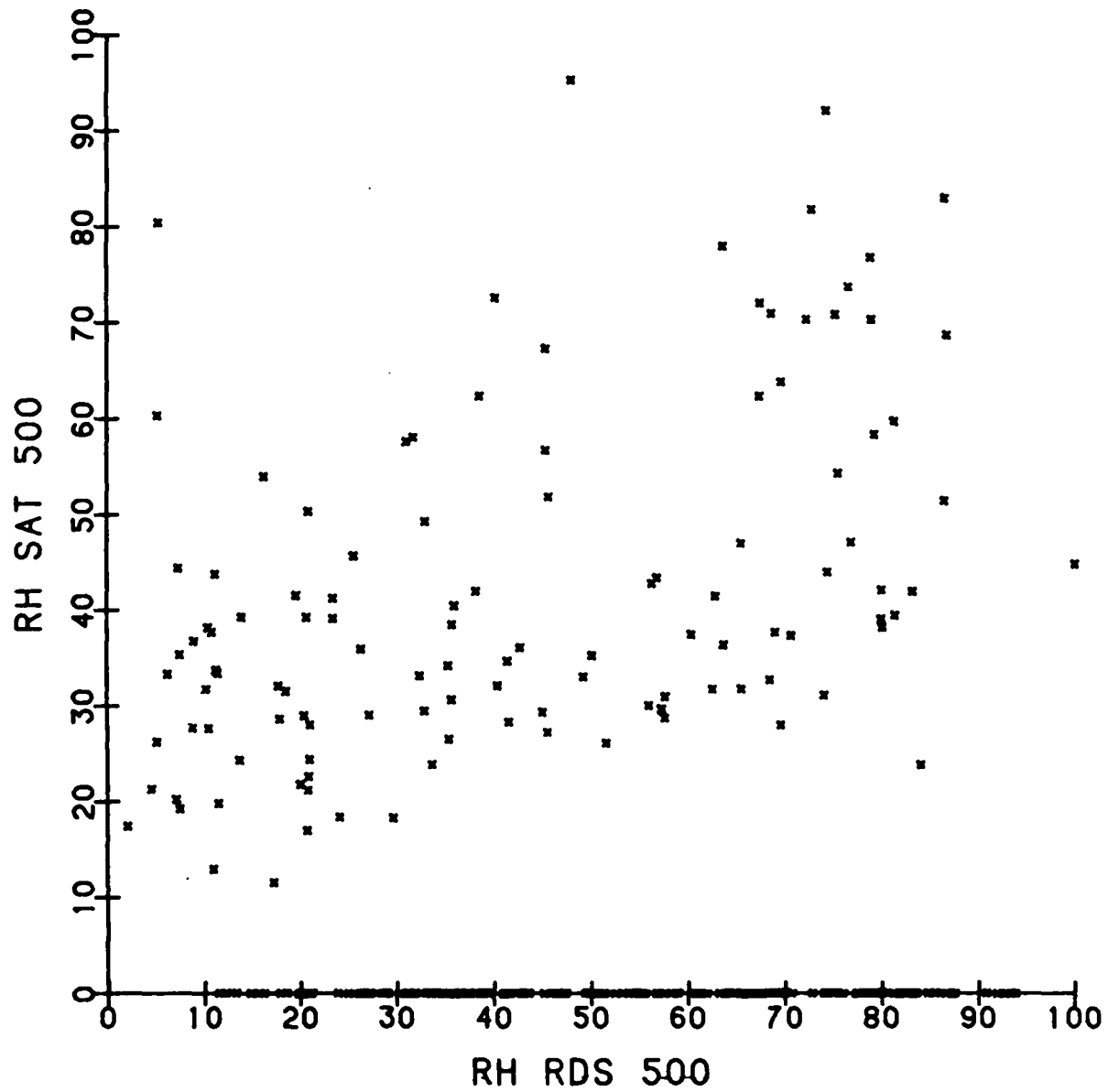


Fig. 3b. Same as for Fig. 3a, except for 500 mb

described by Chu and Parrish (1977),<sup>9</sup> was used as the basic procedure to estimate upper air RH from SWO. The SWO is used to obtain an estimate of the average relative humidity in four layers approximating the planetary boundary layer and the layers used for the classification of low, medium, and high clouds. The details of how the surface weather parameters are used to make these mean layer estimates will not be given here; instead, the following paragraphs will describe how the scheme was actually applied to the FGGE II-B surface observations.

For each surface observation co-located with a rawinsonde observation (within 0.01° in latitude and longitude), the observed surface pressure was used to define the boundaries of the four layers for which the mean RH was to be calculated. For the boundary layer, 60 percent RH was the value assigned for the RH estimate from clouds (RHPBL) if there were no low clouds present or if low clouds had a cloud base height greater than or equal to 600 m. If low clouds were present, the value of RHPBL was set using the expression  $RHPBL = M_{PBL} - A_{PBL} \cos [(\pi/8) OKTAS_{PBL}]$  in which  $OKTAS_{PBL}$  had one of two values: (1) if in the significant cloud record, significant cloud types 6 through 9 are present (cloud types Sc, St, Cu, Cb), the  $OKTAS_{PBL}$  is set to the significant cloud amount for that cloud type, or (2) if significant cloud data are not available, but the amount of low or middle clouds is non-zero and reported low cloud type is identified and the cloud base height is less than or equal to 600 m, the amount of low or middle clouds in the report is used for  $OKTAS_{PBL}$ . Then the algebraic average of RHPBL, RHTD (RH from observed dew point temperature), and RHWW (RH estimated from present weather table) is used to estimate RH for the PBL layer.

A default value of 60 percent RH is also used for RHLC for the "low" cloud layer if no low clouds are present. If low clouds are

---

9. Chu, R., and D. Parrish, 1977: Humidity Analyses for Operational Prediction Models at the National Meteorological Center. National Oceanic and Atmospheric Administration (NOAA), National Meteorological Center Office Note 140.

present, the value of RHLC was set using  $RHLC = M_{LC} - A_{LC} \cos [(w/8) OKTAS_{LC}]$  where  $OKTAS_{LC}$  is set in the same way as for  $OKTAS_{PBL}$  except the condition for cloud base height is removed in circumstance (2). Then the algebraic average of RHLC and RHWW is used to give the RH estimate for the "low" layer.

A value of 45 percent is assigned for the estimate of RH in the "middle" layer if no middle layer clouds (types Ac, As, Nc) are present. If such clouds are present, the significant cloud amount is assigned to  $OKTAS_{MC}$  if the middle layer significant cloud information is available, and if not the amount of low or middle clouds is used for  $OKTAS_{MC}$ . In either of these two cases, the estimate of RH in the "middle" layer is obtained from  $M_{MC} - A_{MC} \cos [(w/8) OKTAS_{MC}]$ .

A value of 45 percent is assigned for the estimate of RH in the "high" layer if no high layer clouds (types Ci, Cc, Cs) are present. If such clouds are present, the significant cloud amount is assigned to  $OKTAS_{HC}$  if the high layer significant cloud information is available. If not, and if the total cloud amount is non-zero and there are no low and middle clouds present, the total cloud amount is assigned to  $OKTAS_{HC}$ . If the latter is not true, "high" layer RH is assigned as missing. The value of  $OKTAS_{HC}$  is then used in  $M_{HC} - A_{HC} \cos [(w/8) OKTAS_{HC}]$  to estimate RH for the "high" layer.

The estimates of SWO RH for the mandatory levels 1000 mb through 300 mb were obtained by simply assigning the computed RH value from the cloud layer into which each mandatory level falls. The mandatory level estimates of RH were then compared with the corresponding rawinsonde values, and the resulting RMS differences for the February period are given in Table 3 (values in parentheses indicate number of observations involved in each calculation). These were judged to be acceptable for approximating humidities in otherwise data void areas, since even with the 20 - 25 percent RMS difference with rawinsonde, one might still be able to judge whether a nearby first guess value of RH was too high or too low with a fair degree of certainty.

The column next to the SWO-rawinsonde RMS difference column in Table 3 contains the estimates of observation error standard deviation for SWO inferred upper air RH. An observation  $\hat{F}_{ik}$  for a variable k at



TABLE 3. RMS AND OBSERVATION ERROR STANDARD DEVIATION FOR RH VALUES FROM THREE TYPES OF MOISTURE INFORMATION

	S = Satellite		S = Surface WX Inferred		S = 3DNEPH Inferred*	
	$\frac{1}{2} \frac{[(R_{sat} - R_{raob})^2]}{(e_{sat})^2}$	$\frac{1}{2}$	$\frac{1}{2} \frac{[(R_{sfc} - R_{raob})^2]}{(e_{sfc})^2}$	$\frac{1}{2}$	$\frac{1}{2} \frac{[(R_{3DNEPH} - R_{raob})^2]}{(e_{3DNEPH})^2}$	$\frac{1}{2}$
1000 mb	--	--	.13 (13554)	.12	--	--
850	--	--	.22 (23393)	.21	.20 (8251)	.20
700	.34 (456)	.34	.25 (15986)	.24	.25 (13570)	.25
500	.53 (305)	.53	.24 (12030)	.23	.24 (10837)	.24
400	--	--	.23 (9536)	.22	.23 (4907)	.22
300	--	--	.22 (8457)	.22	.21 (7342)	.21

\*Using Chu-Parrish method

location  $i$  has an observational error  $e_{ik}$  associated with it such that  $\hat{F}_{ik} = F_{ik} + e_{ik}$ , where  $F_{ik}$  is the true value. Now, at any time  $e_{ik}$  can be positive or negative, and if the error is truly random in time, the true value  $F_{ik}$  can be estimated by an average of  $\hat{F}_{ik}$  over many times of observations. Thus, the quantity  $\overline{(e_{ik}^2)^{1/2}} = \overline{[(\hat{F}_{ik} - F_{ik})^2]^{1/2}}$ , where the overbars represent an average over a large time ensemble, is referred to as the observation error standard deviation, because  $F_{ik} \sim \hat{F}_{ik}$  for temporally random error  $e_{ik}$ . To determine the observation error standard deviation  $\overline{(e_{ik}^s)^2}^{1/2}$  for an observation system  $s$  when the same for observing system  $r$  is known, Bergman (1978)<sup>10</sup> showed that for two types of observations  $\hat{F}_{ik}^r$ ,  $\hat{F}_{ik}^s$  measured sufficiently close in space and time

$$\overline{(e_{ik}^s)^2} \sim \overline{(\hat{F}_{ik}^r - \hat{F}_{ik}^s)^2} - \overline{(e_{ik}^r)^2}$$

where it is assumed that observational errors are uncorrelated with each other or with the difference in true values. Since  $\overline{(\hat{F}_{ik}^r - \hat{F}_{ik}^s)^2}$  is just the square of the RMS difference between the two different types of co-located observations (where invariance in space is assumed, so the overbar represents the average over all co-located observations in time and space), we need only to assign an observational error standard deviation for rawinsonde humidity to calculate the same value for SWO humidity. Dey and Morone (1985) suggested a value of 20 percent, whereas Gustafsson (1981)<sup>11</sup> suggested a random error for rawinsonde humidity of five percent. Although five percent is probably a little optimistic, the value of 20 percent would yield considerably larger values of normalized observation error when divided by

10. Bergman, K. H., 1978: Role of observational errors in optimum interpolation analysis. Bull. Amer. Met. Soc., 59, 1603-1611.

11. Gustafsson, N., 1981: A review of methods for objective analysis. Dynamic Meteorology: Data Assimilation Methods, Vol. 36, Applied Mathematical Sciences Series, L. Bengtsson, M. Ghil, and E. Källén, eds., Springer-Verlag, 330 pp.

the forecast error standard deviation values given in Table 2 and would thus give much less weight to the critically needed rawinsonde humidities in the analysis. For this reason, the value of five percent was used in the analysis and in the computation of observation error standard deviation values shown in Table 3.

The next step was to determine the spatial correlations (if any) between observation errors of RH using a particular observing system. In this case, since upper air RH is not explicitly measured in SWO or cloud analyses, the "observation error" would really be a measure of the error of estimate of the RH inferred from the information given. It will be assumed that observation errors of different observing systems are spatially uncorrelated, and that observational errors are uncorrelated with the true field values. Bergman (1978) showed that, if type "b" observations of RH are compared with co-located type "a" observations in which the latter are assumed to be spatially uncorrelated with each other, the observational error correlation between two type "b" observations at locations i and j is given by

$$\eta_{ij}^b = \frac{\overline{(e_{ib} e_{jb})}}{\overline{(e_{ib}^2 e_{jb}^2)}^{1/2}} = \frac{\overline{\Delta \hat{R}_i \Delta \hat{R}_j}}{\overline{(\Delta \hat{R}_i^2 \Delta \hat{R}_j^2)}^{1/2}}$$

where  $\Delta \hat{R}_i = \hat{R}_{ia} - \hat{R}_{ib}$ , or the difference between observed values at each point in time and location, and the overbar represents an ensemble average over time. This means that for the above assumptions, the observational error correlations for observing system b is equal to the correlation of differences in observed values between observing system a and observing system b.

These correlations were computed for RH values inferred from both SWO and cloud analyses using co-located rawinsondes as the type "a" observation. Traditionally, rawinsonde RH observational errors are assumed to be spatially uncorrelated, and the same assumption was made in this study to allow the correlation of differences to define the correlation of the alternative source estimation error. The above correlation was computed for each pair of RH differences on separate mandatory levels over the time

period 2/3/79 12 Z - 2/22/79 00Z (6 h intervals). Then for each mandatory level, all correlations were grouped by station pair separation distance categories (category 1: 0 - 49.99 km, category 2: 50 - 99.99 km, ..., category 40: 1950 - 1999.99 km) and were averaged within each category, each weighted in the average by the number of time periods included in each correlation. The results of the computation of the isobaric correlations showed that the observation error correlations fell into three categories: observations at 1000 mb and 850 mb seemed to be appreciably less correlated than those at 700 mb and 500 mb, and even less well correlated than those for 400 mb and 300 mb. Thus, the correlation values in these three categories were vertically averaged (weighted by the number of pairs in all correlations over all times at the respective levels), and these averages are plotted vs. separation distance for SWO in Fig. 4 and for cloud analyses in Fig. 5.

Besides the computation of lateral correlations, vertical correlations of observational error were computed for both SWO and cloud analysis RH at each station for all categories of pairs of pressure difference. These were then averaged (each correlation in the average weighted by number of time periods included in the correlation) over all stations to arrive at an averaged correlation for each level pair representing all stations. Fig. 6 shows the results for both SWO and cloud analysis RH. Due to the way RH was estimated from the cloud analyses, the description of which follows, 1000 mb RH was not available for cloud analysis RH.

The method of producing RH estimates from SWO was incorporated as a subroutine into the moisture OI code, being called as an option after all rawinsonde RH observations were processed to form observation-minus-first guess residuals on the sigma layers. Thus, the only difference between its implementation in the OI code and the method to obtain RH estimates on mandatory levels (described earlier) is that in this case the RH value is assigned by whichever of the four cloud layers the sigma pressure falls into.

#### c. Upper Air Relative Humidity Inferred from Cloud Analyses

A global analysis of percentage cloud amounts, generated by the 3DNEPH model of the Air Force Global Weather Central (AFGWC) and

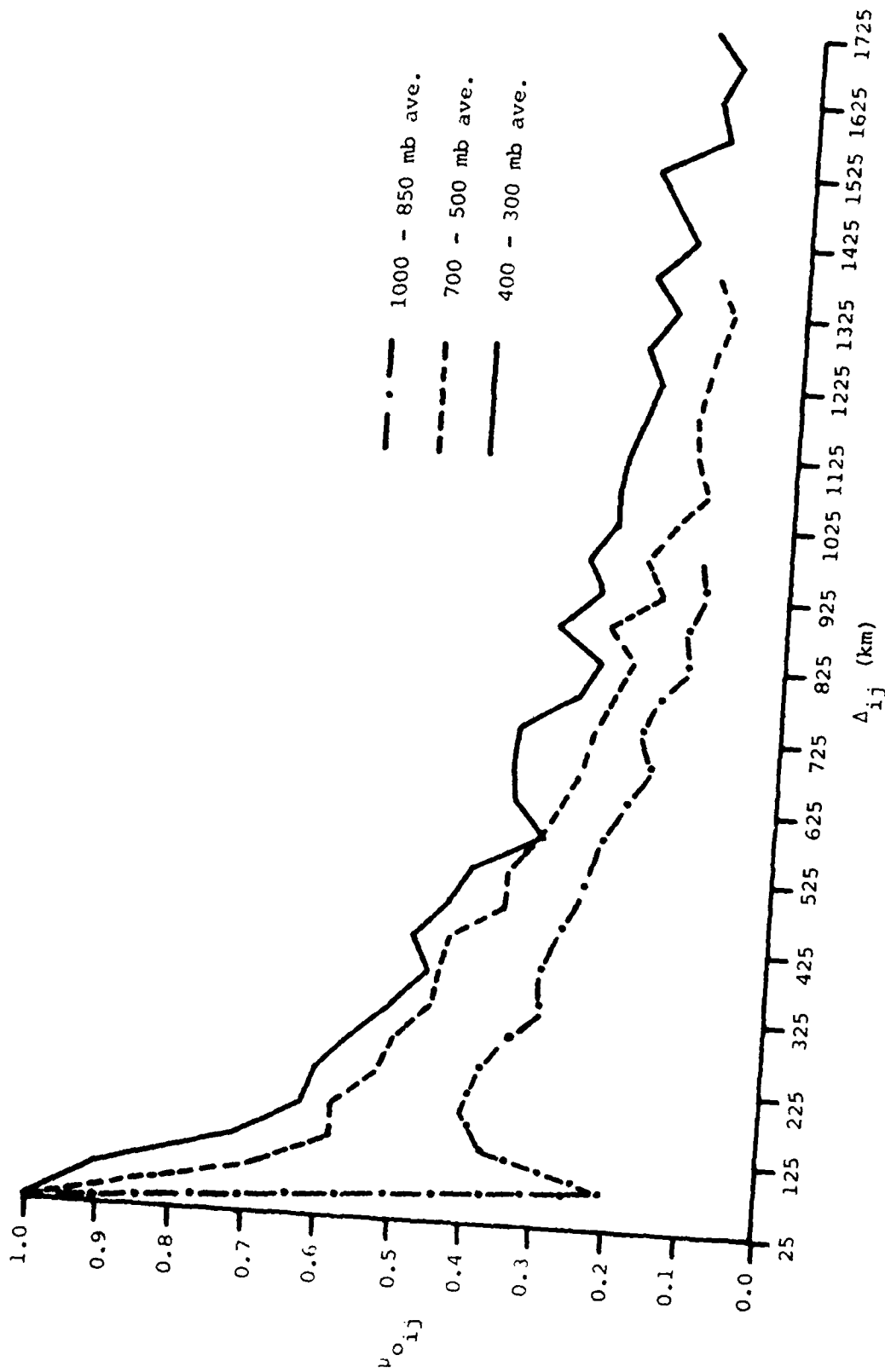


Fig. 4. Isobaric Observation Error Correlation for Surface Wx Observations - Inferred RH Based on RH differences with co-located raob RH for 2/3-22/79.

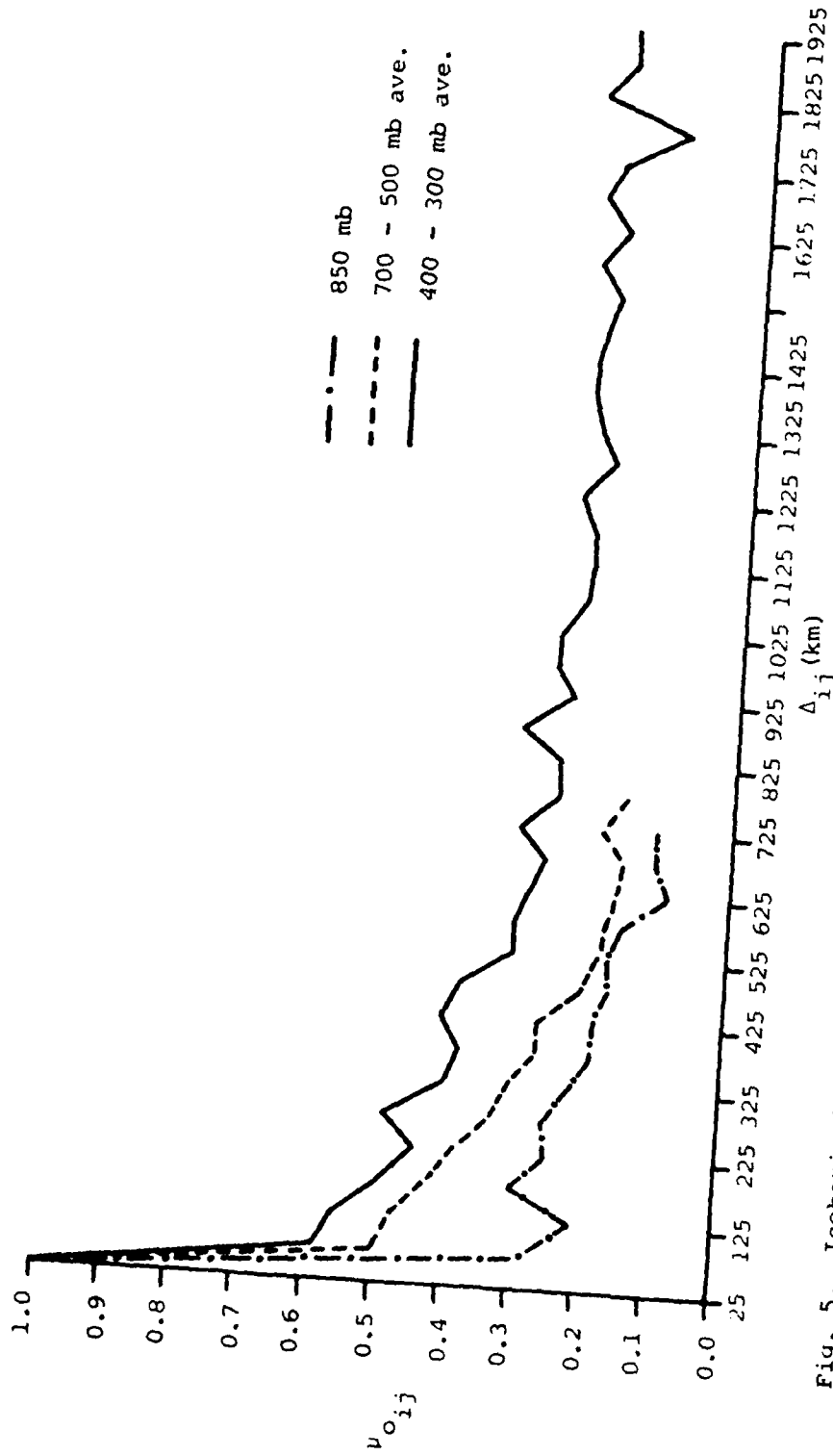


Fig. 5. Isobaric Observation Error Correlation for 3DNEPH - Inferred RH Based on RH differences with co-located raob RH for 2/3-22/79.

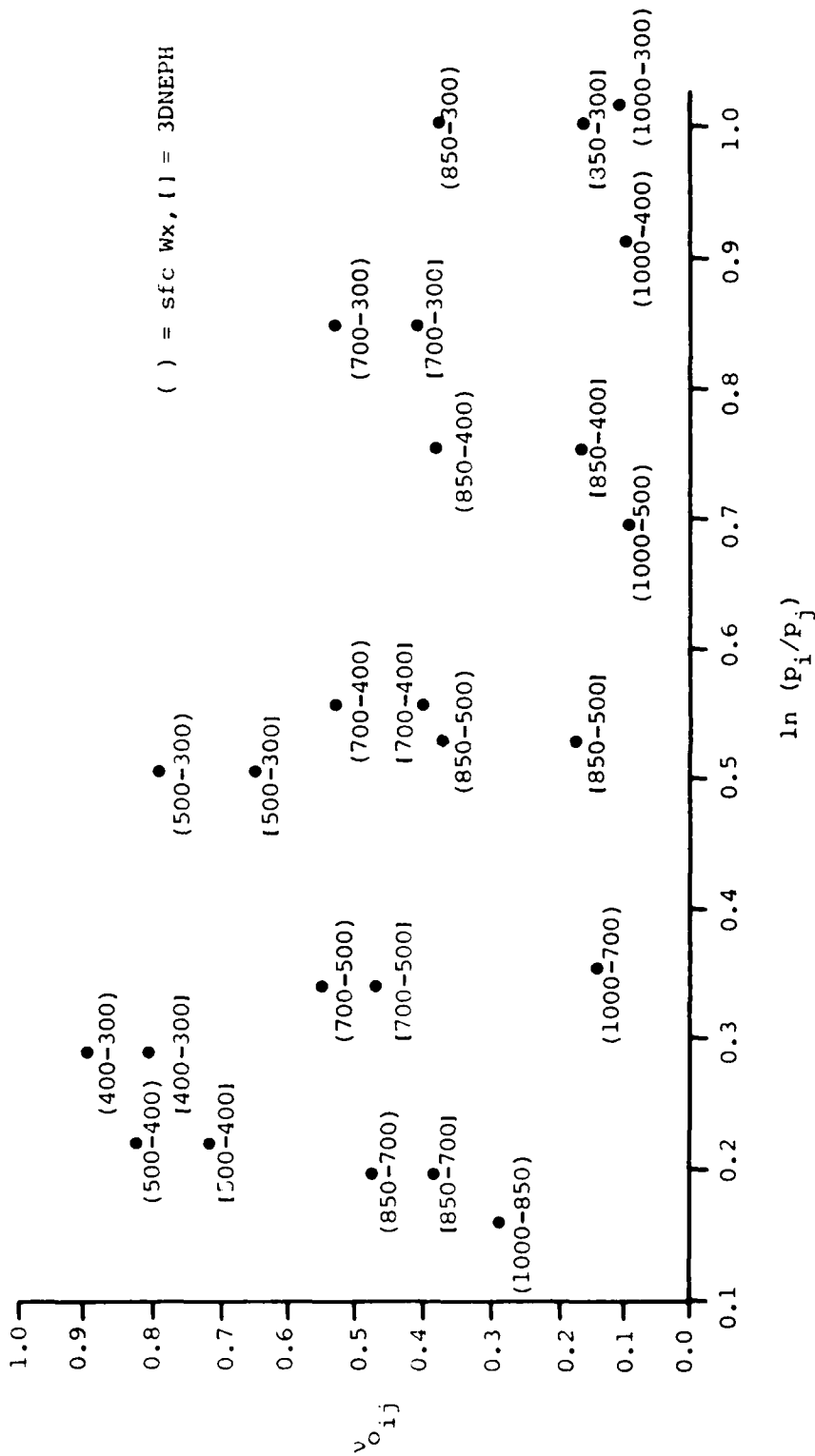


Fig. 6. Vertical Observation Error Correlation for RH  
 Based on RH differences with co-located raob RH for 2/3/79 12Z - 2/22/79 00Z.

available on tapes through the Air Force Environmental Technical Applications Center, was the source of cloud analyses used in this study to infer RH estimates on regular grids. At each time period, the 3DNEPH cloud amounts are available at 15 levels in the atmosphere in 512 X 512 hemispheric grids [eighth mesh on a polar stereographic projection (see Fye, 1978<sup>12</sup>)]. The four steps carried out to get estimates of relative humidity at desired locations were: (1) find the cloud amounts at mandatory levels (vertical compaction), (2) average these values horizontally using 3 point X 3 point arrays of 3DNEPH points to get averaged values at every other eighth mesh point, (3) convert cloud amounts to relative humidity using these averaged cloud amounts, and (4) bilinearly interpolate these relative humidities to desired locations (in the case of comparing with rawinsonde humidities, to the rawinsonde station locations available at each 6 h time period).

These four steps were first applied toward creating files of 3DNEPH RH estimates at all rawinsonde locations for the period 2/3/79 12 Z - 2/22/79 00 Z at 6 h intervals. For each of the 64 X 64 sub-boxes of points in the 3DNEPH grid, the vertical compaction is employed to compact the nine uppermost 3DNEPH cloud layers by computing a weighted average (by approximate pressure thickness of the layers) of layer pairs to form estimates of cloud amounts for the mandatory levels 850, 700, 500, 400, 300 mb. Specifically, 3DNEPH layers 14 and 15 are averaged and assigned to 850, 16 and 17 to 700, 18 and 19 to 500, 20 to 400, and 21 and 22 to 300. Then the horizontal averaging is used to form a 33 X 33 array (every other 3DNEPH point) in the following way: For each 3 X 3 set of 3DNEPH points, if all nine points have cloud percent amounts between 1 and 100 percent, use all nine points in a simple average. If some of the grid points have clear (no cloud) values, average only those with values of cloudiness from 1 - 100 percent if all four triangles of three outermost points have at least one cloudy value in them, and weight the average by the number of cloudy points in each triangle. Throughout the processing of the 3DNEPH data, the philosophy was to use only cloudy areas to estimate humidities, and not try

---

12. Fye, F. K., 1978: The AFGWC Automated Cloud Analysis Model. U. S. Air Force Global Weather Central Technical Memorandum 78-002, Offutt AFB, NE.



to estimate the RH from a cloud free area. In this way, only information from cloudy areas is used as RH input into the analysis.

The next step was to convert the horizontally averaged and vertically compacted cloud amounts to some form of humidity before bilinearly interpolating them to the observation site. This was done in three ways: (1) conversion of cloud amount to condensation pressure spread (CPS) following the AFGWC procedure, (2) conversion of cloud amount to square root of the cloud fraction for use in the Geleyn procedure (Slingo and Ritter, 1985),<sup>13</sup> and (3) conversion of cloud amount to cosine of  $\alpha$  times the fractional cloud amount for use in the Tibaldi (Chu-Parrish) procedure. All three procedures are described in Appendix A. After these conversions, the converted quantities were bilinearly interpolated to observation sites for that particular time and date. Finally the procedures described in Appendix A were used to compute RH from the cloud amount forms, with rawinsonde temperatures being used to convert dew point depression to RH in the AFGWC scheme. The RMS differences and bias values for the February period among the three forms of RH estimates from cloud amounts and the co-located rawinsonde RH values are given in Table 4. On the basis of these results, the Chu-Parrish formula was selected to convert 3DNEPH cloud amount to RH. Observation error standard deviation values (Table 3) and observation error correlations (Figs. 5 and 6) were computed using this method, and were carried out in a manner analogous to that for the SWO computations, so that the mandatory level was assigned an RH value according to which of the four cloud layers it fell into. Finally, values of  $\cos(\alpha \cdot \text{fractional cloud amount})$  on the horizontally averaged grid at the 850 - 300 levels were bilinearly interpolated to a regular grid (3 degrees latitude X  $120 \cdot \cos[\text{latitude}]$  points in longitude) to act as "observations" in the moisture OI subroutine (where first guess surface pressure was used to define the four cloud layers) and were bilinearly interpolated to the 62 X 62 analysis grid for direct replacement of first guess RH at cloudy analysis grid points as a third option in the moisture OI code.

---

13. Slingo, J., and B. Ritter, 1985: Cloud Prediction in the ECMWF Model. European Centre for Medium Range Weather Forecasts Technical Report No. 46, Reading, England.

**TABLE 4. STATISTICS OF DIFFERENCES BETWEEN RELATIVE HUMIDITY INFERRED FROM CLOUD AMOUNT AND THAT MEASURED WITH RADIOSONDES (IN %)**

LEVEL (MB)	AFGWC		ECMWF		NMC	
	BIAS	RMS	BIAS	RMS	BIAS	RMS
850	1	21	10	22	-2	20
700	2	26	15	29	-4	25
500	-7	26	22	32	-5	24
400	-12	30	26	34	-5	23
300	-26	37	31	37	-5	21

THE RESULTS ARE BASED ON OBSERVATIONS  
FOR THE PERIOD 2/3/79 - 2/22/79 00Z

**4. Use of Relative Humidity Observations in the Global Humidity Analysis**

As mentioned previously, the RH optimum interpolation code is currently designed to allow three options: (1) rawinsonde (and, if available, satellite) RH observations only, (2) rawinsonde (and satellite), SWO inferred, and 3DNEPH inferred RH observations, and (3) replace first guess value with 3DNEPH inferred RH at analysis points where it is available (cloudy areas), and perform regular OI using conventional (rawinsonde and satellite) RH observations only at cloud free analysis points. Option 2 is the only case where the supplemental observations are used with the rawinsondes. Because they are estimated rather than observed, the supplementary RH values are to be used primarily where rawinsonde RH observations are few or nonexistent. This philosophy guided development of the option 2 procedure described below.

RH residuals (observation-minus-first guess) for rawinsondes are calculated first at all stations, then if option 2 is selected, the same is done for SWO and 3DNEPH RH estimates. Next, a gross check (40 percent gross limit) and buddy check by sigma layer are performed. For each analysis

site, a search is conducted for nearby observation soundings beginning with rawinsonde observations. For each sounding that has a value of  $\mu$  (where  $\mu = \exp[-k_h \cdot D^2]$ , where  $D$  = separation distance between observation and grid point) greater than 0.1, the total number of "points" (assigned after buddy check, where each sounding gets four points per valid level for rawinsondes and one point per valid level for SWO and 3DNEPH) multiplies its value of  $\mu$  to form  $\mu^*$ . The eight rawinsonde soundings with the largest values of  $\mu^*$  are selected for the analysis at that grid point. If fewer than eight rawinsonde soundings have  $\mu \geq 0.1$ , a search is conducted of the SWO and 3DNEPH RH "soundings" and in this case the eight soundings of any type with the largest values of  $\mu^*$  are selected. Then as the analysis is performed at each sigma layer for that grid point, the correlation of each observation with the grid point (divided by  $1 + \epsilon_i^2$ ) is calculated using the product of isobaric and vertical NMC structure functions (Dey and Morone, 1985) for RH. The ten individual observations with the largest value of the correlation with the grid point (divided by  $1 + \epsilon_i^2$ ) are actually used in the analysis. As in the case of the mass-motion analysis, the division by  $1 + \epsilon_i^2$  of the correlation allows a consideration of the observation quality in both the selection of the observations in the analysis and their computed weights. Thus, a rawinsonde observation considerably farther from the grid point will have just as large a computed correlation as a much nearer SWO or 3DNEPH observation.

Although the planned five day data assimilation runs using the three moisture options have not yet been run, preliminary results from a single analysis of a 12 h global spectral model forecast valid 2/4/79 12 Z are shown in Table 5. Table 5 shows the globally averaged RH values for the forecast and the three analysis options, along with the percentages of the 62 X 62 X 7 analysis points where a correction took place (value in parentheses for RH<sub>3</sub> indicates percent replaced by 3DNEPH value) and the actual number of cases where a matrix singularity was encountered. While no definitive conclusions can be drawn from such preliminary results, it appears that the introduction of the supplemental moisture information has little effect on the global averages, and while they greatly increase the number of grid points where an analysis takes place, their use leads to a disproportionate increase in the number of computationally singular matrices encountered.

TABLE 5. GLOBAL AVERAGE RH ON  $\sigma$  LAYERS 2/4/79 12 FCST AND ANALYSIS

[P $\sigma$ ]	[RH $_{fg}$ ]	[RH $_1$ ]	[RH $_2$ ]	[RH $_3$ ]
948	.83	.80	.76	.76
849	.62	.61	.61	.65
713	.48	.48	.52	.51
565	.47	.47	.47	.47
430	.48	.47	.47	.47
332	.49	.48	.47	.48
270	.50	.48	.47	.48
% Corrected		69.2	96.5	44.2 (34.3)
# Sing. Matrices		38	925	40

RH $_{fg}$ : 12 h fcst

RH $_1$ : analysis (raobs only)

RH $_2$ : analysis (raobs, with SWO and 3DNEPH)

RH $_3$ : 3DNEPH at cloudy analysis pts, raob OI elsewhere

The three experimental data assimilation cycles will be run soon, and their results will be analyzed to determine the effect of including supplemental moisture information in the analysis. This effect will be studied at two levels: (1) in the assimilated analyses, by examining whether or not the extra moisture information leads to more realistic analyses, and (2) what effect such analyses have on long term (to 48 h) forecasts of humidity.

## Appendix A. Conversion of Cloud Amount to Relative Humidity

### 1. AFGWC method

Percent cloud amounts are converted to condensation pressure spread (CPS) using the curves given in Fig. A1. CPS is then converted to dew point depression (DPD) on a pressure surface P (mb) using

$$DPD = CPS[4.9 + 0.93(P/1000) + 9.0 (P/1000)^2]^{-1}.$$

Finally, temperatures from an appropriate source (observation or analysis) are used to convert DPD to relative humidity.

### 2. Geleyn Method

In the ECMWF scheme, total fractional cloud cover is estimated from observed relative humidity at layer k using

$$CLC_k = \left\{ \max \left[ \left( \frac{RH_k - RHC_k}{1 - RHC_k} \right), 0 \right] \right\}^2$$

where

$$RHC_k = 1 - 2\sigma_k + 2\sigma_k^2 + \sqrt{3} \sigma_k (1 - 3\sigma_k + 2\sigma_k^2)$$

$$\sigma_k = \frac{P_k}{P_{sfc}}$$

Curves of relative humidity vs. fractional cloud cover generated from this expression are given for several mandatory pressures in Fig. A2. Solving this expression for  $RH_k$  in terms of fractional cloud cover yields

$$RH_k = RHC_k + \sqrt{CLC(1 - RHC_k)} \quad \text{for } RH_k > RHC_k \leq 1.$$

This computation requires a knowledge of  $\sigma_k$ , which in turn requires a knowledge of the model terrain surface pressure at the geographic location in question. Thus, in the processing of the 3DNEPH data in which surface

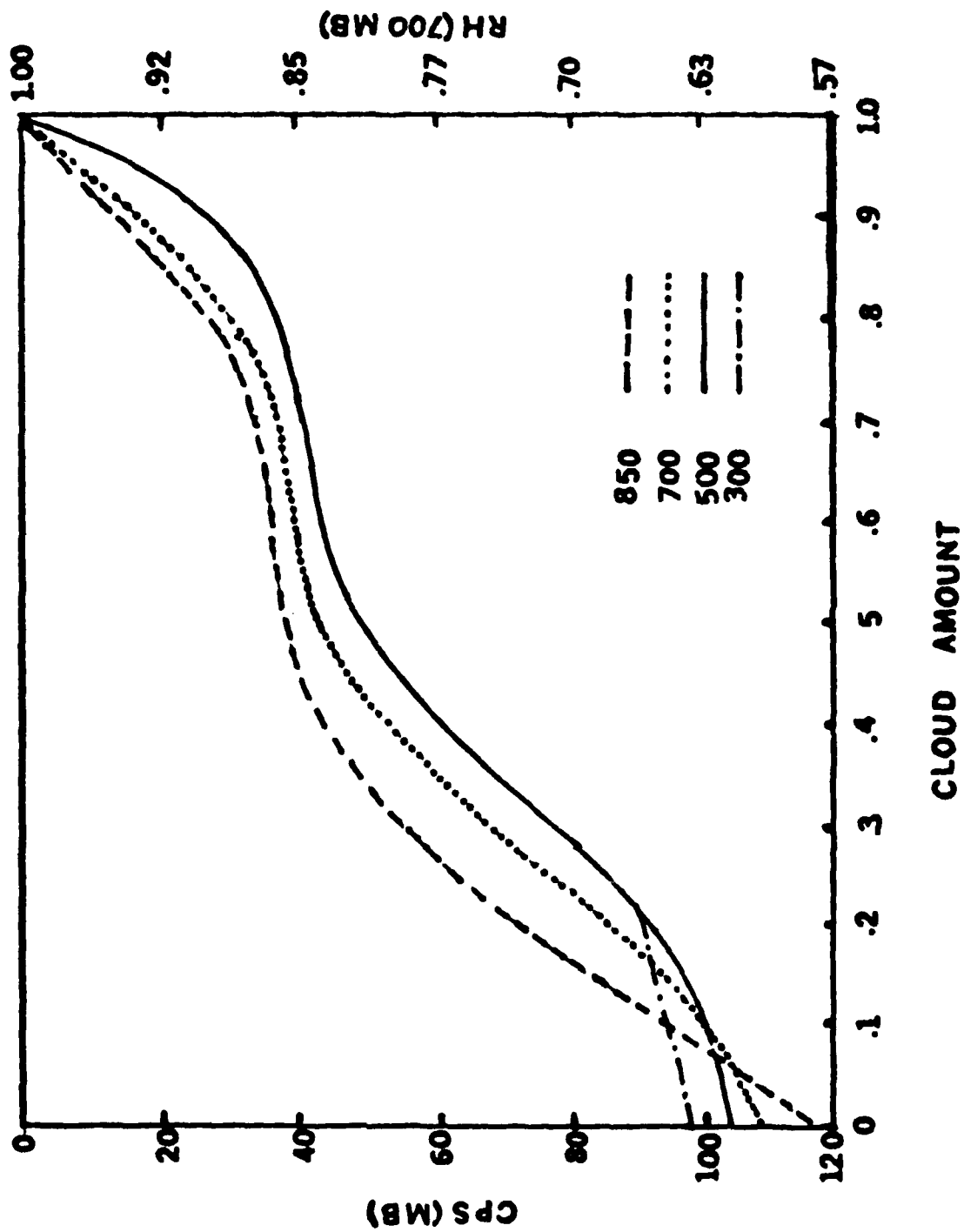


Fig. A1. AFGMC RH-CA Scheme

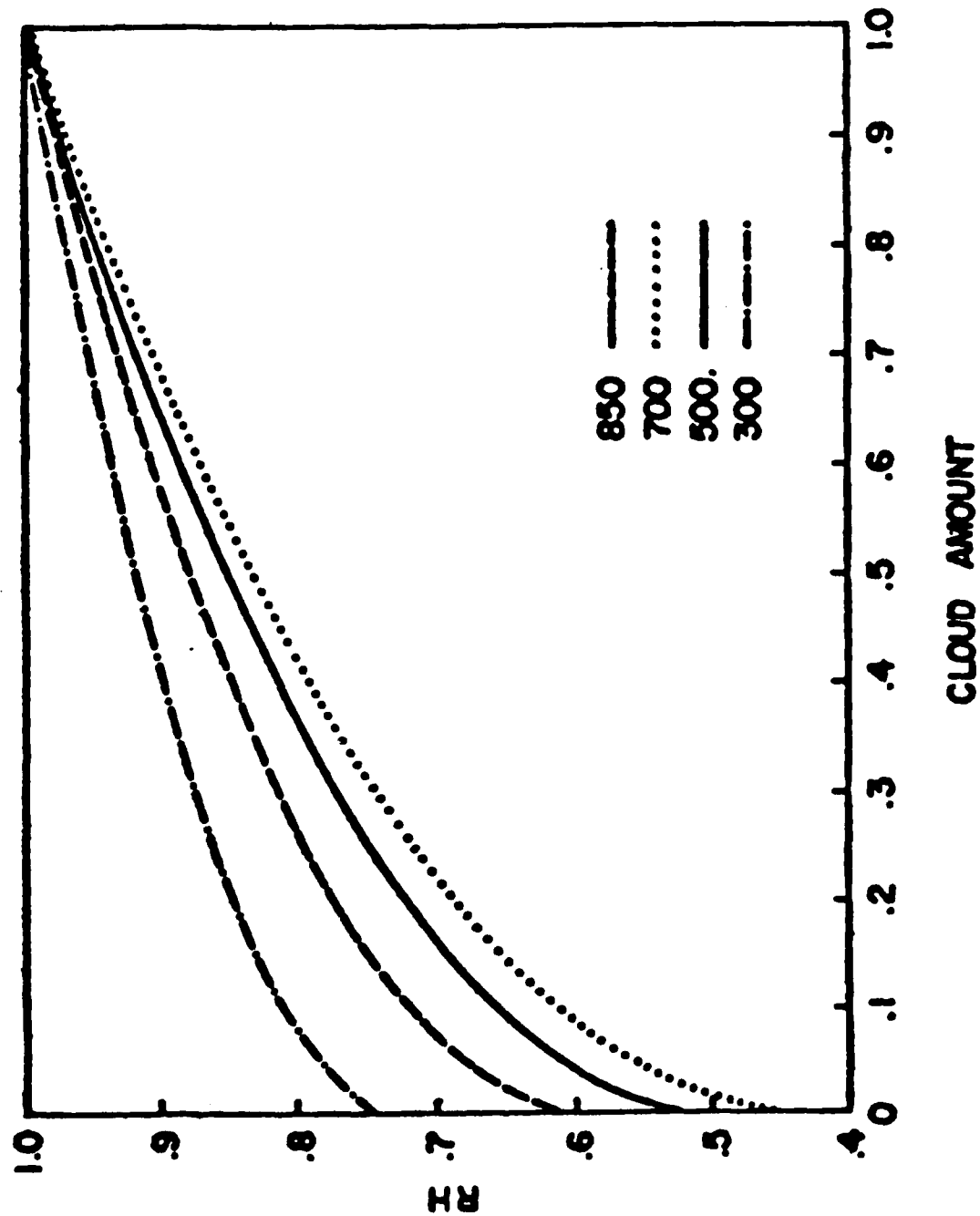


Fig. A2. ECMWF RH-CA Scheme

pressures are unknown, one can go only as far as calculating CLC for  $0.01 \leq 1$ , bilinearly interpolating these to the desired regular latitude-longitude grid, and then later use surface pressures on the same latitude-longitude grid to evaluate  $RH_k$ .

### 3. Tibaldi (from Chu-Parrish) Method

As used in the surface observation of cloud amount-to-RH scheme, this scheme simply uses observed fractional sky cover for four cloud level categories to make one form of estimate of upper level relative humidity. Here, we attempt to apply the same scheme to 3DNEPH cloud amounts to similarly attempt to diagnose upper level RH. The expression used to relate cloud cover to RH is

$$RH_j = M_j - A_j \cos\left(\frac{\pi}{8} \cdot OKTAS_j\right)$$

in which the layers indexed by  $j$  and corresponding values of  $M_j$  and  $A_j$  are given by

<u>j</u>		<u>M<sub>j</sub></u>	<u>A<sub>j</sub></u>
4	High ( $P_4 - P_5$ )	0.55	0.10
3	Middle ( $P_3 - P_4$ )	0.60	0.15
2	Low ( $P_2 - P_3$ )	0.75	0.15
1	P.B.L. ( $P_1 - P_2$ )	0.80	0.20

in which

$$P_1 = P_* \text{ (model surface pressure)}$$

$$P_2 = P_1 - 50 \text{ mb}$$

$$P_3 = P_2 - 1/3(P_2 - P_5)$$

$$P_4 = P_3 - 1/3(P_2 - P_5)$$

$$P_5 = 300 \text{ mb}$$

Fig. A3 shows curves of relative humidity vs. cloud amount (in eighths) for all four cloud layers as generated from this expression. Therefore, here again a knowledge of the model terrain surface pressure is required in order to determine which of the four layers a given 3DNEPH value falls into and thus which values of  $M_j$  and  $A_j$  should be used to compute RH for that



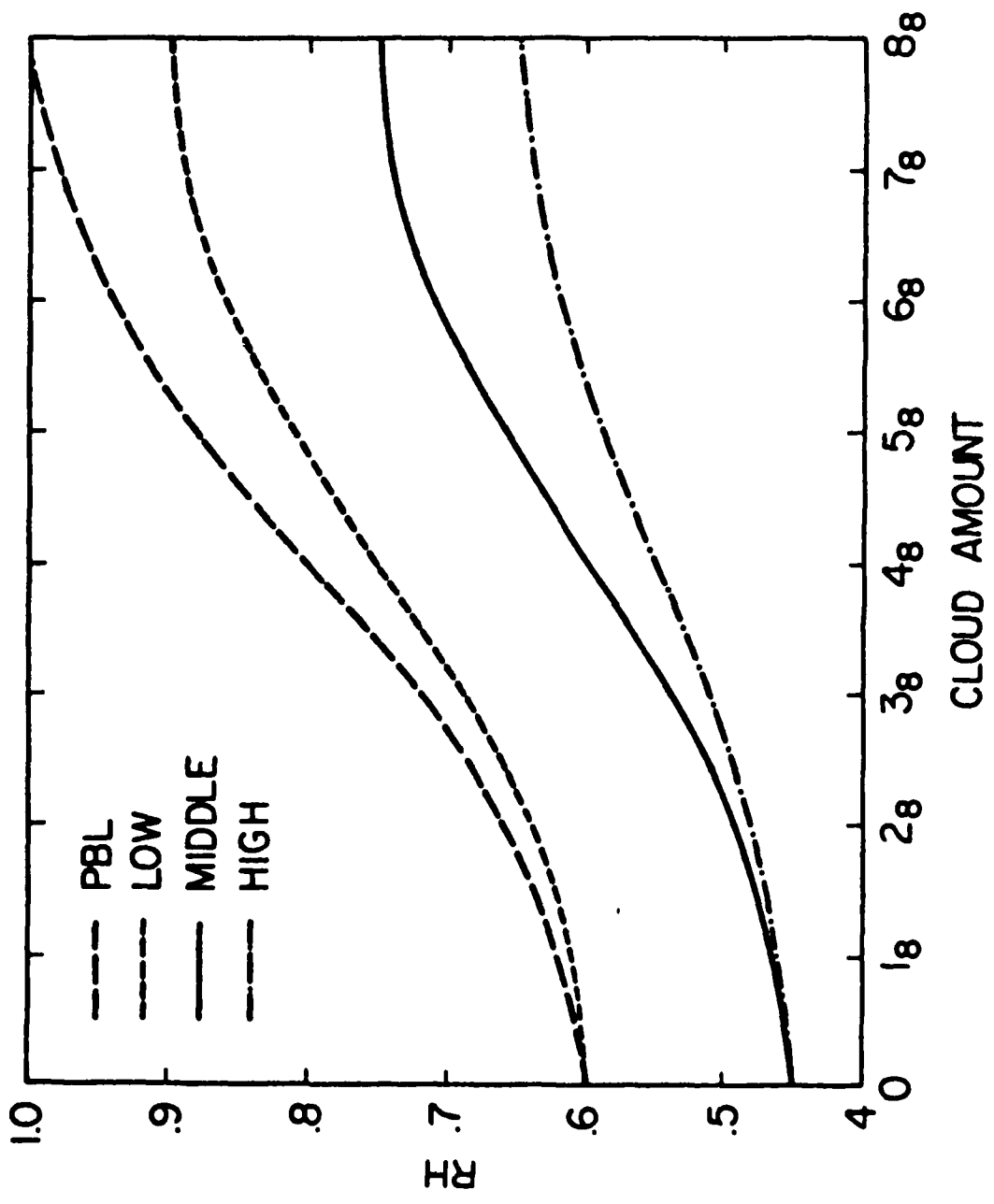


Fig. A3. **BBC** (Chu-Parrish) **BH-CA** Scheme

3DNEPH cloud amount. As far as one can go here in initially representing the 3DNEPH inferred humidities on the desired regular latitude-longitude grid is to calculate  $\cos\left(\frac{\pi}{8} \text{OKTAS}\right)$  where  $\text{OKTAS} = 3\text{DNEPH CLD AMT (in percent)}/12.5$  and bilinearly interpolate these values to the desired latitude-longitude grid. Then surface pressures on this same grid can be used to determine the appropriate layer to use for the 3DNEPH value and thus to compute the relative humidity.

## B. Relocatable Limited Area Model - Progress in Development

### 1. Introduction

Plans for developing a relocatable limited area model (RLAM) were detailed in Gerlach (1984).<sup>14</sup> The plans called for a model that can be easily assigned to any geographical region, that allows for a choice of map projections, that can utilize several differencing schemes, and that has replaceable physics packages. To date the RLAM has been developed and tested but without any physical processes. It contains equations governing momentum, pressure tendency, temperature, and moisture but contains no processes other than advection. However, sources and sinks of energy do exist in the form of boundary conditions formulated for the RLAM. These boundary conditions on the whole were generated from the AFGL global spectral model (GSM). Some tests were performed with a one-level barotropic model where case boundaries were provided by linear solutions of the Rossby-Haurwitz wave equations. The barotropic experiments were for diagnostic purposes only and will not be referenced here. This report on the RLAM is divided into three sections dealing with the initial conditions, boundary correlations, and the model itself, respectively. Results of various tests are in Section 5.

### 2. Initial Conditions

To date, all initial conditions (with the exception of the barotropic tests) have been generated from spectral coefficients derived from either the GSM or the FGGE analysis. They are expanded on each grid point of the desired limited area by computing the latitude and longitude of each grid point and inserting them into the spectral expansion. The computational area is chosen as a rectangular section on either a Mercator, polar stereographic, Lambert conformal, or latitude-longitude (lat-lon) map. The grid points are numbered according to standard maps of each of the projections as given by Hoke et al. (1981).<sup>15</sup> Resolution is nominally one median (381 km) but can be increased by integer division of the mesh size.

---

14. Gerlach, A. M., ed., 1984: Objective Analysis and Prediction Techniques - 1984. AFGL-TR-84-0328, Contract F19628-82-C-0023, Systems and Applied Sciences Corporation, ADA160377.

15. Hoke, J. E., J. L. Hayes, and L. G. Renniger, 1981: Map Projections and Grid Systems for Meteorological Applications. AFGWL/TN-79/003, U. S. Air Force Global Weather Central, Offutt AFB, NE.

The user can select the dimensions of the rectangle, the projection, and the geographic location of the rectangle by specifying certain "namelist" parameters. He has the option of specifying the central latitude and longitude of the projection or the grid point number of the lower left-hand corner of the rectangle in accordance with the standard map. The latter assumes that the user has a standard map with numbered grid boxes for reference. The user must also indicate on which projection he wishes the rectangle to appear. If the boundaries exceed a latitude for which the projection is valid processing will terminate. Future evolution of the code should result in guidelines and warnings for various map projections and specifications of their area of validity. Currently, the program will abort only if the poles are found to be on a projection other than polar stereographic. To this end, the user must also choose which longitude will be central to the map projection. This choice is most crucial in dealing with the Lambert and polar map projections, where the central longitude dictates which longitude will serve as the vertical central line of the projection (i.e., the y-axis). In the Northern Hemisphere, this longitude refers to the line appearing below the central horizontal line (the x-axis), while in the Southern Hemisphere it will appear above the line. For Mercator and lat-lon maps, the selection only rotates the position of the map beneath the grid by defining which longitude should appear at the center. For the Lambert and polar maps, specifying a longitude has the effect of rotating the map about the pole until the desired longitude is aligned with the y-axis.

Once the grid size and resolution and the rectangle's location are selected, the latitude and longitude of each grid point are found by the known relationships between the map projections and the earth as given by Hoke et al. (1981). The map factor, which is computed as a necessary step in finding the latitudes and longitudes, is also preserved for each grid point, as is the coriolis parameter. Derivatives of the map factor in Cartesian coordinates are stored as well for use in calculating the model equations. Once the latitudes and longitudes of the grid points are known, it is theoretically simple to expand the spectral coefficients at each grid point to evaluate the necessary variables. However, the process of spectral expansion at many latitudes can be quite time consuming. For Mercator and lat-lon grids, there is no problem because the grid lines are aligned with

latitudes. For polar and Lambert projections, however, each grid point is at a different latitude and longitude. When very many grid points are involved, it is possible for the sake of expediency to evaluate the necessary variables at fixed latitudes and longitudes and to interpolate to the grid points, but this process inevitably introduces interpolation error. Instead, for reasonably large fields the spectral expansions are bypassed by converting spectral coefficients to polynomial coefficients and expanding the polynomials at each grid point. This procedure is economical and accurate, as described in detail by Halberstam (1985).<sup>16</sup> In short, since it is possible to represent any Legendre function  $P_n^m(\phi)$ , where  $\phi$  is a latitude, as

$$P_n^m(\phi) = (1 - \mu^2)^{m/2} \sum_{j=0}^{n-m} A_j^{n,m} \mu^j$$

where  $\mu = \sin \phi$ , then any expanded variable

$$A(\phi, \lambda) = \sum_{m=-M}^M \sum_{n=|M|}^{|M|+N} b_n^m P_n^m(\phi) e^{im\lambda}$$

where  $\lambda$  is longitude can also be represented as

$$A(\phi, \lambda) = \sum_{m=-M}^M (1 - \mu^2)^{|m|/2} \sum_{j=0}^N C_j^m \mu^j e^{im\lambda}. \quad (1)$$

The  $C_j^m$  are found by combining the spectral coefficients  $b_n^m$  with the known polynomial coefficients of the Legendre functions  $A_j^{n,m}$ . The latter are calculated once by inverting a matrix for each  $n$  and  $m$  and storing the results on disk. The process works effectively for  $N = M = 30$  and considerably reduces the required time for expansions.

Another benefit of this expansion is that it allows for easier calculation at the poles. A detailed description of calculations at the poles for scalar variables and physical wind components and their derivatives is found in Appendix B. For the moment, it is easy to see that expansions of scalar quantities such as for  $A(\phi, \lambda)$  in Eq. (1) are finite

---

16. Halberstam, I. M., 1985: Polynomials as a substitute for Legendre functions in spectral models. Submitted to Mon. Wea. Rev.

at the poles, with only  $m = 0$  contributing to the general sum. Also, with  $m = 0$  there is no dependency on longitude, thus allowing unambiguous definition at the poles.

Figs. 7a - 7d show temperature at the lowest model layer for a Mercator, polar, Lambert, and lat-lon (pictured on a polar projection) configuration, respectively, where the central latitude and longitude were chosen at 90W 45N. Note that because of the differences in the projections the area encompassed will not be the same for all maps.

### 3. Boundary Conditions

The formulation of boundary conditions is necessary because of the limited area in which the calculations are performed. Several boundary conditions have been examined: (1) direct insertion, (2) "sponge," and (3) "porous sponge." Direct insertion refers to replacing the boundaries each time step with values supplied by the GSM. The values at the boundaries can be theoretically supplied by saving output from the GSM at each of its time steps. Because this approach may lead to severe storage problems, the data may also be supplied by interpolation in time between GSM values that are even several hours apart. For second order differencing schemes these data are the values themselves of temperature, winds, humidity, and surface pressure at each level. For fourth order compact differencing, derivatives are required at the boundaries. Again, they may be calculated and stored for each time step or interpolated within a time window. The boundary data are supplied by the initial conditions routine with a switch that can be set to supply the variables and their derivatives at the boundaries only. The derivatives are computed from the spectral quantities by taking the derivatives with respect to  $\lambda$  and  $\phi$  of the polynomial expansions, then imposing the chain rule to derive  $x$  and  $y$  derivatives. (Derivatives of  $\phi$  and  $\lambda$  with respect to  $x$  and  $y$  are known from the projection equations.)

The sponge and porous sponge boundaries refer to the methods of damping discussed by Perkey and Kreitzberg (1976).<sup>17</sup> The sponge boundary assumes that tendencies of the variables are known at the boundaries from an outside source, e.g., the GSM. There is then a buffer or sponge zone of

---

17. Perkey, D. J., and C. W. Kreitzberg, 1976: A time-dependent lateral boundary scheme for limited-area primitive equation models. Mon. Wea. Rev., 104, 744-755.

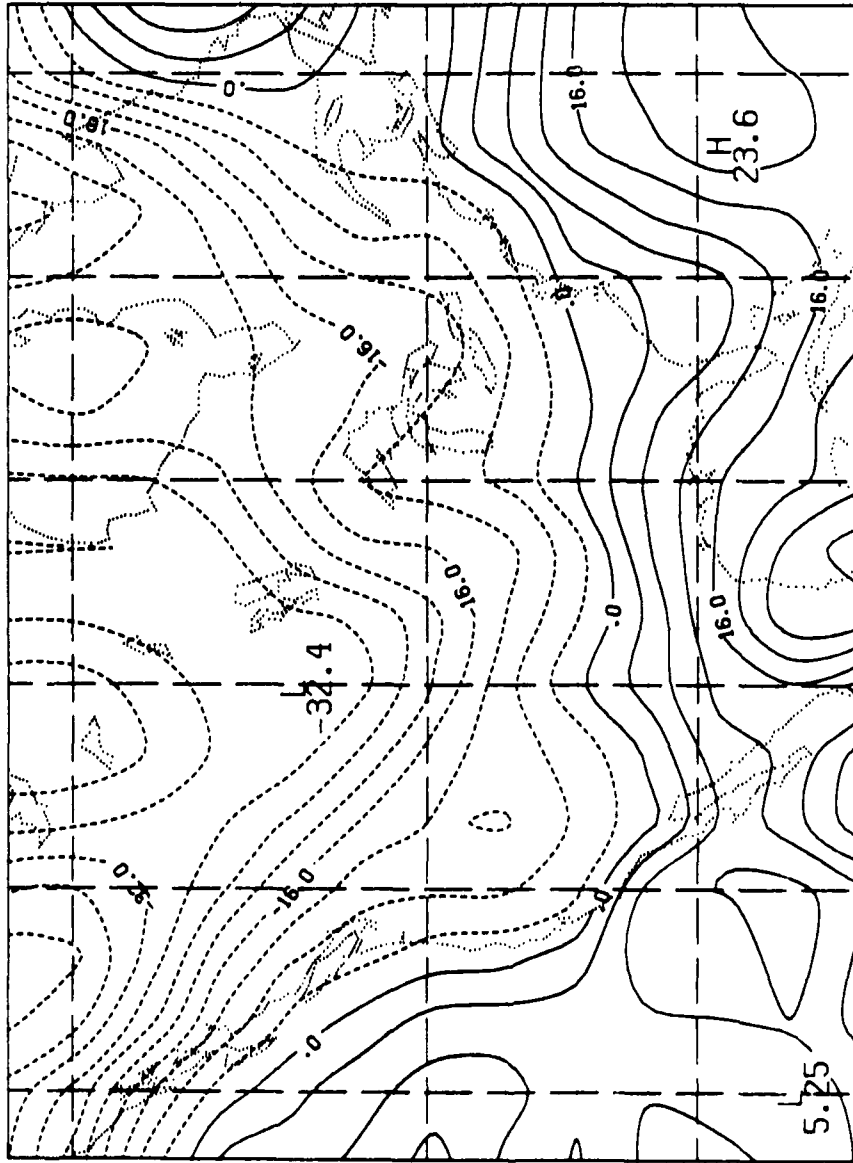


Fig. 7a. Contours of Temperature on  $\sigma$ -layer 1 (near the surface) at 2/4/79  
 00 GMT in a Region Centered at 90W 45N for Mercator Projection: (contour interval  
 is 4<sup>o</sup> C)

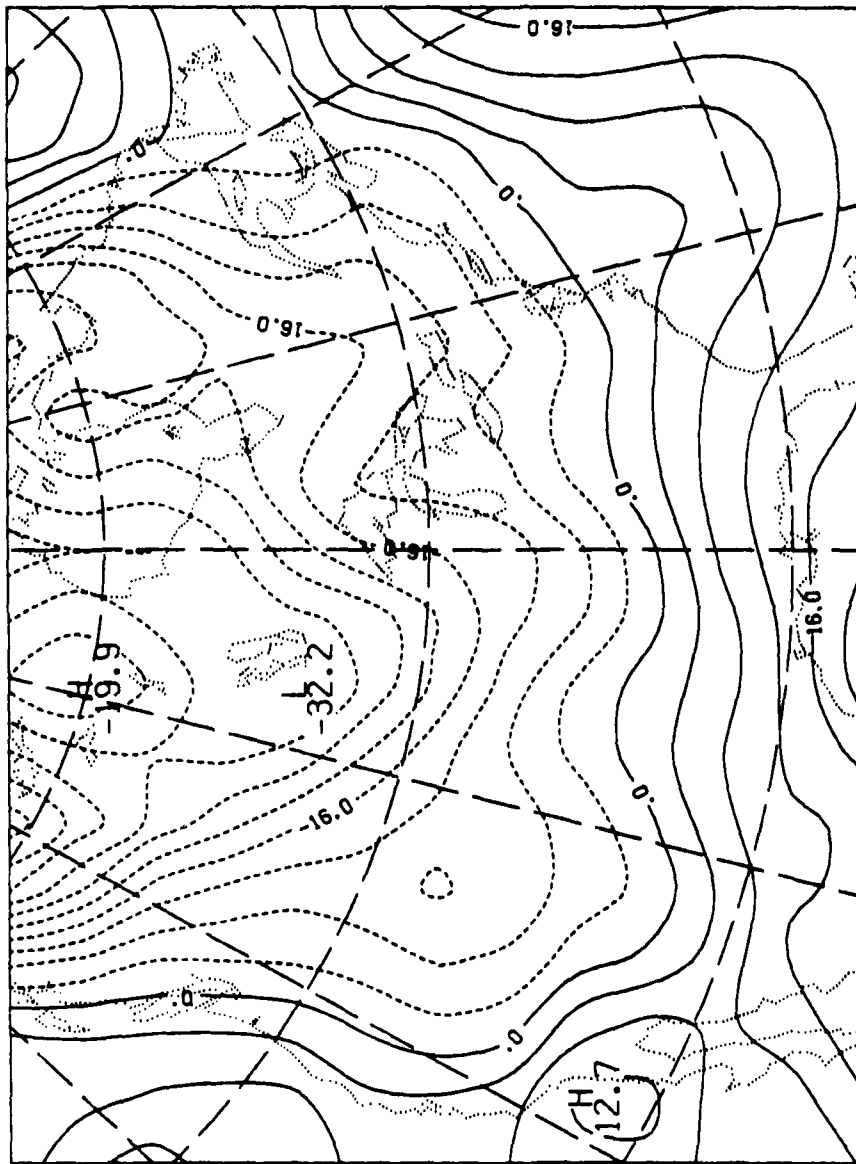


Fig. 7b. Contours of Temperature on  $\sigma$ -layer 1 (near the surface) at 2/4/79 00 GMT in a Region Centered at 90W 45N for Polar Stereographic Projection



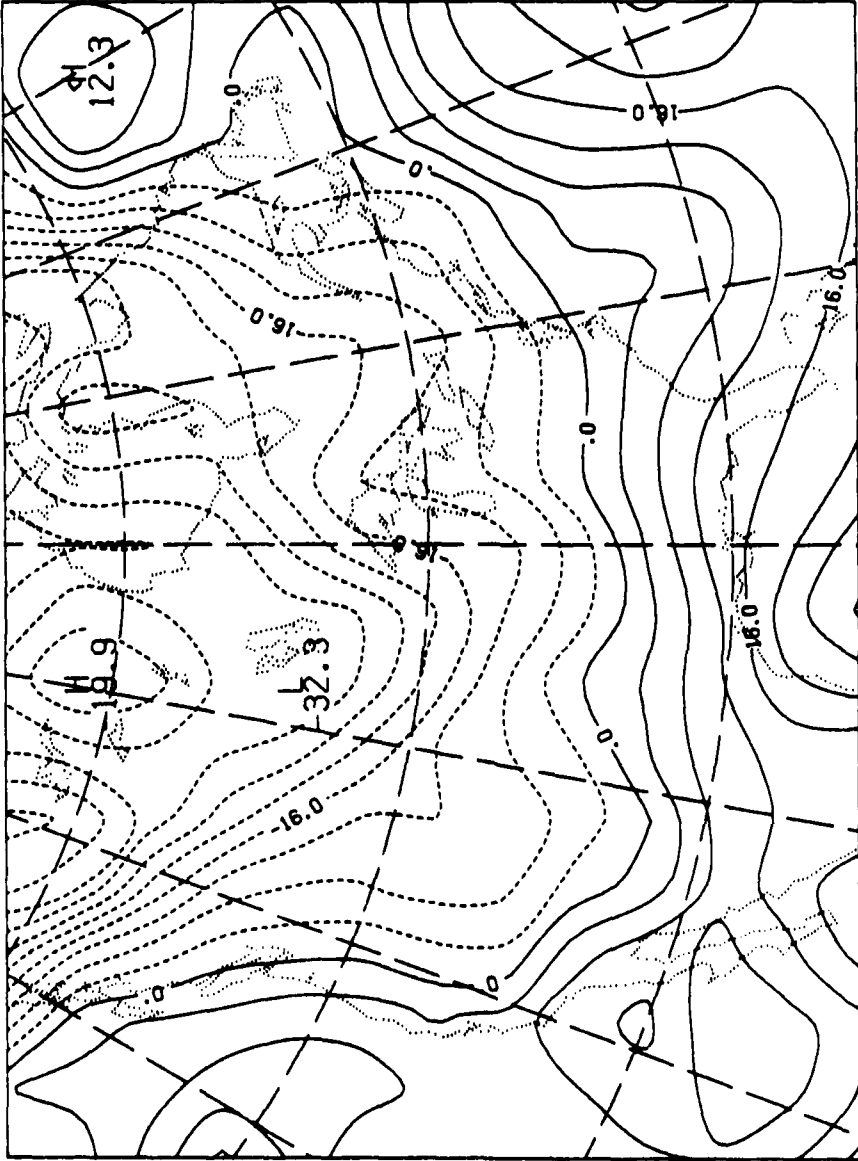


Fig. 7c. Contours of Temperature on  $\sigma$ -layer 1 (near the surface) at 2/4/79  
00 GMT in a Region Centered at 90W 45N for Lambert Conformal Projection

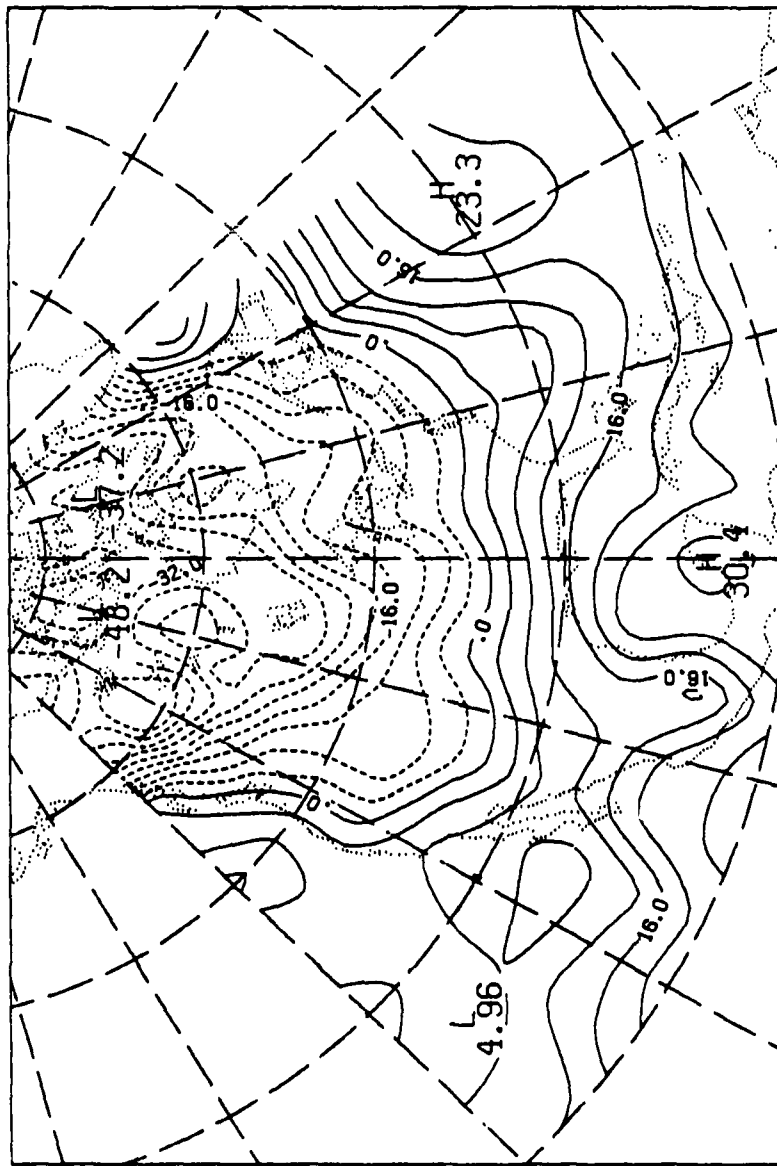


Fig. 7d. Contours of Temperature on  $\sigma$ -layer 1 (near the surface) at 2/4/79 00 GMT in a Region Centered at 90W 45N for Lat-Lon (pictured on a polar stereographic) Projection

approximately four grid distances where tendencies are combinations of both the outside source and the interior, i.e., the model, source. Weights are staggered through the zone to accentuate either the interior or exterior tendencies, the outer rows giving more weight to the outside source and the inner rows to the interior source. The porous sponge does not involve any outside source. The tendencies are calculated at the boundary by extrapolation from the interior, and, again, weights are applied to the transition zone. In both cases a smoother-desmoothing (Shapiro, 1970)<sup>18</sup> filter is applied at every five time steps to the boundaries and at every 15 time steps to the entire field. The filter reduces the effect of high frequency waves that may originate because of reflections at the boundary.

Interpolation in time of the boundary values, whether they be actual variables, derivatives, or tendencies, can be performed in an assortment of ways. A basic question in choosing an interpolation method is how long an interval one should allow. A second question is what kind of interpolation scheme one should invoke. Linear interpolation is simplest and requires the least number of points but is the most inaccurate. To answer these questions an experiment was performed on data from the GSM taken at the boundaries of a Lambert projection centered over North America from February 4, 1979 00 GMT to 06 GMT. Data consisted of temperatures, winds, and humidity and their spatial and time derivatives at 24 min intervals. Linear interpolation was first attempted to the central time step (no. 8) from two surrounding periods, starting from neighboring ones (7 and 9) and continuing to the furthest extremes (1 and 15). Fig. 8a depicts the RMS differences between the interpolated values and the GSM values for the fourth  $\sigma$  layer (approximately 560 mb) for temperature. The smooth, rounded humps are what one would expect because points farthest away from the known end points will deviate most. That is to say that the assumption of linear time change is most valid near the end points of the interpolation. It is surprising, however, that the maximum deviation of temperature is as low as 0.7° C, although the interpolation stretches over a 3 h interval. This result may be related to the particular synoptic situation used in the study.

---

18. Shapiro, R., 1970: Smoothing, filtering, and boundary effects. Rev. Geophys. Space Phys., **8**, 359-387.

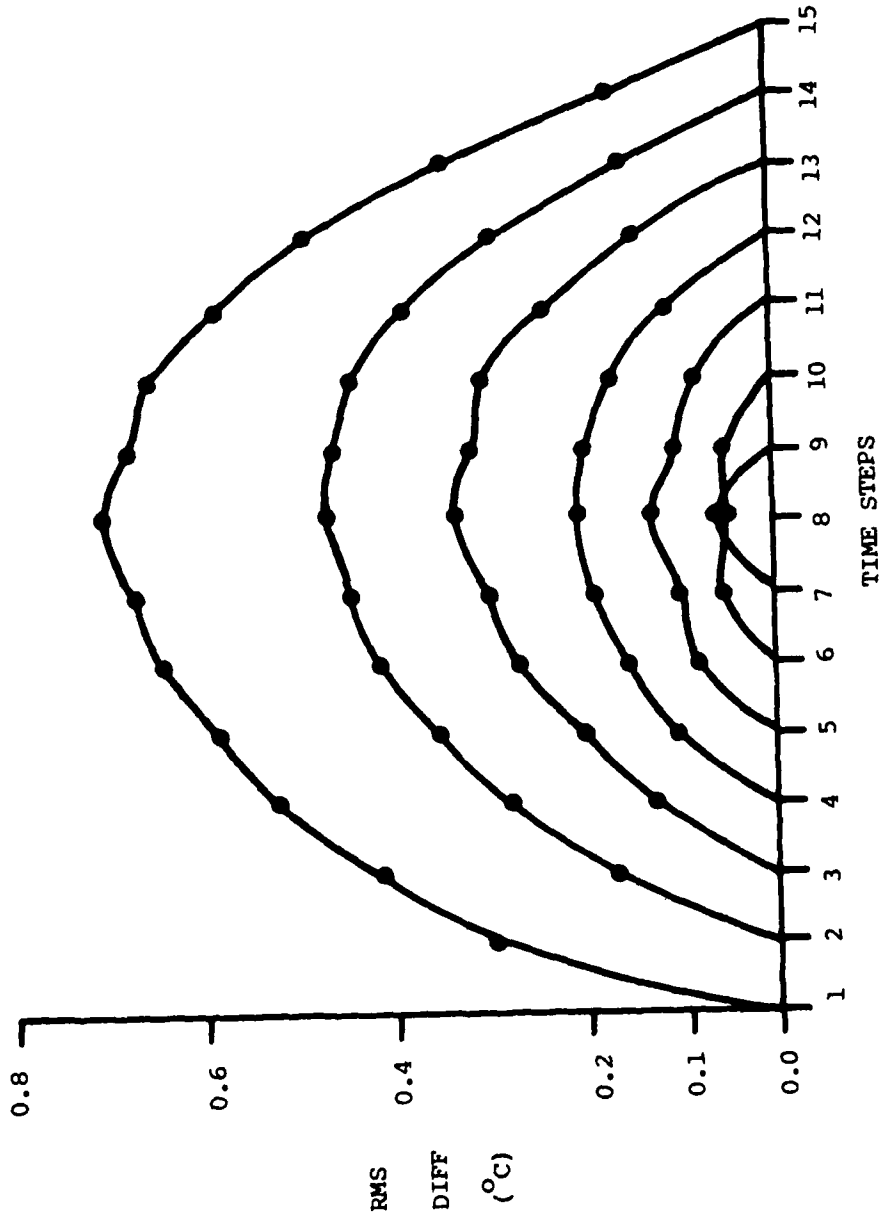


Fig. 8a. RMS Differences between Values of Temperature at  $\sigma$ -layer 1, Linearly Interpolated from the Two End Points to Intermediate Points and Values Computed by the GSM

Errors in interpolation of wind components and surface pressure behave in much the same way, with errors of  $u$  and  $v$  peaking at a little over  $1 \text{ m s}^{-1}$  and surface pressure at about 0.3 mb. Errors in specific humidity, however, did not grow linearly with increased interpolation increment. Fig. 8b shows RMS values of  $q$  (specific humidity) at the first  $\sigma$  layer for the different time spans, and it clearly does not follow the pattern of the other values. Fig. 8c shows the same at layer 4, and there is obviously a significant improvement. Apparently, the moisture near the surface is influenced by other physical effects which cause its error growth to stray from linearity. Errors of spatial derivatives in general were not as well behaved in time as the errors of the variables themselves. Fig. 9a depicts the RMS error of the  $x$ -derivative of temperature near the surface over the same interpolation span. Note that for smaller time periods, the curves are not as smooth as for temperature itself, implying that the derivative errors do not change linearly in time. Figs. 9b and 9c depict the  $x$ -derivative and  $y$ -derivative, respectively, of  $u$  for the same times and  $\sigma$  layer. Here the temporal behavior of the derivative errors is more in concert with the variable errors. The moisture  $x$ -derivative errors depicted in Fig. 9d behave as might be expected, erratically and non-linearly.

Other interpolations were also attempted and compared with linear interpolation. Cubic spline, quadratic, and cubic interpolations were made for various time spans. The cubic spline and the quadratic both require three points to create an interpolation. Cubic interpolation requires a minimum of four points. To ascertain their effectiveness vis-à-vis each other and vis-à-vis linear interpolation, one must employ the same time span in each case. Thus if cubic interpolation requires four points, the most one should use in comparison with the linear case is only one-third of the total or five time steps. Fig. 10 depicts RMS errors for temperature near the surface for various interpolations. The cubic interpolation curves cover only the middle section of their three-section span. The other curves are for the entire span of each respective interpolation, which vary from four time steps for the linear to eight for the quadratic and cubic spline. The latter two go to zero at their mid-points because the mid-point is one of the data points necessary for the interpolation. (The last piece of the cubic spline between time steps 12 and 16 is missing.) What is surprising is that the cubic spline does not do as well as the quadratic. In fact, although the cubic expectedly performs

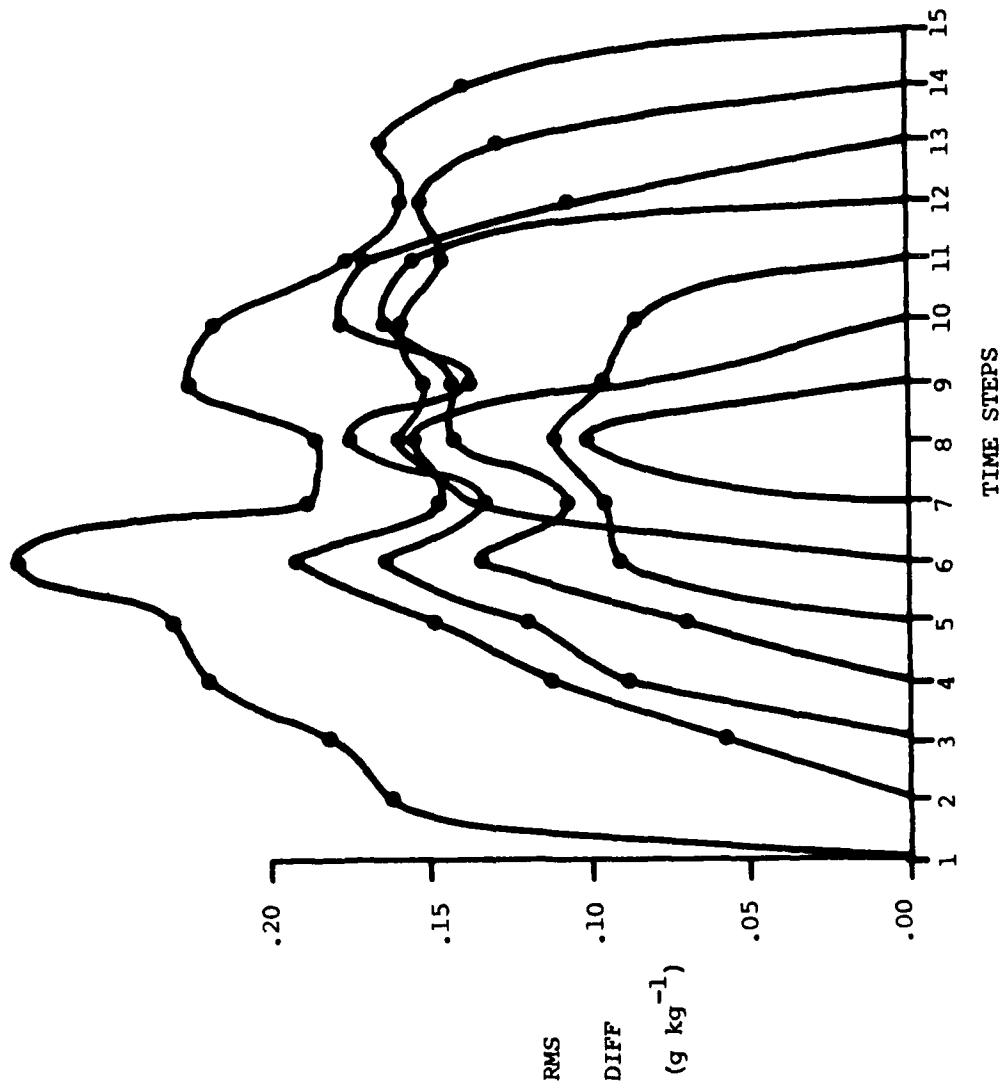


Fig. 8b. RMS Differences between Values of Specific Humidity at  $\sigma$ -layer 1, Linearly Interpolated from the Two End Points to Intermediate Points and Values Computed by the GSM

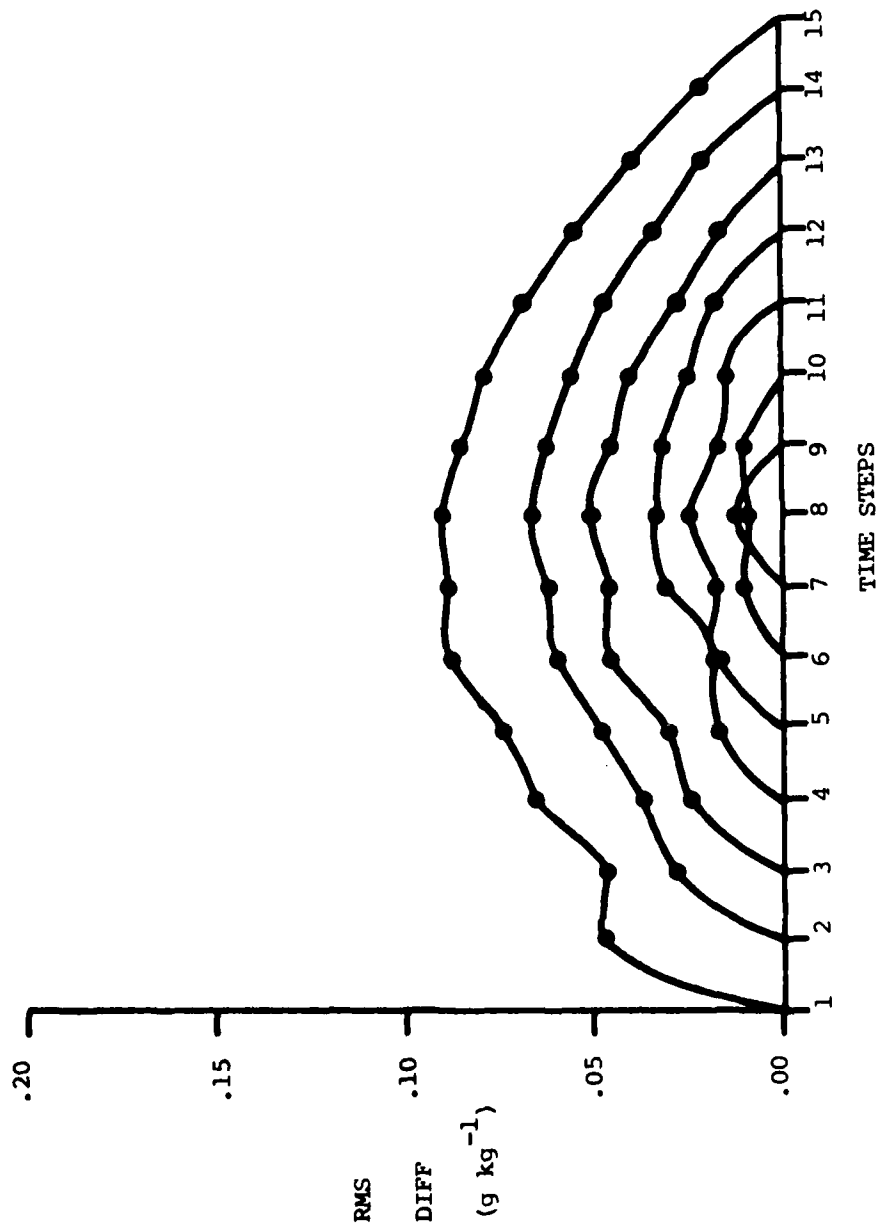


Fig. 8c. RMS Differences between Values of Specific Humidity at  $\sigma$ -layer 4, Linearly Interpolated from the Two End Points to Intermediate Points and Values Computed by the GSM

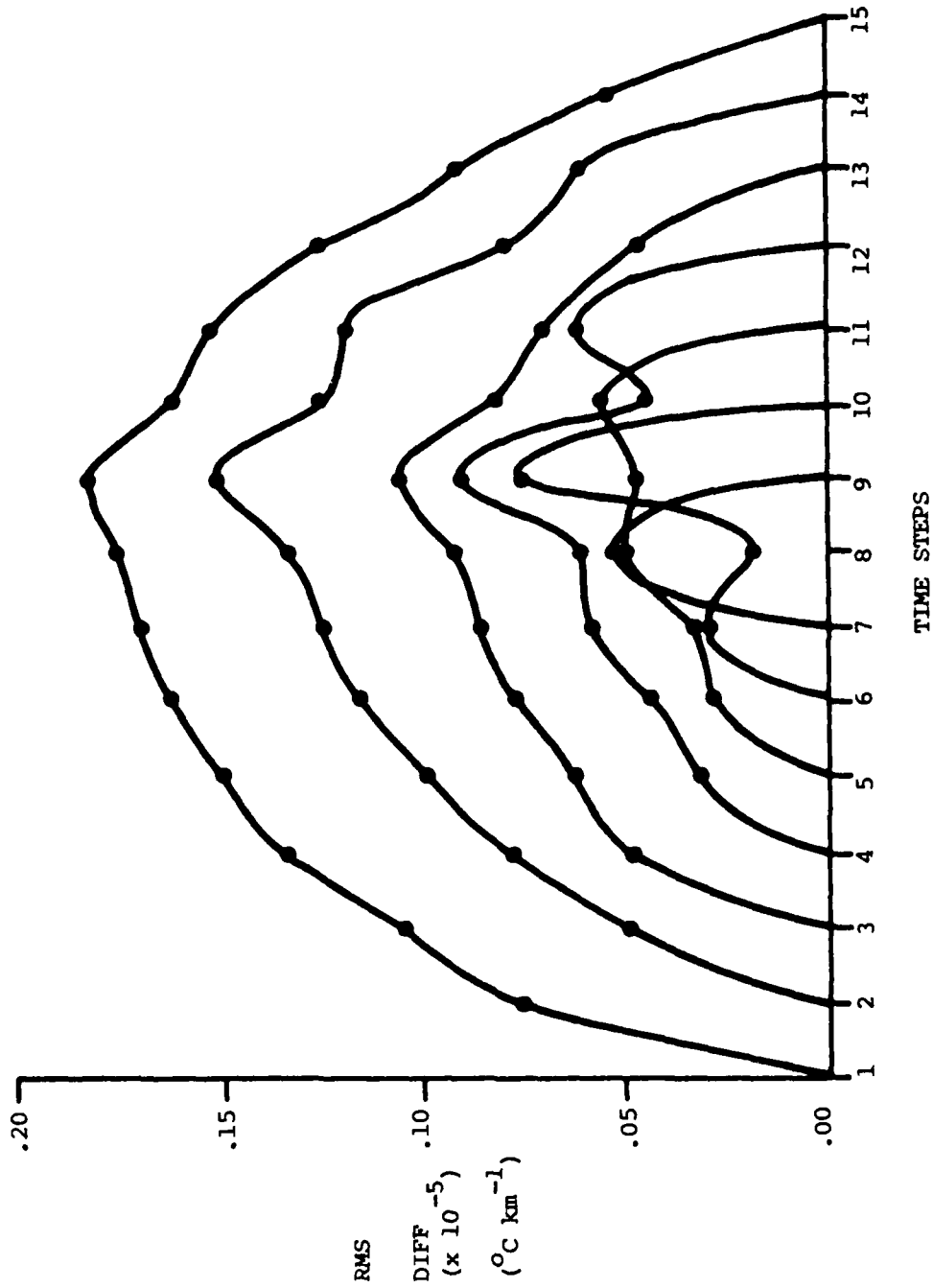


Fig. 9a. Same as for Fig. 8 except for x-derivative of Temperature at  $\sigma$ -layer 1



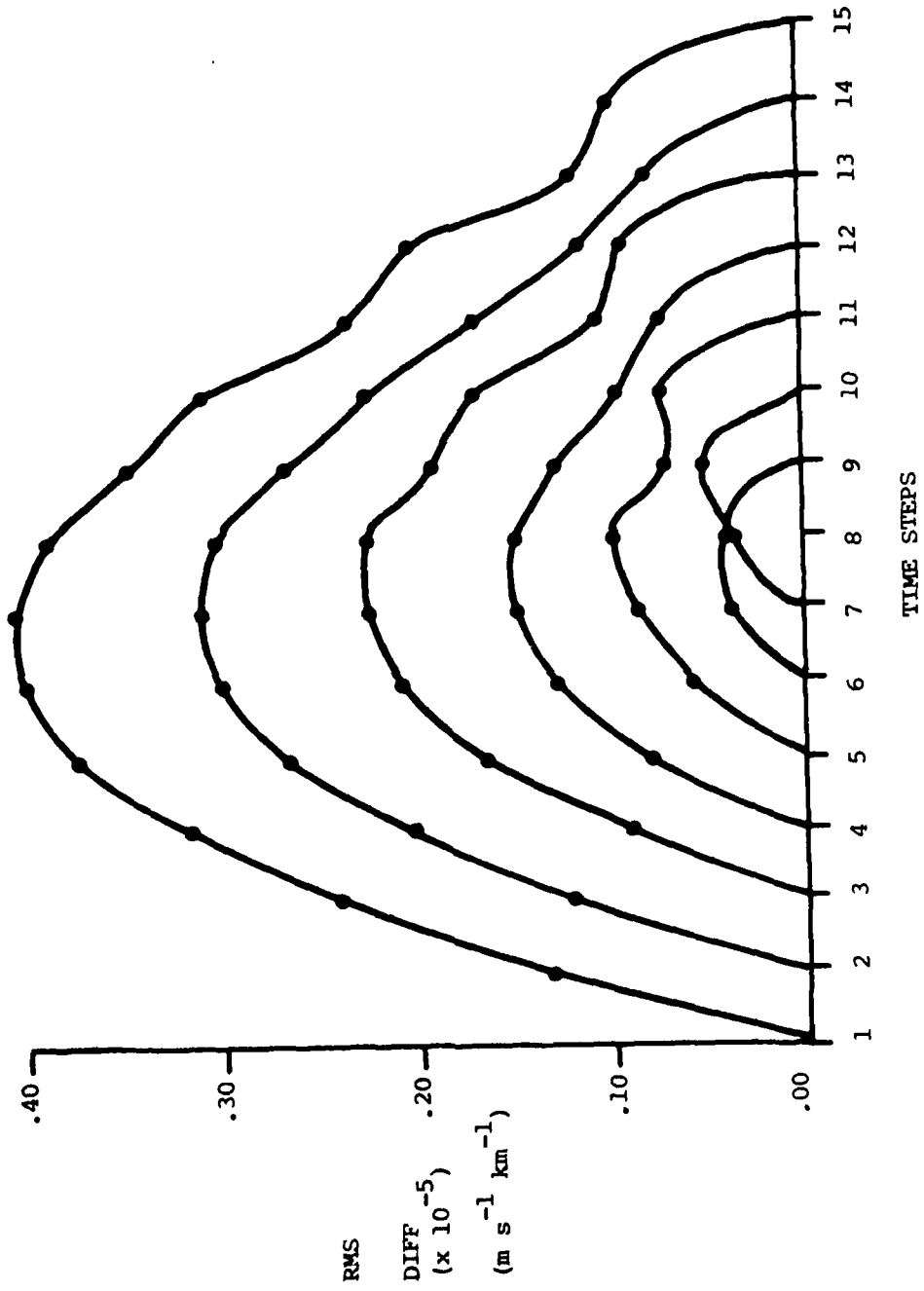


Fig. 9b. Same as for Fig. 8 except for x-derivative of u at  $\sigma$ -layer 1

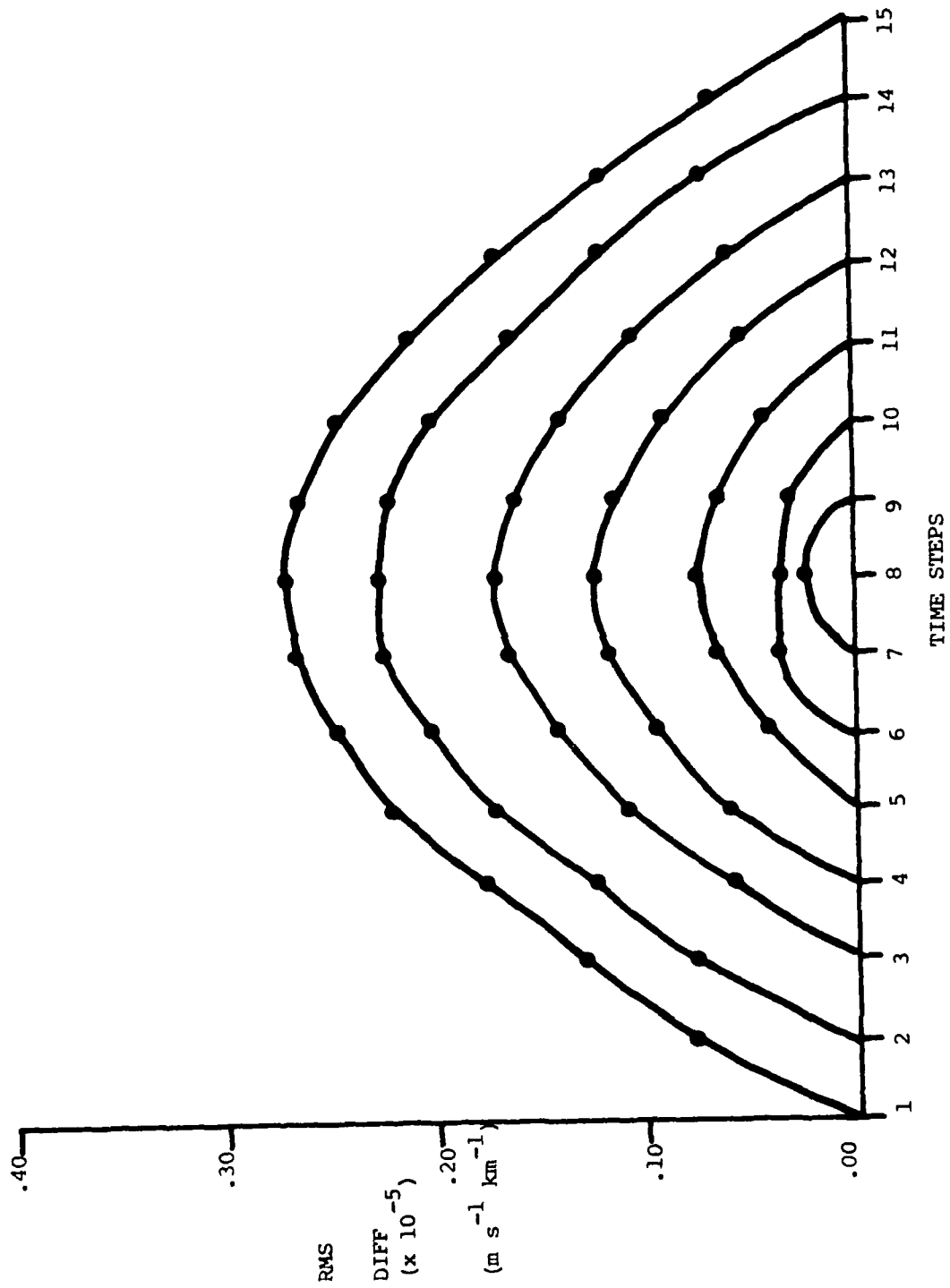


Fig. 9c. Same as for Fig. 8 except for y-derivative of u at  $\sigma$ -layer 1

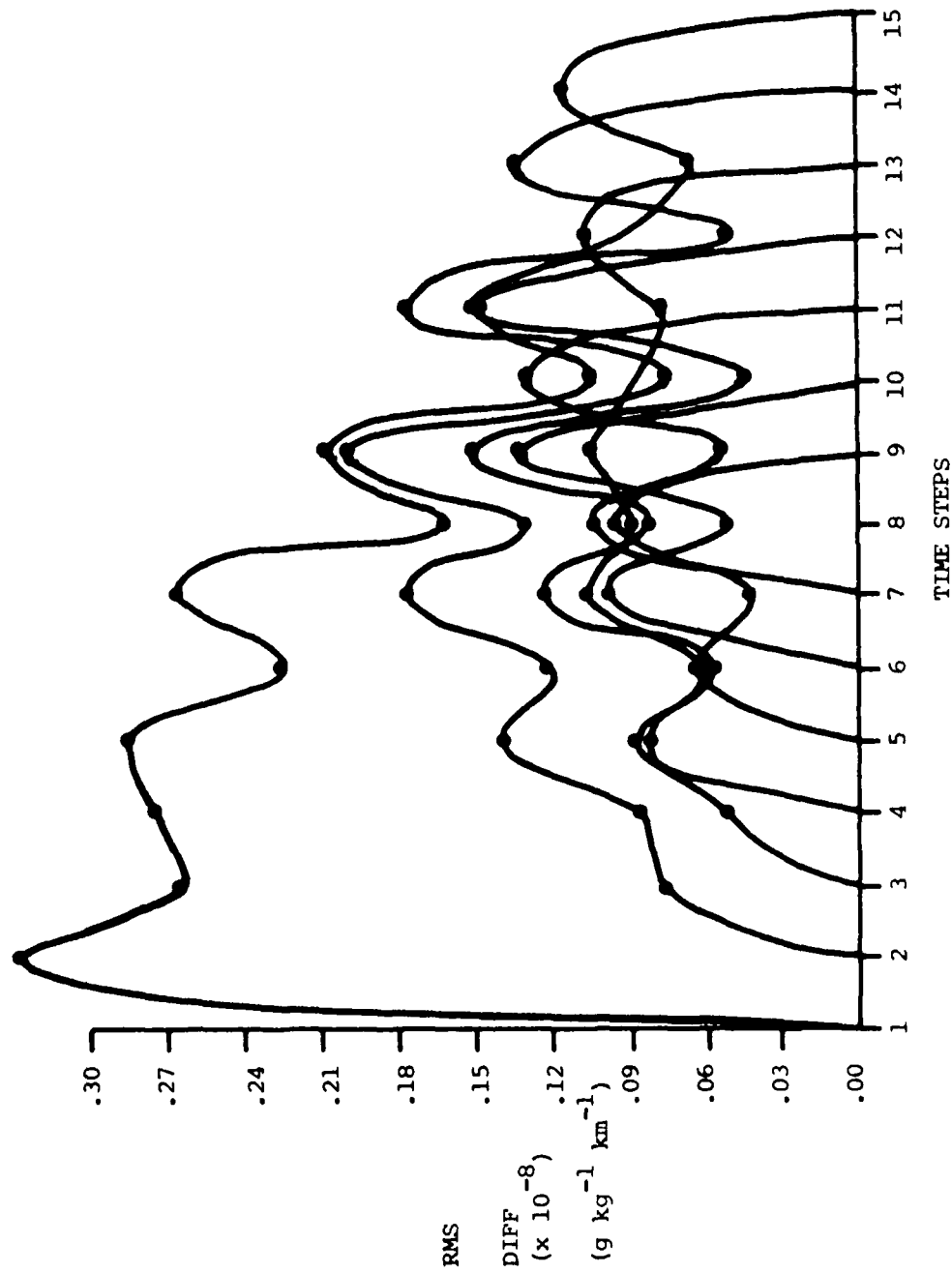


Fig. 9d. Same as for Fig. 8 except for the x-derivative of q at  $\sigma$ -layer 1

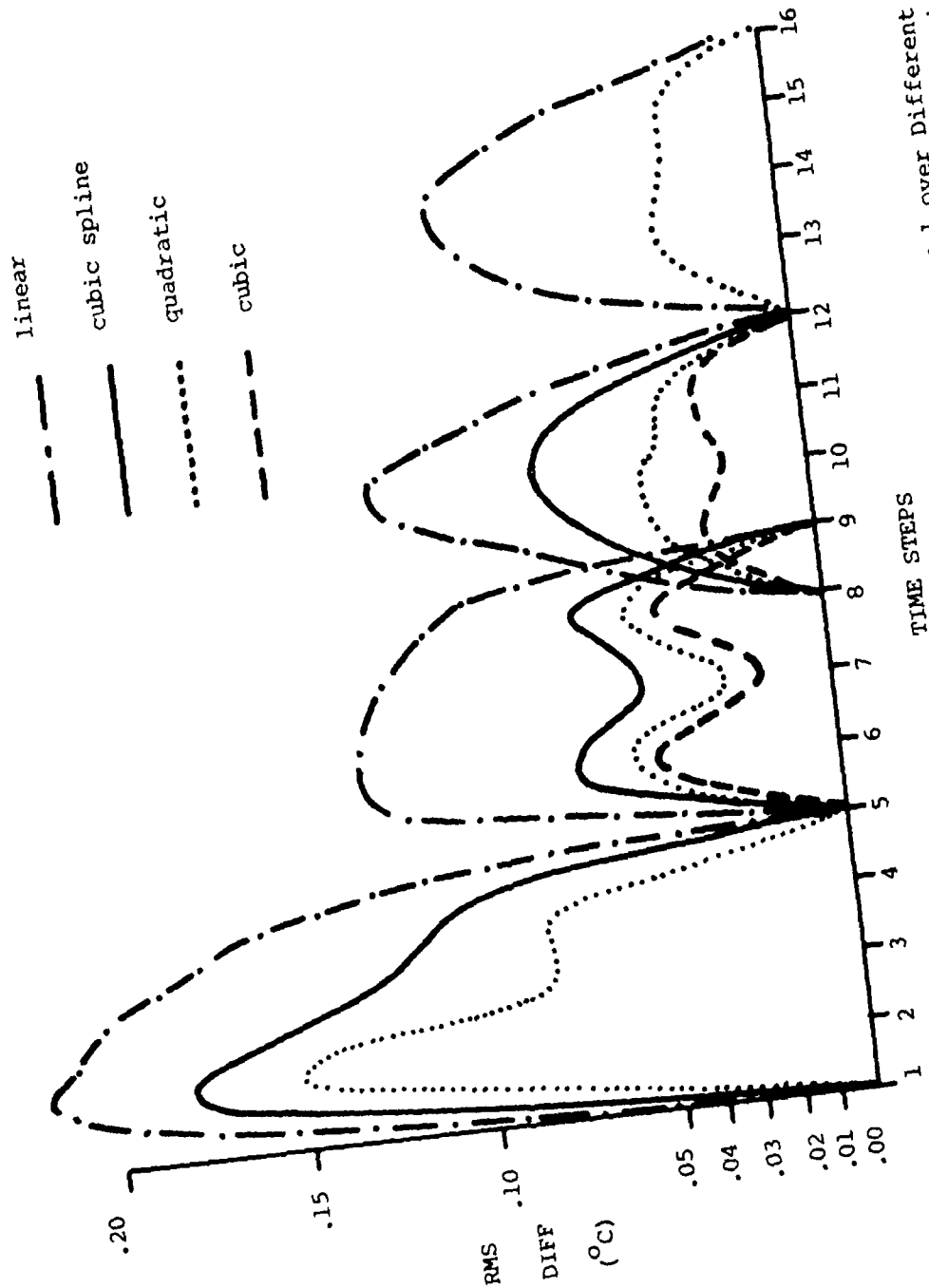


Fig. 10. RMS Errors of Interpolation of Temperature at  $\sigma$ -layer 1 over Different Interpolation Lengths for Linear, Cubic Spline, Quadratic, and Cubic Interpolations

best, it is not much better than the quadratic. Fig. 11 shows the RMS error of the x-derivative of T near the surface. Featured are linear, cubic spline, and quadratic interpolation over the entire time span. The cubic, not shown, again did only slightly better than the quadratic for time spans where comparison could be made. Here, as well, the cubic spline does not perform as well as the quadratic. Derivatives of u and v were studied in similar fashion and produced similar results. As a consequence of these investigations, cubic interpolation was invoked whenever possible because of the advantages of higher accuracy and the feasibility of choosing a central span that is equally affected by all data points, whereas each quadratic and cubic spline interpolation presents an ambiguity concerning which of two possible spans should be selected.

#### 4. The Model

Once the initial and boundary conditions are determined, the actual calculations can proceed. The model equations to date do not contain any physical processes. There is no boundary layer physics, moisture sources or sinks, diabatic heat processes, or diffusion (except for the smoother-desmoothing operations in concert with the sponge boundary). The remaining, chiefly advective, equations are solved by finite differencing either in the advective or flux forms. So far, experiments have been performed only in the advective form except for some experiments where the continuity equation was written in flux form. Details of the equations are listed by Yang and Brenner (1983).<sup>19</sup>

Currently the RLAM has 12 levels equal to the 12 levels of the GSM. No facility has yet been developed to interpolate in the vertical. Upon receiving the initial conditions, the RLAM is oblivious to the projection except that it carries the map factors provided by the initializing routine. For conformal maps two separate but equal map factors are provided. For lat-lon grids, the second map factor is set to 1 everywhere. This broader format, although more complicated and involved than separate single-map codes, provides for more general usage. Indeed, this approach was followed throughout the creation of the RLAM where the

---

19. Yang, C.-H., and S. Brenner, 1983: Toward the Formulation of a Regional NWP Model. Technical Memorandum No. 88, Air Force Geophysics Laboratory, Hanscom AFB, MA.

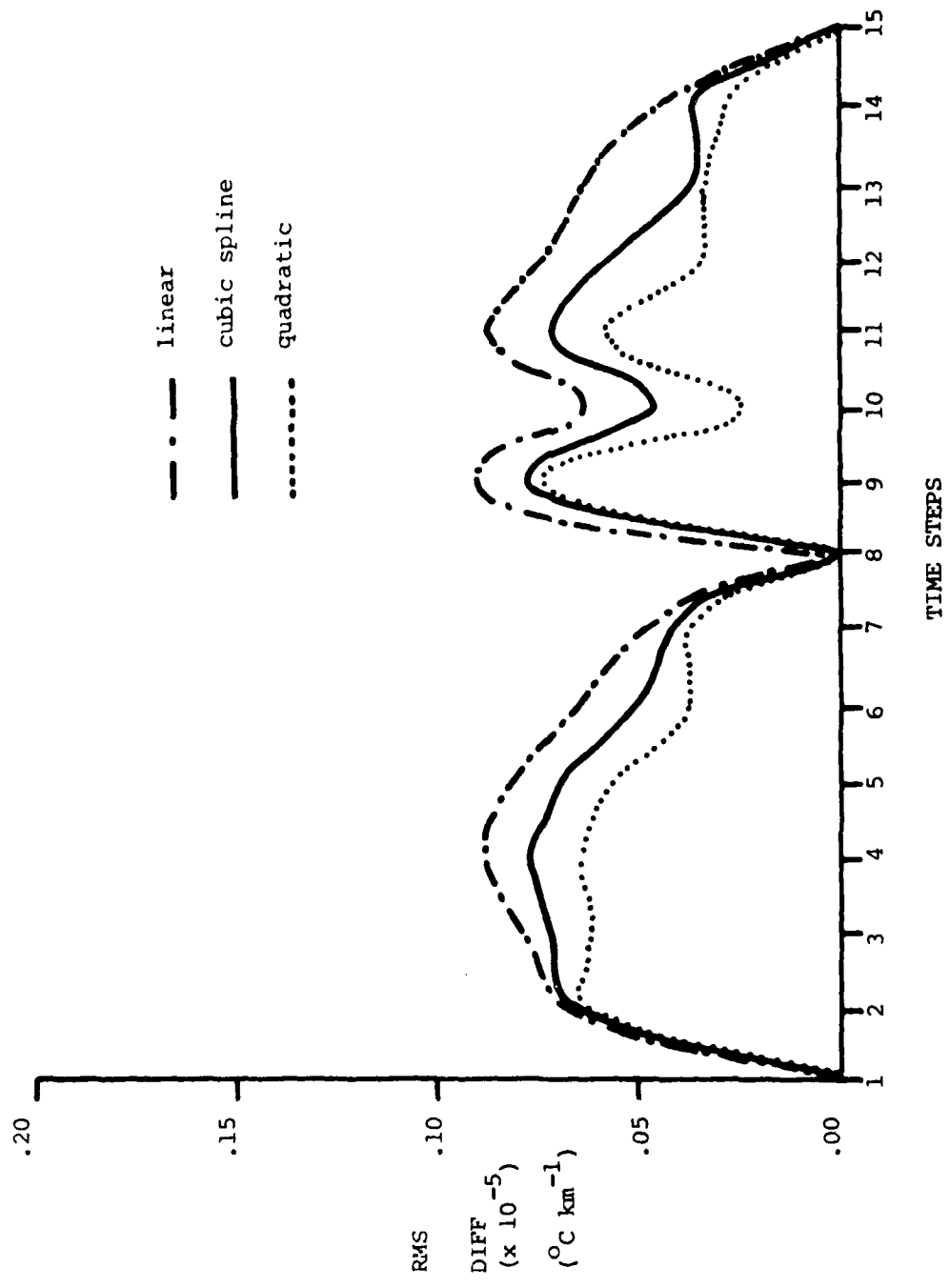


Fig. 11. RMS Errors of Interpolation of x-derivative of Temperature at  $\sigma$ -layer 1 for Linear, Cubic Spline, and Quadratic Interpolations

most general form was chosen, with individual cases being a special form of the general case. Thus, unstaggered grids are special cases of staggered grids, the explicit leap-frog time scheme is a special case of more complicated implicit schemes, second order spatial differencing is a special case of higher order differencing, etc. This approach is not always possible because even when theory allows for the special case to exist, computational problems in the form of round-off or ill-conditioning may impede the calculations. Currently there are several finite differencing alternatives available to the user. For time differencing, one may choose a leap-frog explicit form or a three level scheme developed by Brown and Campana (1978).<sup>20</sup> For spatial differences one may employ a second order central differencing or fourth order compact (Hirsh, 1975)<sup>21</sup> for both staggered and unstaggered grids. The staggering of the variables can be changed arbitrarily but is geared currently to the Arakawa C-grid (Arakawa and Lamb, 1977).<sup>22</sup> The choice of boundary conditions at present also affects the choice of differencing scheme. For instance, the fourth order compact does not function with the sponge or porous sponge because it requires spatial derivatives at the boundary, whereas the sponge supplies tendencies at the boundaries. Also, whereas the grid resolution is arbitrary, the leap-frog scheme requires a time step that does not violate the Courant-Friedrichs-Lewy (CFL) condition for stability. The condition is even more restrictive for fourth order compact spatial differencing. The Brown-Campana scheme, on the other hand, is stable for high resolution grids and can tolerate fairly large time steps, making it much more economical in the long run.

---

20. Brown, J. A., Jr., and K. A. Campana, 1978: An economical time-differencing system for numerical weather prediction. Mon. Wea. Rev., 106, 1125-1136.

21. Hirsh, R. S., 1975: High order accurate difference solutions of fluid-mechanics problems by a compact differencing technique. J. Comput. Physics, 16, 383-390.

22. Arakawa, A., and V. R. Lamb, 1977: Computational design of the basic dynamical processes of the UCLA general circulation model. Methods in Computational Physics, Vol. 17, J. Chang, ed., Academic Press, Inc., 174-265.

## 5. Results

Because of the ongoing developmental nature of this project, results presented here should be regarded as no more than interim. Some portions of the code are still in the debugging stage. Some of the experiments attempted with the RLAM did not converge and blew up before 6 h. One such unsuccessful version is the advective form with the fourth order compact differencing and direct insertion of boundaries. It is not clear what the source of the problem is, but it seems to be linked to the effect of the boundaries. Since a fourth order scheme depends on more boundary information than does a second order one, it is possible that poor boundary specification destroys the fourth order before the second order. The second order reaches 6 h even in the advective form with direct insertion at the boundaries but there were many high frequency waves present in the forecast, and it is likely that the second order would have failed after several more hours. Applying the sponge and porous sponge boundaries helped significantly in filtering the short waves. The flux form of the continuity equation was much more successful in keeping the small waves smooth and stable for the second order schemes. The flux form for fourth order compact has not been perfected yet and blows up after several time steps.

Table 6 depicts the RMS differences between either the flux form with direct insertion, the advective form with sponge boundary, or the advective form with porous sponge, and the GSM forecast at 6 h (i.e., 06 GMT on February 4, 1979) at all levels. Note that the RMS differences of all quantities at the lowest layer are sharply larger than the ensuing upper layers, possibly due to boundary layer effects on the GSM which are absent in the RLAM. The RMS differences for the sponge and porous sponge contain 18 X 13 interior grid points, while the direct insertion case contains 16 X 11 interior points. The greater RMS differences for the sponge cases are probably due to the greater influence of the GSM on the forecasts produced with direct insertion than on the forecasts produced with the sponge and, certainly, the porous sponge boundaries. Fig. 12a is the GSM 6 h field of temperatures at  $\sigma$  layer 4, while 12b - 12d are the forecasts with direct insertion, sponge, and porous sponge, respectively. There is general agreement despite some slight deviations, but these seem minor. The agreement at the center of the maps is noteworthy.



TABLE 6. RMS DIFFERENCES OF TEMPERATURES AND WINDS AT ALL LEVELS OF THE RLAM BETWEEN THE GSM 6 H FORECAST (VI 06 GMT 4 FEB 1979) AND THE 6 H FORECAST OF RLAM WITH DIRECT INSERTION AT THE BOUNDARIES (DI) (FLUX FORM), SPONGE BOUNDARY, AND POROUS SPONGE BOUNDARY

Variable	Layer												
	1	2	3	4	5	6	7	8	9	10	11	12	
DI	T°C	5.48	1.62	0.90	0.72	0.81	0.87	0.92	1.01	0.93	0.85	0.73	0.52
	u m s <sup>-1</sup>	5.00	3.17	2.76	2.71	3.54	4.39	4.61	3.68	3.33	3.11	3.06	2.68
	v m s <sup>-1</sup>	5.47	3.03	2.51	2.51	3.02	3.39	3.49	3.31	3.19	2.42	2.39	2.15
Sponge	T	5.07	1.65	1.43	1.56	1.56	1.72	2.22	2.70	2.99	3.24	1.89	1.32
	u	6.93	5.50	4.98	4.61	5.04	6.28	7.07	6.99	7.76	10.37	12.95	14.27
	v	6.02	5.38	4.77	4.45	4.80	5.35	5.52	5.45	6.03	8.21	10.90	12.66
Porous Sponge	T	5.21	1.79	1.49	1.58	1.57	1.72	2.20	2.70	2.96	3.22	1.92	1.59
	u	8.56	7.32	7.03	6.76	7.04	8.15	8.95	8.81	9.23	11.33	13.71	15.78
	v	8.98	8.32	7.81	7.35	7.48	7.74	7.70	7.72	8.11	9.67	12.14	15.14

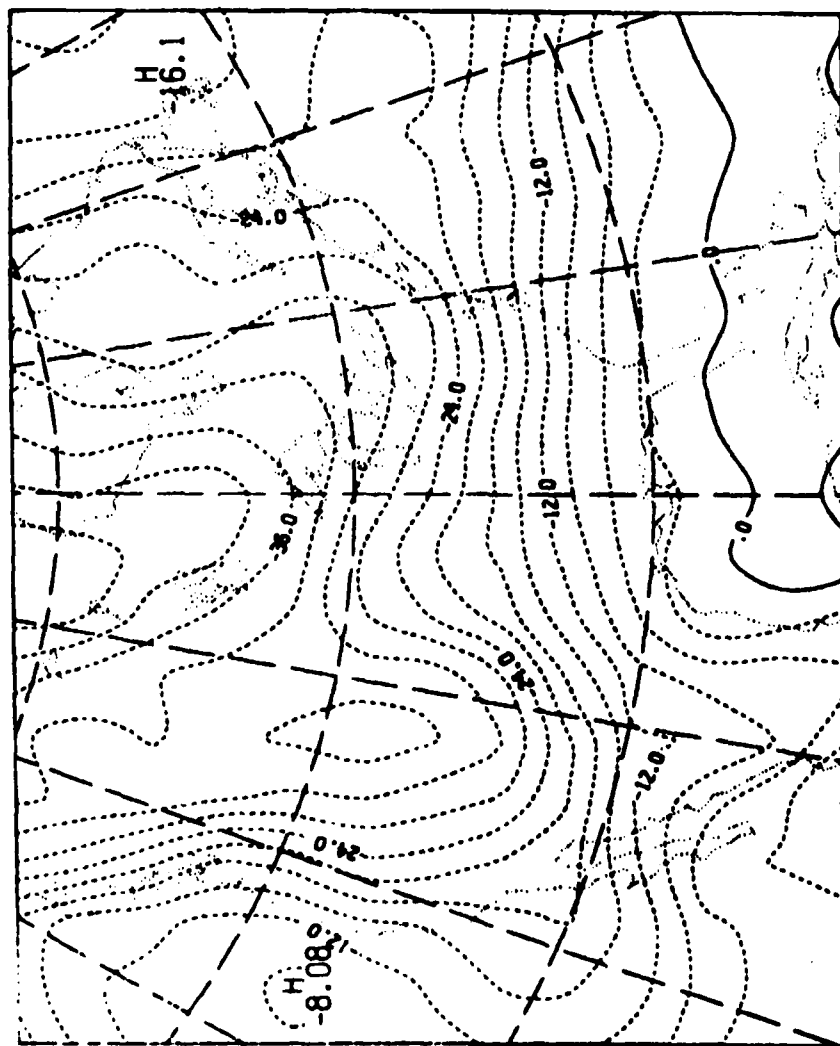


Fig. 12a. Contours of Temperature at  $\sigma$ -layer 4 for 6 H Forecast Produced by the GSM

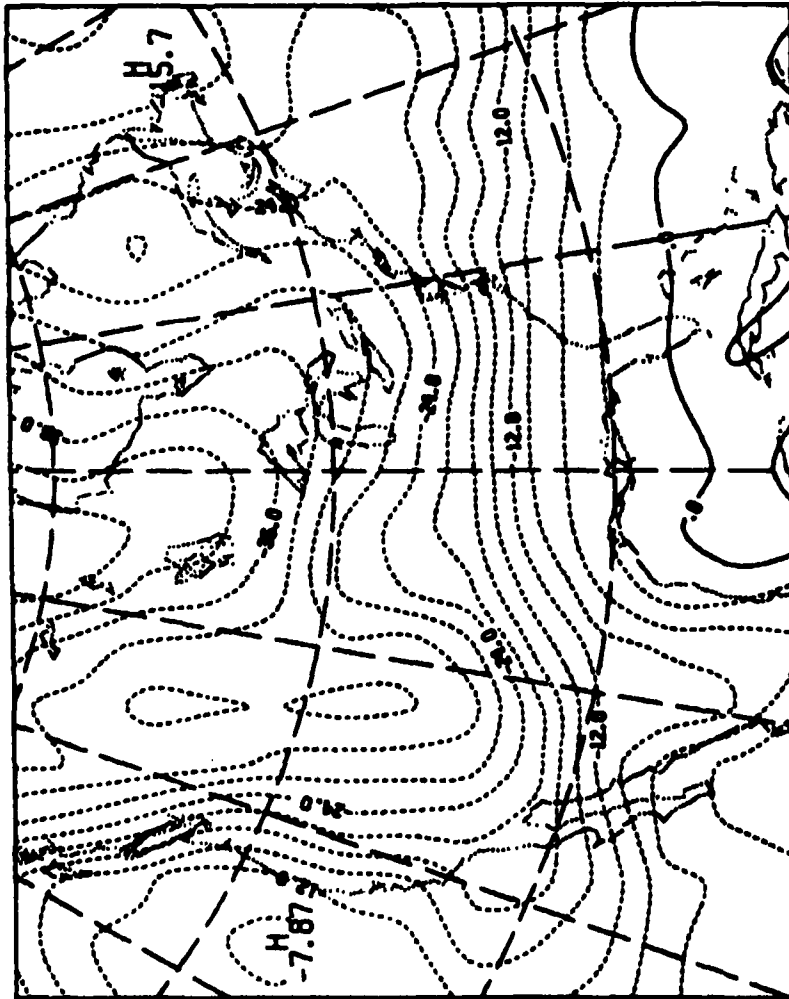


Fig. 12b. Contours of Temperature at  $\sigma$ -layer 4 for 6 H Forecast Produced by the RLAM with Direct Insertion of Boundary Values

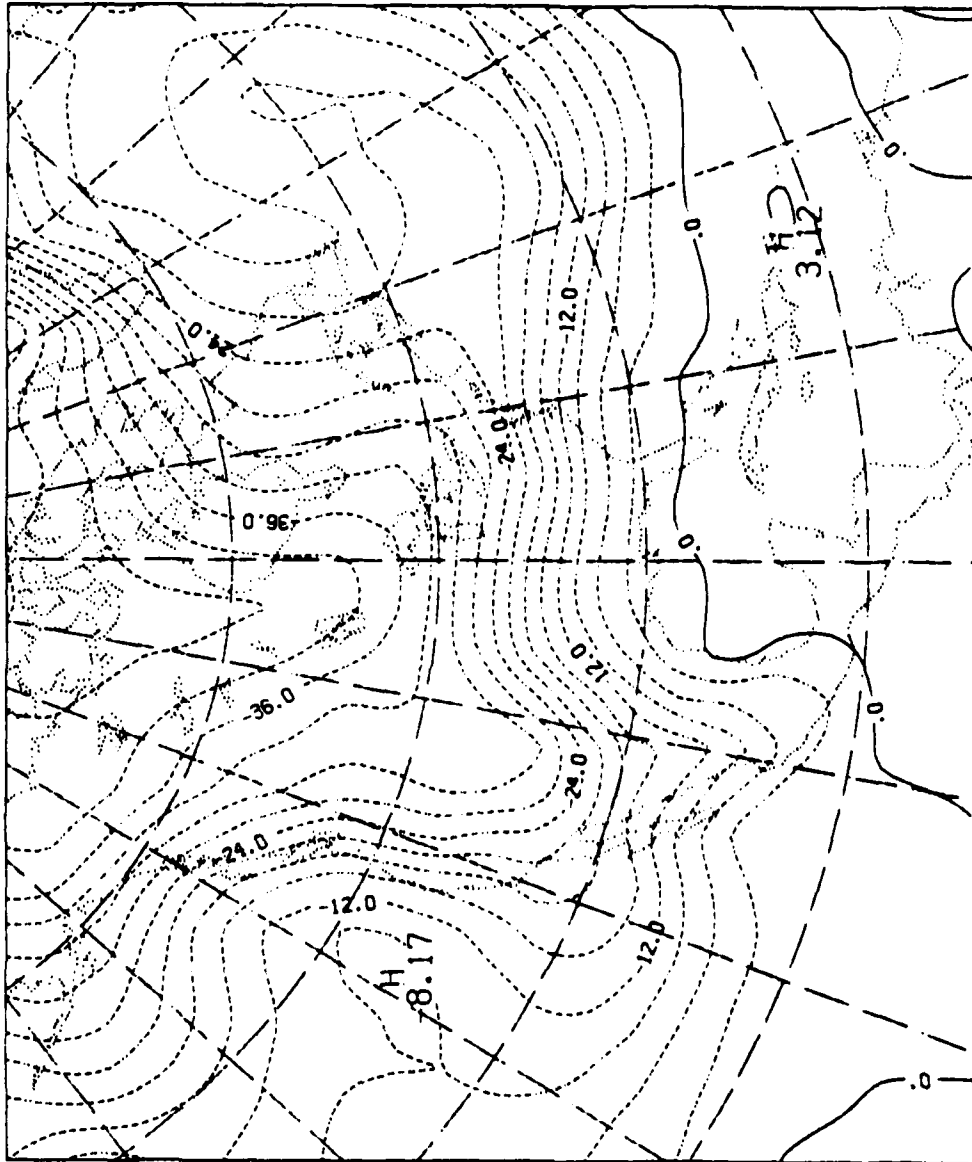


Fig. 12c. Contours of Temperature at  $\sigma$ -layer 4 for 6 H Forecast Produced by the RLAM with Sponge Boundary

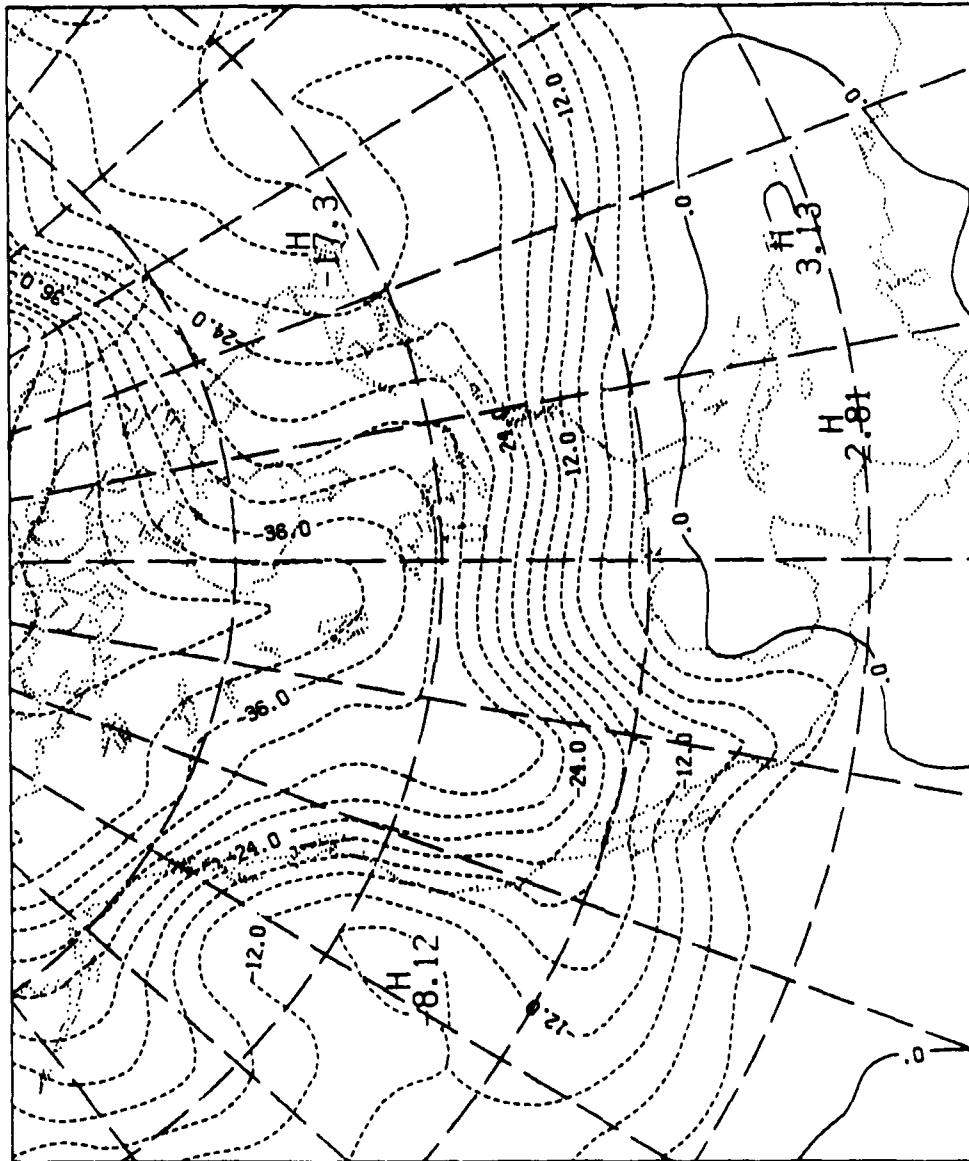


Fig. 126. Contours of Temperature at  $\sigma$ -layer 4 for 6 M Forecast Produced by the RLAI with Porous Sponge Boundary

Fig. 13a - 13d are the same as 12a - 12d, except that they depict the u component of velocity at  $\sigma$  layer 4. Here there is obvious disagreement among the forecasts, especially in areas near the boundaries. For the sponge boundaries there even appear to be some high frequency waves developing in the northeast corner of the map. These computations, as the figures indicate, were all performed on a Lambert projection. On a lat-lon grid, the agreement with the GSM was better, at least for the directly-inserted boundaries. This may be due simply to the fact that the GSM calculations are in principle also based on a lat-lon configuration.

#### 6. Outlook

Development of RLAM has been going reasonably well. Certainly modularity and movability are assets that make the RLAM superior to many other limited-area models, which are normally not as flexible. While there are many models that offer users a choice in geographic location, there are few that offer choices in numerical schemes, including boundary conditions. The benefit in this is that since some numerical schemes are better than others for certain situations, allowing a user to select a scheme may result in a better forecast. There is, of course, the danger that a selection will result in a divergent or non-physical solution. This can be prevented by the implementation of warnings and automatic stops within the program whenever an incompatible selection is made.

In the coming year physics, also in modular packages, will be introduced into the RLAM. Moisture management in terms of condensation and precipitation will be added to the model with regard taken to the number of levels selected by the user. Also a boundary layer and a radiation package will be added. Addition of these modular physical packages to the RLAM should make it a versatile and expedient research tool.

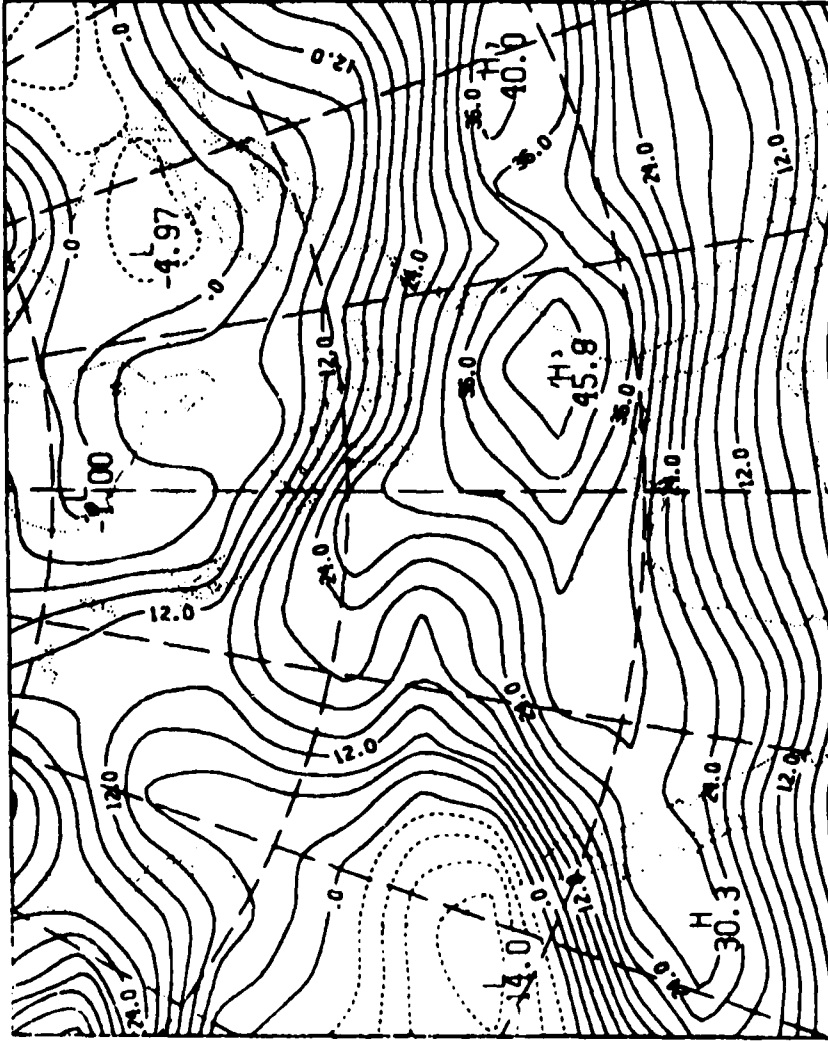


Fig. 13a. Same as Fig. 12a, except for u-component of Velocity at  $\sigma$ -layer 4 (contour interval is  $3 \text{ m s}^{-1}$ )

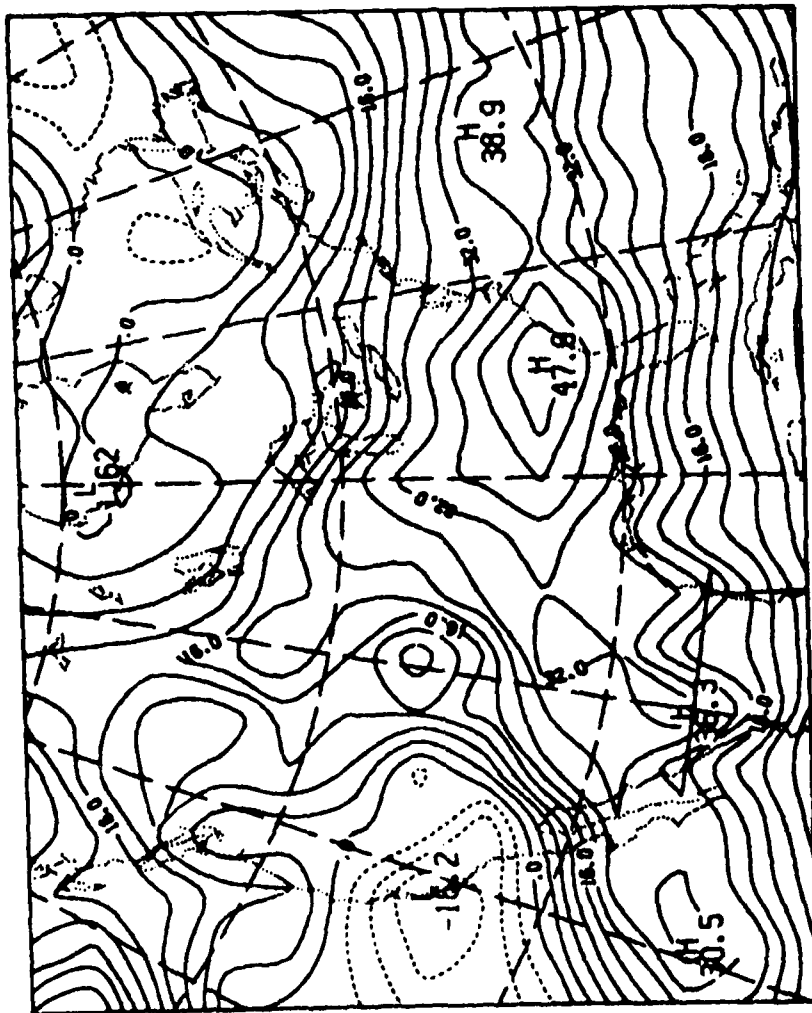


Fig. 13b. Same as Fig. 12b, except for u-component of Velocity at  $\sigma$ -layer 4 (contour interval is  $4 \text{ m s}^{-1}$ )



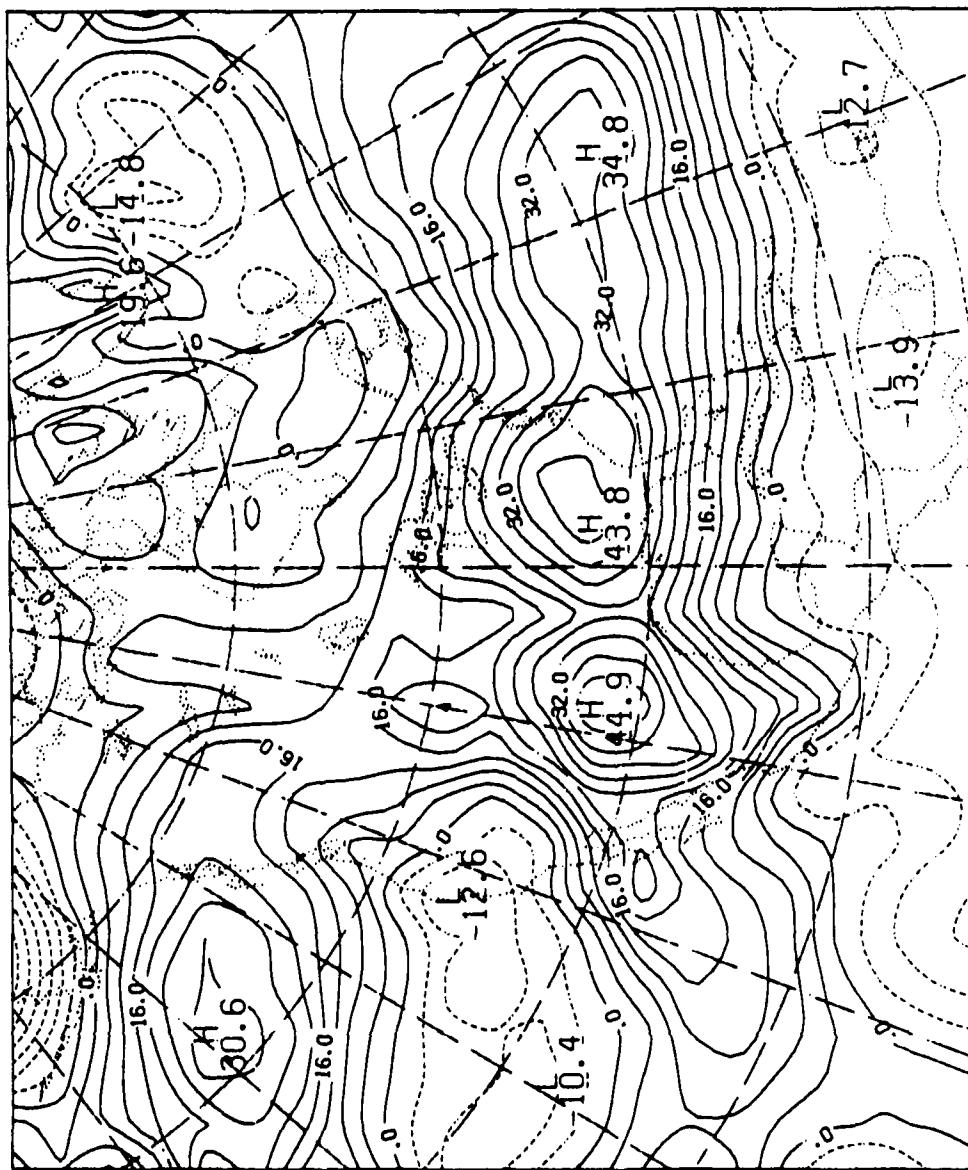


Fig. 13c. Same as Fig. 12c, except for u-component of Velocity at  $\sigma$ -layer 4 (contour interval is 4 m s<sup>-1</sup>)

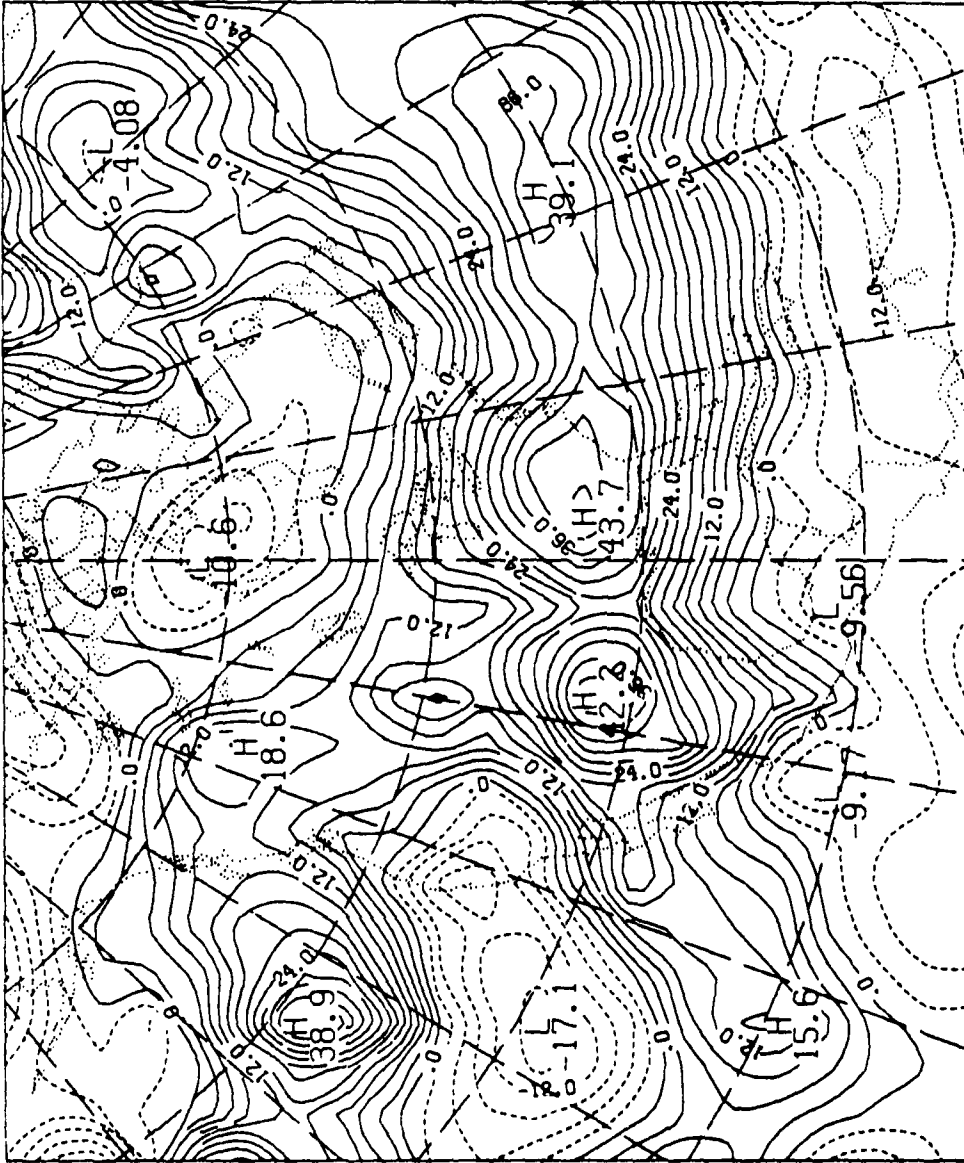


Fig. 13d. Same as Fig. 12d, except for u-component of Velocity at  $\sigma$ -layer 4 (contour interval is  $3 \text{ m s}^{-1}$ )

## Appendix B. Spectral Evaluation at the Poles

Because the RLAM may encompass the poles, it is necessary to specify initial conditions from the GSM at the poles. If a pole happens to be on the boundary, it may also be necessary to specify the derivatives of these quantities at the pole. Since the GSM supplies spectral coefficients, one could obtain values at the poles by simply expanding the spectral series at the poles. This presents no problems, except that the velocity coefficients produced by the model are pseudo-velocity coefficients derived from the vorticity and divergence. To obtain physical velocities at the pole, one would have to divide by the cosine of latitude ( $\cos \phi$ ) which becomes zero at the pole. Likewise, derivatives with respect to  $\phi$  can also involve  $\cos \phi$  in the denominator, implying a non-defined quantity. However, this need not be so if the numerator also tends to zero at a pace equal to or greater than  $\cos \phi$ .

As mentioned in the text, it is easier to study the behavior of the spectral quantities by rewriting the spectral expansions in terms of equivalent expansions in  $\mu = \sin \phi$ . A quantity  $A(\phi, \lambda)$  which is defined by the expansion

$$A(\phi, \lambda) = \sum_{m=-M}^M \sum_{n=|m|}^{|m|+N} A_n^m P_n^m(\phi) e^{im\lambda}$$

where  $P_n^m(\phi)$  are the associated Legendre functions, can be rewritten in terms of powers of  $\mu$  because

$$P_n^m(\mu) = (1-\mu^2)^{|m|/2} \sum_{j=0}^{n-|m|} p_j^{n,m} \mu^j.$$

Thus,

$$A(\phi, \lambda) = \sum_{n=-M}^M (1-\mu^2)^{|n|/2} \sum_{j=0}^N a_j^m \mu^j e^{im\lambda} \quad (B1)$$

where the  $a_j^m$  are linear combinations of  $A_n^m$  and  $p_j^{n,m}$ .

Now at the poles,  $\mu = \pm 1$ , Eq. (B1) approaches a finite sum equal to

$$A(\pm \pi/2, \lambda) = \sum_{j=0}^N a_j^0 S^j,$$

where  $S = +1$  at  $\phi = \pi/2$  and  $S = -1$  at  $\phi = -\pi/2$ . Note that the ambiguity of specifying longitude at the pole is not a factor here because the sum does not involve longitude.

Finding derivatives at the pole is also possible by estimating the limits of the expressions as  $\mu$  approaches  $\pm 1$ . Thus with  $i = \sqrt{-1}$ ,

$$\lim_{\mu \rightarrow \pm 1} \frac{\partial A}{\partial \lambda} = \lim_{\mu \rightarrow \pm 1} \sum_m (1-\mu^2)^{|m|/2} e^{im\lambda} \sum_{j=0}^N a_j^m \mu^j = 0 \text{ for all } m.$$

$$\lim_{\mu \rightarrow \pm 1} \frac{\partial A}{\partial \phi} = \lim_{\mu \rightarrow \pm 1} \frac{\partial A}{\partial \mu} \frac{d\mu}{d\phi} = \lim_{\mu \rightarrow \pm 1} (1-\mu^2)^{1/2} \frac{\partial A}{\partial \mu} =$$

$$\lim_{\mu \rightarrow \pm 1} \sum_m e^{im\lambda} \sum_{j=0}^N (1-\mu^2)^{\frac{|m|+1}{2}} \frac{1}{j} a_j^m \mu^{j-1} - \sum_{j=0}^N (1-\mu^2)^{\frac{|m|-1}{2}} |m| a_j^m \mu^{j+1}.$$

The sum (1) will be zero for all  $m$ . (2) will be zero for all  $|m| > 1$  and for  $|m| = 0$ .

$$\text{For } |m| = 1, (2) = \pm \sum_{j=0}^N a_j^{\pm 1} S^{j+1}.$$

$$\text{Thus, } \left( \frac{\partial A}{\partial \phi} \right)_{\phi = \pm \pi/2} = - \sum_{j=0}^N (a_j^1 e^{i\lambda} + a_j^{-1} e^{-i\lambda}) S^{j+1}. \quad (B2)$$

Thus the derivative with respect to  $\phi$  exists but creates a necessity for defining a longitude at the pole. This problem is alleviated, as will be shown, when the values are projected onto a polar stereographic map.

The components of wind velocity,  $u$  and  $v$ , are normally not used in spectral evaluations because they are discontinuous at the poles. It is easy to see that  $u$  and  $v$  will be of opposite sign for the same wind velocity on either side of the pole because the definitions of east and west, north and south are reversed. Thus, the GSM prefers to work with pseudo-velocities  $U$  and  $V$  which are  $U = u \cos \phi$ ,  $V = v \cos \phi$  and are necessarily continuous and equal to zero at the poles. They are derivable

from the divergence and vorticity. Thus if U and V are given by

$$U(\phi, \lambda) = \sum_m e^{im\lambda} (1-\mu^2)^{|m|/2} \sum_{j=0}^{N+1} U_j^m \mu^j$$

$$V(\phi, \lambda) = \sum_m e^{im\lambda} (1-\mu^2)^{|m|/2} \sum_{j=0}^{N+1} V_j^m \mu^j$$

then the coefficients are obtained from the stream function  $\psi$  and velocity potential  $\chi$ , as

$$U_j^m = (j + |m| - 1)\psi_{j-1}^m - (j+1)\psi_{j+1}^m + im\chi_j^m. \quad (B3)$$

$$V_j^m = (j + 1)\chi_{j+1}^m - (j + |m| - 1)\chi_{j-1}^m + im\psi_j^m.$$

Because the assumed truncation of  $\chi$  and  $\psi$  is M and N, the U and V expansions must go to N + 1.

To obtain physical velocities one need only divide by  $\cos\phi = (1-\mu^2)^{1/2}$ . To calculate u and v at the poles, one must find

$$\lim_{\mu \rightarrow \pm 1} u = U/\cos\phi = \lim_{\mu \rightarrow \pm 1} \sum_m (1-\mu^2)^{\frac{|m|-1}{2}} e^{im\lambda} \sum_{j=0}^{N+1} U_j^m \mu^j$$

with the same equation for v. It is obvious that the sum equals zero for all values of  $|m| > 1$ . At  $m = \pm 1$  the sum becomes

$$\lim_{\mu \rightarrow \pm 1} \sum_j U_j^m e^{\pm i\lambda} \mu^j = \sum_{j=0}^{N+1} (U_j^1 e^{i\lambda} + U_j^{-1} e^{-i\lambda}) \mu^j.$$

For  $m = 0$ , we are faced with an apparent singularity, i.e.,

$$\lim_{\mu \rightarrow \pm 1} (1-\mu^2)^{-1/2} \sum_{j=0}^{N+1} U_j^0 \mu^j.$$

But, in fact, since the pseudo-velocities must be zero at the poles, the

sum  $\sum_{j=0}^{N+1} U_j^0 S^j$  must equal zero. Applying L'Hôpital's rule yields

$$\lim_{\mu \rightarrow \pm 1} \frac{\sum_{j=0}^{N+1} U_j^0 \mu^j}{(1-\mu^2)^{1/2}} = \lim_{\mu \rightarrow \pm 1} - \frac{\sum_{j=0}^{N+1} j U_j^0 \mu^{j-1}}{\mu(1-\mu^2)^{-1/2}} = \lim_{\mu \rightarrow \pm 1} \frac{(1-\mu^2)^{1/2} \sum_{j=1}^{N+1} j U_j^0 \mu^{j-1}}{\mu} = 0.$$

$$\text{Thus, } u = \sum_{j=0}^{N+1} (U_j^1 e^{i\lambda} + U_j^{-1} e^{-i\lambda}) S^j$$

$$v = \sum_{j=0}^{N+1} (V_j^1 e^{i\lambda} + V_j^{-1} e^{-i\lambda}) S^j.$$

Here again there is a problem in defining  $\lambda$  at the pole, but the ambiguity can be resolved by projection onto a polar map, as will be demonstrated.

Obtaining derivatives of  $u$  and  $v$  becomes even more complicated.

We have for  $u$ ,

$$\frac{\partial u}{\partial \lambda} = \frac{\partial U / \cos \phi}{\partial \lambda} = i \sum_m m e^{im\lambda} (1-\mu^2)^{\frac{|m|-1}{2}} \sum_{j=0}^{N+1} U_j^m \mu^j$$

and similarly for  $v$ . For  $m = 0$  and  $|m| > 1$ , the above goes to zero at the poles. At  $m = \pm 1$ , we have

$$\lim_{\mu \rightarrow \pm 1} i e^{\pm i\lambda} \sum_{j=0}^{N+1} U_j^{\pm 1} \mu^j = i \sum_{j=0}^{N+1} (U_j^1 e^{i\lambda} + U_j^{-1} e^{-i\lambda}) S^j,$$

and similarly for  $\frac{\partial v}{\partial \lambda}$ .

To determine derivatives with respect to  $\phi$ , we have

$$\begin{aligned} \frac{\partial u}{\partial \phi} &= \frac{\partial U}{\partial \mu} \frac{d\mu}{d\phi} = \sum_m e^{im\lambda} \left[ \sum_j^{(1)} (1-\mu^2)^{\frac{|m|}{2}} U_j^m \mu^{j-1} \right. \\ &\quad \left. - \sum_j^{(2)} (1-\mu^2)^{\frac{|m|-2}{2}} (|m|-1) U_j^m \mu^{j+1} \right]. \end{aligned}$$

(1) yields zero at the poles except when  $m = 0$ , for which

$$(1) = \sum_j j U_j^0 s^{j-1}.$$

(2) has apparent singularities at  $|m| = 0$  and 1. For  $m = 0$

$$(2) = \lim_{\mu \rightarrow \pm 1} \sum_j (1 - \mu^2)^{-1} U_j^0 \mu^{j+1}.$$

Again, applying L'Hôpital's rule yields

$$\begin{aligned} \lim_{\mu \rightarrow \pm 1} \frac{\sum_j U_j^0 \mu^{j+1}}{(1-\mu^2)} &= \lim_{\mu \rightarrow \pm 1} \frac{\sum_{j=0}^{N+1} (j+1) U_j^0 \mu^j}{-2\mu} = \lim_{\mu \rightarrow \pm 1} -1/2 \sum_{j=0}^{N+1} (j+1) U_j^0 \mu^{j-1} \\ &= -1/2 \sum_{j=1}^{N+1} j U_j^0 s^{j-1} \end{aligned}$$

where the second term of the  $(j+1)$  factor disappears because

$$\sum_{j=0}^{N+1} U_j^0 s^{j-1} = s^{-1} \sum_{j=0}^{N+1} U_j^0 s^j = 0.$$

At  $|m| = 1$ , (2) is identically zero because of the factor  $|m| - 1$ .

$$\text{At } m = \pm 2, (2) \text{ becomes } - \sum_{j=0}^{N+1} U_j^{\pm 2} s^{j+1}.$$

Then,

$$\left( \frac{\partial u}{\partial \phi} \right)_{\phi = \pm \pi/2} = \sum_{j=0}^{N+1} (j/2 U_j^0 - U_j^2 e^{i2\lambda} - U_j^{-2} e^{-i2\lambda}) s^{j+1}. \quad (B5)$$

The same applies to  $\partial v / \partial \phi$ . Note that the results are always real, as one would expect.

To obtain  $x$  and  $y$  derivatives on a polar stereographic projection, one must invoke the chain rule. Thus, for scalar quantities such as temperature,  $T$ , we express derivatives in terms of  $x$  and  $y$  as

$$\tilde{\frac{\partial T}{\partial x}} = \frac{\partial T}{\partial \phi} \frac{\partial \phi}{\partial x} + \frac{\partial T}{\partial \lambda} \frac{\partial \lambda}{\partial x}$$

where the  $\sim$  indicates a function of  $x$  and  $y$  rather than  $\phi$  and  $\lambda$ . For polar projections, we have

$$\frac{\partial \phi}{\partial x} = \frac{-S \cos(\lambda - \lambda_0)}{aq}, \quad \frac{\partial \lambda}{\partial x} = \frac{-\sin(\lambda - \lambda_0)}{aq \cos \phi}, \quad \frac{\partial \phi}{\partial y} = \frac{-\sin(\lambda - \lambda_0)}{aq}$$

$$\frac{\partial \lambda}{\partial y} = \frac{S \cos(\lambda - \lambda_0)}{aq \cos \phi},$$

where  $a$  is the earth's radius,  $q$  is the map factor ( $= 2(1 + \sin \phi)^{-1}$ ), and  $\lambda_0$  is the longitude of the positive  $x$ -axis. The term  $\frac{\partial T}{\partial \phi} \frac{\partial \phi}{\partial x}$

presents no problems at the pole, and based on Eq. (B2) will simply become

$$\frac{\partial T}{\partial \phi} \frac{\partial \phi}{\partial x} = \sum_{j=0}^N (T_j^1 e^{i\lambda} + T_j^{-1} e^{-i\lambda}) S^{j+1} \left( \frac{S \cos \alpha}{aq} \right) = \frac{\cos \alpha}{aq} \sum_{j=0}^N (T_j^1 e^{i\lambda} + T_j^{-1} e^{-i\lambda}) S^j$$

because  $S \cdot S^{j+1} = S^j$ . (Here  $\alpha = \lambda - \lambda_0$ .)

To determine  $\frac{\partial T}{\partial \lambda} \frac{\partial \lambda}{\partial x}$ , however, we must look at the expansion

$$\frac{\partial T}{\partial \lambda} \frac{\partial \lambda}{\partial x} = \frac{-\sin \alpha}{aq} \sum_m i m (1 - \mu^2)^{\frac{|m|-1}{2}} \sum_j T_j^m \mu^j e^{i m \lambda}$$

The sum is zero for  $m = 0$  and  $|m| > 1$ . At  $|m| = 1$ , however, the value at the pole is

$$\frac{-i \sin \alpha}{aq} \sum_j (T_j^1 e^{i\lambda} - T_j^{-1} e^{-i\lambda}) S^j$$

Combining with the previous term and remembering that  $\cos \alpha + i \sin \alpha = e^{i\alpha}$  gives

$$\frac{\partial T}{\partial x} = \frac{1}{aq} \sum_{j=0}^N (T_j^1 e^{i\lambda} e^{-i\alpha} + T_j^{-1} e^{-i\lambda} e^{i\alpha}) S^j = \frac{2}{aq} \sum_{j=0}^N \text{Re}(T_j^1 e^{i\lambda_0}) S^j \quad (B6)$$

Note that here again there is no longitudinal dependency. For  $y$  derivatives, there is a similar expression, i.e.,



$$\tilde{\frac{\partial T}{\partial y}} = \frac{-2}{aq} \sum_{j=0}^N \text{Im}(T^1 e^{i\lambda_0}) S^{j+1}.$$

For physical velocities, the computations are not that simple. For one thing, one would not expect  $\frac{\partial u}{\partial x}$  or  $\frac{\partial v}{\partial y}$  to exist at the poles, because  $u$  and  $v$  are discontinuous at the poles as mentioned earlier. Mathematically, one observes that although  $\partial u/\partial \lambda$ ,  $\partial v/\partial \lambda$  exist, the product  $\frac{\partial u}{\partial \lambda} \frac{\partial \lambda}{\partial x}$  blows up at the pole. However, upon projection onto a polar map, the derivatives should exist. Indeed, the rotation of  $u$  and  $v$  from a global configuration to a polar map configuration is given by

$$\begin{aligned} \tilde{u} &= -u \sin \alpha - Sv \cos \alpha \\ \tilde{v} &= Su \cos \alpha - v \sin \alpha. \end{aligned}$$

The  $x$ -derivative is then

$$\begin{aligned} \tilde{\frac{\partial u}{\partial x}} &= \frac{\partial \tilde{u}}{\partial \phi} \frac{\partial \phi}{\partial x} + \frac{\partial \tilde{u}}{\partial \lambda} \frac{\partial \lambda}{\partial x} = S \frac{\cos \alpha}{aq} \left( \frac{\partial u}{\partial \phi} \sin \alpha + S \frac{\partial v}{\partial \phi} \cos \alpha \right) + \\ & \frac{\sin \alpha}{aq \cos \phi} \left( \frac{\partial u}{\partial \lambda} \sin \alpha + u \cos \alpha + S \frac{\partial v}{\partial \lambda} \cos \alpha - Sv \sin \alpha \right). \end{aligned}$$

The  $\phi$ -derivatives present no problem, because they are finite and defined by Eq. (B5). The second term must be handled carefully. We first expand the terms and divide them by  $(1-\mu^2)^{1/2}$ , giving

$$\begin{aligned} \frac{\sin \alpha}{aq} & \left[ i \sin \alpha \sum_m e^{im\lambda} (1-\mu^2)^{\frac{|m|-2}{2}} \sum_j U_j^m \mu^j + \cos \alpha \sum (1-\mu^2)^{\frac{|m|-2}{2}} e^{im\lambda} \sum_j U_j^m \mu^j \right. \\ & \left. + iS \cos \alpha \sum_m e^{im\lambda} (1-\mu^2)^{\frac{|m|-2}{2}} \sum_j V_j^m \mu^j - S \sin \alpha \sum (1-\mu^2)^{\frac{|m|-2}{2}} e^{im\lambda} \sum_j V_j^m \mu^j \right]. \end{aligned}$$

When  $m = 0$ , the first and third terms go to zero, while the second and fourth terms reach a finite limit as mentioned earlier. When  $m = \pm 2$ , all terms also approach finite limits at the poles. The problem arises when  $m = \pm 1$ . Here, apparently, the individual terms seem to become infinite at the poles. However when one collects terms, one reduces the above expression when  $m = \pm 1$  to

$$e^{i\alpha} e^{i\lambda} (1-\mu^2)^{-1/2} \sum_j (U_j^1 + iSV_j^1) \mu^j \quad \text{for } m = 1$$

$$e^{-i\alpha} e^{i\lambda} (1-\mu^2)^{-1/2} \sum_j (U_j^{-1} - iSV_j^{-1}) \mu^j \quad \text{for } m = -1.$$

By invoking Eq. (B3), we can demonstrate that the sums for both  $m = 1$  and  $m = -1$  approach zero as  $\mu \rightarrow \pm 1$ . Substituting for  $U_j^1$  and  $V_j^1$  we get in the limit,

$$\sum_j (U_j^1 + iSV_j^1) S^j = \sum_j \{ j \psi_{j+1}^1 - (j+1) \psi_{j+1}^1 + i \chi_j^1 + iS(j+1) \chi_{j+1}^1 - iSj \chi_{j-1}^1 - S \psi_j^1 \} S^j.$$

By separating sums and changing the indices we can rewrite this expression as

$$\begin{aligned} & \sum_{k=0}^N (k+1) \psi_k^1 S^{k+1} - \sum_{k=1}^N k \psi_k^1 S^{k-1} + i \sum_{k=0}^N \chi_k^1 S^k + i \sum_{k=1}^N k \chi_k^1 S^{k-1} - \sum_{k=0}^N (k+1) \chi_k^1 S^k - \sum_{k=0}^N \psi_k^1 S^{k+1} \\ & = 0, \text{ because } S^{k+1} = S^{k-1}. \end{aligned}$$

For  $m = -1$ , we have

$$\begin{aligned} & \sum_j (U_j^{-1} - iSV_j^{-1}) S^j = \sum_j \{ j \psi_{j-1}^{-1} - (j+1) \psi_{j+1}^{-1} - i \chi_j^{-1} - iS(j+1) \chi_{j+1}^{-1} + iSj \chi_{j-1}^{-1} - S \psi_j^{-1} \} S^j \\ & = \sum_{k=0}^N (k+1) \psi_k^{-1} S^{k+1} - k \psi_k^{-1} S^{k-1} - i \chi_k^{-1} S^k - ik \chi_k^{-1} S^{k-1} + i(k+1) \chi_k^{-1} S^k - \psi_k^{-1} S^{k+1} = 0. \end{aligned}$$

L'Hôpital's rule will show that the numerator reaches zero more quickly than the denominator; so the sums for  $m = \pm 1$  will vanish. Thus, rotation of the velocities to coincide with Cartesian coordinates allows one to calculate the derivatives.

Summing over  $m = 0$ ,  $m = +2$ , and  $m = -2$ , after determining the limits of the expressions from previous discussion, gives

$$\begin{aligned} \frac{\partial \tilde{u}}{\partial \lambda} \frac{\partial \lambda}{\partial x} = \frac{\sin \alpha}{a q} & \left[ 1/2 \sin \alpha \sum_j v_j^0 s^{j+1} - 1/2 \cos \alpha \sum_j u_j^0 s^j \right. \\ & + 2i e^{i2\lambda} \sin \alpha \sum_j u_j^2 s^j + e^{i2\lambda} \cos \alpha \sum_j u_j^2 s^j + 2i e^{i2\lambda} \cos \alpha \sum_j v_j^2 s^{j+1} \\ & - e^{i2\lambda} \sin \alpha \sum_j v_j^2 s^{j+1} - 2i e^{-i2\lambda} \sin \alpha \sum_j u_j^{-2} s^j + e^{-i2\lambda} \cos \alpha \sum_j u_j^{-2} s^j \\ & \left. - 2i e^{-i2\lambda} \cos \alpha \sum_j v_j^{-2} s^{j+1} - \sin \alpha e^{-i2\lambda} \sum_j v_j^{-2} s^{j+1} \right], \end{aligned}$$

while from Eq. (B5)

$$\begin{aligned} \frac{\partial \tilde{u}}{\partial \phi} \frac{\partial \phi}{\partial x} = \frac{\cos \alpha}{a q} & \left[ 1/2 \sin \alpha \sum_j u_j^0 s^j - 2 \sin \alpha \sum_j \operatorname{Re}(u_j^2 e^{i2\lambda}) s^j + 1/2 \cos \alpha \sum_j v_j^0 s^{j+1} \right. \\ & \left. - 2 \cos \alpha \sum_j \operatorname{Re}(v_j^2 e^{i2\lambda}) s^{j+1} \right]. \end{aligned}$$

After combining and cancelling appropriate terms, we have

$$\begin{aligned} \frac{\partial \tilde{u}}{\partial x} = & \left[ 1/2 \sum_j v_j^0 s^{j+1} - 2 \sum_j \operatorname{Re}(v_j^2 e^{i2\lambda}) s^{j+1} - 4 \sin^2 \alpha \sum_j \operatorname{Im}(u_j^2 e^{i2\lambda}) s^j \right. \\ & \left. - 4 \cos \alpha \sin \alpha \sum_j \operatorname{Im}(v_j^2 e^{i2\lambda}) s^{j+1} \right] / a q \end{aligned}$$

and similarly,

$$\begin{aligned} \frac{\partial \tilde{u}}{\partial y} = \frac{1}{a q} & \left[ 1/2 \sum_j u_j^0 s^{j+1} - 2 \sum_j \operatorname{Re}(u_j^2 e^{i2\lambda}) s^{j+1} + 4 \cos^2 \alpha \sum_j \operatorname{Im}(v_j^2 e^{i2\lambda}) s^j \right. \\ & \left. + 4 \sin \alpha \cos \alpha \sum_j (u_j^2 e^{i2\lambda}) s^{j+1} \right]. \end{aligned} \quad (B7)$$

For  $v$  we have

$$\begin{aligned} \frac{\partial \tilde{v}}{\partial x} = \frac{1}{a q} & \left[ -1/2 \sum_j u_j^0 s^{j+1} + 2 \sum_j \operatorname{Re}(u_j^2 e^{i2\lambda}) s^{j+1} + 4 \cos \alpha \sin \alpha \sum_j \operatorname{Im}(u_j^2 e^{i2\lambda}) s^{j+1} \right. \\ & \left. - 4 \sin^2 \alpha \sum_j \operatorname{Im}(v_j^2 e^{i2\lambda}) s^j \right] \end{aligned}$$

and

$$\frac{\partial \tilde{v}}{\partial y} = \frac{1}{a q} \left[ \frac{1}{2} \sum_j V_j^0 S^{j+1} - 2 \sum_j \operatorname{Re}(V_j^2 e^{i2\lambda}) S^{j+1} - 4 \cos^2 \alpha \sum_j \operatorname{Im}(V_j^2 e^{i2\lambda}) S^j + 4 \cos \alpha \sin \alpha \sum_j \operatorname{Im}(V_j^2 e^{i2\lambda}) S^{j+1} \right].$$

The apparent arbitrariness in choosing a longitude at the pole for  $u$  and  $v$  and their derivatives is really a non-existent problem once they are projected onto a polar map, despite the indication in Eq. (B4) of a dependence on  $\lambda$ . This can be shown easily if we write  $W = U + iV$ , and the transformation to polar maps becomes  $W = iSWe^{iS\alpha}$ .

In expanded form, based on Eq. (B4), this becomes, at the pole,

$$\tilde{W} = \tilde{U} + i\tilde{V} = i \sum_j (W_j^1 e^{i\lambda} + W_j^{-1} e^{-i\lambda}) e^{iS\alpha} S^{j+1}.$$

At the North Pole, the second term becomes independent of longitude because  $e^{i\alpha} e^{-i\lambda} = e^{-i\lambda_0}$ . At the South Pole the first term is neutralized. However at the North Pole we have

$$\sum_j W_j^1 e^{i\lambda} e^{i\alpha} S^{j+1} = \sum_j (U_j^1 + iV_j^1) S^{j+1} e^{i(\alpha+\lambda)}.$$

But this sum has already been demonstrated to vanish even under division by  $\cos \phi$ . The second term, however, does not vanish when  $S = 1$ . It does vanish, however, at the South Pole when the first does not. Thus the velocities are dependent only on the specific rotation angle  $\lambda_0$  of the map projection.

The derivatives of  $u$  and  $v$  with respect to  $x$  and  $y$  should also not be dependent on latitude. This can be proven by noting that, with the aid of Eq. (B3),

$$\begin{aligned} \sum_j \operatorname{Re}(U_j^2) S^j &= 2 \sum_k \operatorname{Re}(\psi_k^2) S^{k+1} - 2 \sum_k \operatorname{Im}(\chi_k^2) S^k = S \sum_j \operatorname{Im}(V_j^2) S^j \\ \sum_j \operatorname{Im}(U_j^2) S^j &= 2 \sum_k \operatorname{Im}(\psi_k^2) S^{k+1} + 2 \sum_k \operatorname{Re}(\chi_k^2) S^k = -S \sum_j \operatorname{Re}(V_j^2) S^j. \end{aligned}$$

Substituting for appropriate terms in Eq. (B7) along with the trigonometric identities  $\sin 2\alpha = 2 \sin \alpha \cos \alpha$ ,  $2 \sin^2 \alpha = 1 - \cos 2\alpha$ , gives the following simplified and longitude independent results,

$$\frac{\partial \tilde{u}}{\partial x} = \frac{1}{aq} \left[ \frac{1}{2} \sum_{j=0}^{N+1} j V_j^o S^{j+1} - 2 \sum_{j=0}^{N+1} \operatorname{Re}(V_j^2 e^{i2\lambda} e^{-i2\alpha}) S^{j+1} \right]$$

$$\frac{\partial \tilde{u}}{\partial y} = \frac{1}{aq} \left[ \frac{1}{2} \sum_{j=0}^{N+1} j U_j^o S^{j+1} + 2 \sum_{j=0}^{N+1} \operatorname{Re}(U_j^2 e^{i2\lambda} e^{-i2\alpha}) S^{j+1} \right]$$

(B8)

$$\frac{\partial \tilde{v}}{\partial x} = \frac{1}{aq} \left[ -\frac{1}{2} \sum_{j=0}^{N+1} j U_j^o S^{j+1} + 2 \sum_{j=0}^{N+1} \operatorname{Re}(U_j^2 e^{i2\lambda} e^{-i2\alpha}) S^{j+1} \right]$$

$$\frac{\partial \tilde{v}}{\partial y} = \frac{1}{aq} \left[ \frac{1}{2} \sum_{j=0}^{N+1} j V_j^o S^{j+1} + 2 \sum_{j=0}^{N+1} \operatorname{Re}(V_j^2 e^{i2\lambda} e^{-i2\alpha}) S^{j+1} \right]$$

with  $e^{i2\lambda} e^{-i2\alpha} = e^{i2\lambda}$ .

## II. MESOSCALE FORECASTING

### A. Evaluation of the Generalized Exponential Markov (GEM) Technique Using Hourly Observations at Patrick Air Force Base, Florida

A version of GEM had previously been adapted to the AFGL McIDAS by SASC meteorologists (Gerlach, 1982) with the cooperation and assistance of scientists at the National Weather Service Techniques Development Laboratory. It was used at AFGL as part of a Mesoscale Forecast Experiment (MFE) reported on by Chisholm and Jackson (1984).<sup>23</sup> The Eastern Space and Missile Center weather facility (ESMC/WE) requested an evaluation of the GEM technique for possible use as short range forecast guidance for launch operations at the Kennedy Space Center (KSC).

The GEM technique is a fundamental statistical weather forecasting procedure developed by Miller (1981)<sup>24</sup> who defines GEM as "a statistical technique for predicting the probability distribution of local surface weather elements hour by hour. It uses only the current local surface weather conditions as predictors. From these probability distributions, categorical predictions are made for each surface weather element." For its use in the MFE and in this study the GEM technique was adapted to generate wind, cloud cover, and ceiling height forecasts which were verified at 1, 2, 4, and 6 h intervals coincident with the MFE verification procedures. Patrick Air Force Base, FL (COF) was chosen as the location to test GEM since it is the closest station to KSC routinely reporting the weather elements necessary for application of the GEM forecast technique and subsequent verification.

Three factors must be recognized regarding the application of GEM to COF data: First, GEM is founded on a Markov assumption (that is, the future state is completely determined by the present state and is independent of the way in which the present state has developed). Second, it uses multivariate linear regression equations that were developed from continuous observational samples that spanned a 12 year period (1954-1965) at a number of locations and thus are climatologically and statistically

---

23. Chisholm, D. A., and A. J. Jackson, 1984: An Assessment of Interactive Graphics Processing in Short-Range Terminal Weather Forecasting. AFGL-TR-84-0029, Air Force Geophysics Laboratory, Hanscom AFB MA, ADA142706.

24. Miller, R. G., 1981: GEM: A Statistical Weather Forecasting Procedure. NOAA-TR-NWS-28.

sound. Third, it was applied only to available hourly observations for two one-month periods (July and December 1983). It therefore may not reflect the characteristics of the full sample from which the GEM statistical operators were developed. It was felt, however, that applying it to demonstrate the general performance of GEM vs. persistence was proper and appropriate.

The available hourly observations at COF for July and December 1983 comprised the database used to evaluate GEM. Surface observations were available to the AFGL McIDAS facility via the FAA WB604 line. Routine software to ingest, decode, and archive these data on an hourly cycle (i.e., no specials) exists in McIDAS, although substantial modifications to the GEM and MFE software were necessary to perform the experiment. Specifically, data taken from 12 GMT through 03 GMT were used to generate GEM forecasts valid 1, 2, 4 and 6 h later. Forecasts were not made from available 04 GMT data since COF does not report between 05 GMT and 11 GMT and therefore no verifying observations were available. For this application GEM generated deterministic surface wind vector forecasts and probability forecasts of cloud cover and ceiling height in the "standard" MOS categories shown in Table 7. Category 6 of ceiling height also includes all "no ceiling" cases.

TABLE 7

GEM Categories

	1	2	3	4	5	6
CLOUD COVER	CLEAR	SCATTERED	BROKEN	OVERCAST	--	--
CEILING HEIGHT (100 ft)	0 - 1	2 - 4	5 - 9	10 - 29	30 - 75	> 75

Conversion from probability to categorical forecast was based on a simple maximum probability approach. Figs. 14 and 15 are examples of a full GEM forecast for Patrick AFB in July and December respectively.

The cloud cover and ceiling probabilities and categorical forecasts and the deterministic wind vector forecasts were verified against observed conditions 1, 2, 4 and 6 h after forecast times. As will be seen in the verification results below, the number of forecasts verified decreased as

```

GGG EFFF M M
G E M M
G GGG EFF M A M
G G E M M
GGG EFFF M M

```

TOL AND NIEDZIELSKI  
FOR AFGL  
FOR STATION LUP  
VALID FOR 4 HOURS AFTER JUL 23, 12 LOCAL

[ HOUR [	[ TT	[ DRU	[ VV	WEATHER	DIFF	PPP	C1	M1	C2	M2	TS	CIG [
[ 12 [	[ 92	[ 17	[ 1000		2605	0076	SCT	30	HKN	160	BKN	160 [
[ 13 [	[ 92	[ 17	[ 1000		2605	0076	SCT	30	HKN	160	BKN	160 [
[ 14 [	[ 92	[ 17	[ 1000		2605	0076	SCT	30	HKN	160	BKN	160 [
[ 16 [	[ 92	[ 17	[ 1000		2605	0076	SCT	40	HKN	160	BKN	160 [
[ 18 [	[ 92	[ 17	[ 1000	T,A	1715	0076	SCT	40	BKN	160	BKN	160 [

FIRST FORECAST VERIFICATION TIME (MFF) IS 231700

FORECAST INTERVAL = 1 HOUR(S)

CLOUD AMOUNT-	CLEAR	SCATTERED	BROKEN	OVERCAST
	6	26	67	15

CEILING HEIGHT-	<2	2-4	5-9	10-29	30-75	>75
	0	0	0	2	12	85

FORECAST INTERVAL = 2 HOUR(S)

CLOUD AMOUNT-	CLEAR	SCATTERED	BROKEN	OVERCAST
	6	29	60	18

CEILING HEIGHT-	<2	2-4	5-9	10-29	30-75	>75
	0	0	0	2	14	84

FORECAST INTERVAL = 4 HOUR(S)

CLOUD AMOUNT-	CLEAR	SCATTERED	BROKEN	OVERCAST
	5	36	44	25

CEILING HEIGHT-	<2	2-4	5-9	10-29	30-75	>75
	0	0	0	3	18	79

FORECAST INTERVAL = 6 HOUR(S)

CLOUD AMOUNT-	CLEAR	SCATTERED	BROKEN	OVERCAST
	0	35	36	28

CEILING HEIGHT-	<2	2-4	5-9	10-29	30-75	>75
	0	0	1	5	16	78

Fig. 14. Example of Numerical (Categorical) and Probability Forecasts Generated by Generalized Exponential Markov (GEM) Technique Based on Surface Observation at COF at 1200 LST 23 July 1983



GGG EFFF M M  
 G E MM MM  
 G GGG EFF M M M  
 G G E M M  
 GGG EFFF M M

TDL AND NIEDZIELSKI  
 FOR AFGL  
 FOR STATION CUF  
 VALID FOR 6 HOURS AFTER DEC 27, 9 LOCAL

HOUR	TT	DPO	VV	WEATHER	ODPF	PPP	L1	H1	C2	H2	TS	CIG
9	47	4	1000		3505	0176	BKN	30	BKN	100	OVC	30
10	47	4	1000		3505	0176	BKN	30	BKN	100	OVC	30
11	47	4	1000		3505	0176	BKN	30	BKN	100	OVC	30
14	47	13	1000		3505	0176	BKN	30	OVC	60	OVC	30
15	47	13	1000		3015	0176	BKN	30	OVC	60	OVC	30

FIRST FORECAST VERIFICATION TIME (MFF) IS 271500

FORECAST INTERVAL = 1 HOUR(S)

CLOUD AMOUNT-	CLEAR	SCATTERED	BROKEN	OVERCAST
	0	0	10	82

CEILING HEIGHT-	<2	2-4	5-9	10-29	30-75	>75
	0	0	1	15	63	27

FORECAST INTERVAL = 2 HOUR(S)

CLOUD AMOUNT-	CLEAR	SCATTERED	BROKEN	OVERCAST
	1	5	20	76

CEILING HEIGHT-	<2	2-4	5-9	10-29	30-75	>75
	0	0	0	15	56	30

FORECAST INTERVAL = 4 HOUR(S)

CLOUD AMOUNT-	CLEAR	SCATTERED	BROKEN	OVERCAST
	1	11	25	66

CEILING HEIGHT-	<2	2-4	5-9	10-29	30-75	>75
	0	0	0	17	42	40

FORECAST INTERVAL = 6 HOUR(S)

CLOUD AMOUNT-	CLEAR	SCATTERED	BROKEN	OVERCAST
	1	14	25	60

CEILING HEIGHT-	<2	2-4	5-9	10-29	30-75	>75
	0	1	1	17	33	46

Fig. 15. Example of Numerical (Categorical) and Probability Forecasts Generated by Generalized Exponential Markov (GEM) Technique Based on Surface Observation at COF at 0900 LST 27 December 1983

one goes from 1 to 6 h because of the lack of observations from 05 - 11 GMT in December and 04 - 10 GMT in July. The measures of skill used in this evaluation were the RMS error for the deterministic forecasts and the p-score for the probability forecasts. RMSE scores were provided for persistence and the Heidke (or percent improvement) score of GEM (relative to persistence) was also provided.

Table 8 lists the RMSE statistics obtained in this evaluation. Differences between GEM and persistence are generally too small to be statistically significant. Where differences exist, the smaller RMSE are for persistence. The worst GEM errors occur when going from 4 to 6 h wind vector forecasts, especially in December where there is more than a 75 percent increase in RMSE from 4 (6.9 knots) to 6 h (12.3 knots).

Table 9 lists the p-scores and Heidke skill score vs. persistence probability of the cloud cover and ceiling height probability forecasts. Persistence was used in probability form by assigning a probability forecast of 100 percent to the category that existed at observation time and assigning a forecast value of 0 percent to each of the other categories. With the exception of summertime ceiling height, the GEM probability forecasts score better than does persistence probability. Note also that the percent improvement (Heidke skill scores) statistics get better as the forecast interval increases. The summer ceiling height results are inconclusive in that the skill score figures merely reflect small differences between very small p-score values. Recall that the smaller the p-score the "better" the forecast. In this case, the occurrence of ceiling conditions below 7,500 ft is so rare that it is not a particularly appropriate forecast problem to evaluate in the summer.

In conclusion, the extent to which GEM could or should be used as forecast guidance at KSC in support of launch operations cannot be clearly determined from this evaluation. If a yes/no type of guidance better than persistence is desired, GEM will not provide it. GEM does, however, offer better probability guidance than persistence probability.

#### B. FOUS Guidance Error Study

As part of a continuing effort to analyze systematic errors in the Limited Area Fine Mesh Model (LPM-II), FOUS data were collected from October 1, 1984 through November 30, 1985. The concurrent error analysis is being

TABLE 8. RMSE STATISTICS FOR GEM (G) AND PERSISTENCE (P) FORECASTS FOR PATRICK AFB (COF) IN 1983

	July							
	1-hr		2-hr		4-hr		6-hr	
	G	P	G	P	G	P	G	P
Wind Vector (Knots)	4.1	3.5	4.4	4.0	5.5	5.0	8.4	5.5
Cloud Cover (Categories)	0.46	0.46	0.60	0.60	0.77	0.74	0.93	0.78
Ceiling Height (Categories)	0.29	0.29	0.33	0.33	0.33	0.38	0.39	0.37
No. of Events	350		324		271		221	
	December							
Wind Vector	4.9	3.5	5.4	4.4	6.9	5.6	12.3	6.2
Cloud Cover	0.49	0.49	0.61	0.60	1.03	0.75	1.24	0.85
Ceiling Height	0.61	0.61	0.75	0.74	0.89	0.88	0.91	0.98
No. of Events	398		372		315		266	

TABLE 9. P-SCORE FOR GEM (G) AND HEIDKE SKILL SCORE (SS) VS. PERSISTENCE PROBABILITY FOR PATRICK AFB (COF) IN 1983

	July							
	1-hr		2-hr		4-hr		6-hr	
	G	SS	G	SS	G	SS	G	SS
Cloud Cover (4 categories)	0.06	+ 4%	0.09	+15%	0.11	+20%	0.12	+27%
Ceiling Height (6 categories)	0.01	-28%	0.02	-14%	0.02	- 9%	0.02	-27%
No. of events	350		324		271		221	
	December							
Cloud Cover	0.07	+10%	0.09	+16%	0.13	+25%	0.14	+31%
Ceiling Height	0.04	+15%	0.05	+23%	0.06	+30%	0.07	+35%
No. of events	398		372		315		266	

performed by summing individual forecast errors for 89 stations and calculating average errors over various time spans.

Individual forecast errors from 89 stations were obtained from the FOUS 60-78 bulletins decoded by McIDAS. Forecast values for each variable at each station for 12, 24, 36 and 48 h forecasts were obtained from the appropriate location in the FOUS 60-78 bulletins. Verification values were obtained from the initial conditions in the relevant successive FOUS 60-78 bulletins derived from the LFM-II initial analysis. Forecast errors of the variables were accumulated at each of the 89 locations by subtracting the verification value from a variable forecast value. The variables analyzed included sea-level pressure, 1000 - 500 mb thickness, mean relative humidity, boundary layer relative humidity, lower tropospheric relative humidity, and boundary layer temperature.

By calculating the forecast errors in the manner described, a positive number indicates an overforecast (i.e., the forecast was too warm, too moist, pressure too high, etc.) and a negative number indicates an underforecast (too cold, too dry, pressure too low, etc.). To examine the sensitivity of the forecast errors to diurnal influences, the data at each of the 89 stations were stratified into error sums from 00 GMT model runs and 12 GMT model runs. For a more complete description of the methodology employed in this study, see Schechter (1984)<sup>25</sup> and Gerlach (1983).

This study differs in some respects from the earlier work done on systematic FOUS guidance errors (Gerlach, 1983, 1984). An additional parameter (lower tropospheric relative humidity) has been included in the error analysis. The analysis has been broadened to include forecasts from the warm season in order to determine if the error patterns change noticeably over the course of a year. Errors from individual forecast episodes have been saved for all cases so that statistical testing of the significance of the error fields can be performed. As of yet, no satisfactory technique has been found to test for statistical significance.

Since only about one-half of the FOUS data collected have been processed, no definitive statements about the 1984-85 error fields can be

---

25. Schechter, R., 1984: An error analysis of LFM-II forecasts during the 1982-1983 winter season. Bull. Amer. Met. Soc., 65, 1073-1080.

made. However, error fields stratified by month have been generated for October 1984 - March 1985 and July 1985; hence comments on these preliminary results can be made.

Total relative humidity is generally forecast too dry along the Gulf Coast and too wet in the northern Rockies during the cool season (Fig. 16) although the moist bias almost disappears during January. In July (the only warm season month processed thus far) the moist bias in the northern Rockies is absent (or very weak) (Fig. 17) while the dry bias in the Gulf States grows a little larger relative to the cool season dry bias found there. These general features are present for both 00 and 12 GMT forecasts.

For 1000 - 500 mb thickness there is a negative bias in the northern Rockies in early fall (Fig. 18) which tends to move south and eastward in early winter (Fig. 19). By mid-winter the northern Rockies show the development of a positive thickness bias (Fig. 20). A negative bias re-establishes itself here by early spring (Fig. 21) and is also apparent in the results for July (Fig. 22). A positive thickness bias can be found in the Great Lakes in early fall (Fig. 18). By December (Fig. 19) this area has a slightly negative thickness bias and thereafter the magnitude of the average thickness errors is negligible, changing sign from month to month. July finds a positive thickness bias in the western United States for 00 GMT 36 h forecasts (not shown) and a negative bias in this area for 00 GMT 48 h forecasts (Fig. 22). At 12 GMT in July (not shown) there is a strong negative bias at 36 h and a weaker negative thickness bias at 48 h in the west.

Boundary layer temperature is forecast too warm across most of the U.S. in the fall for 00 GMT forecasts (Fig. 23). The largest warm bias can be found around Florida. A cold bias develops in the Great Lakes in December which grows larger in January (Fig. 24) and then decreases in magnitude. At 00 GMT in July the nation is forecast too warm except in the Pacific Northwest for 24 and 48 h forecasts (Fig. 25). The largest warm bias occurs near (24 and 48 h forecasts) or west (12 and 36 h forecasts) of the Great Lakes. This is radically different from the error pattern found in the Great Lakes during the cool season (see Fig. 24). At 12 GMT (not shown) the boundary layer temperature error patterns are much the same except the cold bias in the Great Lakes persists strongly into March. In

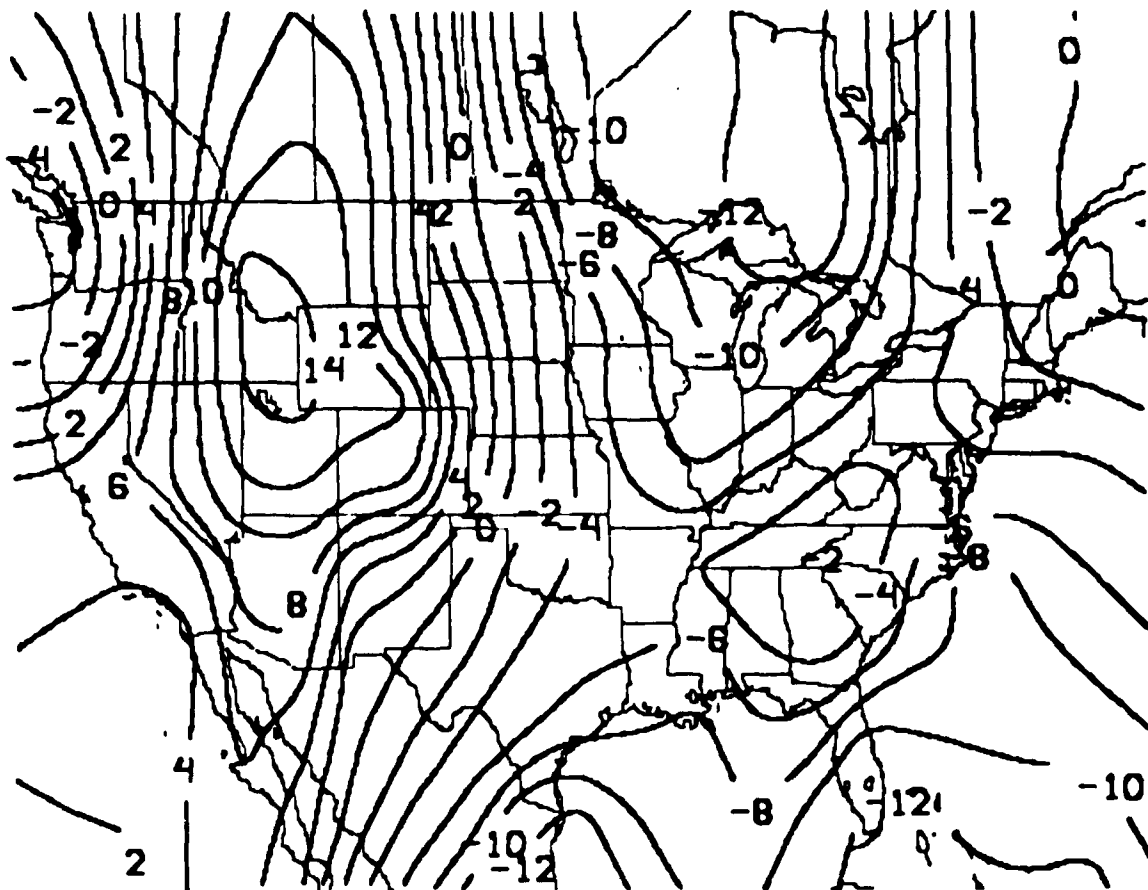


Fig. 16. Average LFM Forecast Relative Humidity Error (whole percent) from 00 GMT November 36 Hour Forecasts

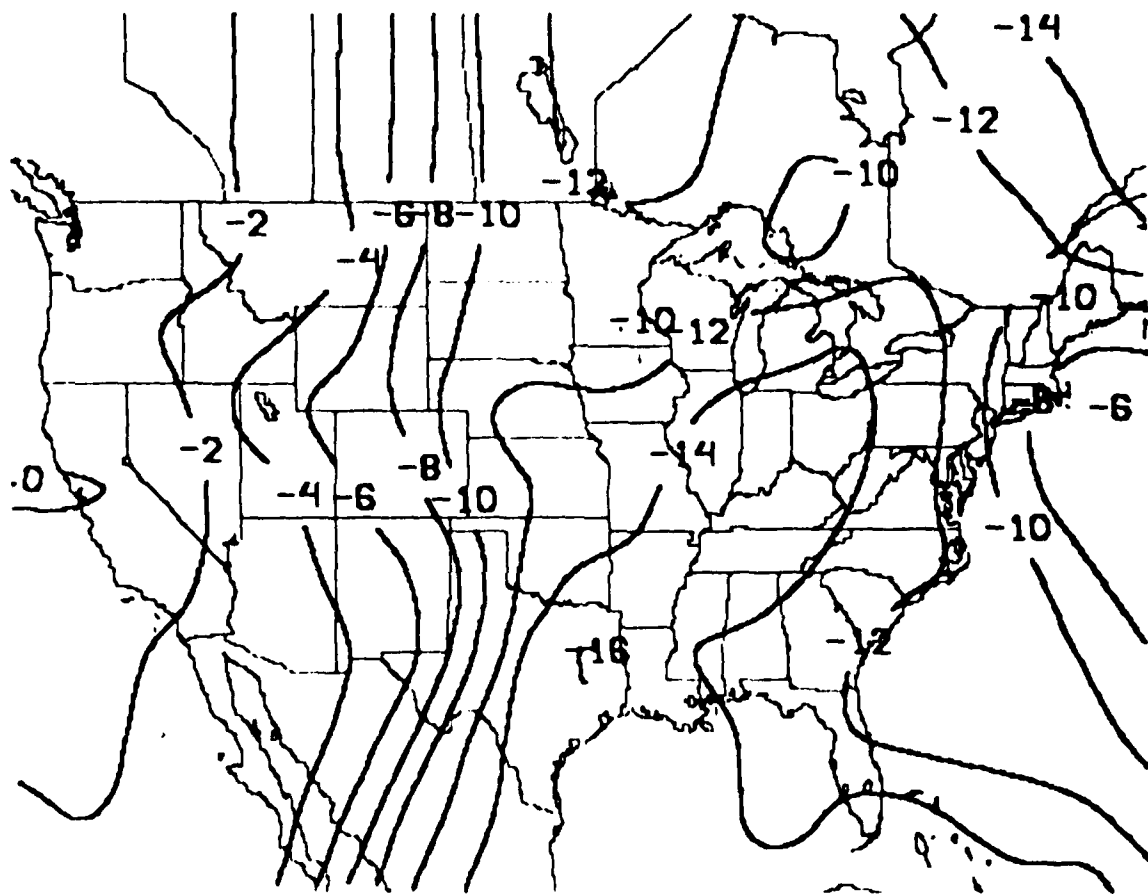


Fig. 17. Average LFM Forecast Relative Humidity Error (whole percent) from 12 GMT July 48 Hour Forecasts



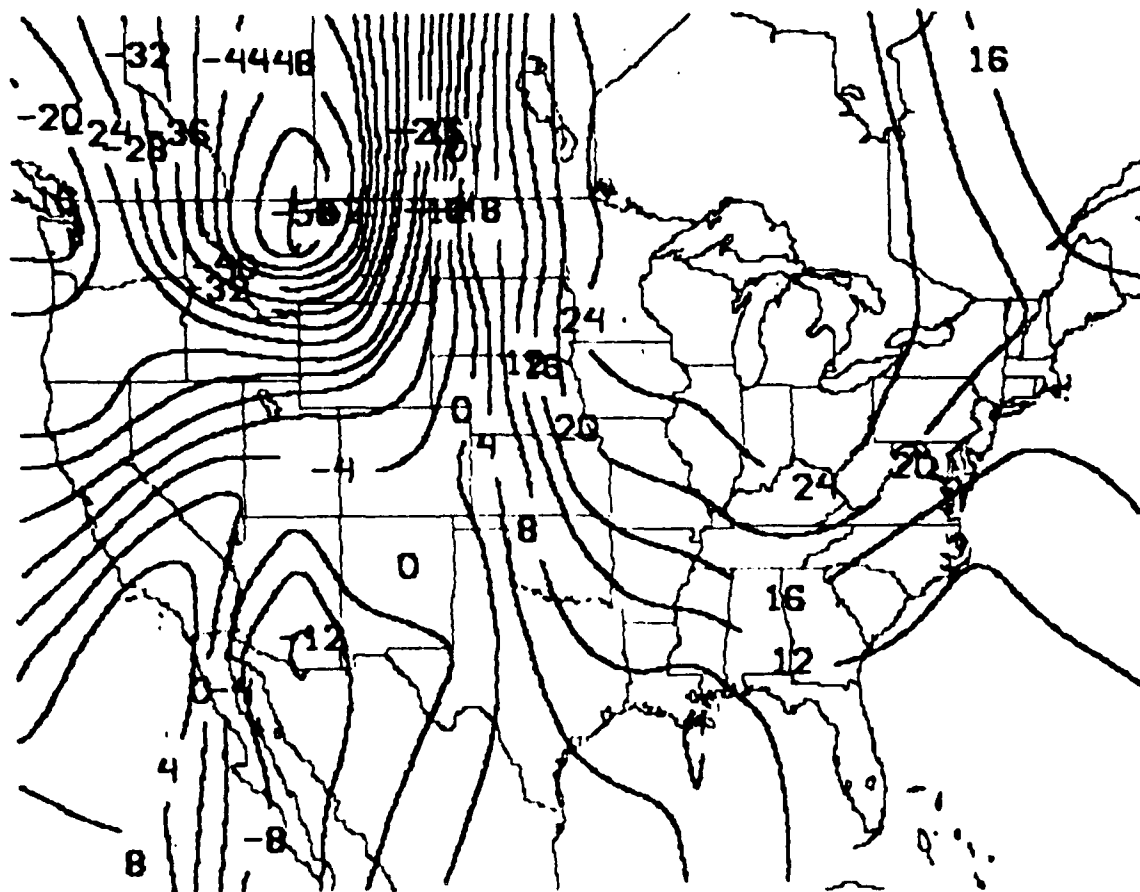


Fig. 1B. Average LPM Forecast 1000 - 500 mb Thickness Error (meters)  
 From 00 GMT October 48 Hour Forecast:

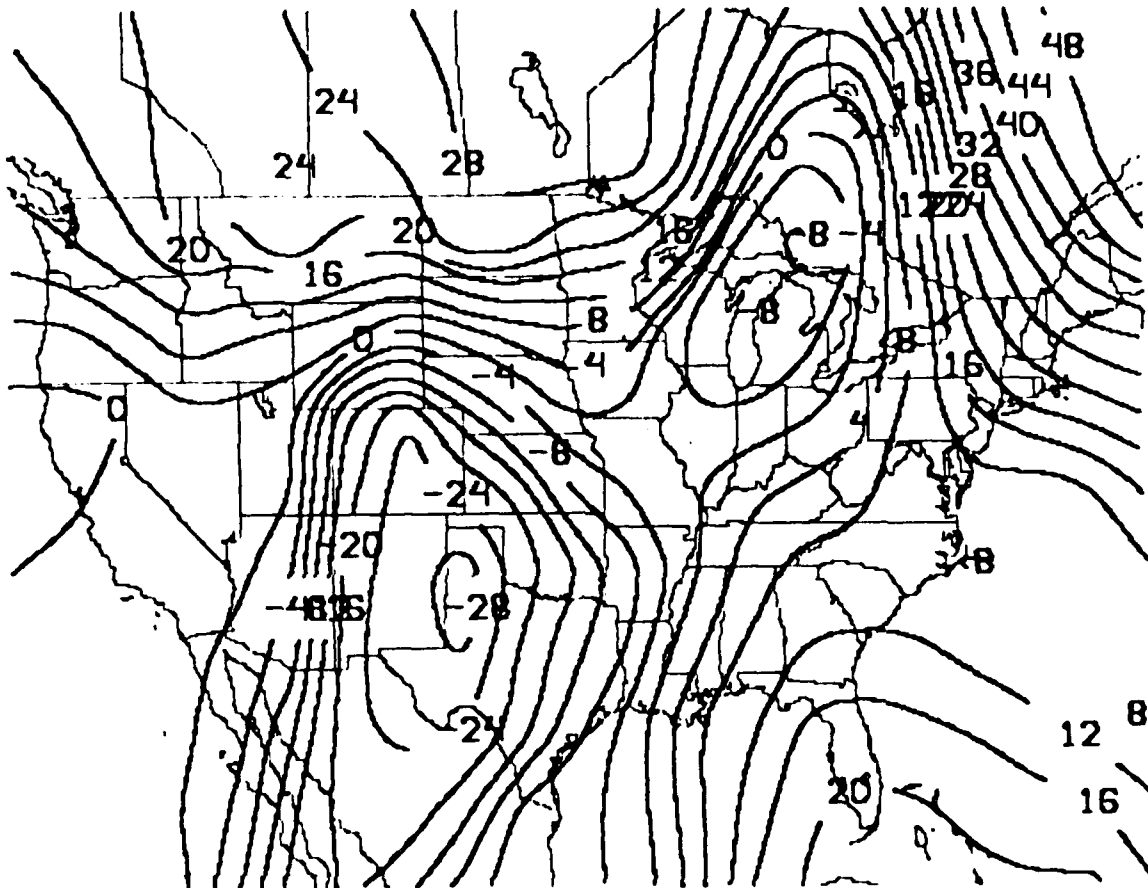


Fig. 19. Average LFM Forecast 1000 - 500 mb Thickness Error (meters)  
 from 00 GMT December 48 Hour Forecasts

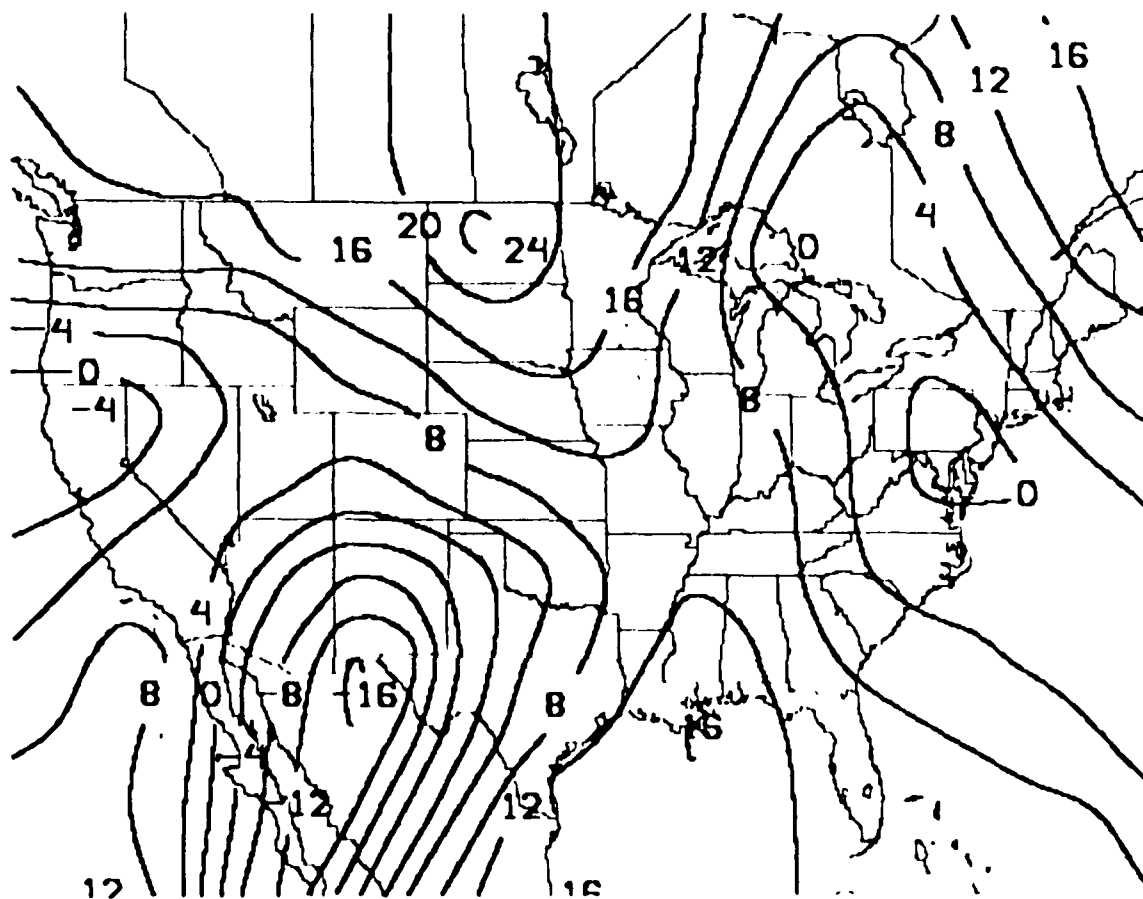


Fig. 20. Average 1PM Forecast 1000 - 500 mb Thickness Error (meters)  
 From 00 GMT February 48 Hour Forecasts

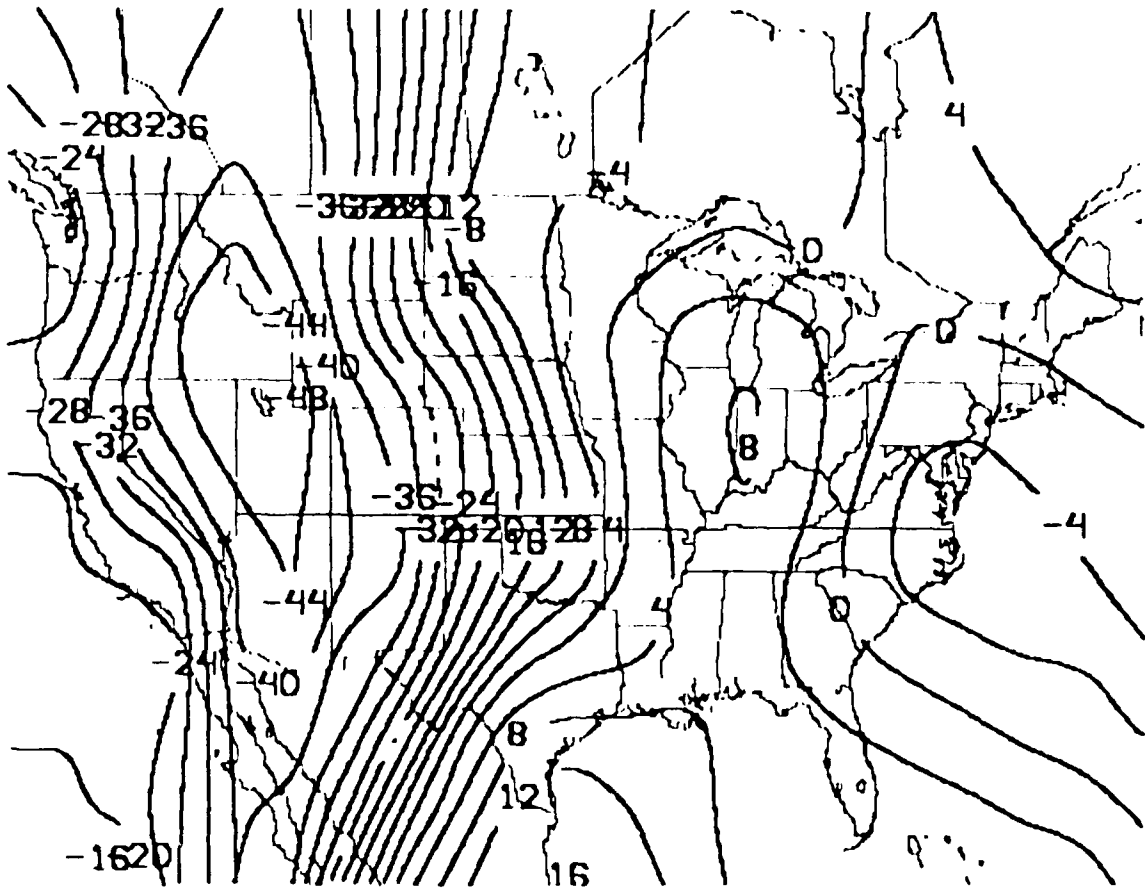


Fig. 21. Average LFM Forecast 1000 - 500 mb Thickness Error (meters)  
 From 00 GMT March 48 Hour Forecasts:

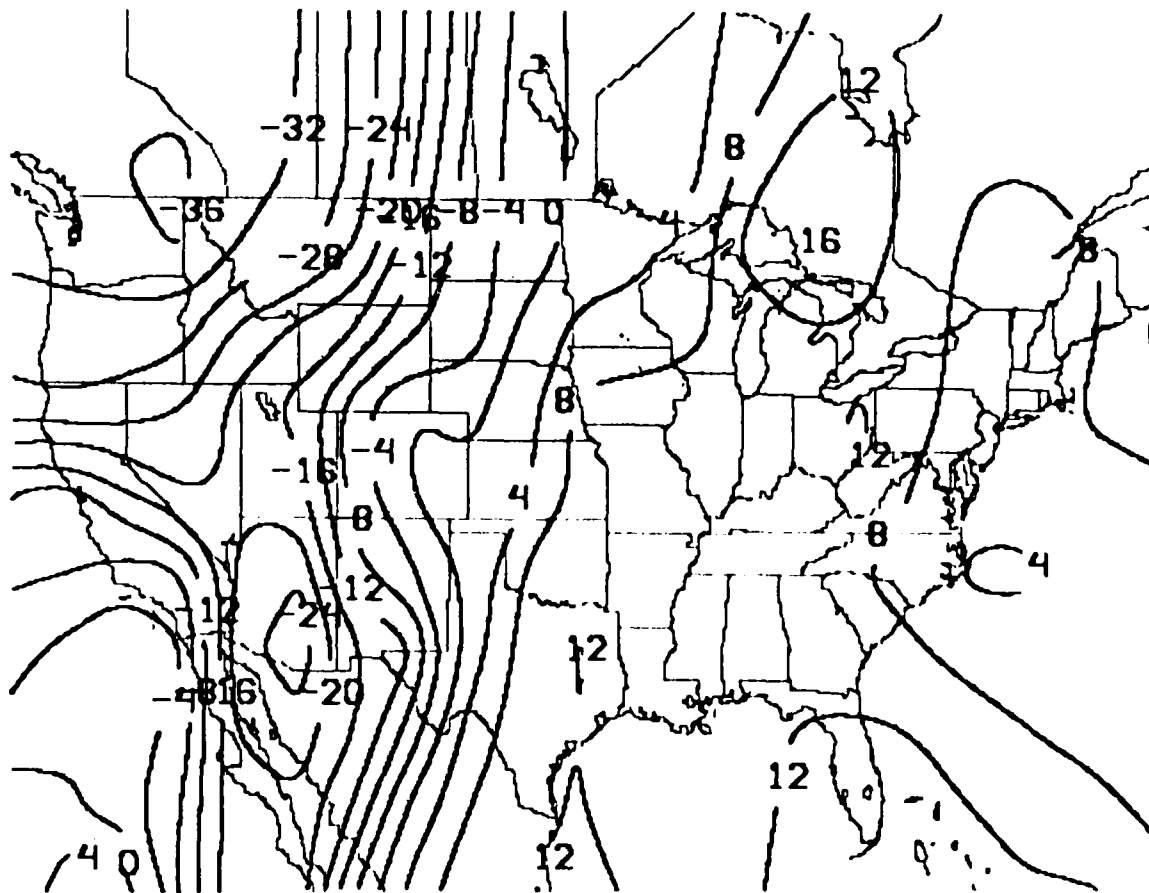


Fig. 22. Average LFM Forecast 1000 - 500 mb Thickness Error (meters)  
 from 00 GMT July 48 Hour Forecasts

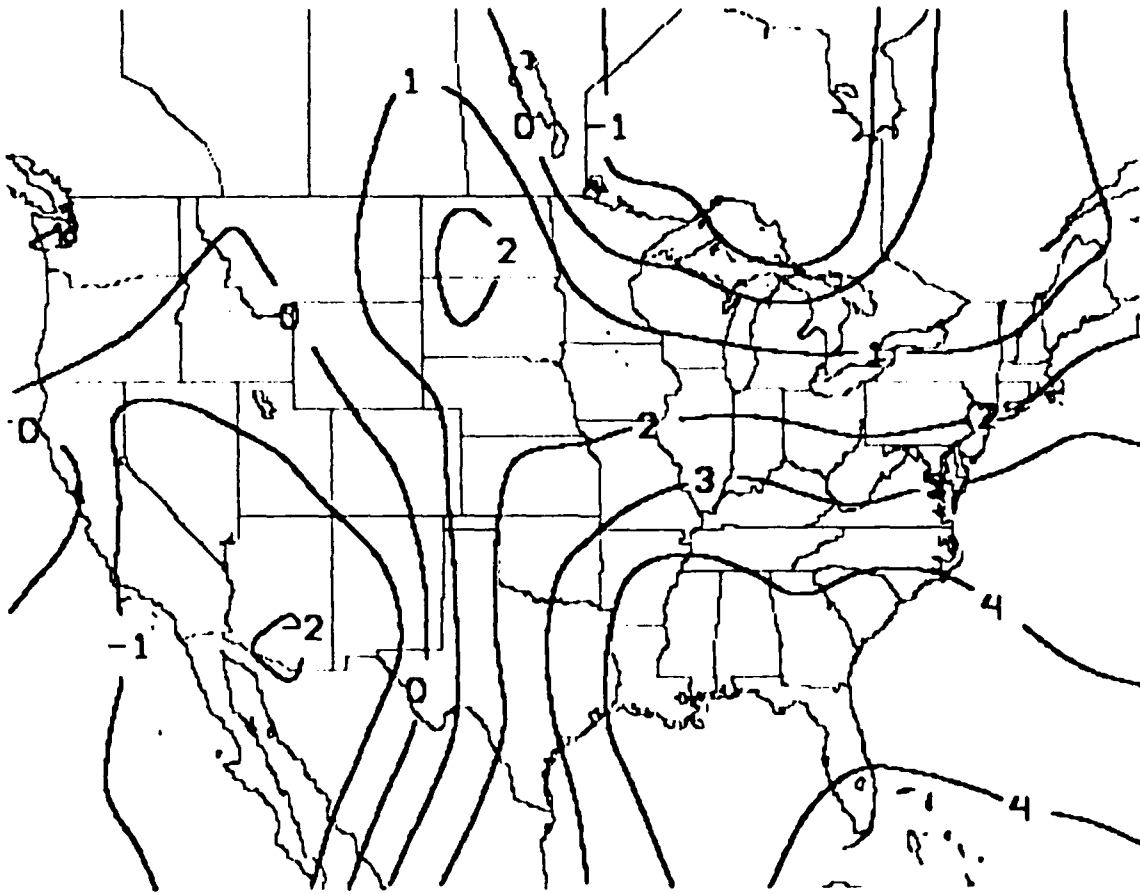


Fig. 23. Average IPM Forecast Boundary Layer Temperature Error ( $^{\circ}\text{K}$ )  
From 00 GMT November 48 Hour Forecasts

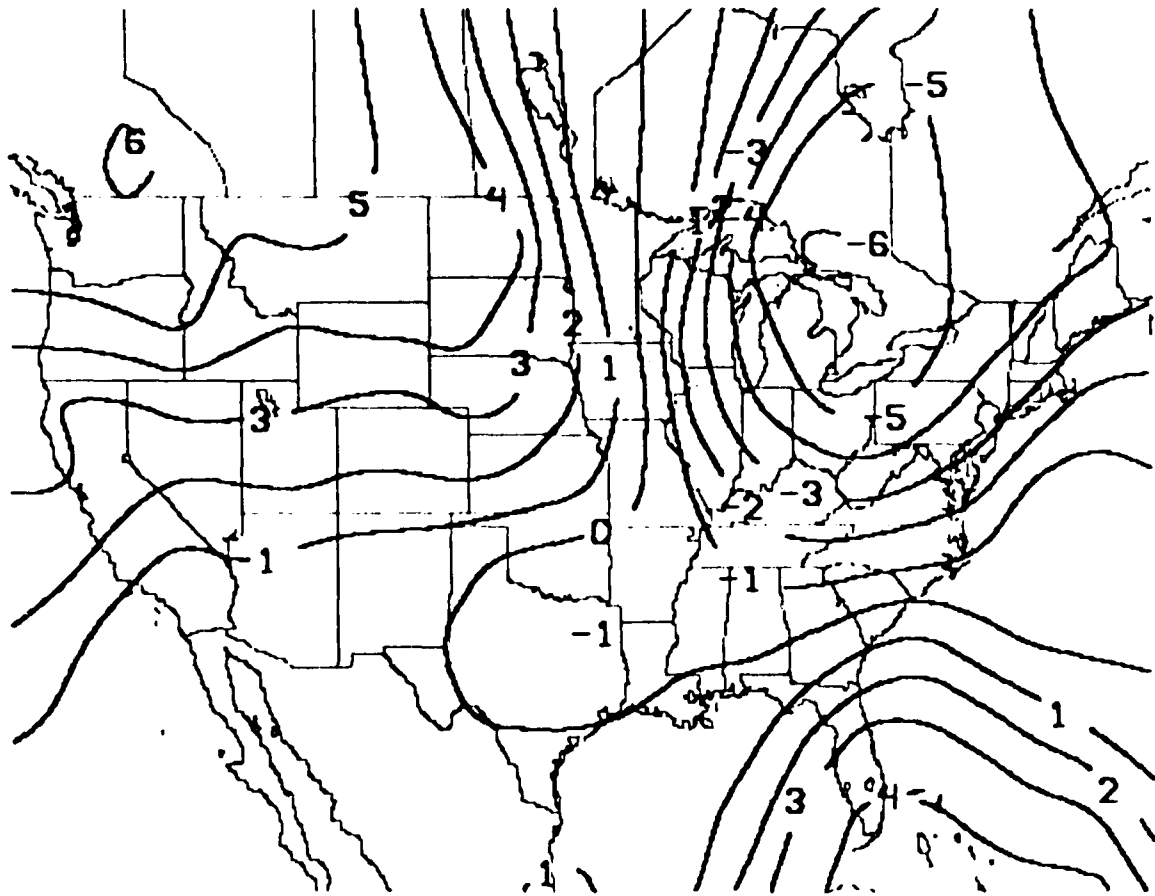


Fig. 24. Average LPM Forecast Boundary Layer Temperature Error ( $^{\circ}$ K)  
 from 00 GMT January 48 Hour Forecasts

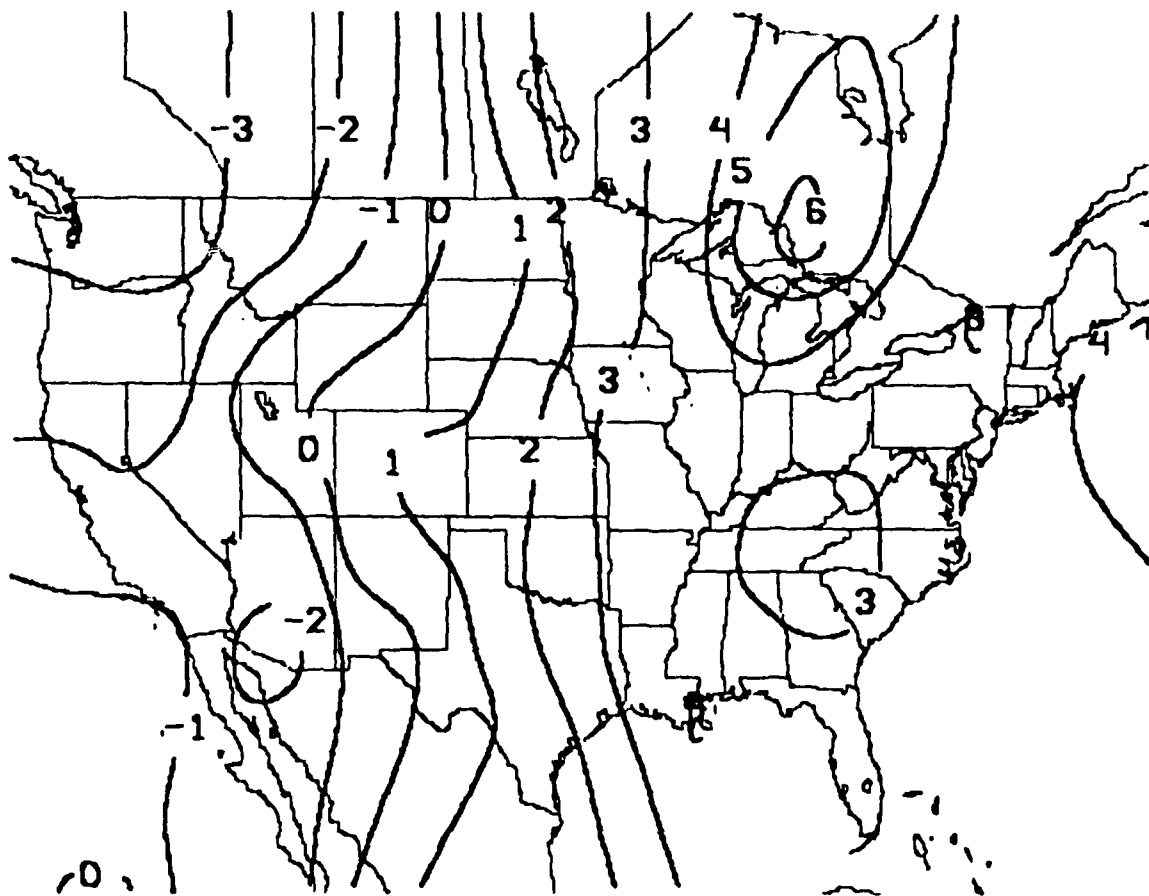


Fig. 25. Average LFM Forecast Boundary Layer Temperature Error ( $^{\circ}$ K)  
from 00 GMT July 48 Hour Forecasts



July for 12 GMT forecasts (not shown) there is a negative bias at 12 and 36 h nationwide (with the exception of Florida) and a positive bias at 24 and 48 h. The diurnal differences in the boundary layer temperature error patterns are very similar to those found in the earlier studies (Gerlach 1983, 1984).

Sea-level pressure errors at 00 GMT show a tendency to have positive errors in the western third of the United States and a negative bias in the nation's mid-section (Fig. 26). No seasonal trend is apparent. In July the magnitude of the sea-level pressure errors is much smaller (Fig. 27), as should be expected, since the daily pressure patterns are usually much less intense in the warm season. Sea-level pressure forecasts for 12 GMT (not shown) show a negative bias in the Pacific Northwest for fall and early winter, a positive bias in the southern Rockies (except January and February), and a negative bias in the nation's mid-section. In July there is a positive bias in the Southwest; otherwise the average errors are negligible.

Errors in boundary layer relative humidity are negative across the entire nation with the exception of the Rocky Mountain states where a moist bias can often be found (Fig. 28). This pattern is apparent for all months examined so far. In early fall the largest dry bias is found in the upper Great Lakes but by early winter the worst dry bias is located near the Texas Gulf Coast. The dry bias is of about equal magnitude for both locations in July. The same patterns are apparent at 12 GMT except in July where there is a moist bias in Texas for the 12 and 36 h forecasts (Fig. 29).

The error patterns for lower tropospheric relative humidity are very similar to those for boundary layer relative humidity. A dry bias is found nationwide except for a moist bias in the Rockies (mostly the northern Rockies) (Fig. 30). The strongest dry bias is found along the Gulf Coast. Few differences are apparent between 00 GMT and 12 GMT forecasts.

Many of the error patterns described above are quite similar to those found in the 1982-83 and 1983-84 FOUS guidance error analyses. No direct comparison can be made however since the error fields for the earlier studies represented composite errors for the entire cool season whereas only monthly biases are currently available for the present study. Some of the present error patterns are different from those in previous years; possible causes for these differences will be sought.

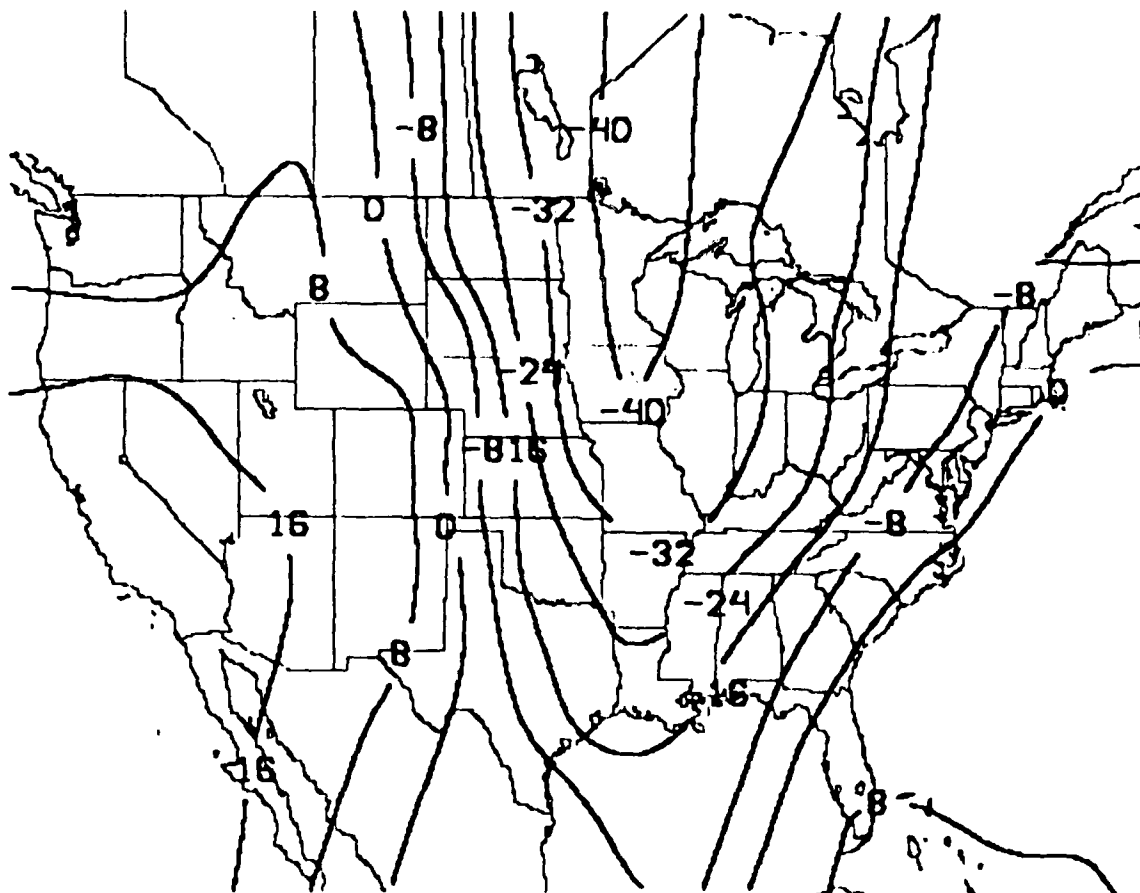


Fig. 26. Average LFM Forecast Sea Level Pressure Error (tenths of mb)  
 from 00 GMT November 48 Hour Forecasts

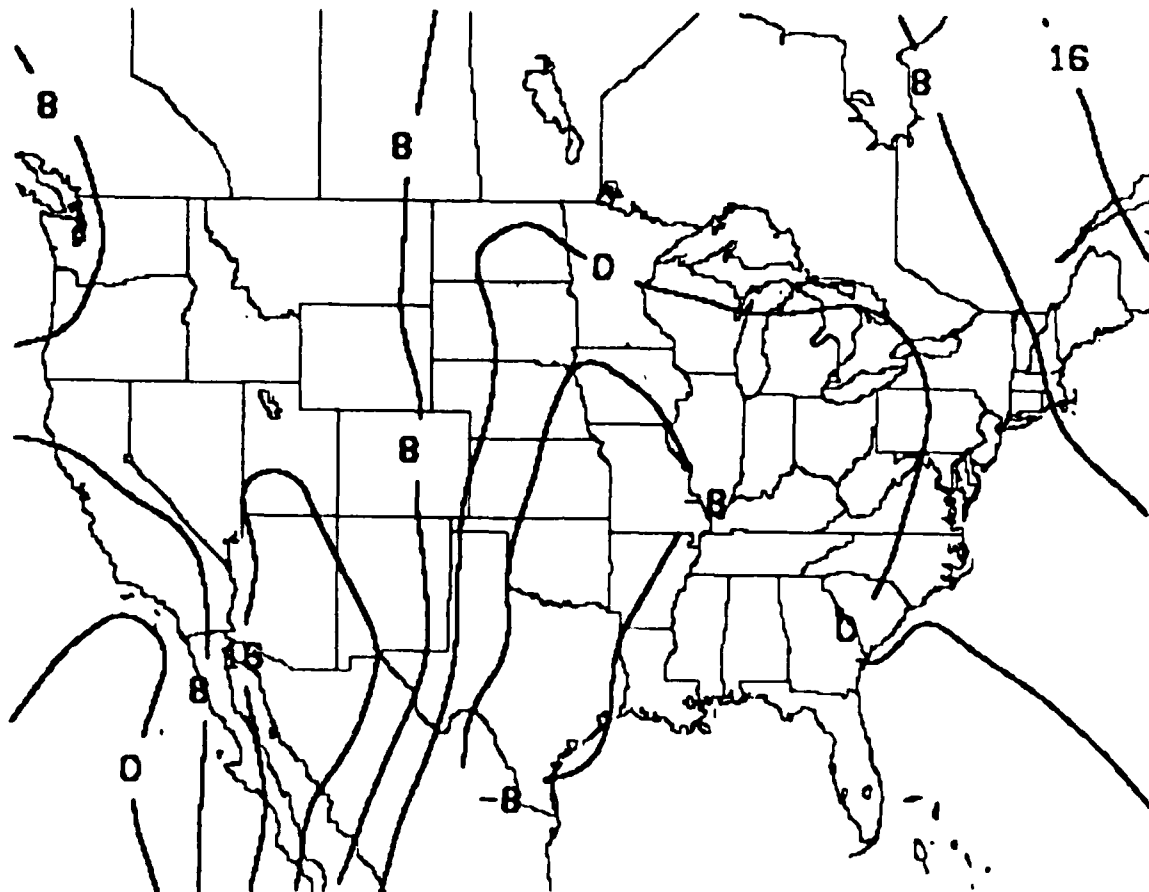


Fig. 27. Average LFM Forecast Sea Level Pressure Error (tenths of mb)  
from 00 GMT July 48 Hour Forecasts

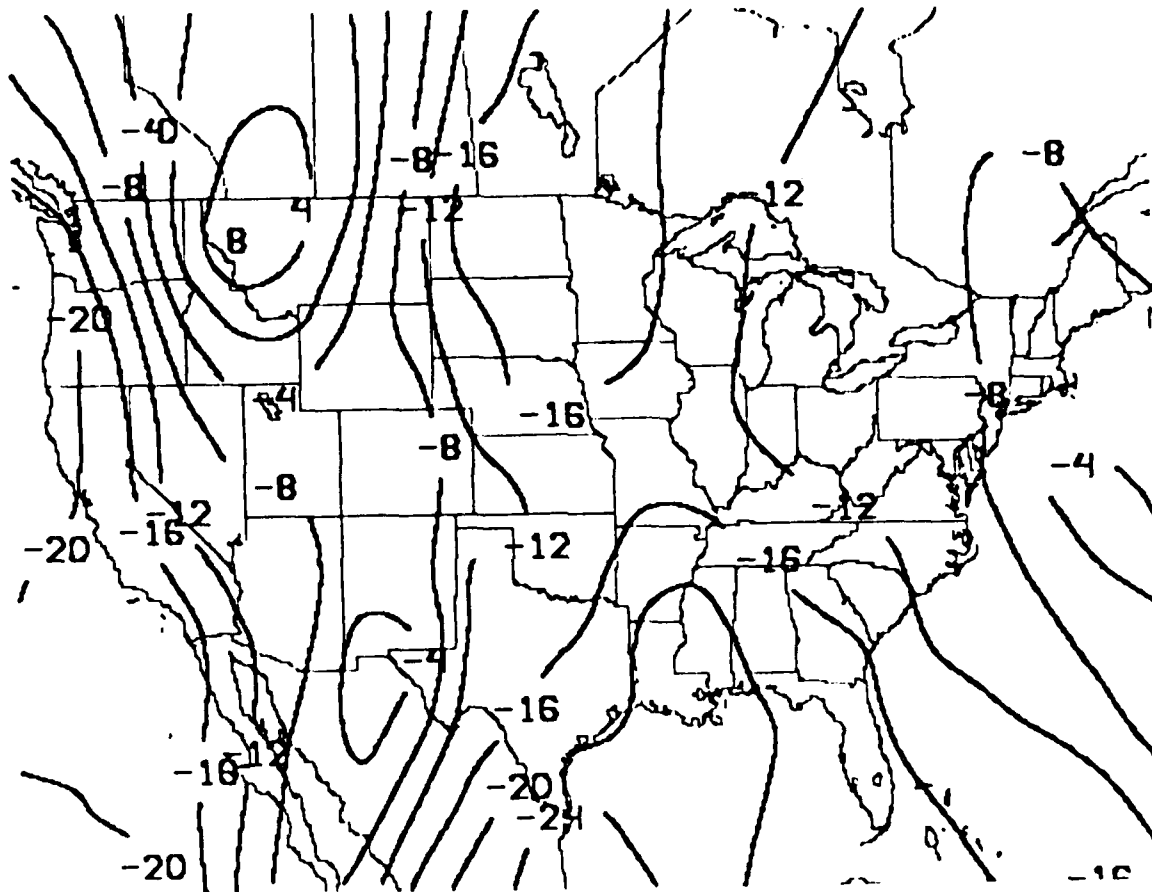


Fig. 28. Average LFM Forecast Boundary Layer Relative Humidity Error (whole percent) from 00 GMT February 36 Hour Forecasts

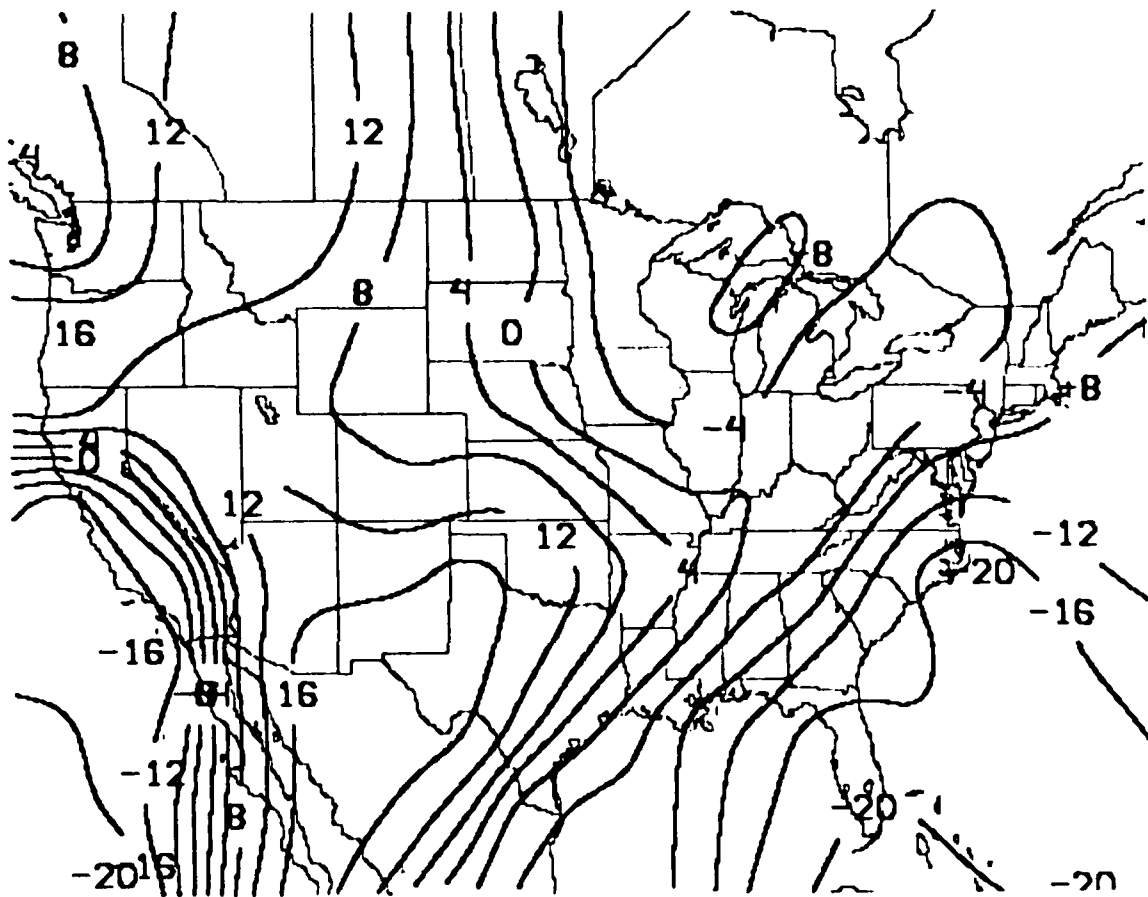


Fig. 29. Average JFM Forecast Boundary Layer Relative Humidity Error (whole percent) from 12 GMT July 36 Hour Forecasts:

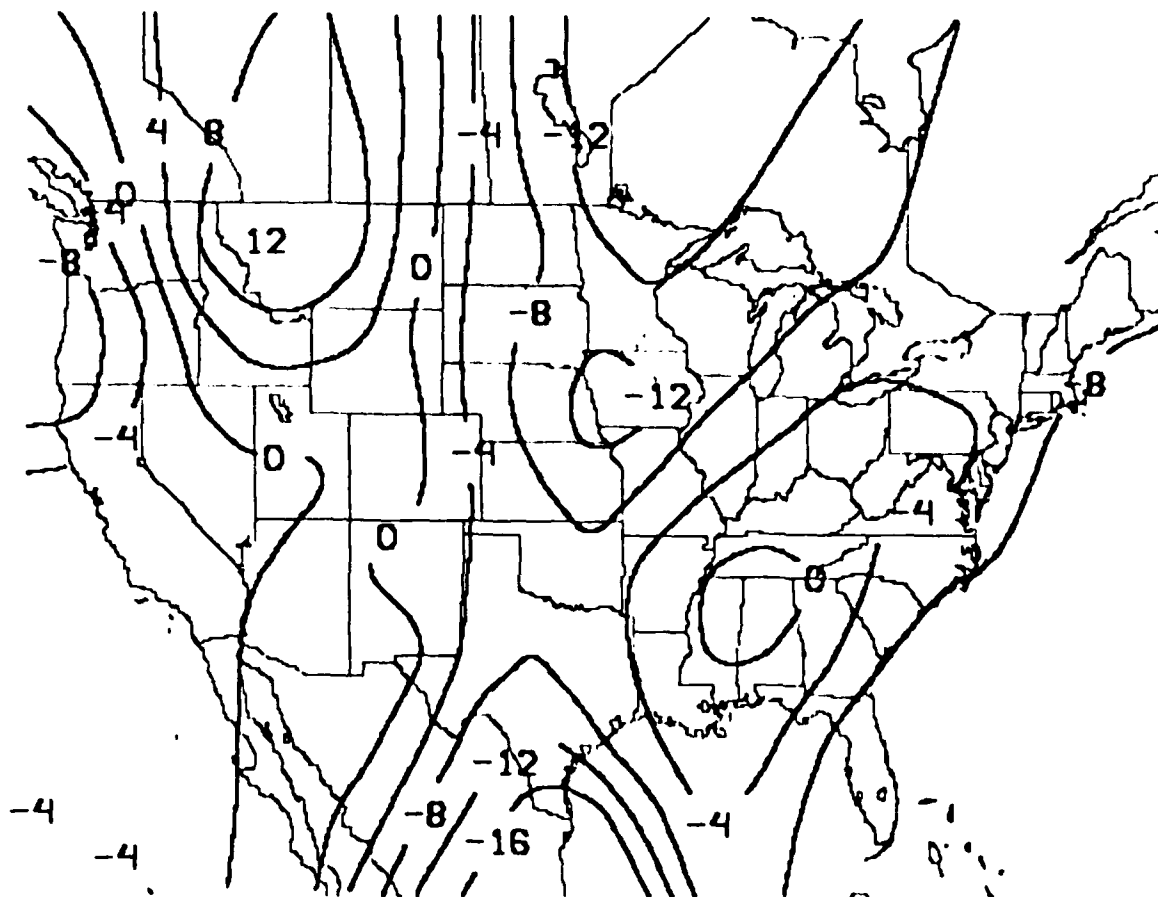


Fig. 30. Average LFM Forecast Lower Tropospheric Relative Humidity Error (whole percent) from 00 GMT February 36 Hour Forecasts

Obviously much work remains to be done. The remaining FOUS data (April - June, August - November) will be processed and analyzed. The analysis will be done by month as well as in composite format and possibly by season (i.e., 3 - 4 month periods). Physical causes will be sought for error patterns that show year to year (and month to month) consistency. For example, the large warm bias in boundary layer temperature found near Florida may be the result of the inability of the LFM to represent physically a land mass protruding into the warm waters of the Gulf of Mexico. Also, it is planned to perform statistical testing on the three years of data collected to help determine the significance of the error patterns.

#### C. Forecast Guidance Displays

Techniques developed at Pennsylvania State University that use the fields of wet bulb temperature and wet bulb potential temperature in identifying and forecasting frontal zones led to a requirement to add those parameters to the McIDAS analysis routines. This necessitated modification of programs SAKONT (surface analysis) and RBKONX (upper air analysis).

Subroutine WETBUL was modified and incorporated into the analysis routines so that wet bulb temperature and wet bulb potential temperature at the surface and wet bulb temperature at the mandatory upper levels could be displayed. Figs. 31 - 33 show examples of surface wet bulb temperature, wet bulb potential temperature, and 500 mb wet bulb temperature analyses respectively.

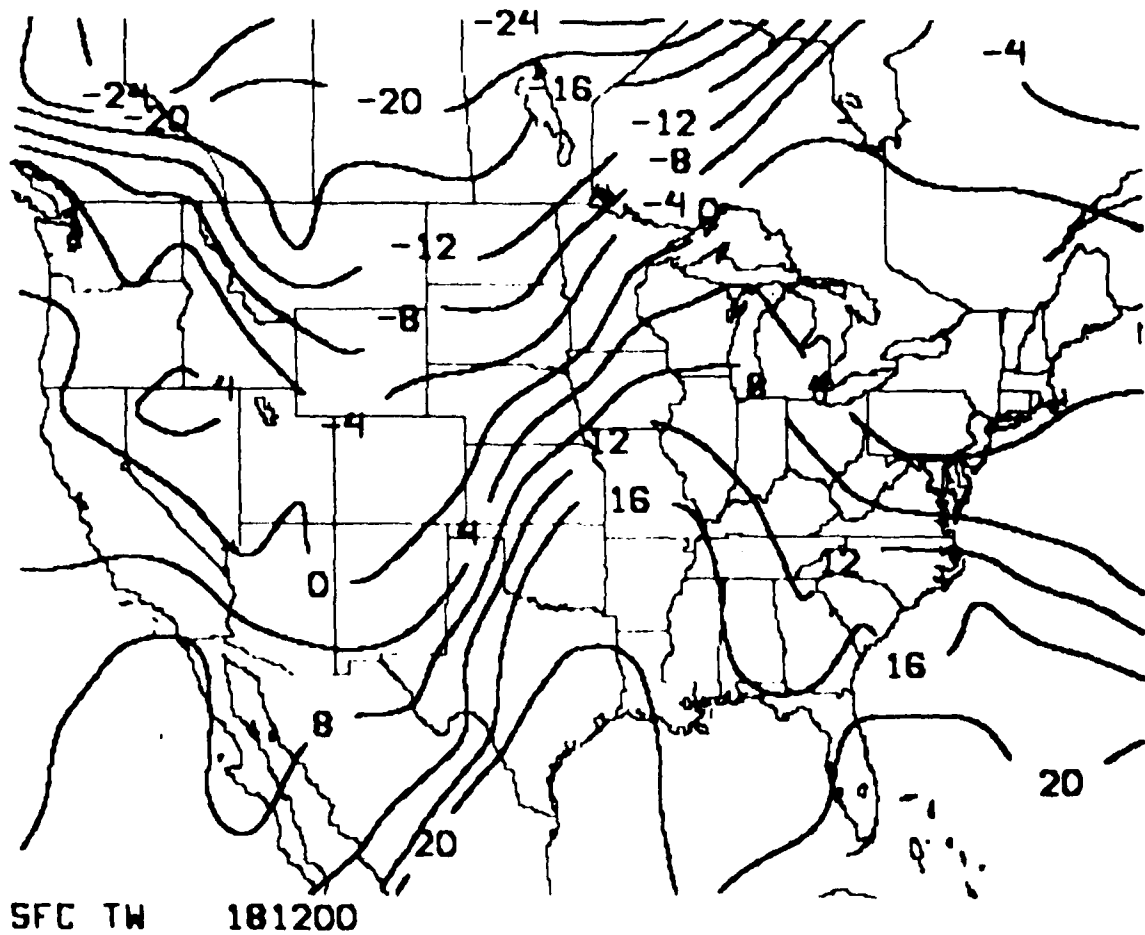


Fig. 31. Analysis of Surface Wet Bulb Temperature ( $^{\circ}\text{C}$ ) from November 18, 1985 at 12 GMT



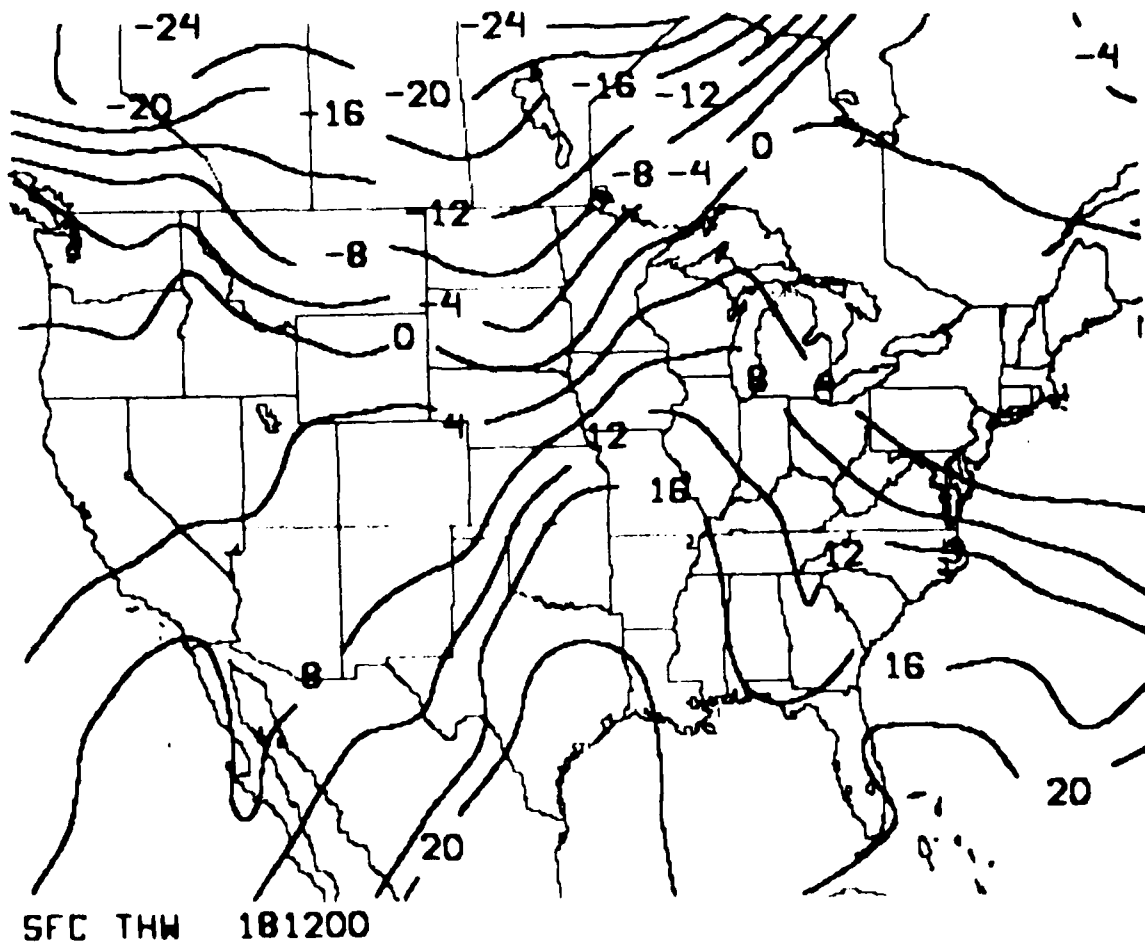


Fig. 3. Analysis of Surface Wet Bulb Potential Temperature ( $^{\circ}\text{C}$ ) from November 18, 1985 at 12 GMT

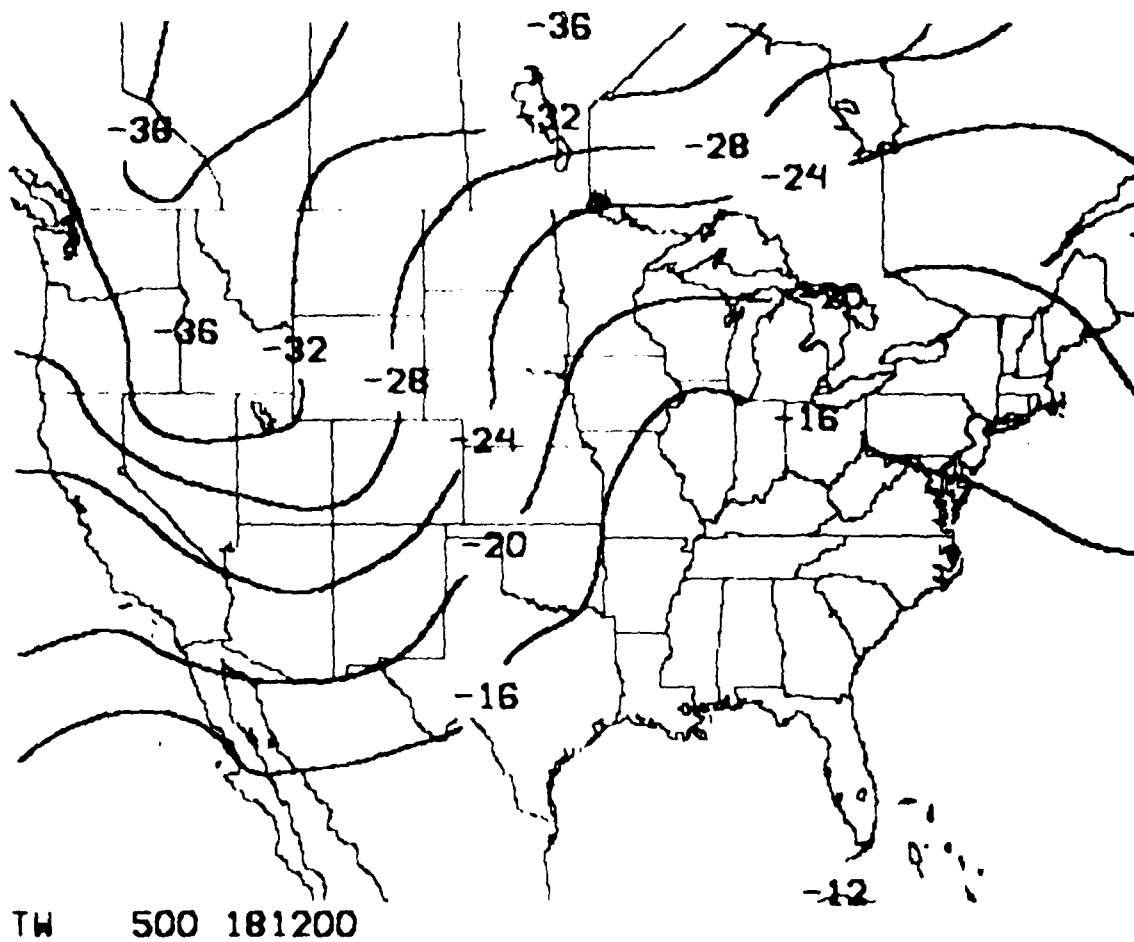


Fig. 33. Analysis of 500 mb Wet Bulb Temperature ( $^{\circ}\text{C}$ ) from November 18, 1985 at 12 GMT

### III. Boundary Layer Meteorology

#### A. Refractive Index Study

AFGL has been conducting measurements and thereby characterizing refractive index ( $C_N^2$ ) fluctuations in the atmosphere in support of an Air Force investigation of tactical tropospheric scatter radio links.

To measure  $C_N^2$ , refractometers together with temperature and pressure sensors were mounted on aircraft and flown in different seasons and in various geographic locations. Digitized data from these sensors were archived onto magnetic tape during flight for later processing and evaluation.

A new data retrieval system using multi-channel software controlled electronics was installed by AFGL in 1985. It was therefore necessary to alter the C language operating program to customize the system for a variety of field test scenarios. In its final form the software accepts up to six fast response channels of information at a rate of 64 values per second, and six slow response channels at a rate of two values per second. The operator was given more flexibility by being provided a menu that allowed him to select among various options corresponding to the configuration of sensors flown on a particular flight. Space was provided for header information on the slow response channel records. Allowance was made for two 157 character buffers to be inserted for identification. The first buffer permits the operator to make entries once at the beginning of the flight. Typically, these might be date, place, surface pressure, temperature, humidity, winds, and operator comments or observations. The second buffer enables the operator to enter data manually at the start of each file created during flight. Usually these describe the file as a level or spiral flight recording and may include altitude, heading, air speed, cloud observation, and degree of mechanical turbulence for the particular file.

The recorded data were obtained in 1985 from field tests conducted by AFGL in flights over Korea, over Crestview and later at Punta Gordo, FL, at Gila Bend, AR, and at Chatham, MA. Each of the field tests required modification of data reduction programs to accommodate various instrument gain curves and input voltages.

The sampled refractometer data were converted to frequency by means of Fast Fourier Transform. The spectra thus obtained had to be corrected to remove the filter characteristics of the refractometer used to prewhiten the data.

Three methods were employed to restore the spectra. A look up table was developed for use with the early Florida test data. For later flights a complex analog was inserted following the Fourier Transform to restore spectral characteristics. Finally, the Chatham data, which contained results from two refractometers recording simultaneously, were adjusted by a 10 point frequency gain calibration array used as a basis of interpolation to obtain transformed values.

Although most reduction and analysis of turbulence data was done on the CDC Cyber 860, it was necessary to create similar software for the VAX 780. Analysis routines are now available on VAX to detrend data, perform power spectrum and cross spectrum averaging, calculate coherence, and edit spurious data points interactively. Data were easily transferred from Cyber to VAX using a hyperchannel network. Data derived from direct input of flight tapes proved inconsistent and required interpretive software to remove discrepancies. Some data have been examined; more remain to be analyzed.

Turbulence profiles were completed for data archived in 1984 from Hyannis, MA, Florida, and Arizona, and during 1985 in Korea, Florida, and Arizona.

#### B. Surface Layer Windflow Model

In early 1984 AFGL acquired a surface layer windflow model from the U.S. Army Atmospheric Sciences Laboratory (ASL), White Sands, NM. It was to be tested for use in conjunction with a Gaussian puff diffusion model to produce for Air Weather Service a prediction system for toxic chemical spill transport over regions of complex terrain.

The ASL numerical model computer program is used to estimate surface layer wind fields over complex terrain at horizontal resolutions of 60 to 400 m. A driver program was supplied by ASL to initialize disk random mass storage containing 100 m resolution simulated terrain and vegetation data for a 5 X 5 km area on the Ft. Polk Military Reservation, LA. However, it was necessary to rewrite the program code to adapt the model to run on

the Cyber 750. As test runs were made, a newer, compacted version of the model was constructed that yielded greater efficiency both in central processing time and in storage needed.

To exercise the model with or without vegetation added to the terrain data, a new version of the driver program to initialize storage files was accomplished. This allowed variations of surface roughness as a preset parameter for model runs.

The model produces a two-dimensional surface layer windflow analysis by using Gauss' Principle of Least Constraints to adjust an initially uniform windfield to conform with topography, mass conservation, and buoyancy forces. A number of sweeps or relaxation steps are performed to compute velocity corrections and windfield adjustments until minimum value convergence is obtained.<sup>26</sup>

Tests were conducted by making many computer runs, varying the model to include stable or unstable conditions, vegetation or no vegetation, wind speeds from calm to strong, and relaxation steps from 60 to 200. Nearly 25 variations of input conditions were used through a system of external parameterizing files devised to adjust the many variables resident in the model to reflect the particular conditions being tested. A significant number of wind profile plots were produced showing stability influenced, terrain driven windflow under both light and high wind speeds. As required, buoyancy magnitudes were provided in printed form along with wind components, temperature, and the minimum convergence value for the number of relaxation steps used in each model run.

The Ft. Polk tests demonstrated that over gently rolling terrain windflow patterns are influenced by modifying terrain geometry with the addition of vegetation. For surface layer windflow and with fairly uniform buoyancy due to relatively flat terrain at Ft. Polk, the model seemed to function well.

The compact version of the ASL model was successfully transferred from the Cyber onto a floppy disk for use on a Zenith minicomputer (Z-100).

---

26. Lanicci, J. M., 1985: Sensitivity Tests of a Surface Layer Windflow Model to Effects of Stability and Vegetation. AFGL-TR-85-0265, Air Force Geophysics Laboratory, Hanscom AFB, MA.

Compilation and execution of the model were achieved using Ft. Polk data. Model runs were generated to produce windflow vector plots on a Houston color plotter.

AFGL also acquired terrain data descriptive of Vandenberg AFB, CA, a location of considerably more varied topography than Ft. Polk. The model domain chosen for study varies from ocean coastline to moderately high mountain peaks, includes at least two valleys, and is situated in the southern shuttle launch area where ten meteorologically instrumented towers are located. The tower data acquired from the Naval Postgraduate School, Monterey, CA, can be used both for multiple observation input to the model (as contrasted with Ft. Polk single observation input) and for verification.

Initial work to prepare the Vandenberg terrain data for model input produced contours that showed no similarity to Vandenberg maps. This showed clearly that the data acquired were not from south Vandenberg. Correct data were subsequently received and successful contours of south Vandenberg were produced.

Work is underway to convert tower data to a form compatible with Cyber software so that extensive tests similar to those done on Ft. Polk data can be undertaken with the Vandenberg data.

#### C. Troposcatter Raytrace Models

Development of improved, cost efficient troposcatter propagation programs for two and three dimensions was the main focus of work in 1985. These programs are used to examine the scattering of microwave energy by upper air turbulence in the common volume.

Previously developed troposcatter models used two predetermined one degree beams emanating from the transmitter and receiver to define the common volume. It was divided into cells from which rays were traced downward toward transmitter and receiver using a search technique. The new models initiate the raytrace from the transmitter instead of the scattering beam, thus eliminating the search process, and seek only to trace the ray scattering to the receiver within the beam. In addition, the method for selecting initial angles for the search subroutine was improved and a more efficient search technique was developed. Incompatibility with certain refractive profiles was eliminated. The three dimensional program was modified to make it more representative of the physical situation. The

second and third layers of raytrace drew rays emanating along set radials from the transmitter rather than having them directed at a surface parallel and slightly displaced behind the two dimensional surface. The improved programs allow the transmitter and receiver beams to be modified independently in both beam width and elevation. Also included was an antenna gain function. The final two-dimensional and three-dimensional programs were run with England data and comparisons were made with the results of the earlier programs. Korean data were also used with these programs.

An example of a plot generated from the 2-D model is shown in Fig. 34.

A separate plotting program was developed to be used in conjunction with the 2-D and 3-D programs to plot the energy (normalized) in each of the time delay bins and illuminate the role that the scattering angle, antenna gain, and turbulence ( $C_N^2$ ) play in the energy/time delay distributions.

#### D. Raytrace

Extensive plotting of line of sight raytraces was accomplished using Pt. Mugu, CA and England data as input to the Wassky raytrace program, which was modified to run on a Tektronix. Resolution of the rays was increased to see if other rays entered the shadow zone or if one raytube covered the whole shadow zone. The purpose was to pinpoint the critical angle that defines the trapping of a ray. The method was chiefly trial and error.

The Z-100 was successfully linked to the ADAS (Automatic Data Acquisition System - an RS 232 device). Programs written for the Apple IIe were reformulated for use with the Zenith.

#### E. AFGL Weather Test Facility

SASC Technologies, Inc. is responsible for maintaining and operating the Weather Test Facility located on Otis Air National Guard Base (ANGB) near Falmouth, MA. In addition to daily site and instrumentation maintenance and repair, special activities were undertaken, of which the following are characteristic.

A VR-301 visibility sensor manufactured by HSS, Inc., Bedford, MA was returned to the manufacturer to be modified to identify type and

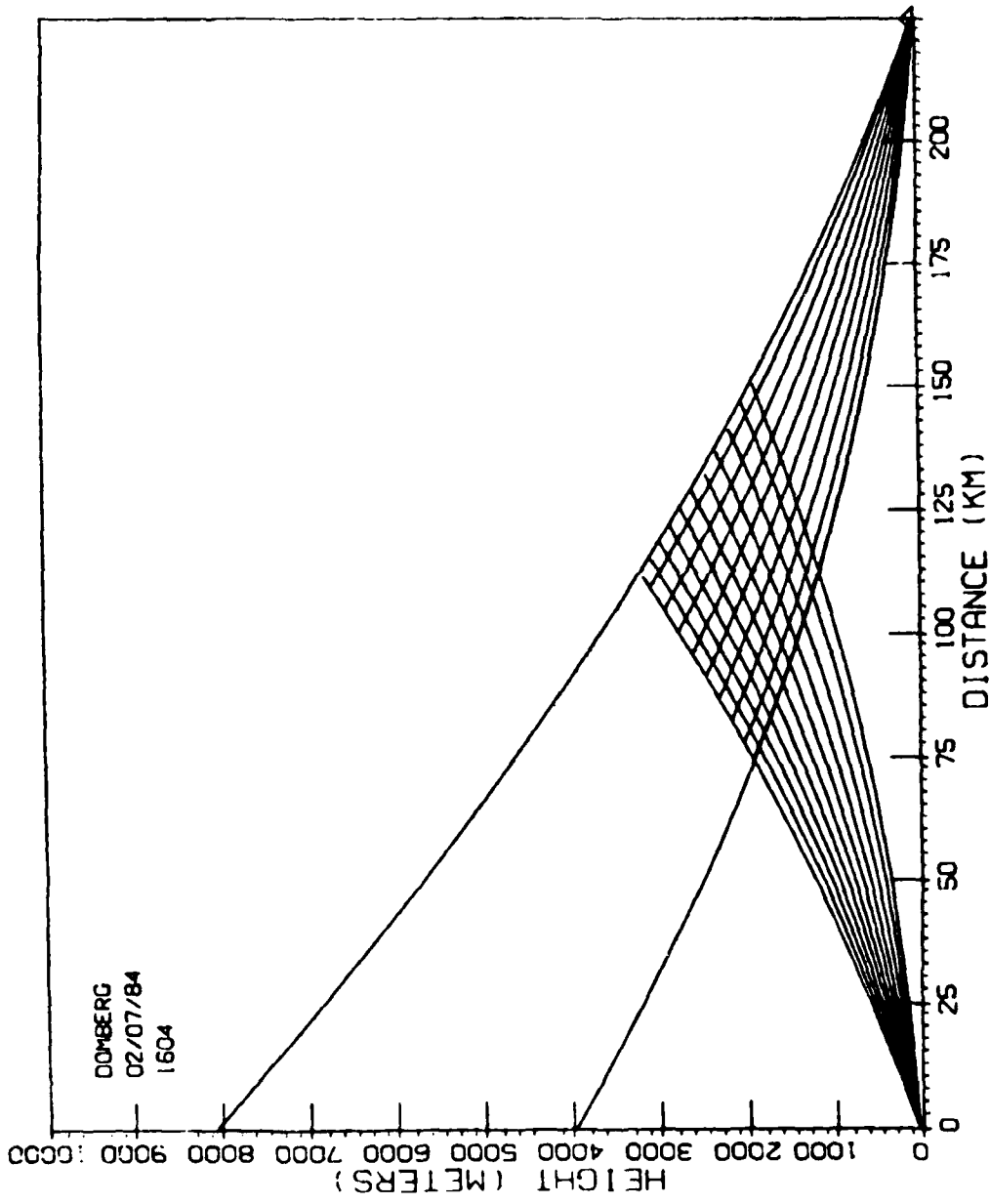


Fig. 34. Example of Plot Generated by 2-D Troposcatter Propagation Model Starting Raytrace from Transmitter



intensity of precipitation as well as visibility. Redesignated a Present Weather Set (PWS), it was installed and is operating at the test site.

GM2-32 transmissometers, Model 301 forward scatter meters, rain gauges, and human observers are being used to calibrate and check the accuracy of the PWS. Rain is simulated using special design water nozzles that generate water droplets in an evenly distributed pattern at different rainfall rates, depending on the specific nozzle used. The PWS will be operated throughout the winter for further comparison with human observations during periods of sleet and snow.

A prototype forward scatter visibility measuring set manufactured by Weather Measure, Inc., Sacramento, CA was installed. Only limited data have been acquired because of problems programming the set's microprocessor and because of lightning damage. However, the set is now operating satisfactorily.

A weighting/tipping bucket rain gauge was installed and simultaneous rain and wind data were recorded. Upon completion of the test the gauge was returned to AFGL/LYC.

Unusually severe thunderstorms with nearby lightning strikes caused data system and meteorological sensor outages during Summer 1985. Repairs have been made as parts have become available.

The MAWS data acquisition system has been returned to near full operational status. Buffer/formatters used to interface the tape recorder with the data system were sent to the manufacturer for repair. The data system will be fully operational when the repaired units are received.

#### IV. RADAR METEOROLOGY

##### A. Detection of Synoptic Scale Wind Anomalies

###### 1. Introduction

A wind field within a particular region can be expressed as a mean vector, indicating wind speed and direction, plus spatial and temporal derivatives of first and higher orders. If the wind field contains suitably reflective tracers that follow the wind (e.g., precipitation), it can be detected by means of Doppler radar. However, a Doppler radar can detect only the component of motion aligned along its antenna beam, so complete specification of a three-dimensional wind vector would require three Doppler radars viewing the same point from different angles. Multi-Doppler arrays are often used in research experiments, but operational forecasters have to make the best use of only a single Doppler radar.

One of the most efficient approaches to analysis of a wind field by single Doppler radar is the VAD (Velocity-Azimuth Display) scanning technique. The radar is set into a conical scan about a vertical axis, at a fairly low elevation angle in order to prevent excessive contamination of Doppler velocity measurements by precipitation fall speeds. These measurements are recorded at a particular range during a complete 360° scan in azimuth. The resultant pattern provides information on the wind field throughout the VAD scanning circle in a horizontal plane at a height given by range and elevation angle. Each VAD scan requires less than a minute, so temporal variability is negligible. Lhermitte and Atlas (1961)<sup>27</sup> suggested the VAD technique and showed how mean wind speed and direction could be estimated. Browning and Wexler (1968)<sup>28</sup> considered the kinematic properties of the wind field (divergence, mean wind, vorticity, shearing deformation, and stretching deformation) and demonstrated how all of these properties except vorticity can be calculated through a harmonic analysis of

---

27. Lhermitte, R. M., and D. Atlas, 1961: Precipitation motion by pulse Doppler. Proceedings, Ninth Weather Radar Conference, Kansas City; AMS, Boston, 218-223.

28. Browning, K. A., and R. Wexler, 1968: The determination of kinematic properties of a wind field using Doppler radar. J. Appl. Meteor., 7, 105-113.

the VAD pattern. Donaldson and Harris (1984),<sup>29</sup> challenged by the elusiveness of vorticity, investigated possibilities for distinguishing curvature and crosswind shear, the two terms of vorticity, and suggested their utility, when combined, as a cyclonic intensity indicator for remote assessment of the threat of an offshore hurricane or intense extra-tropical cyclone.

## 2. Terms of the Kinematic Properties

The kinematic wind field properties may be expressed in natural coordinates, aligned along and normal to the streamlines. Variability in wind direction owing to curvature and diffluence are directly revealed in natural coordinates. By convention, the positive directions are downwind and to the left of the wind, facing downwind. The first derivative kinematic properties are composed of sums and differences of four terms:

$$\text{Divergence} = \text{Downwind Shear} + \text{Diffluence} \quad (2)$$

$$\text{Stretching Deformation} = \text{Downwind Shear} - \text{Diffluence} \quad (3)$$

$$\text{Shearing Deformation} = \text{Curvature} + \text{Crosswind Shear} \quad (4)$$

$$\text{Vorticity} = \text{Curvature} - \text{Crosswind Shear} \quad (5)$$

The four terms on the right-hand side of these equations induce asymmetries in the Doppler VAD pattern. Downwind shear has the most direct effect: It is revealed by a difference in Doppler velocity magnitude in the downwind and upwind directions of the mean wind vector. The indicator of diffluence (or confluence) is a displacement upwind (or downwind) of the loci of zero Doppler velocity from their usual positions normal to mean wind direction when there is no diffluence. Curvature and crosswind shear, unfortunately, share the same indicator, which is a displacement of the Doppler velocity extrema toward the center of curvature and/or the direction of shear from their usual positions opposite one another along the mean wind vector when both these terms are absent. Despite this ambiguity, several methods have been investigated for distinguishing these two terms under certain favorable circumstances. When this can be accomplished, a new capability, the estimation of vorticity, is achieved for Doppler VAD pattern analysis.

---

29. Donaldson, R. J., Jr., and F. I. Harris, 1984: Detection of wind field curvature and wind speed gradients by a single Doppler radar. Preprints, 22nd Conference on Radar Meteorology, Zurich; AMS, Boston, 514-519.

### 3. A Realistic Difffluence Model

Difffluence, like curvature, is characterized by a change in wind direction. Unlike curvature, the diffluent directional shift is along a line normal to the axis of flow. Heretofore, the quantitative measurement of difffluence by Doppler radar has not been considered, although Baynton et al. (1977)<sup>30</sup> showed that the presence of difffluence is very easily recognized by an asymmetric zero Doppler line in the Doppler VAD display.

A field of constant difffluence within a horizontal plane is not a realistic possibility, because streamline continuity would be compromised. A similar situation exists for curvature: A field of constant curvature would require an infinite number of streamline intersections. That problem is solved by assuming a model with a fixed center of curvature, maintaining streamline integrity by varying curvature inversely with distance from the center of curvature. In a similar manner, the field of difffluence in a realistic model varies inversely with distance from a fictitious streamline apex beyond the limits of the field, and streamline integrity is maintained. Fig. 35 shows the radar scanning circle within the difffluence model. The angle  $\epsilon$  (subscript L for left of wind direction and R for right of wind) is the displacement, owing to difffluence, of the zero Doppler location from its non-diffluent position normal to the mean wind vector.

The geometry of Fig. 35 indicates that  $\sin \epsilon = r/F$ , where  $r$  is radius of the radar scanning circle and  $F$  is distance from radar to streamline apex. At the zero Doppler location on the radar scanning circle, difffluence =  $(V/r) \tan \epsilon$ , where  $V$  is wind speed. However, a more complex expression is needed to characterize the variable field of difffluence around the radar scanning circle:

$$\text{Difffluence} = \phi^{-1/2} V/F = (V/r) \phi^{-1/2} \sin \epsilon \quad (6)$$

where  $\phi = 1 + r^2/F^2 + 2(r/F) \sin \alpha$  and  $\alpha$  is the radar azimuth angle

---

30. Baynton, H. W., R. J. Serafin, C. L. Frush, G. R. Gray, P. V. Hobbs, R. A. Houze, Jr., and J. D. Locatelli, 1977: Real-time wind measurements in extra-tropical cyclones by means of Doppler radar. J. Appl. Meteor., 16, 1022-1028.

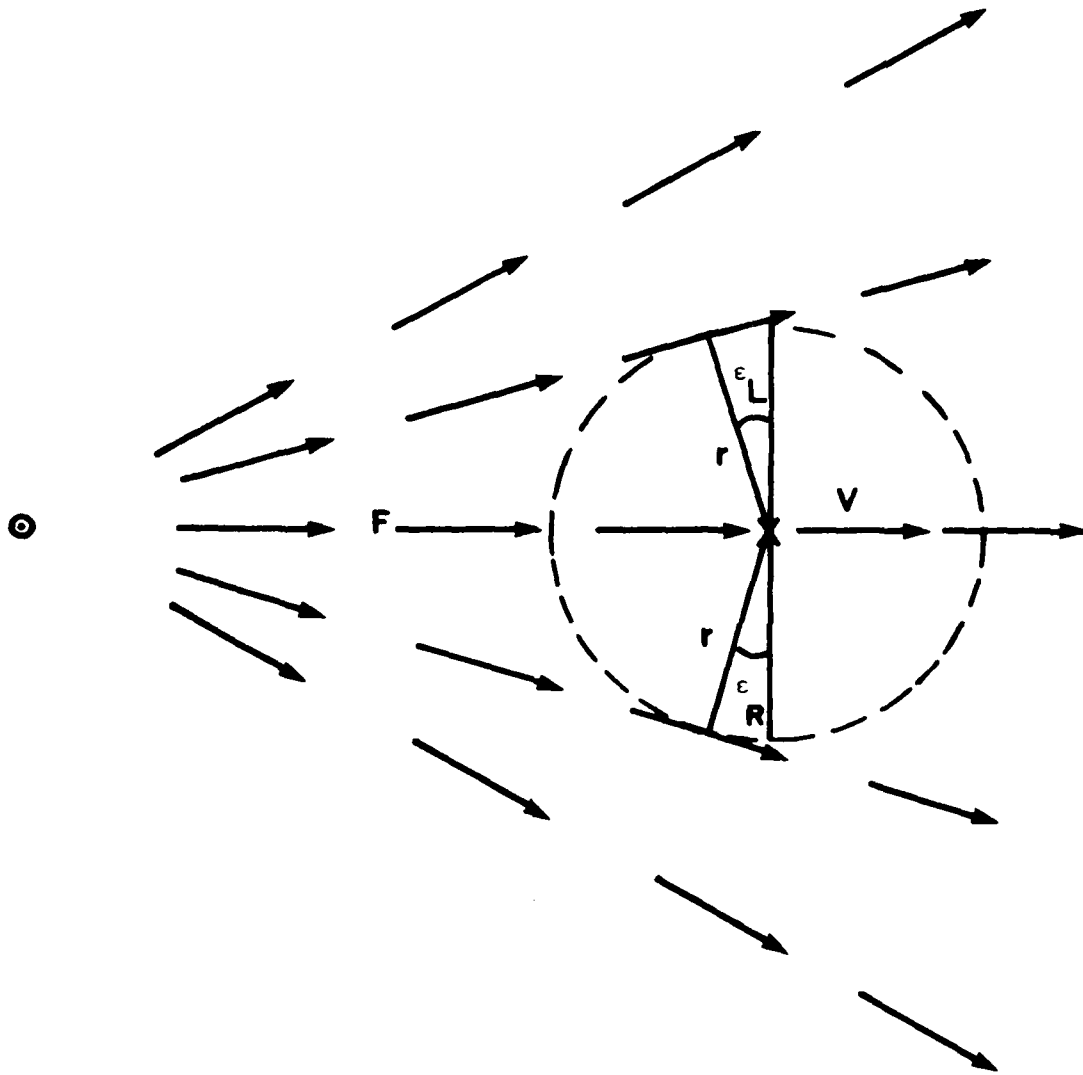


Fig. 35. Geometry of Radar Scanning Circle (dashed line) within a Diffluent Wind Field

Arrows represent wind vectors diverging from a fictitious streamline apex (●);  $V$  is the mean wind vector across the radar position (X). Radius of scanning circle is  $r$ ;  $F$  is distance from radar to streamline apex. The angles  $\epsilon_L$  and  $\epsilon_R$  indicate displacements from the normal to the mean wind vector to the  $L$  and  $R$  locations on the radar scanning circle tangent to streamlines, where zero Doppler velocity would be measured.

measured clockwise from the top of the diagram. At the radar location  $\phi = 1$  and diffluent is simply  $V/F$ , or, in radar-observable terms,  $(V/r) \sin \epsilon$ .

The solutions for radar measurement of a diffluent and a curved wind field are orthogonal. For example,  $\sin \delta = r/R$ , where  $R$  is distance from radar to the center of curvature and  $\delta$  is the angular displacement, owing to curvature, of the location of maximum Doppler velocity from the mean wind vector across the radar. The curvature term at the radar location is  $V/R$ , but around the radar scanning circle this term varies as  $\rho^{-1/2} V/R = (V/r) \rho^{-1/2} \sin \delta$ , where  $\rho = 1 + r^2/R^2 - 2(r/R) \cos \alpha$ .

#### 4. Interactions Among the Kinematic Terms

A natural wind field is unlikely to feature only curvature, or only diffluent, or only shear along or normal to the wind direction. In general, all four of these terms are present in varying degrees. Accordingly, the effect of each of the terms on measurement of the others was studied, in order to provide guidance for the analysis of natural VAD patterns.

Several of the term interactions required implicit solutions, and these were obtained over suitable ranges of parameter values. On the other hand, for certain pairings of terms there were no interactions. This favorable circumstance provided the opportunity to evaluate two of the terms with reasonable accuracy.

For example, there is no effect of either crosswind shear or diffluent on the measurement of downwind shear. This is because downwind shear is measured along the vector of mean wind crossing the radar, and crosswind shear and diffluent, as defined with respect to the radar, have no effects along the axis of mean wind. Curvature does have a small effect on the measurement of downwind shear, because a curved path length from upwind to downwind directions on the radar scanning circle is underestimated by assuming a linear length  $2r$  (the diameter of the scanning circle); but wind speed upwind and downwind is also underestimated because a small component of the curved wind is normal to the radar beam. These two underestimates tend to compensate for one another, keeping the total error within tolerable limits except for very large curvatures. For example, the error is less than eight percent for  $r/R = 0.5$ . After recovery of at least a rough estimate of curvature by other means, the small error could be reduced further.

The other favorable development is in the measurement of diffluence by observation of  $\epsilon$ , the angle between zero Doppler and normal to the mean wind vector. Neither crosswind shear nor downwind shear has any effect on  $\epsilon$ , although curvature does have a substantial effect. However, the implicit solutions of the effect of curvature on  $\epsilon$  reveal two very useful characteristics: First, the mean value of the two angles is remarkably stable over a wide range of curvature values. Under the condition of zero curvature,  $\epsilon_L = \epsilon_R$ . With increasing curvature, a decrease in  $\epsilon_L$  is almost matched by a corresponding increase in  $\epsilon_R$ . Consequently, the error in estimation of diffluence in the presence of curvature exceeds three percent only in the exceptional and unlikely circumstance wherein the sum of the diffluence and curvature parameters ( $r/F + r/R$ ) is greater than unity.

Secondly, the two  $\epsilon$  angles provide a useful estimate of curvature in the presence of small to moderate values of diffluence. The function  $(\epsilon_R - \epsilon_L)/(\epsilon_R + \epsilon_L)$  approximates the curvature parameter  $r/R$  over its entire range, with less than a five percent error for non-zero values of the diffluence parameter up to an exceptionally high magnitude of 0.5. This technique offers promise for recovery of curvature, even when its presence and magnitude are masked by crosswind shear.

#### 5. Techniques for Distinguishing Curvature and Crosswind Shear

Two of the kinematic wind field terms, curvature and crosswind shear, offer the greatest challenge in the analysis of the Doppler VAD pattern because their signatures are similar. Both terms cause displacement of the Doppler velocity extrema, down-shear in the case of crosswind shear or toward the circulation center in the case of curvature. The angle between mean downwind direction and location of maximum Doppler velocity is labeled  $\delta_D$ ; similarly,  $\delta_u$  is the angle between mean upwind direction and minimum Doppler velocity.

The sum of curvature and crosswind shear is shearing deformation, a kinematic property of the wind field that is easily calculated by Fourier analysis of the Doppler VAD pattern. Vorticity, however, which is curvature minus crosswind shear, cannot be calculated straightforwardly from measurements of a Doppler radar imbedded within the vorticity field. Within the context of traditional analysis techniques,

vorticity is intractable. On the other hand, an opportunity for at least a rough estimate of vorticity would be presented by a method for distinguishing curvature and crosswind shear. There appear to be four possibilities to approach this task.

a. Information External to the Doppler VAD Pattern

If a hurricane or intense extra-tropical cyclone has an eye or circulation center that can be located by satellite or aircraft, the distance  $R$  from cyclone center to radar is determined. Under the simplest realistic assumption of circular, concentric streamlines the curvature term at the radar is wind speed divided by  $R$ , and the curvature parameter in a VAD pattern with radius  $r$  is  $r/R$ .

b. Isolation and Examination of Second Order and Higher Derivatives of the VAD Pattern

This method relies on the fact that crosswind shear has no derivatives above the first order. The VAD coordinates  $(r, \alpha)$  are aligned such that the mean wind direction is from  $\alpha = 270^\circ$  toward  $\alpha = 90^\circ$ . Then the zeroth, first, and second Fourier moments involving  $\sin n\alpha$  are calculated. These moments are  $a_0/2$ ,  $b_1$ , and  $b_2$  in the notation of Browning and Wexler (1968). All moments are divided by the cosine of the radar elevation angle to recover their magnitudes in the horizontal plane of the radar scanning circle. The first moment  $b_1$  is equal to mean wind speed across the radar. The products of  $2/r$  and the zeroth and second moments are, respectively, divergence and shearing deformation. Next a remainder function  $V_{DR}(\alpha)$  is calculated by subtracting from the observed Doppler velocity function  $V_D(\alpha)$  the contributions owing to divergence, translation, and equivalent crosswind shear:

$$V_{DR}(\alpha) = V_D(\alpha) - a_0/2 - b_1 \sin \alpha [1 + 2(b_2/b_1) \cos \alpha]. \quad (7)$$

The term  $2b_2/b_1$  is the equivalent crosswind shear parameter  $c_e$  if all of the second Fourier moments  $b_2$  were due to crosswind shear alone. Whether or not this is true is inconsequential; it matters only that a function has been created from which all traces of crosswind shear have been removed.



The  $V_{DR}$  function owing to curvature alone has two maxima and one minimum in the downwind semicircle, and corresponding two minima and one maximum in the upwind semicircle. The peak magnitude of the largest maximum as a ratio to wind speed is 0.13 for  $r/R = 0.5$  but less than 0.06 for  $r/R = 0.35$ . The mean magnitude of  $V_{DR}$  is slightly less than one-half its peak magnitude, but may be a more reliable measure of curvature in the presence of perturbations manifested in derivatives of second and higher order. Time integration, for example, averaging two or more VAD patterns over a period of several minutes, might also be helpful in reducing the effect of higher order perturbations, because most of the higher order contributions are probably involved with relatively small spatial structures and therefore provide less stable patterns in time than the field of curvature. The  $V_{DR}$  method appears capable of detection of fairly large values of curvature, but the limits of its usefulness in noise and perturbations await experimental determination.

c. Comparison of Equivalent Crosswind Shear Parameter  $c_e$  with Displacements of the Doppler Velocity Extrema  $\delta$

This method depends on the differing capability of curved and cross-sheared wind fields in effecting displacements of the Doppler velocity maximum and minimum in the VAD pattern. The first part of the procedure is calculation of an equivalent crosswind shear parameter  $c_e = 2b_2/b_1$ , identical to the procedure used in the previous sub-section. The next step is determination of the angular locations of the Doppler velocity extrema and their displacement  $\delta$  from the mean wind vector. No allowance has been made for different  $\delta$  values upwind and downwind, owing to asymmetries induced by downwind shear and/or diffluence. However, as discussed previously, these two wind field terms may be estimated fairly accurately and, in principle, employed for correction of differing  $\delta$  values.

With  $c_e$  and  $\delta$  determined, an algorithm is entered which yields the ratio of the true crosswind shear parameter  $c$  to the curvature parameter  $r/R$ . The sum of these two parameters ( $c + r/R$ ) closely approximates the value of  $c_e$ . These relationships are depicted in Fig. 36.

There are, however, serious problems in the implementation of this process with natural wind fields. Inspection of Fig. 36 shows that

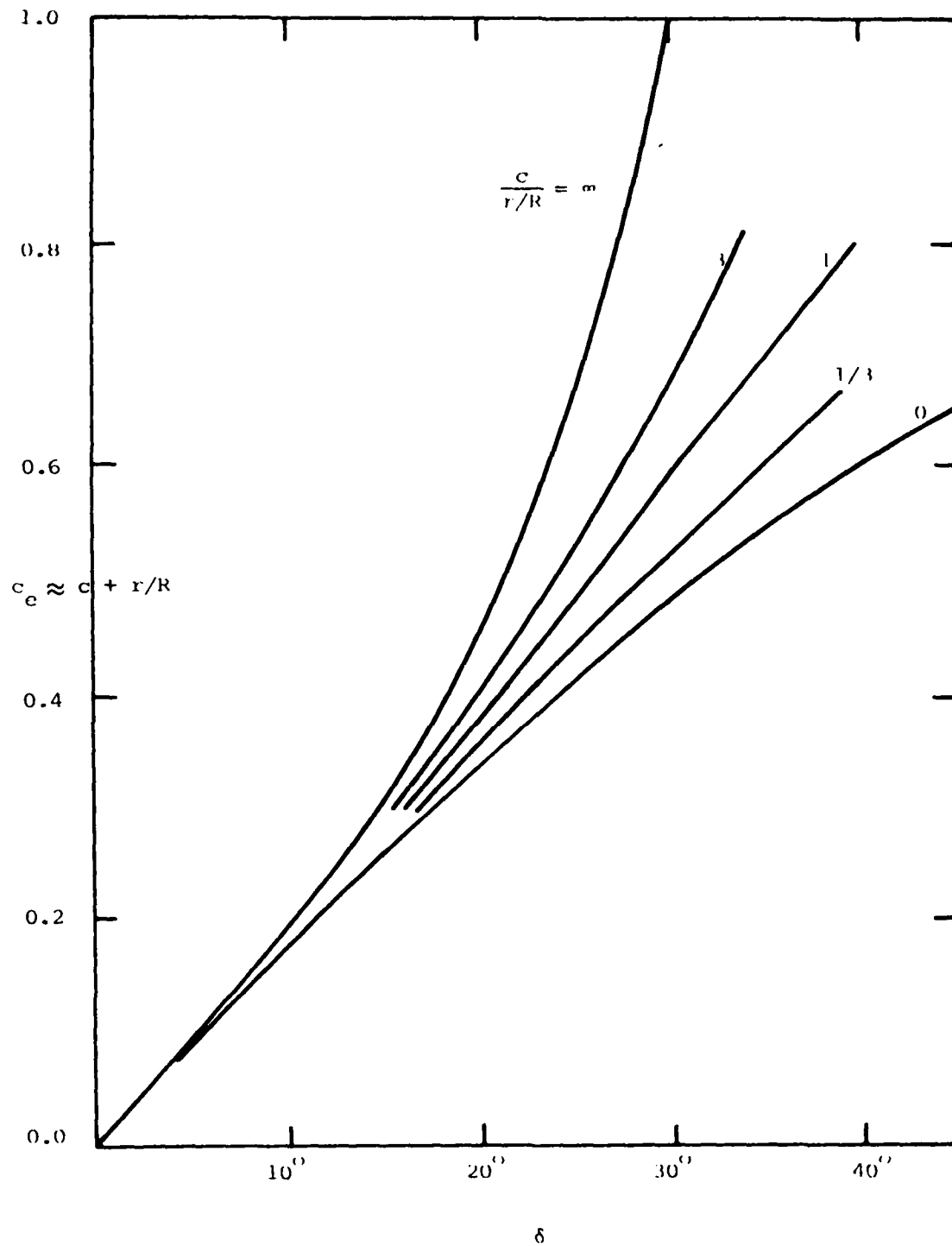


Fig. 36. Equivalent Crosswind Shear Parameter ( $c_e$ ) as a Function of Angular Displacement ( $\delta$ ) of the Doppler Velocity Extrema from the Mean Wind Vector

The family of curves specifies this function over the entire range of the ratio of true crosswind shear parameter  $c$  to curvature parameter  $r/R$ .

very little discrimination of curvature from crosswind shear is possible with  $c_e$  values below 0.3. At this level of  $c_e$ , there is a very narrow range of  $\delta$ , from  $15^\circ$  with pure crosswind shear to  $18^\circ$  with pure curvature. Another problem is the likely contamination of  $c_e$  by higher order, small scale perturbations that contribute neither to curvature nor to shear on the scale of the VAD circle. As indicated previously, time integration might be helpful in reducing perturbational effects. Finally, the measurement of  $\delta$ , even without the distraction of perturbations, is not highly accurate because the derivative of Doppler velocity with respect to azimuth angle is minimal in the vicinity of a maximum or minimum.

#### d. Effect of Curvature on the Difffluence Signature

The opportunity to estimate curvature through its unique effect on the locations of zero Doppler velocity was discussed in the previous section. Two significant advantages are gained by this technique: accuracy, and sensitivity to small values of curvature. The zero Doppler locations are more definitively measured than the locations of the Doppler velocity maximum and minimum, because the change of Doppler velocity with azimuth angle is greatest at or near a zero crossing. The major disadvantage is the requirement of a sufficient magnitude of difffluence (or confluence) to provide a measurable difference in the two  $c$  angles.

In conclusion, under certain favorable conditions it is possible to distinguish curvature, at least roughly, from crosswind shear, and thereby estimate vorticity with comparable accuracy.

#### 6. Future Work

This theoretical study, supplemented by earlier work described by Donaldson and Harris (1984), will be prepared for publication. Attention will next be directed toward application of these capabilities to an analysis of Hurricane Gloria (September 27, 1985) and one or more intense winter storms. A preliminary survey of Hurricane Gloria indicates a surprisingly rapid deterioration of its circulation in the eye region after its landfall. Study of the evolution and interaction of the kinematic wind field terms will focus on this event.

## B. Gust Front Detection

### 1. Introduction

A serious hazard confronting aircraft is the abrupt change of wind associated with gust fronts. Gust fronts are the leading edges of low level outflow air from thunderstorms produced by the downdrafts within the thunderstorm. Typically, the downdraft air is deflected by the ground in all directions, producing the strongest shears where the deflected air encounters the low level inflow feeding the storm. Wind shifts of greater than  $90^\circ$  and shears of greater than  $0.01 \text{ s}^{-1}$  are common. There is thus the potential for drastic and abrupt changes in the lift characteristics of an aircraft, potentially a cause for a crash.

Gust fronts are typically a few kilometers across as measured from where the wind shift occurs to the point within the front where the maximum outflow winds occur. In length gust fronts can vary from the order of ten kilometers for a single storm cell to hundreds of kilometers for a squall line situation. These scales are ideal for detection by Doppler radar. This report presents a technique for the real time detection of gust fronts using Doppler radar data. A preliminary account of this technique was presented in Gerlach (1984) with an update in Harris *et al.* (1985).<sup>31</sup> A review of the nature of Doppler measurements and an update of the technique are presented here.

### 2. Radar Measurements

Doppler radar measures the component of the motion of the scatterers parallel to the radar beam. For example, if the radar were to sample a precipitation system embedded in a uniform flow field, it would measure a maximum radial velocity when looking downwind, a minimum when looking upwind, and zeros when looking perpendicular to the wind. Thus at any point in space, the radial velocity measurement is equal to or less than the true particle motion. Also, since only one component of the velocity can be measured, the wind direction at all points cannot be readily

---

31. Harris, F. I., K. M. Glover, and G. R. Smythe, 1985: Gust front detection and prediction. Preprints, 14th Conference on Severe Local Storms, Indianapolis; AMS, Boston, 342-345.

determined. Therefore it is not possible to determine the true wind field associated with a gust front with a single Doppler radar.

Fig. 37 is a contour plot of the radial velocity field as measured by the National Severe Storms Laboratory Doppler radar located in Norman, OK. The concentration of contours in the central portion of the plot delineates the transition region between the storm inflow region on the right and the outflow on the left. It is in this region that the winds are undergoing dramatic changes in speed and direction; it is therefore the region that presents the greatest hazard for aircraft. The surface gust front is located near the right edge of this sheared region. The technique presented does not attempt to delineate the surface position of the gust front but instead concentrates on delineating the potentially hazardous shear region.

### 3. The Technique

As shown in Fig. 37 gust front regions are readily evident in radial velocity data as strong gradients of the radial velocities. It would therefore seem reasonable to derive a technique based on estimations of these gradients. This indeed does form the basis of the technique presented.

The gradient of the radial velocity field is given in polar coordinates as

$$\text{del } VR = \frac{\partial VR}{\partial R} \hat{R} + 1/R \frac{\partial VR}{\partial \theta} \hat{\theta} \quad (8)$$

and in rectangular Cartesian coordinates as

$$\text{del } VR = \frac{\partial VR}{\partial x} \hat{x} + \frac{\partial VR}{\partial y} \hat{y} \quad (9)$$

where VR is radial velocity, R is range,  $\theta$  is azimuth in radians, x is distance towards the east, and y is distance towards the north. The quantities  $\hat{R}$ ,  $\hat{r}$ ,  $\hat{x}$ , and  $\hat{y}$  are the unit vectors in their respective directions. Although the resultant vectors are in theory identical, differences in processing result in some deviations. These will be discussed later. Currently, there are two algorithms, one that computes the magnitude and direction of the gradient in polar coordinates and one that performs the calculations in Cartesian coordinates. The advantages of each will be discussed.

# AVER VEL

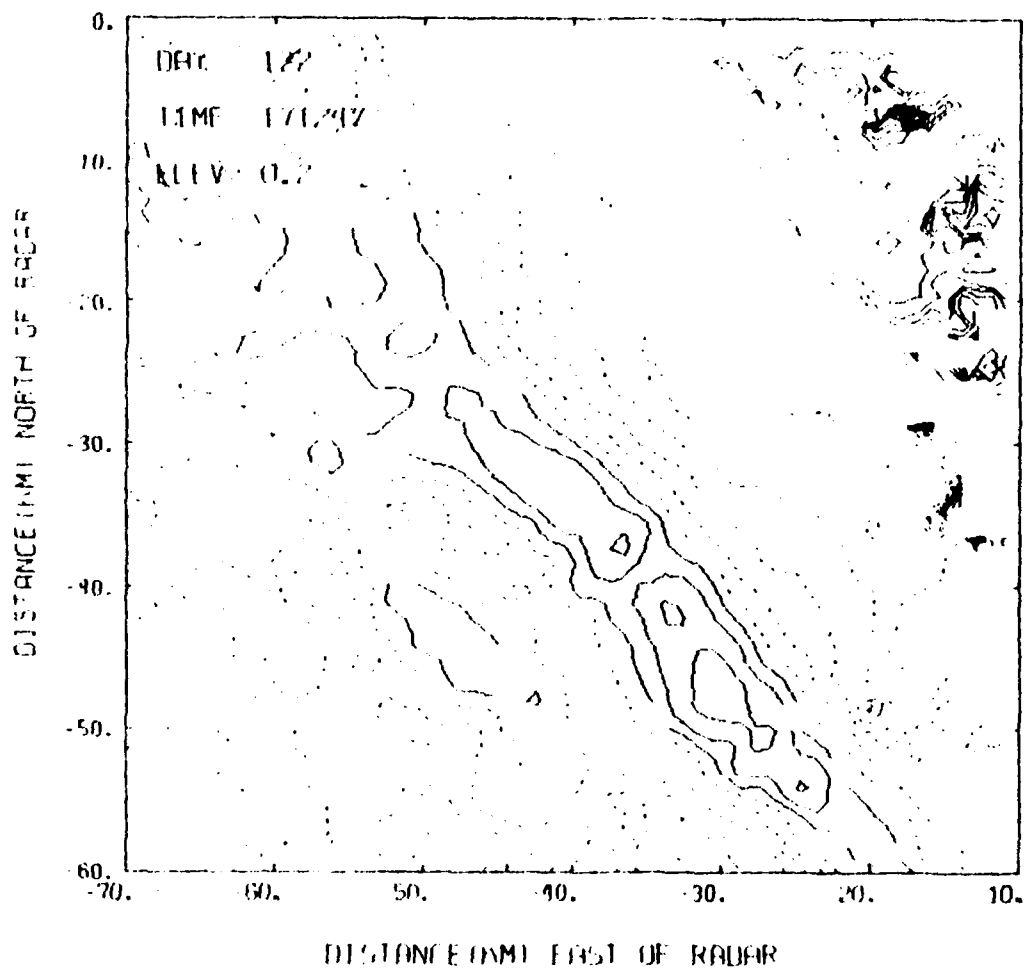


Fig. 37. Contour Analysis of Radial Velocities for Gust Front Case of May 2, 1978

Contours are at  $5 \text{ m s}^{-1}$  intervals with dashed contours depicting velocities away from the radar and solid contours towards the radar. Storm is located in southwest quadrant.

a. Polar Computations

For the computations in polar coordinates there are five steps:

- \* Compute running means in range.
- \* Compute derivatives of means in range - first term on right of Eq. (8).
- \* Compute derivatives of means in azimuth - second term on right of Eq. (8).
- \* Interpolate derivatives onto a Cartesian grid; a uniform filter 1 km on a side is used to interpolate to a grid with 1 km resolution.
- \* Combine the two derivatives vectorally to produce the gradient vector.

Computation of the running means was essential in order to reduce the noisiness of the gradient estimations. Averaging five range gates (750 m) was found to be sufficient to allow retention of the significant shear and to reduce to acceptable levels the effects of small eddies and uncertainties in the velocity estimates. The advantage of this technique is that the estimates of the gradient appear to be reasonably consistent with what is seen in the raw data. However, this technique is computationally intensive since there are so many computations made on the polar coordinate data.

b. Cartesian Computations

For the calculations in the Cartesian framework there are three steps:

- \* Interpolate the radial velocities onto a Cartesian grid using the same uniform filter as was used for the polar computations.
- \* Compute the two derivatives on the right side of Eq. (9).
- \* Compute the magnitude and direction of the gradient vectors.

This technique is much simpler to implement and is much less intensive computationally. However, as will be seen, the estimates of the magnitude of the gradient are significantly less than those for the polar coordinate computations. Gust fronts are readily apparent in both gradient fields.

#### 4. Application

##### a. Gust Fronts

Both computational schemes were applied to data collected from three gust fronts observed by the National Severe Storms Laboratory radar at Norman, OK. Examples of the gradient vector plots for each of these cases are presented in Figs. 38-40. The vectors are oriented in the positive direction of the shear, i.e., they point towards the regions of maximum radial velocities. The frames on the left of each figure contain the results of the polar computations and those on the right are for the Cartesian computations. The vector length is proportional to the magnitude of the gradient; vectors are plotted only if their magnitudes are greater than  $0.007 \text{ s}^{-1}$  for the radial computations and  $0.003 \text{ s}^{-1}$  for the Cartesian case. The strong gradient regions associated with gust fronts are readily distinguished as the elongated regions of vectors pointing to the maximum winds behind the front. Smaller gradient regions to the west of that associated with the front are also seen associated with perturbations in the outflow, such as might be expected with downbursts and with the rear side of the maximum in the outflow producing the gust front. In all three cases, the gust front was detectable over an extended period of time.

A comparison of the results from the two techniques shows the diminished magnitudes resulting from the Cartesian computations. This reduction is due to the greater averaging and the larger scale used for the derivative computations in the Cartesian calculations. However, the vector directions are for the most part consistent and the gradient regions are equally detectable with both techniques. Further comparisons are required before definitive recommendations can be made.

##### b. Mesocyclones and Downbursts

Since these techniques are detecting significant gradient regions in the radial velocity data and both downbursts and mesocyclones produce such regions, an attempt was made to see how successfully these



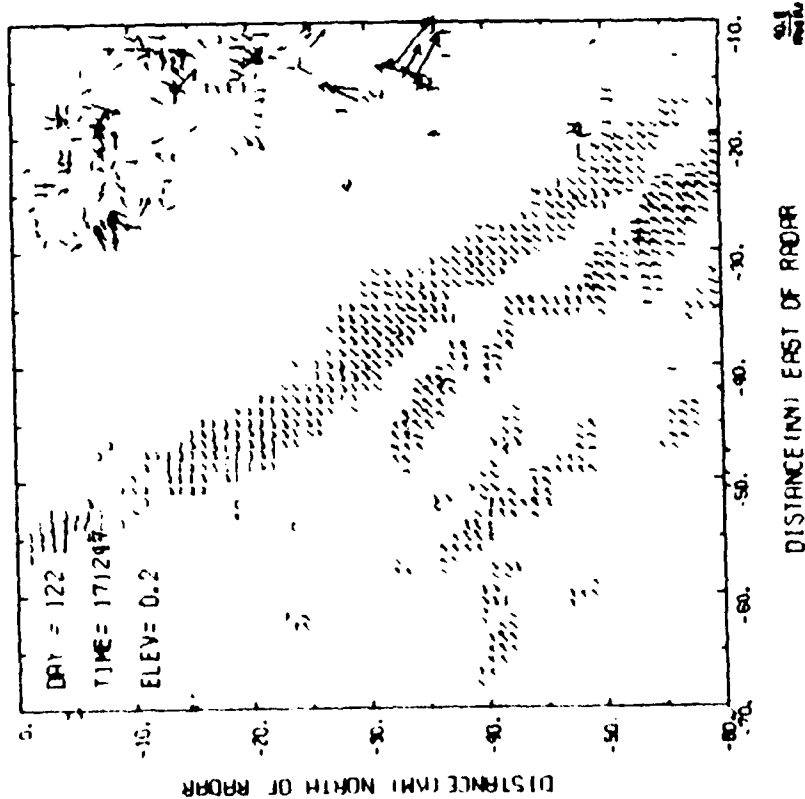
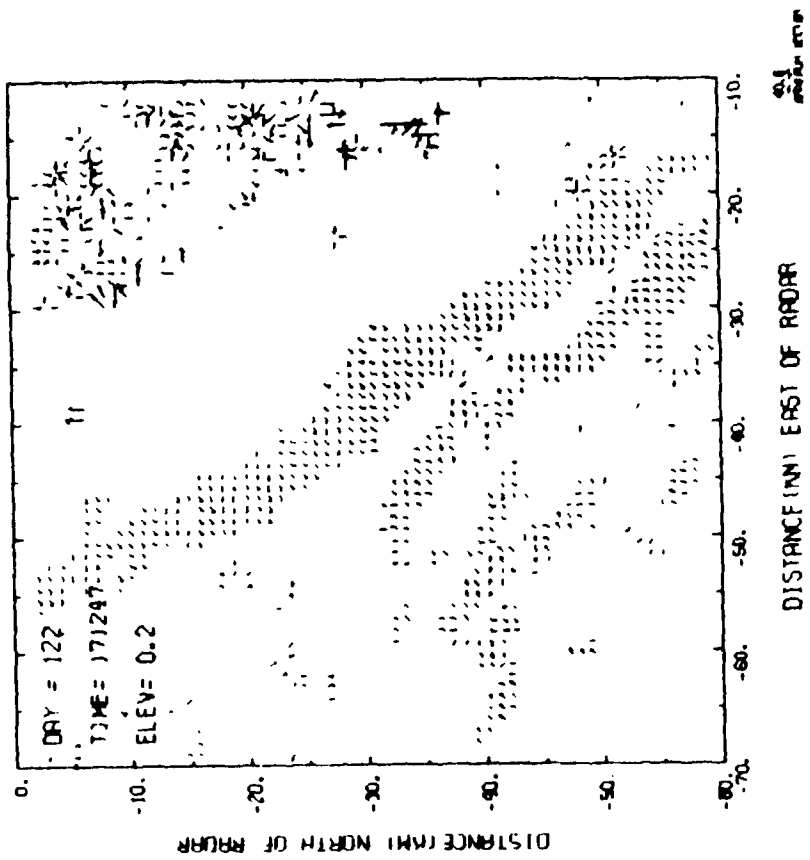


Fig. 38. Vectors of Total Gradient of Radial Velocity for May 2, 1978 Corresponding to Radial Velocity Field in Fig. 37

Left figure is for polar computations while right figure is for Cartesian computations. Gust front is the longest feature (from upper left to lower right) with the vectors all pointing toward the southwest. Other features to the left of the front are smaller shear regions associated with the storm system.

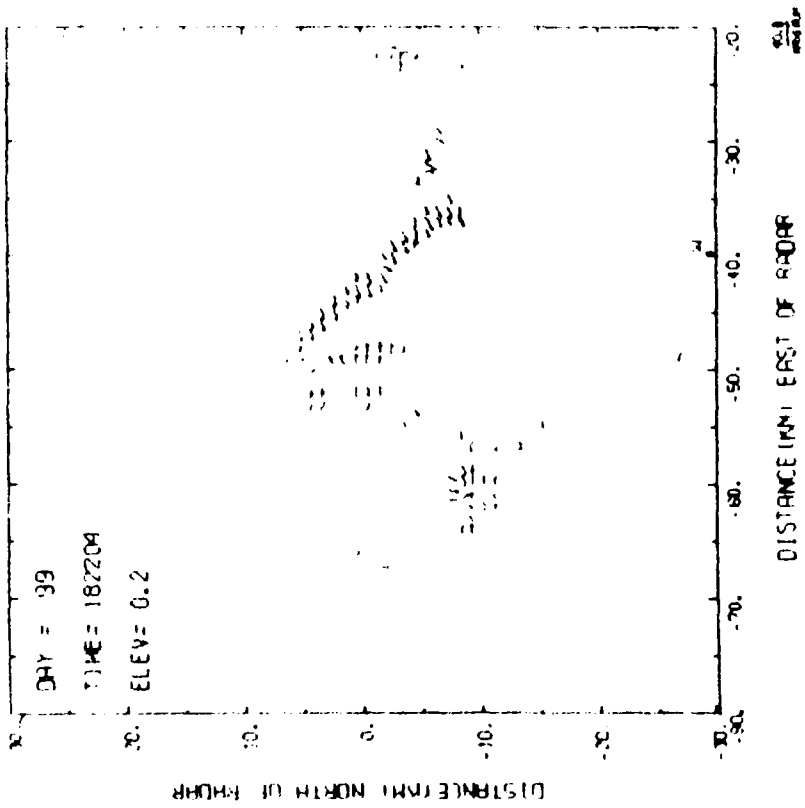
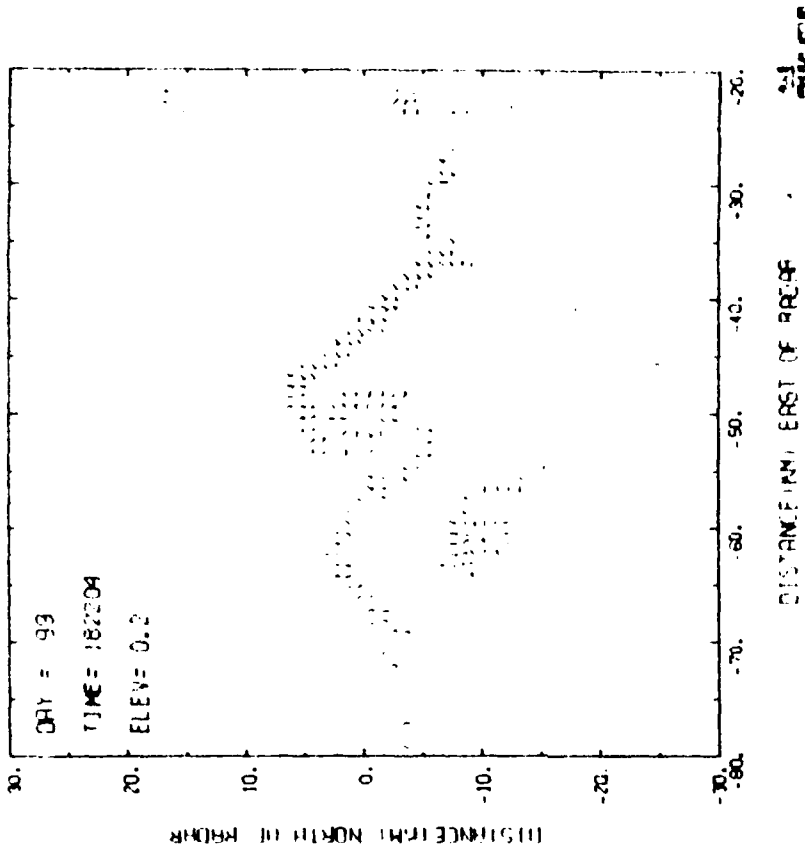


Fig. 39. Vector Plots as in Fig. 38 but for April 9, 1978

Gust front appears to be better depicted in the Cartesian processing (figure on the right).

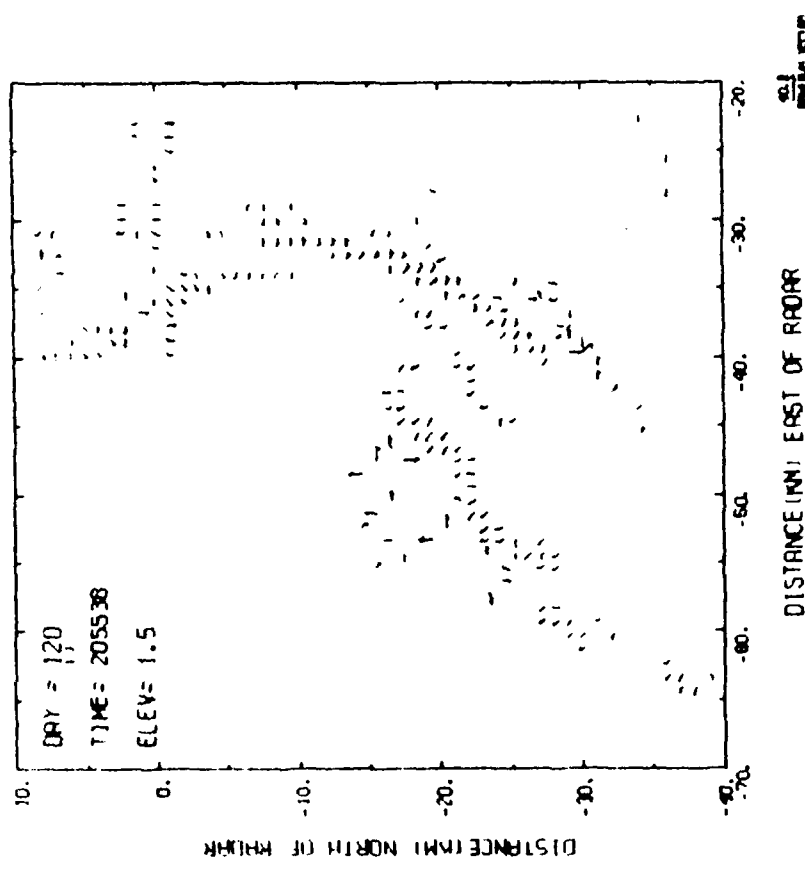
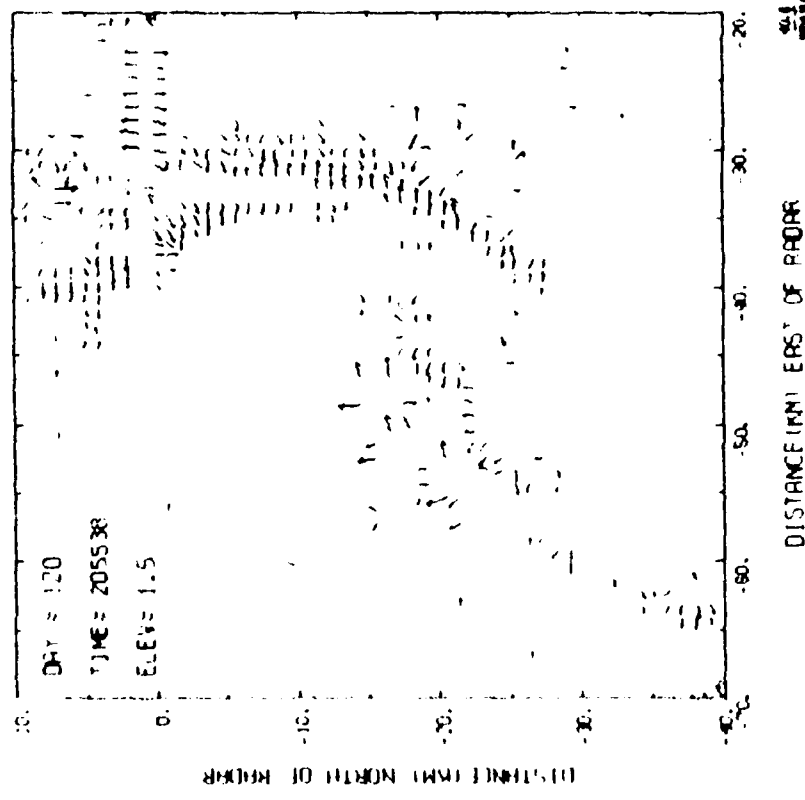


Fig. 40. Vector Plots as in Fig. 38 but for April 30, 1978

phenomena could be detected. To assess the nature of the signatures one might expect in the gradient fields from these two phenomena, a simple model was constructed of each. Sampling of these models was simulated and the gradients were computed. Results for the mesocyclone are presented in Fig. 41 and for the downburst in Fig. 42. In both cases the features are depicted as regions containing a couplet of convergent and divergent vectors. In the case of the mesocyclone (Fig. 41) the axis connecting the centers of the couplet is oriented orthogonal to the beam while for the downburst (Fig. 42) the axis lies along the beam. While the features are readily discernible in these figures, identification of the phenomenon producing the signatures depends on a knowledge of the orientation of the beam. Therefore it is concluded that current mesocyclone and divergence algorithms are more efficient and less likely to produce confusion than this gradient algorithm in the detection of mesocyclones and downbursts.

#### 5. Area Thresholding

Attempts were made at using area thresholds to focus attention on the gust front and eliminate the small and less significant features. To accomplish this it was necessary to search the field of gradient values and to associate them into regions. These regions were then checked for areal extent; those not passing the area threshold were eliminated. Results of this exercise were presented by Harris *et al.* (1985) and will not be reproduced here. The feasibility of this approach is being assessed in light of its potential to detect small scale downbursts and mesocyclones.

#### 6. Future Development

The result of this effort has been the derivation of a field in which strong shear regions are readily distinguished. More cases need to be examined in order to assess more adequately the strength and weaknesses of the two techniques. Also, techniques will be examined to provide predictive positions for the more significant features.

#### 7. NEXRAD Documentation

Initial results from the polar computation technique showed so much more promise than the shear algorithm currently in the Next Generation Weather Radar (NEXRAD) algorithm inventory that it was accepted by the NEXRAD office. The algorithm was then documented and submitted to NEXRAD,

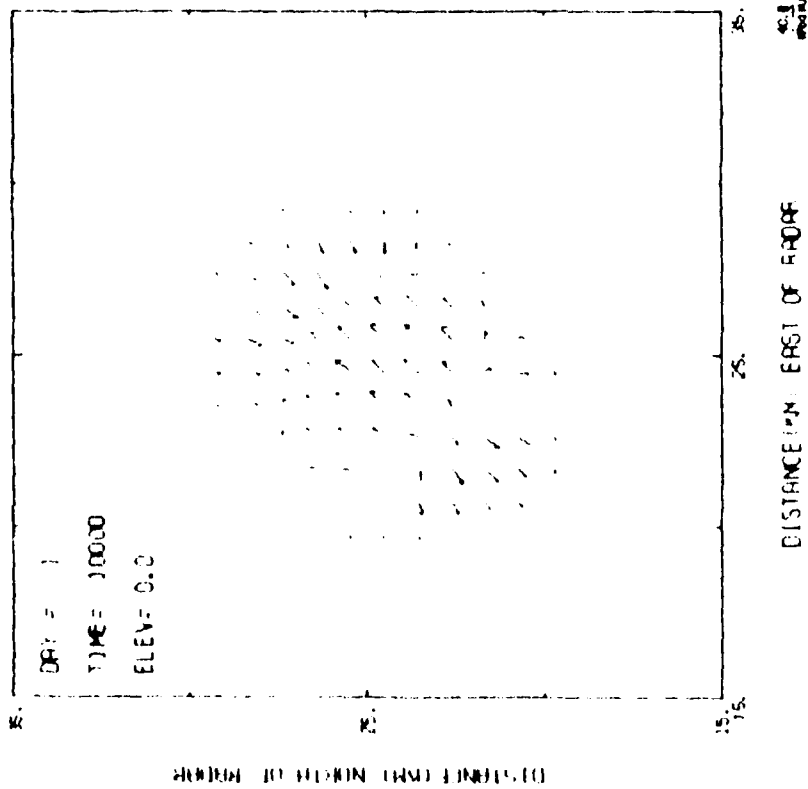


Fig. 41. Vector Plot for a Simulated Mesocyclone

Note the convergent vectors at the lower right and divergent vectors at the upper left, depicting the proper orientation of the velocity couplet associated with a typical mesocyclone signature. The radar is located at (0,0).

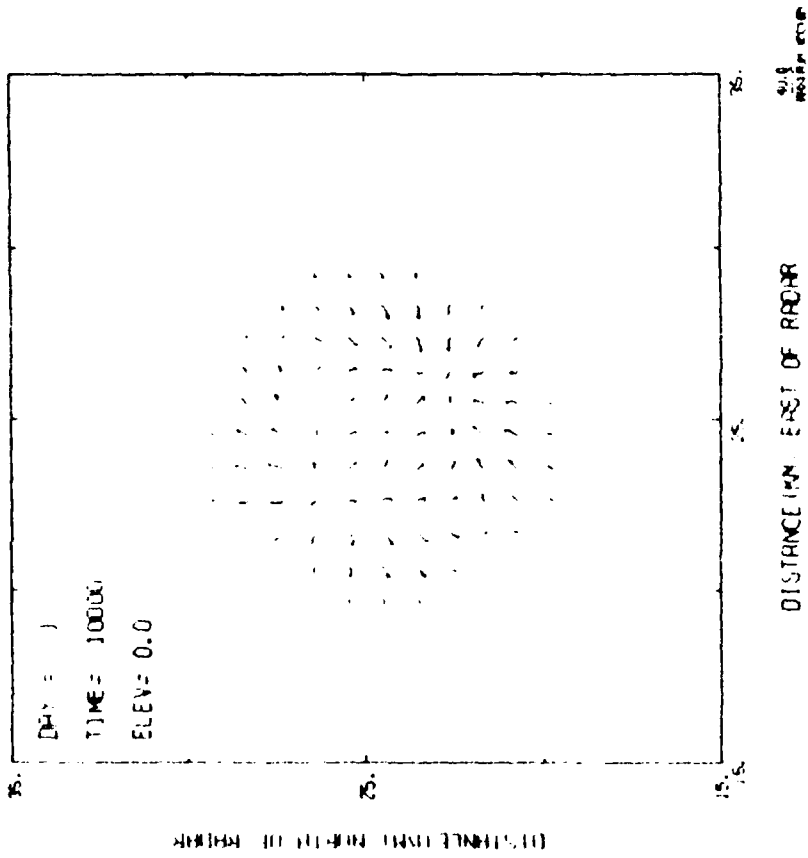


Fig. 42. Vector Plot for a Simulated Downburst

The convergent region is at the upper right and divergent region at the lower left, depicting the proper orientation of the velocity couplet associated with a typical downburst signature.

which accepted it as a Category 1 algorithm, that is, one that must be included in the prototype NEXRAD radars. The staff of the NOAA Prototype Regional Observation and Forecast Service (PROFS) has implemented the algorithm using this documentation and has added it to the NEXRAD library of algorithms to be tested operationally.

### C. Three-Dimensional Cloud and Precipitation Mapping

#### 1. Introduction

A project was initiated to develop techniques and corresponding software for the real time mapping of clouds and precipitation using meteorological radar data and meteorological satellite imagery. This effort must mesh with a short-range forecasting effort by AFGL/LYR in order that the resultant product will demonstrate the utility of these data sources for short range predictions of paths available for satellite-to-ground transmissions. New communication satellites to be launched in the 1990's will operate at high microwave frequencies, which will be highly susceptible to attenuation by precipitation and in some cases perhaps even cloud. These systems will require guidance as to which communication links will not experience significant attenuation and thus can be utilized successfully.

This section describes the efforts undertaken to develop such a forecast system.

#### 2. RAPID System Development

AFGL/LYR acquired new computational hardware in the form of a VAX 11/750 and an ADAGE 3000 image processor. These processors and their associated peripherals are called the Remote Atmospheric Probing Information Display (RAPID) System. SASC Technologies, Inc., is responsible for developing system and applications software which will be used by the developers of the analysis routines.

To this end the following have been accomplished:

- \* The VAX operating systems VMS3.7 to 4.2 were installed with VMS 4.2 the one currently in use. Modifications were made to the system software to accommodate the ADAGE and peripherals.

- \* A bitpad was interfaced to RAPID and software routines were written to allow easy basic drawing on the ADAGE using the bitpad.
- \* The operating systems of both the VAX and the P-E 3242 were modified to allow communication between them. Software was written to allow the transfer of data between the two machines.
- \* The TRILOG printer plotter was interfaced with the VAX and software was written to allow the transfer of images resident in the ADAGE through the VAX to the TRILOG. Both color (eight colors with three shades of each) and black and white images are supported with this software.
- \* A display list processing system was developed and documented for easy interactive access to the ADAGE processor and memory. With this system it is possible to download a number of procedures to the ADAGE for processing, start the processes, and return to VAX, leaving the ADAGE to perform its tasks. The processes are easily modified by simply downloading another list of procedures. To utilize this system all user-supplied software must be written in ICROSS, a C-like language for which there is a compiler that produces code usable by the ADAGE.
- \* A comprehensive image storage system for two- and three-dimensional data was designed and implemented for use on the VAX.
- \* An interactive version of the NCAR graphics package was acquired from the National Center for Atmospheric Research and was installed on the VAX. This package was modified to accommodate the ADAGE, to allow the user easier control over color (to load one's own color table and to control the background color), and to allow the saving or recalling of an image. Also, the documentation was improved.

### 3. Precipitation Mapping

The first task was to write software for the VAX that would allow the reading of AFGL radar data. A new modularized version of the routine resident on the P-E 3242 was implemented. Then software was written to rasterize the radar data and to display these with the ADAGE. These software packages were all written to allow flexibility as to the location within the data where the processing would be performed, as to what data would be processed (velocity or reflectivity), and where in the ADAGE memory the data would be stored. Since it is possible to generate multiple images in the ADAGE memory, another software routine was developed to allow time lapse displays of these images.

ADAGE memory software was written to save and recall the images and to manipulate them. These manipulation routines were written in ICROSS and use the display list processing system mentioned in Section 2. Routines were developed to move images, to filter the data using a uniform filter, to compute derivatives, and to threshold the data using another field.

The above software production yielded quick and easy displays of AFGL radar data. A more complete and flexible software package for processing any radar data in universal format was acquired from NCAR. As outlined in Mohr *et al.* (1981)<sup>32</sup> and Mohr and Miller (1983)<sup>33</sup>, this package allows preprocessing perusal of the data, interpolation into rectangular Cartesian coordinates, multiple Doppler analysis, a variety of field manipulations, and display capabilities using the NCAR graphics package. Modifications will be made to accept the AFGL dual frequency data and the AFGL data format, thereby eliminating converting the data tapes to universal format.

---

32. Mohr, C. G., L. J. Miller, and R. L. Vaughan, 1981: An interactive software package for the rectification of radar data to three-dimensional Cartesian coordinates. *Preprints*, 20th Conference on Radar Meteorology, Boston; AMS, Boston, 690-695.

33. Mohr, C. G., and L. J. Miller, 1983: CEDRIC - A software package for Cartesian space editing, synthesis and display of radar fields under interactive control. *Preprints*, 21st Conference on Radar Meteorology, Edmonton; AMS, Boston, 569-574.



Another effort will result in the real time interpolation of radar data on the ingest computer for the radar data (P-E 3242) and the subsequent transfer to RAPID for further processing. Since the P-E 3242 will be upgraded by AFGL/LYR to 16 megabytes of memory, it is thought that this large task will best be accomplished on the P-E 3242, leaving RAPID with more time for the prediction problem.

#### 4. Cloud Mapping

Cloud mapping is to be accomplished by using satellite infrared and visible imagery. These data will help in establishing cloud boundaries in regions where the radar has problems "seeing" the precipitation systems. However, problems with data navigation and temporal resolution (30 min) will probably make the satellite data of secondary importance to the radar data. Nevertheless, every attempt will be made to glean the most information possible from the satellite data to assist in the prediction problem.

First efforts at displaying satellite data were to write routines to read the imagery data as provided by AFGL/LYS and to reformat a selected subset to the same format used for the radar images. As a result, the same software but with different color tables is used to display both satellite and radar data.

In addition, software was acquired from the Prototype Regional Observation and Forecast Service (PROFS) which will remap the satellite data onto a rectangular Cartesian frame consistent with that used for the radar data. This software will be installed in the next few months.

#### 5. Detection and Prediction Techniques

In addition to software development a survey was conducted jointly with AFGL/LYR into candidate techniques for detecting and forecasting the locations of precipitation, to be used for short-range predictions of clouds or precipitation along arbitrary satellite-to-ground communication links. This resulted in the conclusion that the most viable representations of satellite and radar data are contour plots of satellite derived cloud brightness temperatures and radar derived reflectivity factors. Techniques for deriving these contours were explored. Results

of this survey are presented in Bohne and Harris (1985)<sup>34</sup>.

## 6. Future Development

In 1986 additional tools will be developed to make RAPID more flexible and easier to use. Prototypes of potential real time cloud and precipitation algorithms will be developed and tested in a non-real time environment. Some aspects required for real time operations will be implemented, such as the transfer of radar data in Cartesian coordinates from the P-E 3242 to RAPID.

### D. Icing Detection

#### 1. Introduction

The need for improved forecasting of aircraft icing conditions was pointed out in Gerlach (1984). This report describes the implementation of an icing detection technique that uses weather radar data and a color graphics display depicting regions of potential icing in real time. The technique is based on an existing algorithm.

#### 2. Algorithm

Aircraft icing results when supercooled water comes in contact with and subsequently freezes on an aircraft's surface. Extensive measurements have been made on the amount of supercooled water and other microphysical parameters needed to produce significant icing. Icing typically can occur at supercooled water contents (SWC) of  $0.6 \text{ g m}^{-3}$  and in clouds containing droplets of  $15 \text{ }\mu\text{m}$  diameter (Perkins, 1978).<sup>35</sup> The S band NEXRAD radar with a proposed sensitivity of  $-8 \text{ dBz}$  at  $50 \text{ km}$  range will not be sensitive enough to detect supercooled water droplets at the above values. In general radar detects precipitation, not cloud droplets or small ice crystals. Therefore the use of radar as an icing detection tool

---

34. Bohne, A. R., and F. I. Harris, 1985: Short Term Forecasting of Cloud and Precipitation Along Communication Paths. AFGL-TR-85-0343, Air Force Geophysics Laboratory, Hanscom AFB, MA.

35. Perkins, P. J., 1978: Proceedings, Second Annual Workshop on Meteorological and Environmental Inputs to Aviation Systems. NASA Conference Publication 2057, 85-99.

will be limited to precipitation situations and will be heavily dependent upon the inference of the presence of supercooled water from the precipitation structure.

The necessary conditions for significant icing to occur are temperatures below 0° C, sufficient supercooled water, and the presence of updrafts. Observations show that significant regions of supercooled water can be found within deep meso- $\alpha$  scale cloud systems (Politovich, 1982).<sup>36</sup> These regions are associated with embedded convection within stratiform precipitation. Most of the currently proposed methods of using radar to find these areas involve first detecting indicators of updrafts and then inferring the existence of supercooled water. Two methods along this line were tested in field experiments during the WMO Precipitation Enhancement Program (PEP) in Spain.

One of the methods (Austin *et al.*, 1983)<sup>37</sup> (hereafter referred to as AMM) utilizes the reflectivity gradient. The method is based on the calculation of alpha, a derived parameter related to the reflectivity gradient, defined as

$$\alpha = \frac{dBz_2}{dBz_1}$$

where  $dBz_1$  is the reflectivity factor at the height of the 0° C isotherm and  $dBz_2$  is the reflectivity factor at a height 2 km above the height of the 0° C isotherm. AMM states that when  $0.8 < \alpha \leq 1.2$  a convective cell is in an early or mature stage of development during which an updraft is present. An alpha value of  $\leq 0.8$  indicates that the convective cell is in the decaying stage, when no updraft is expected to be present. Alternatively,

---

36. Politovich, M. K., 1982: Characteristics of icing conditions in wintertime stratiform clouds. Preprints, Conference on Cloud Physics, Chicago; AMS, Boston, 404-407.

37. Austin, G. L., O. Massambani, and M. C. Martinez, 1983: Digital radar analysis of 1981 PEP data. Precipitation Enhancement Project, Report No. 29, PEP Site Selection Phase-3, Based on Data Acquired by Radar, World Meteorological Organization, Geneva, 1-28.

the gradient of reflectivity above the melting layer can give an indication of the microphysical processes present. If reflectivity increases markedly with decreasing height there is a strong suggestion of aggregational growth of ice. That is, as the ice crystals/flakes fall they collect smaller crystals that fall more slowly. The collection efficiency of ice crystals increases with increasing temperature; that is, aggregation becomes more effective the closer the temperature of the crystals/flakes is to  $0^{\circ}\text{C}$ . On the other hand, if the gradient is near 0 (i.e.,  $\alpha = 1$ ) there is little or no growth by falling precipitation. In either case there is the strong potential of supercooled water being present.

In testing this algorithm during the PEP project, AMM found that in regions with  $0.8 < \alpha \leq 1.2$  the probability of finding supercooled water was 90 percent. In areas where  $\alpha \leq 0.8$  the probability was 20 percent.

Another supercooled water detection technique tested during the PEP experiments in Spain was a method that looked for radial velocity inhomogeneity areas (RVIA), developed by Melnichuk et al. (1983).<sup>38</sup> Their incoherent radar was able to detect zones of velocity inhomogeneities of 1.3 to  $1.6 \text{ m s}^{-1}$  over 0.5 km. These zones would be expected to correspond to areas of convergence and hence localized updrafts. A knowledge of the thermodynamic profile would be needed in order to infer the presence of supercooled water. The Spanish tests showed that in rain forming clouds the probability of finding supercooled water contents greater than or equal to  $0.1 \text{ g m}^{-3}$  was 75 percent when located above a RVIA; this is 30 - 40 percent higher than in precipitation areas where no RVIA's were recorded.

In comparing the two techniques (Koloskov et al., 1983)<sup>39</sup>, it was found that the same general regions of precipitation were detected but

---

38. Melnichuk, Y. V., and B. P. Koloskov, 1983: The analysis of the radar data obtained during the SSP-3 and the evaluation of seedability of Class A and Class C cloud systems. Precipitation Enhancement Project, Report No. 29, PEP Site Selection Phase-3, Based on Data Acquired by Radar, World Meteorological Organization, Geneva, 29-49.

39. Koloskov, B. P., O. Massambani, C. M. Lope, and G. L. Austin, 1983: Report of joint USSR/Canada/Spain work on the radar detection of areas of supercooled liquid water. Precipitation Enhancement Project, Report No. 29, PEP Site Selection Phase-3, Based on Data Acquired by Radar, World Meteorological Organization, Geneva, 49-57.

that the alpha model tested better against the aircraft data. It is also expected that the alpha model will not be sensitive to the aspect angle, as is the RVIA technique. For these reasons the alpha model was selected for implementation.

### 3. Implementation

Based on the alpha model of AMM, a potential icing product was developed. The results of the alpha model are displayed on a Chromatics 7900 color graphics terminal. The display provides a quick and easy way for the evaluation of the current threat of icing.

The data processing is performed on a P-E 3242 computer and follows the basic outline described by AMM. A flowchart of the software is given in Fig. 43 and a description of the individual program modules is given in Table 10. The algorithm requires the user to input the estimated height of the 0° C isotherm. CAPPI maps with a resolution of 2 X 2 km square are then constructed for the input height and a level 2 km above. For each grid square an alpha value is computed assuming that an echo exists at both levels and a Vertical Profile Indicator (VPI) map is constructed on the color terminal. Map regions where  $0.8 < \alpha \leq 1.2$ , representing potential icing hazard areas, and those where  $\alpha \leq 0.8$ , which represent bright band regions and hence non-icing regions, are distinguished as separate regions.

Augmenting the VPI map, two radially oriented vertical cross sections of reflectivity are selected by the user and then constructed and displayed concurrently above and to one side of the VPI map. These are included to give the user more information concerning the reflectivity structure throughout the precipitation system. The user specifies the two axes that cross the radar site for the cross sections. The cross sections are then constructed with the radial beams that are oriented along the particular axis. The data are converted to horizontal and vertical (x,z) coordinates and averaged to produce 0.5 km vertical and 2.0 km horizontal resolution. The reflectivity is plotted in contour increments of 2 dBz.

The software was tested with data collected during the Boston Area NEXRAD Demonstration (BAND) program. One problem arose due to the fact that while the radar beam width is one degree, the elevation steps used during volume scans were greater than one degree. This resulted in data gaps in the CAPPI maps which consequently caused gaps in the VPI map. When

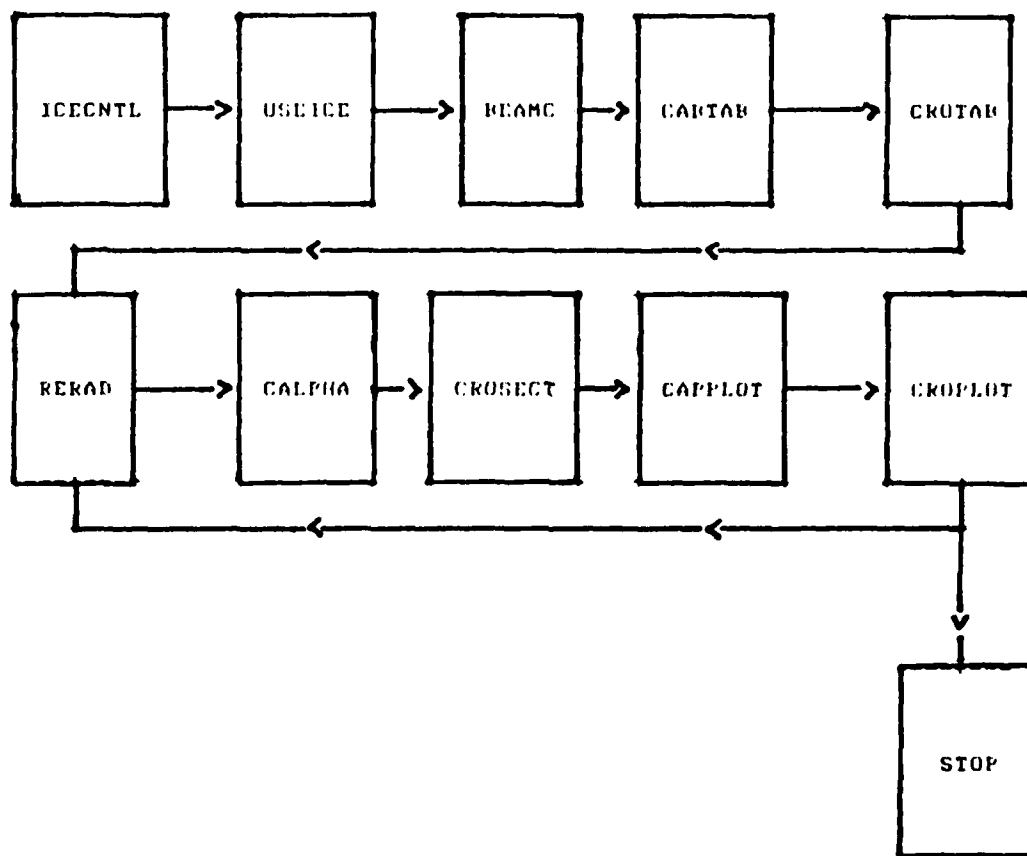


Fig. 43. Flowchart of Subroutines Used to Produce the Icing Hazards Display

data from one or both heights were missing, no alpha value could be computed. Algorithm users will obtain best results when one degree elevation steps are used when processing the volume.

TABLE 10. ICING DISPLAY SUBROUTINE DESCRIPTION

icecntl	-	controlling program, calls all the subroutines
useice	-	asks the user for the elevation angles of the volume scan, estimated zero degree isotherm height, and axes for cross section plots
beamc		computes the upper and lower height boundaries of the radar beam for each elevation angle
captab	-	sets up tables of the particular range cells and elevation angles corresponding to 2 x 2 km grid boxes for the CAPPI maps
crosec	-	sets up tables of the elevation angles and range cells corresponding to 0.5 vertical by 2 km horizontal grid boxes for the reflectivity cross sections
rerad	-	reads in the radar data radial by radial
calpha	-	forms reflectivity cross sections
caplot	-	plots the VPI map at the graphics terminal
croplot	-	plots the reflectivity cross sections

#### 4. Sensitivity Tests

Since the algorithm requires reflectivities at the height of the 0° C isotherm it was important to determine how sensitive the algorithm is to the input heights for the 0° C isotherm. For a test case of April 6, 1984 the regional radiosondes reported the 0° C isotherm at the following heights: Portland, ME - 2.0 km; Chatham, MA - 2.5 km; and Albany, NY - 2.7 km. VPI maps are reproduced in Fig. 44. It is evident that there is little

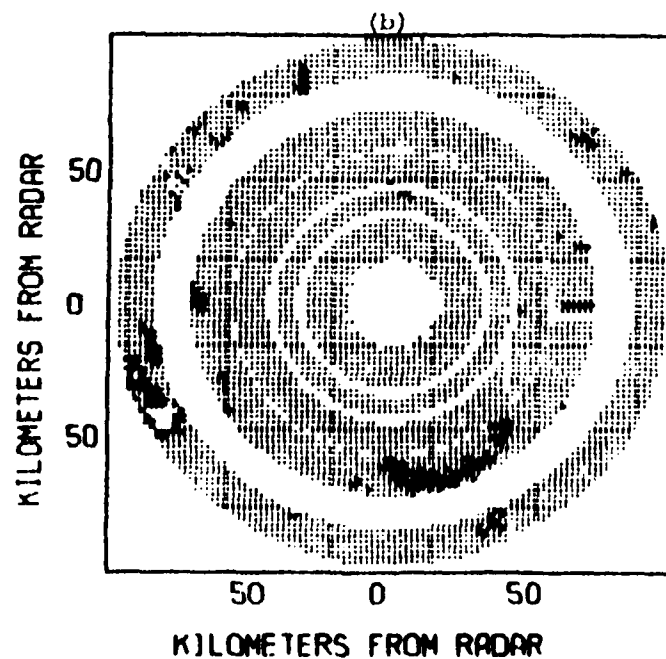
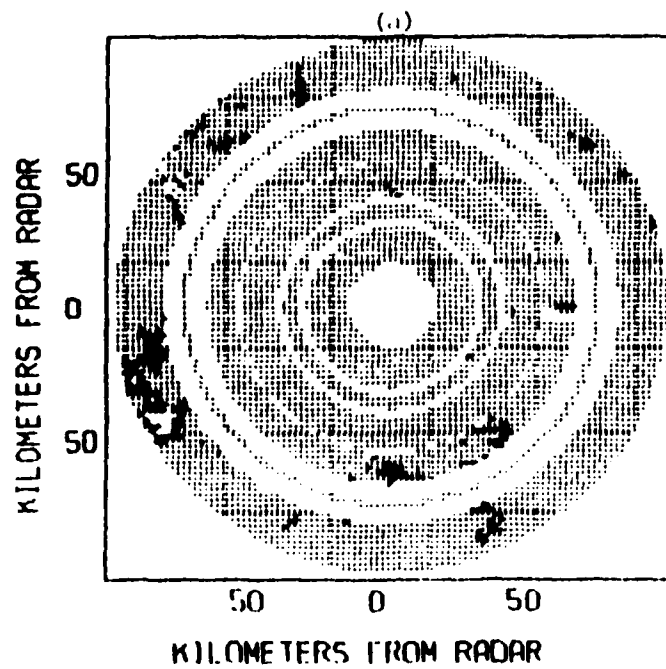


Fig. 44 a-b. Vertical Profile Indicator (VPI) Maps for 1435 LST April 6, 1985 Using (a) 2.1 km and (b) 2.3 km Estimated Heights of 0°C Isotherm

Dark shaded areas depict potential icing regions. Light hatched areas depict regions where data density is sufficient for model calculations and no icing is anticipated. Clear areas depict data sparse regions.



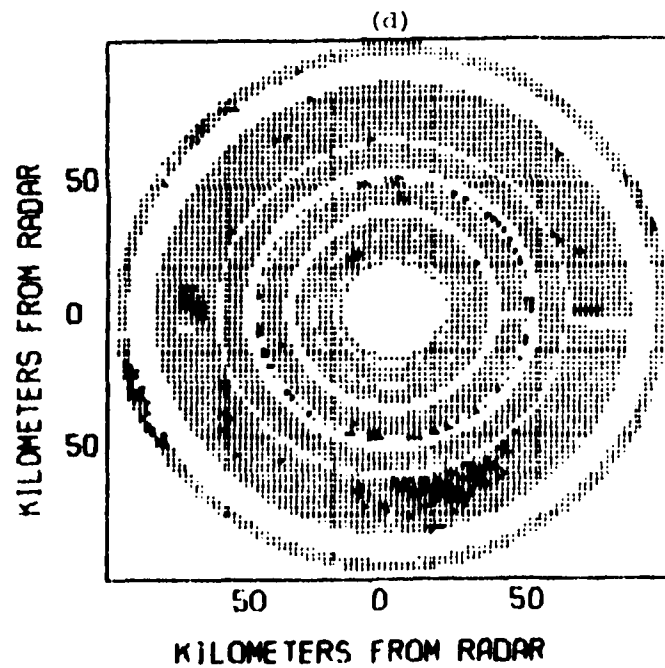
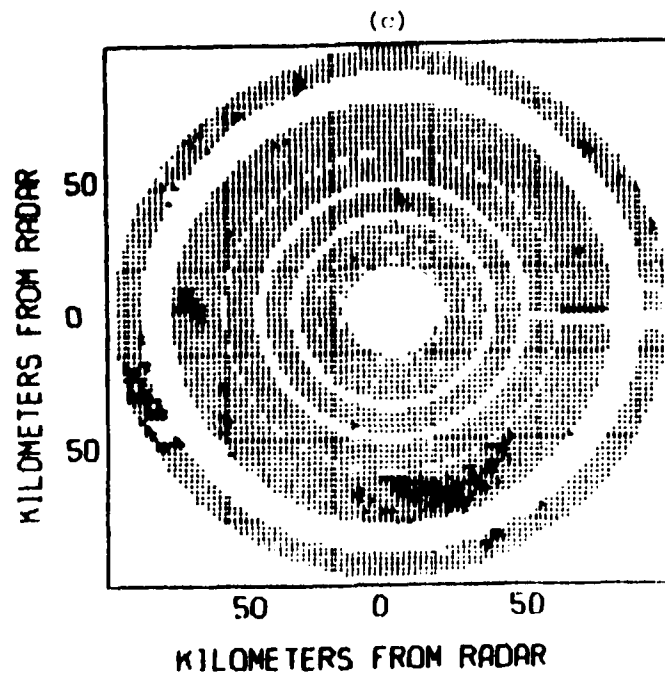


Fig. 44 c-d. Same as Fig. 44 a-b except Using (c) 2.5 km and (d) 2.7 km Estimated Heights

difference in the demarkation of the areas where icing is projected. This is not surprising given the limited vertical resolution of the volume scan. The resolution ranges from 0.349 km at 20 km distance from the radar to 1.745 km at 100 km. This is important given the temporal and spatial limitations of the radiosonde soundings and the fact that the 0° C isotherm height would not be expected to be constant throughout the radar scan area.

## 5. Conclusion

A potential icing hazards display has been implemented. Based on an algorithm developed by AMM, it uses reflectivity gradients to provide real time detection of icing regions in precipitation. A display of the results is generated on a color graphics terminal that provides quick and easy to use information. Additional information regarding the reflectivity profile is available in the reflectivity cross sections that are also plotted in the display.

## E. Severe Storm Indicators

### 1. Introduction

Mesocyclones are circulations often observed within severe thunderstorms, particularly within those that produce tornadoes. About half of the observed mesocyclones have accompanying tornadoes and are initially observed an average of 20 minutes before tornado touchdown. These circulations originate in the upper mid-troposphere and build upward and downward with time (Burgess *et al.*, 1982).<sup>40</sup> Near the time of tornado genesis the vertical component of the vorticity strengthens in the lower troposphere (Lemon and Doswell, 1979;<sup>41</sup> Rotunno and Klemp, 1985,<sup>42</sup>)

---

40. Burgess, D. W., V. T. Wood, and R. A. Brown, 1982: Mesocyclone evolution statistics. Preprints, 12th Conference on Severe Local Storms, San Antonio; AMS, Boston, 422-424.

41. Lemon, L. R., and C. A. Doswell, III, 1979: Severe thunderstorm evolution and mesoscale structure as related to tornado genesis. Mon. Wea. Rev., 107, 1184-1197.

42. Rotunno, R., and J. Klemp, 1985: On the rotation and propagation of simulated supercell thunderstorms. J. Atmos. Sci., 42, 271-292.

which is manifested in a corresponding strengthening of the mesocyclone. Also, recent observations by Wieler and Donaldson (1983)<sup>43</sup> suggest that tornado development may be related to mesocyclone strength. It would therefore appear that the development of techniques to monitor the development of mesocyclones might well prove valuable in exploring the relationship of the lifecycle of mesocyclones and tornado development. This is the thrust of the effort being reported here.

## 2. Automatic Mesocyclone Detection

The Mesocyclone Tornado vortex signature Detection Algorithm (MTDA) (Wieler and Donaldson, 1983) was developed for real time automatic identification of rotating features on the meso-gamma scale. The algorithm was tested on five severe thunderstorms where it successfully detected severe weather features existing in the Doppler velocity field (Wieler, 1986).<sup>44</sup>

The MTDA is based on the detection and compilation of pattern vectors; that is, azimuthally oriented vectors delineating regions along a radial where the shear does not change sign and where the shear and velocity differences across the mesocyclone satisfy certain criteria (Hennington and Burgess, 1981).<sup>45</sup> These criteria for vector acceptance as a pattern vector are that the velocity difference across the vector be at least  $15 \text{ m s}^{-1}$  and that the shear be at least  $0.005 \text{ s}^{-1}$ . However, it has been found that this shear threshold prevents accurate assimilation of mesocyclone features at many levels of the atmosphere. The shear threshold was subsequently reduced to  $0.002 \text{ s}^{-1}$  and this appears to have solved the problem.

---

43. Wieler, J. G., and R. J. Donaldson, Jr., 1983: Mesocyclone detection and classification algorithm. Preprints, 13th Conference on Severe Local Storms, Tulsa; AMS, Boston, 3-6.

44. Wieler, J. G., 1986: Real-time automated detection of mesocyclones and tornado vortex signatures. Accepted for publication in J. Atmos. Oceanic Technol.

45. Hennington, L. D., and D. W. Burgess, 1981: Automatic recognition of mesocyclones from single Doppler radar data. Preprints, 20th Conference on Radar Meteorology, Boston; AMS, Boston, 704-706.

In the software implementing of the MTDA there is a problem with pattern vector construction. Pattern vectors produced in the MTDA do not represent actual azimuthal shears of the Doppler field. More work is needed to correct this.

Zrnic et al. (1982)<sup>46</sup> show that when certain thresholds and correlation criteria are applied, these pattern vectors can be organized into identifiable mesocyclone signatures and Tornadic Vortex Signatures (TVS). The objective of the MTDA is to use this organizational technique to consolidate automatically pattern vectors from each elevation scan into two-dimensional features, and then to combine appropriate two-dimensional features from different elevation scans into three-dimensional features. Substantial problems existed with the original MTDA in this regard. Among these consolidation difficulties were the inability to resolve multiple two-dimensional features with the same rotation direction, and the tendency to produce gross inaccuracies when joining two-dimensional features from multiple elevation scans into three-dimensional features. These problems have been solved through fine tuning of thresholds and the development of a three-dimensional consolidation method that screens two-dimensional features according to their rotational energy and combines these two-dimensional features according to their relative shear and horizontal separation. The mesocyclones and TVS's detected by the algorithm are in good qualitative agreement with those detected through visual analysis. Eventual corrections to the method for pattern vector construction should result in a reliable detection tool.

### 3. Mesocyclone Discriminators

Given the capability to detect mesocyclones, the next step is to examine their temporal and spatial characteristics to determine if there is a way of estimating subsequent tornado development. Work has focussed on mesocyclone strength. Two potential discriminators of mesocyclone strength that have been investigated are Excess Rotational Kinetic Energy (ERKE) and Excess Rotational Power (ERP), defined as

---

46. Zrnic, D. S., L. D. Hennington, and J. Skelton, 1982: Automatic Recognition of Mesocyclones from Single Doppler Radar Data. AFGL-TR-82-0291, NOAA, National Severe Storms Laboratory, Norman, OK, ADA125854.

$$ERKE = \zeta \Delta h \pi r^2 (V_r - r S_m)^2 / 4$$

$$ERP = \zeta \Delta h \pi r (V_r - r S_m)^3 / 4$$

where  $\zeta$  is the air density at height  $h$ ,  $V_r$  is the rotational velocity coinciding with the mesocyclone's radius  $r$ , and  $S_m$  is an arbitrary shear threshold defining mesocyclonic rotation.

These equations represent rotational kinetic energy and rotational power in excess of the minimum energy and power required to identify a feature as a mesocyclone. Because of dependence on size these minima are highly variable among mesocyclones but are contingent upon a constant critical shear across a mesocyclone. Donaldson (1970)<sup>47</sup> proposed and Burgess (1976)<sup>48</sup> confirmed that a rotational shear of about  $0.005 \text{ s}^{-1}$  was required for mesocyclone detection. This value has been used for the present study. A threshold of this magnitude allows for the early detection of rotation preceding tornado formation while eliminating spurious phenomena such as slowly rotating couplets typically observed in severe as well as non-severe storms. In an attempt to standardize, all magnitudes of mesocyclone ERKE and ERP are compared to those for a Climatologically Mature Mesocyclone (CMM) located in the lower troposphere (Burgess *et al.*, 1982). A CMM represents an average mesocyclone in its strongest stage of development and is characterized by a diameter of 5.5 km and a tangential velocity of  $23.3 \text{ m s}^{-1}$ , with corresponding ERKE and ERP per unit vertical thickness of approximately  $5.4 \times 10^8 \text{ joules m}^{-1}$  and  $1.8 \times 10^6 \text{ watts m}^{-1}$  respectively.

For a more detailed discussion of the analysis criteria and energy parameterization the reader is referred to Donaldson and Desrochers (1985).<sup>49</sup>

---

47. Donaldson, R. J., Jr., 1970: Vortex signature recognition by a Doppler radar. *J. Appl. Meteor.*, 9, 661-670.

48. Burgess, D. W., 1976: Single Doppler radar vortex recognition, Part 1, mesoscale signatures. *Preprints*, 17th Conference on Radar Meteorology, Seattle; AMS, Boston, 97-103.

49. Donaldson, R. J., Jr., and P. R. Desrochers, 1985: Doppler radar estimates of the rotational kinetic energy of mesocyclones. *Preprints*, 14th Conference on Severe Local Storms, Indianapolis; AMS, Boston, 52-55.

#### 4. Analysis

So far in this study ten complete mesocyclone histories have been examined with their rotational characteristics determined through manual analysis. The objective is to determine the usefulness of one or more aspects of mesocyclone energy to predict more accurately which mesocyclones are likely to produce tornadoes and what degree of tornadic severity is likely to result.

The most severe tornadic mesocyclone examined was that associated with the April 30, 1978 Piedmont, OK storm. This storm dropped 2 1/2-in hail and produced a number of tornadoes, including an F 4 maxi-tornado that devastated 25 homes in and around Piedmont. Fig. 45 depicts the lifetime of the storm in terms of the maximum ERKE. The ERKE height is a mean height that is weighted linearly with respect to the ERKE magnitude and in most cases represents the level where ERKE is concentrated. The profile for ERP is very similar to that of ERKE and is not presented.

When first detected the maximum ERKE of the mesocyclone was less than 1/10 that of a CMM. Volume scan analysis showed this energy to be concentrated at about 9 km. This agrees with the findings of Burgess *et al.* (1982) for the location of initial mesocyclone detection. As the mesocyclone developed, its mean height, as evident in the lower plot of Fig. 45, descended on average while the magnitude of the ERKE increased, eventually exceeding that of the CMM at 1726. The mean height of the ERKE continued to descend until 1810 when it reached its minimum of 0.9 km. During this period and the ensuing period until mesocyclone dissipation the ERKE underwent minor fluctuations but remained on average three times that of the CMM.

The first tornado occurred about 15 minutes after the ERKE ratio exceeded unity and about the time the mean height passed through the 5 km level. This tornado was essentially a dust swirl at the ground with F-1 intensity as reported by an NSSL chase team (Burgess *et al.*, 1979).<sup>50</sup> Three small tornadoes developed at about 1800 producing up to F-2 damage as

---

50. Burgess, D. W., and JDOP Staff, 1979: Final Report on the Joint Doppler Operational Project (JDOP) 1976 - 1978. NOAA Technical Memorandum, KRL NSSL. 86.

PIEDMONT - 30 APRIL 1978

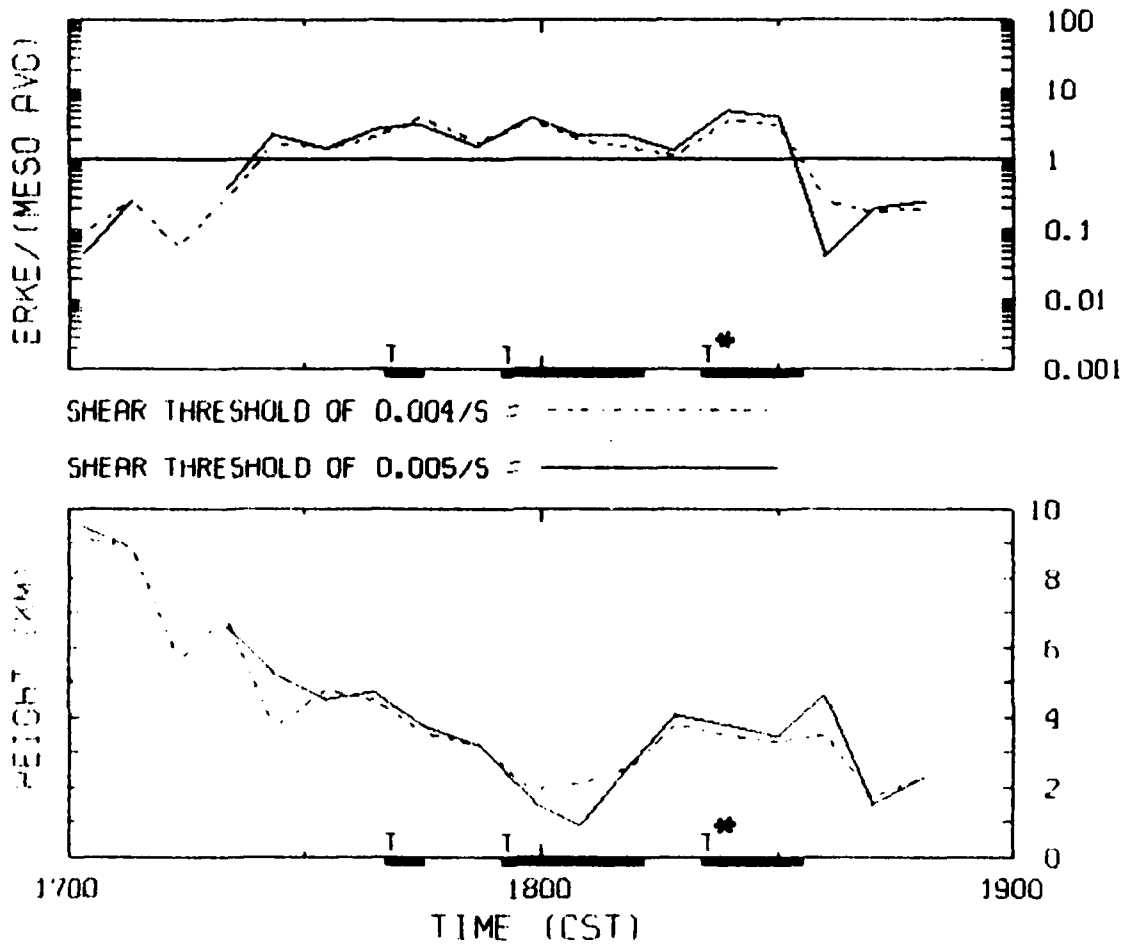


Fig. 45. Lifetime of Piedmont, OK Mesocyclone as Depicted Through The Weighted Mean Height of ERKE (lower diagram) and the Ratio of Maximum ERKE to that of a Climatologically Mature Mesocyclone (upper diagram)

ERKE was computed according to the shear thresholds indicated. Mini- and maxi-tornado touchdown times are indicated by T and T\* respectively. Thick bars correspond to tornado duration.

the mean height of the ERKE descended to 2 km. A rise in the mean height of the ERKE is then noted as the mesocyclone became revitalized aloft. Within minutes, the maxi-tornado formed. It should be noted that the mean height of the ERKE remained in the lower troposphere (below 5 km) during this time.

The mesocyclone history for a non-tornadic storm that occurred in Oklahoma on April 29, 1978 is shown in Fig. 46. This storm produced 2 1/2-in hail and a funnel cloud over Ada, OK. Comparison of the ERKE profiles of this storm and the Piedmont storm reveals some obvious differences. The ERKE for the mesocyclone of the Ada storm when first detected is similar to that of the Piedmont. However, the mean height of ERKE appears more erratic for the Ada storm, suggesting less overall organization. The magnitude of ERKE is generally less than that of the CMM and except for a brief incursion the mean height of ERKE never settled into the lower troposphere (below 5 km).

The Rush Springs, OK storm of May 20, 1977, depicted in Fig. 47, produced a mesocyclone that developed in the mid-troposphere. The mean height of the ERKE quickly descended below 5 km, although ERKE magnitudes remained small relative to the CMM and no tornadoes were produced by the storm. However, a funnel cloud and 2-in hail were reported.

These three storms point to a relationship between mesocyclone ERKE and tornado development. Two criteria appear always to have been met before tornadoes touched down; namely, the magnitude of mesocyclonic ERKE must be at least comparable to that of the Burgess CMM, and the mean height of the ERKE must be at or below 5 km. On the basis of the sample of ten mesocyclones, unless these conditions were met no tornado followed.

These criteria are evaluated below.

## 5. Evaluation

The utility of the two criteria in estimating tornado development was determined in an operational sense. The Critical Success Index (CSI) (Donaldson *et al.*, 1975<sup>51</sup>) of the method was calculated according to the standard form

51. Donaldson, R. J., Jr., R. M. Dyer, and M. J. Kraus, 1975: An objective evaluator of techniques for predicting severe weather events. *Preprints*, 9th Conference on Severe Local Storms, Boston; AMS, Boston, 321-326.



ADA - 29 APRIL 1978

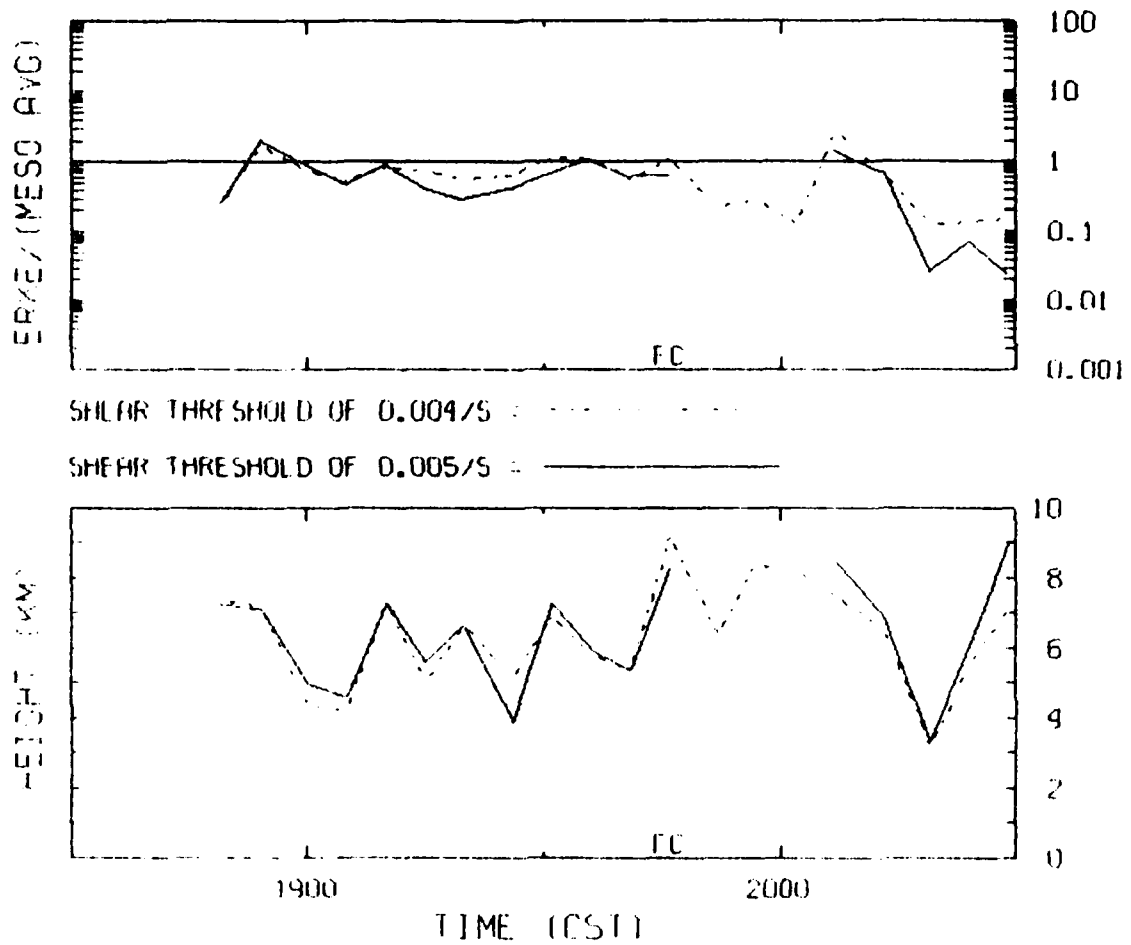


Fig. 46. As in Fig. 45 but for Ada, OK Mesocyclone  
Funnel cloud observation time indicated by FC.

RUSH SPRINGS 20 MAY 1977

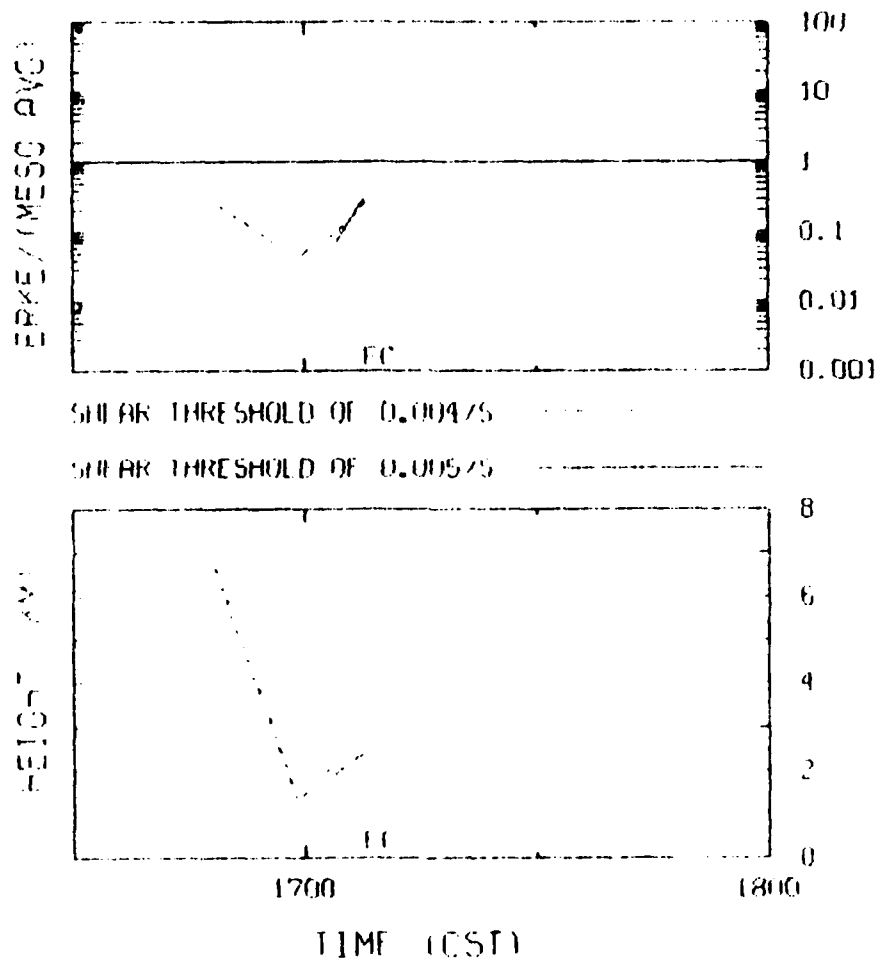


Fig. 47. As in Fig. 45 but for Rush Springs, OK Mesocyclone  
 Funnel cloud observation time indicated by FC.

$$CSI = H / (H + F + M)$$

where for this study H (hit) represented the successful prediction of a tornadic event, F (false alarm) represented prediction of a tornado that did not occur, and M (miss) represented tornado formation that went undetected by the method. The parameter critical to the threshold for height was changed from the weighted mean height of ERKE to the actual height of the maximum ERKE to facilitate analysis. Thresholds were adjusted for the criteria of magnitude and height of ERKE in order to optimize mesocyclone detection. A maximum magnitude of the ERKE of at least 400 megajoules per meter ( $MJ m^{-1}$ ) with the stipulation that this energy exist at or below a level of 5 km was used to discriminate for tornadic mesocyclones. This value is about two-thirds that of the CMM.

This method with these thresholds was applied to ten mesocyclone cases, some tornadic, some not. The resulting CSI was 0.67, a value somewhat better than simply using the climatology of the data set since only half of the mesocyclones were tornadic.

In addition, a threshold of  $1080 MJ m^{-1}$  (twice the energy of the CMM) was used as a predictor of maxi-tornadoes. Analysis of the same mesocyclone cases produced a CSI for maxi-tornado prediction of 0.64. Only one maxi-tornado is contained in the sample but the ability to predict it is over six times the climatological probability of the sample. This is considered very encouraging, although the sample was small.

Closer examination of the energy threshold criterion for tornado development reveals that tornado severity may be related to mesocyclone strength. Table 11 presents the maximum mesocyclone strength that occurred before each tornado. Generally, the tornadic strength appears to be somewhat proportional to the associated magnitude of ERKE and ERP, especially for the stronger tornadoes. For example, the Piedmont maxi-tornado was associated with the strongest mesocyclone in the entire sample, with maximum magnitudes of ERKE and ERP 4.1 and 13.0 times that of the CMM, respectively. However, for the less severe tornadoes this relationship is not as well defined. Consider, for example, that the Piedmont F-1 tornado was associated with a larger relative magnitude of ERKE and ERP than were the Fort Cobb and Del City F-2 tornadoes, suggesting that the ERKE and ERP are not that accurate in discriminating small differences

TABLE 11. TORNADIC MESOCYCLONES

Mesocyclone Name and Date	Tornado	Tornado Severity	Magnitude	
			ERP	ERKE
Foster - 5/19/77	*	F-1	0.5	0.8
	Foster	F-2	4.0	3.0
	White Bead	F-2	4.0	3.0
Fort Cobb - 5/20/77	Fort Cobb	F-2	0.6	0.6
	Binger	F-2	11.0	2.4
Del City - 5/20/77	Del City	F-2	3.0	1.5
Arcadia - 5/20/77	Arcadia	F-3	7.5	3.5
Piedmont - 4/30/78	*	F-1	6.0	2.0
	*	F-2	12.0	3.0
	Piedmont	F-4	13.0	4.1

\* indicates no identifying name given to tornado

in tornado intensity. Also, the method may not accurately predict the intensity of all tornadoes produced by a single mesocyclone. These qualifications aside it appears that there is considerable promise of distinguishing which storms will produce severe tornadoes from those that will not.

Selection of ERKE or ERP for an optimum forecast is quite difficult from the present very limited data set. ERP is more sensitive to shear than ERKE and as a result is more responsive to mesocyclone intensification. Examination of Table 11 also indicates that ERP appears to be more sensitive to tornado types than ERKE. ERP in this sense would appear to be superior to ERKE. The only exception in this sample to this statement is the Binger tornado, which caused only F-2 damage but had a large ERP of 11.0. This is many times larger than that of any of the other F-2 tornadoes in the sample and also larger than the ERP magnitude associated with the F 3 Arcadia tornado. A plausible explanation is not apparent when it is noted that the magnitude of ERKE for the Binger tornado was in close agreement with other F 2 tornadoes and was much less than that of Arcadia.

## 6. Summary

Although the method may not be able to discriminate among all six categories of tornado severity, in the current data set it does discriminate violent tornadoes from their less intense counterparts. Violent tornadoes account for only about eight percent of the population of tornadoes but are responsible for most tornado-related deaths (Colquhoun, 1985).<sup>52</sup> Fortunately, the associated strong mesocyclones appear to take a long time to develop and therefore offer considerable warning potential.

During the next year efforts will continue to examine mesocyclone energy.

### F. Turbulence Algorithm Implementation

A turbulence algorithm developed by AFGL/LYR personnel (Bohne, 1981)<sup>53</sup> and proposed for the NEXRAD program was implemented as part of the Modular Radar Analysis Software System (MRAS) (Forsyth et al., 1981).<sup>54</sup> The algorithm itself provides intensity estimates of turbulence in terms of the generally accepted parameter  $\epsilon^{1/3}$ , where  $\epsilon$  is the eddy dissipation rate. This information is computed from Doppler radar spectral width data and a given estimate of the turbulence outer scale length.

User input of the outer scale estimate is read into the system before processing of data begins. In addition, the user may also specify the number of range gates to be averaged together and a minimum threshold power in dB for the processing of the spectral width data. These parameters are kept in the WEA.PAR file of MRAS and can be changed using the LISPAR command. As a prelude to actually reading in data, appropriate tables are

52. Colquhoun, J. R., and D. J. Shephard, 1985: The relationship between tornado intensity and the environment of its parent severe thunderstorm. Preprints, 14th Conference on Severe Local Storms, Indianapolis; AMS, Boston, 1-4.

53. Bohne, A. R., 1981: Estimation of turbulence severity in precipitation environments by radar. Preprints, 20th Conference on Radar Meteorology, Boston; AMS, Boston, 446-453.

54. Forsyth, D. E., C. Bjerkaas, and P. Petrocchi, 1981: Modular radar analysis software system (MRAS). Preprints, 20th Conference on Radar Meteorology, Boston; AMS, Boston, 696-699.

created to ease the computational effort necessary during processing. As each radial is processed, values of the spectral width are read and averaged over the number of user specified range gates. From the spectral width data, values of  $c^{1/3}$  are calculated and written to disk. At the end of the volume scan the values are given bin values of 0, 1, or 2 corresponding respectively to none, moderate, or severe turbulence. The values of  $c^{1/3}$  at which levels of turbulence are categorized are

$$\text{None} \quad c^{1/3} < 3.5 \text{ cm}^{2/3} \text{ s}^{-1}$$

$$\text{Moderate} - 3.5 \text{ cm}^{2/3} \text{ s}^{-1} \leq c^{1/3} < 5.2 \text{ cm}^{2/3} \text{ s}^{-1}$$

$$\text{Severe} - c^{1/3} \geq 5.2 \text{ cm}^{2/3} \text{ s}^{-1}$$

These turbulence intensity estimates are then written to disk in a form addressable by the turbulence plotting program.

The turbulence display can be retrieved by the color graphics terminal used for the MRAS displays any time after the first volume has been completely processed. The display is called up by typing "E AAA, RRR" at the graphics terminal, where AAA and RRR are the azimuth and range respectively from the radar site at which the user wishes to center the display. The display is a pseudo three dimensional plot. Contours of turbulence severity are plotted on a 100 X 100 km horizontal projection for the lowest nine elevation angles with a separate contour map plotted at each level of constant elevation angle.

The completion of this task now gives AFGL/LYR the capability of plotting turbulence severity estimates in real time as part of its overall radar processing capabilities.

## V. SATELLITE METEOROLOGY

### A. Microprocessor-Based Satellite Data Ingest System

#### 1. Introduction

Under a contractual agreement between the National Oceanic and Atmospheric Administration and AFGL, a redundant data path in the AFGL GOES mode A ground station is being made available to a consortium of users known as the Northeast Area Remote Sensing System (NEARSS). Included in the agreement is a requirement to develop a central processing facility to ingest, store, and transmit over a dedicated communications line subsets of the GOES imagery transmission. To that end, an Intel 8086-based microprocessor with fixed disk mass storage was purchased and assembled. AFGL scientists developed software to handle configuration of the central processor. SASC participated in various phases of the software system specification and development, including database design and management, automated scheduling of the ingest/store/transmit cycle, and terminal command processing (see Gerlach, 1983).

Subsequently SASC and AFGL completed testing of developed applications software configured under the iRMX 86 operating system, specified the NEARSS communication network format, developed a communication network manager, and developed system software for hardware component configuration and integration (see Gerlach, 1984).

This section details the work completed by SASC, including communications testing and broadcast of imagery data over a dedicated line, configuration of the Offline Data Ingest System (ODIS) as the input source of GOES mode A data, development of software for real time ingest, data transmission, exception handling, and real time clock capability, and integration of previously developed software.

#### 2. Communications Testing

The Zendex Z-86 single board computer (SBC) was originally chosen over the Intel 86/30 SBC as the target computer to take advantage of its more flexible design, including its ability to support two serial ports for terminal and network communications. However, unsuccessful attempts to load and execute the preconfigured iRMX 86 operating system rendered the system unusable when configured with this SBC. Hardware support from Zendex

Corporation to correct problems with the product proved inadequate. Consequently, AFGL decided to design and build a custom communications board configured with an 8251A Universal Synchronous Asynchronous Receiver Transmitter (USART) to handle network communications and replace the Z-86 with the Intel 86/30 SBC.

Initial non-coordinated synchronous communications testing over the carrier line was conducted using software to poll the status register of the USART to determine the condition of receive and transmit ready signals. Micom Micro 4000 data modems located at AFGL and the Massachusetts Institute of Technology (MIT) were programmed in digital loopback to simulate a point-to-point network for testing modem functions and line transmission of data from a single source. Data received back at AFGL were stored in system memory and examined with utilities from the ISBC 957B IAPX 86, 88 Interface and Execution Package. Software time delays were later inserted to test the USART's ability to fill gaps in the line transmission with programmed sync characters.

Coordinated synchronous communications testing between AFGL and MIT incorporated polling software under iRMK 86 to output automatically a string burst containing the ASCII alphabet once every 60 seconds. At MIT the data were ingested, examined, interactively redirected back through the line, and output to the console CRT at AFGL.

The addition of an 8259A Programmable Interrupt Controller (PIC) to the custom communications board introduced cascaded interrupt capability for USART receive and transmit ready signals. Interrupt-driven software was developed to replace software that implemented processor-intensive polling techniques to transmit and receive data. Formal communications resumed using interrupt software to transmit the NEARSS polling protocol once every ten seconds. At MIT, resident software was activated to ingest and retransmit the protocol without operator intervention. The data received back at AFGL were examined for embedded sync characters and loss of data.

### 3. ODIS Configuration

To provide NEARSS users with GOES data in a timely manner, AFGL decided to configure the ODIS as the input source of GOES mode A data for ingest. The ODIS is an interactive, microprocessor-based system that reformats the serial six and nine-bit imagery data from mode A into



computer-compatible eight-bit bytes and records the data on magnetic tape for future use. The ODIS also performs hardware averaging of data when requested. The user schedules the ingest function through commands entered on the terminal keyboard, specifying the geographical area of interest and data resolution. Scheduling can also be activated remotely from McIDAS. In configuring the ODIS, interfacing hardware was installed on the custom communications board to support the flow of control information and data redirected from the ODIS tape unit to the target system. A signal derived from the ODIS microprocessor which originally was used to signal the tape controller to initiate the write function was configured as an interrupt signal to the cascaded 8259A PIC. Software activated by the interrupt would then read bytes through an I/O port address until the required number had been ingested. Software was later developed to test this configuration and data ingested were verified with ODIS recording the same information on magnetic tape.

#### 4. Software Development

##### a. Ingest Routines

Image and navigation ingest software was developed to meet the requirement of real time acquisition of GOES mode A data. The software executes in an interrupt environment managed by iRMK 86 to handle data transfers from the ODIS.

Prior to ingest of imagery data the ODIS transmits a header record containing information describing the image block that follows. The information is used by the ingest software to initialize variables that are accessed to monitor the ingest. Included in the header record is a mode number that indicates the data resolution chosen (see Table 12) and a code that defines the horizontal width of the image block in bytes (see Table 13).

As indicated in Table 12, the ODIS imposes certain restrictions on the east west coverage of data depending on the resolution (mode) chosen. These restrictions are due to the relative time involved to write data to the magnetic tape drive, which is the storage device originally configured for the ODIS. However, all modes of operation can be ingested for the entire scan of the earth disk (north-south coverage). In addition to the modes listed, 8 km resolution data are available to the

TABLE 12. MODE DESCRIPTION

<u>Mode</u>	<u>Data Types</u>	<u>Resolution</u>	<u>Sector West-East Line Length Limits (bytes)</u>
0	infrared only	2 mi	383 to 3711
1	visible	1 mi	509 to 2048
	infrared	2 mi	383 to 3711
2	visible	2 mi	509 to 3837
	infrared	2 mi	383 to 3711
3	visible	3 mi	509 to 3837
	infrared	2 mi	383 to 3711
4	visible only	1/2 mi	1008, fixed length

NEARSS users as data ingested at 4 km resolution and then sampled digitally in software to degrade the image to the 8 km resolution. Following the header record, infrared and visible data blocks are ingested, aligned, and written to pre-mapped sectors within the designated disk file selected from the rotating archive. Although it is the ODIS that is programmed to provide satellite data as input to the target system, the ingest software stores information describing each image from the event file. The software will verify at the time of ingest that the ODIS has been programmed properly to provide imagery data as specified in the event file.

Navigation ingest software was developed to provide NEARSS users with orbit and attitude information necessary to earth-locate image data. The navigation ingest immediately follows image ingest, buffering 20 scan lines required to collect the entire orbit and attitude information block subcommutated within the infrared documentation. The additional scan lines are provided by programming the ODIS to sectorize an area large enough to include the image block and scan lines for navigation extraction. Once collected, the information is decoded, reformatted to conform to conventions used by transformation software, and written to the appropriate disk file.

#### b. Transmission Routine

The transmission task was developed to prepare the visible and infrared data sets containing the digital area directory, navigational parameters, and image data for broadcast over the network. The software is

TABLE 13. COVERAGE CODE DESCRIPTION FOR MODE NUMBERS 0 - 3

West - East Coverage Code (hexadecimal)	Infrared (length in bytes)		Visible (length in bytes)		Data Line Length		Physical Record Length	
	Documentation Length	Data Line Length	Documentation Length	Data Line Length	Documentation Length	Data Line Length	Documentation Length	Data Line Length
2	129	383	3	512	3	509	3	512
3	129	639	3	768	3	765	3	768
4	129	895	3	1024	3	1021	3	1024
5	129	1151	3	1280	3	1277	3	1280
6	129	1407	3	1536	3	1533	3	1536
7	129	1663	3	1792	3	1789	3	1792
8	129	1919	3	2048	3	2045	3	2048
9	129	2175	3	2304	3	2301	3	2304
A	129	2431	3	2560	3	2557	3	2560
B	129	2687	3	2816	3	2813	3	2816
C	129	2943	3	3072	3	3069	3	3072
D	129	3199	3	3328	3	3325	3	3328
E	129	3455	3	3584	3	3581	3	3584
F	129	3711	3	3840	3	3837	3	3840

activated by the scheduler routine to read each file from disk, assemble data into protocol format, calculate and insert both the error detection bytes for control and the data sections of the protocol, and transfer each protocol to low-level network transmission software to activate the broadcast.

#### c. Exception Handler

Programming errors are generally found and corrected during the debugging phase of software development. However, when software is subjected to performance evaluation, environmental errors may appear. Environmental errors result from exceptional conditions related to the environment in which the software runs rather than from the software itself. Examples would be insufficient memory to satisfy a request or an I/O error resulting from device malfunction.

To provide the NEARSS system with the ability to detect environmental errors and report them for possible human intervention, software was developed and configured under iRMK 86 as the default system exception handler. The handler is designed to trap all environmental errors relayed by the operating system and record the errors along with the date and time on log file ERRLOG. This information is also displayed on the console CRT. The log file is a rotating archive capable of holding five days of error information with a maximum of 32 entries for any one day. The contents of this file can be recalled to monitor system software performance and mass storage device behavior. Documentation of the structure of ERRLOG is provided in Appendix C.

The handler also performs an orderly shutdown of the system. This involves closing all file connections, deleting file and directory connections, and detaching online mass storage devices. Once a shutdown is completed, the handler initiates the bootstrap process under program control. A routine written in ASM86, Intel's 8086 assembler language, is called by the handler to transfer execution control to the first stage of the bootstrap loader located in ROM.

#### d. Clock/Calendar Software

Following a restart of the NEARSS system, random access memory is normally flushed of its original contents and replaced by operating-system and resident-applications locatable object code read from

disk. The only information that cannot be restored after a system restart is the internal date and time managed by the clock task and accessed by the scheduler routine. To support the need for continuous timing information, a Zendex ZBX-348 clock/calendar module was purchased and installed on the Intel 86/30 SBC. The ZBX-348 board is a battery-backed, iSBX compatible module providing time in hours, minutes, and seconds (military format); day of the week; and month, day, and year. Driver software was written and incorporated into the initializing section of the clock task to read this information after a system restart in order to update the internal date and time.

## 5. Software Integration

### a. Network Manager

The network manager and associated interrupt software to handle NEARSS protocol communications were integrated and tested. Upon startup, the basic state of the network manager is to poll user sites to determine if a site is online and/or has a request to conduct inter-user communications. User sites respond with a request or simply echo back the polling protocol to gain online status. The network manager was run to test protocol formation, transmission, reception, and logging functions using the local and remote modems in digital loopback. The network manager will currently wait one-half second to receive responses to the polling protocol. If no response is received, the software will time-out and poll the next user site on its list. This function was tested with both modems set in the normal mode of operation.

### b. Coordinate Transformation Software

McIDAS earth-satellite coordinate transformation software originally coded in FORTRAN IV for the Harris minicomputer was rewritten in FORTRAN 86 and implemented as a link ready object module library. The software is used to compute satellite starting line and element numbers based on the most recent orbit and attitude information available. The coordinates are used to define an image and determine timing for ingest activation. The software is accessed indirectly by the scheduler routine via the FORTRAN 86 system link module XFORMS. The latitude longitude center point of the requested image is passed to XFORMS which returns the satellite coordinates corresponding to the top left-hand corner of the image. It also

calculates solar zenith angle to determine if ingest of visible data is warranted.

#### 6. Summary

Synchronous communications testing over the conditioned line was conducted with MIT. The ODIS was configured as the input source of mode A data; software was written and implemented on McIDAS to automate ODIS scheduling. Software was developed, debugged, and integrated to provide real time ingest of mode A data, data transmission, exception handling, an auto-restart procedure, and continuous real time clock information. Previously developed software routines, including network manager, scheduler, clock task, and coordinate transformation software, were integrated and tested. Broadcast of the NEARSS sector on an operational basis was begun.

## Appendix C. Data File Structures Description

**File Name:** ERRLOG  
**Size:** 6 sectors (768 16-bit words)  
**Type:** All integer data  
**Purpose:** Contains system error information

<u>Sector(s)</u>	<u>Purpose</u>
0	Day and entry tables
1 - 5	Error log entries

Allocation of words in sector 0:

<u>Word(s)</u>	<u>Purpose</u>
1 - 5	Day table
6 - 10	Entries table
11 - 125	Reserved
126	Current day pointer
127	Maximum day entries (5)
128	Maximum entries per day (sector) (32)

Allocation of words in sectors 1 - 5:

<u>Word(s)</u>	<u>Purpose</u>
1 - 4	Error entry 1
5 - 8	Error entry 2
9 - 12	Error entry 3
125-128	Error entry 32

Error entry structure:

<u>Word</u>	<u>Purpose</u>
1	Greenwich time of error (hours and minutes)
2	Error code
3	Argument index indicating the parameter within the calling routine associated with the error For concurrent I/O errors it is the number of bytes requested for transfer
4	If error is not concurrent I/O, then = 0 Otherwise, it is the actual number of bytes transferred

## B. AFGL Interactive Meteorological System (AIMS)

### 1. Introduction

The AFGL man-computer interactive data access system (McIDAS) is being replaced by new computer processing and display equipment. The new system, designated the AFGL Interactive Meteorological System (AIMS), is being assembled to provide an environment for receipt, storage, processing, and interactive display of high density meteorological data, notably satellite imagery. The hardware specification and software design and implementation work performed by SASC scientists in support of the AIMS development is described in this section.

### 2. System Overview

Fig. 48 is a schematic representation of the hardware elements in the new system. The system design specification (Reifenstein and Ali, 1985)<sup>55</sup> calls for a system of distributed processors, each functionally unique, linked by a local area network (LAN). To date the system has been divided into three functional areas.

#### a. Batch Processing

Although emphasis is on interactive data analysis, certain procedures do not lend themselves to an interactive environment. These procedures make heavy demands on system resources and would tend to degrade system performance for interactive users to an unacceptable level. A VAX 11/750 computer was selected as the general purpose, batch processing node. Functionally this node must accommodate large processes such as the AFGL RDNEPH cloud analysis or the SSM/I environmental parameter extraction routines. Additionally system wide database management and network communications are performed here. The 11/750 has two large 450 Mbyte disks, two multi-density tape drives and 24 asynchronous communication ports.

---

55. Reifenstein, E. C., and A. D. Ali, 1985: Meteorological Data Acquisition, Management, and Processing System for Air Force Geophysics Laboratory Satellite Meteorology Branch, System Specification. Subcontractor report by Technology Systems, Inc., for Systems and Applied Sciences Corporation.



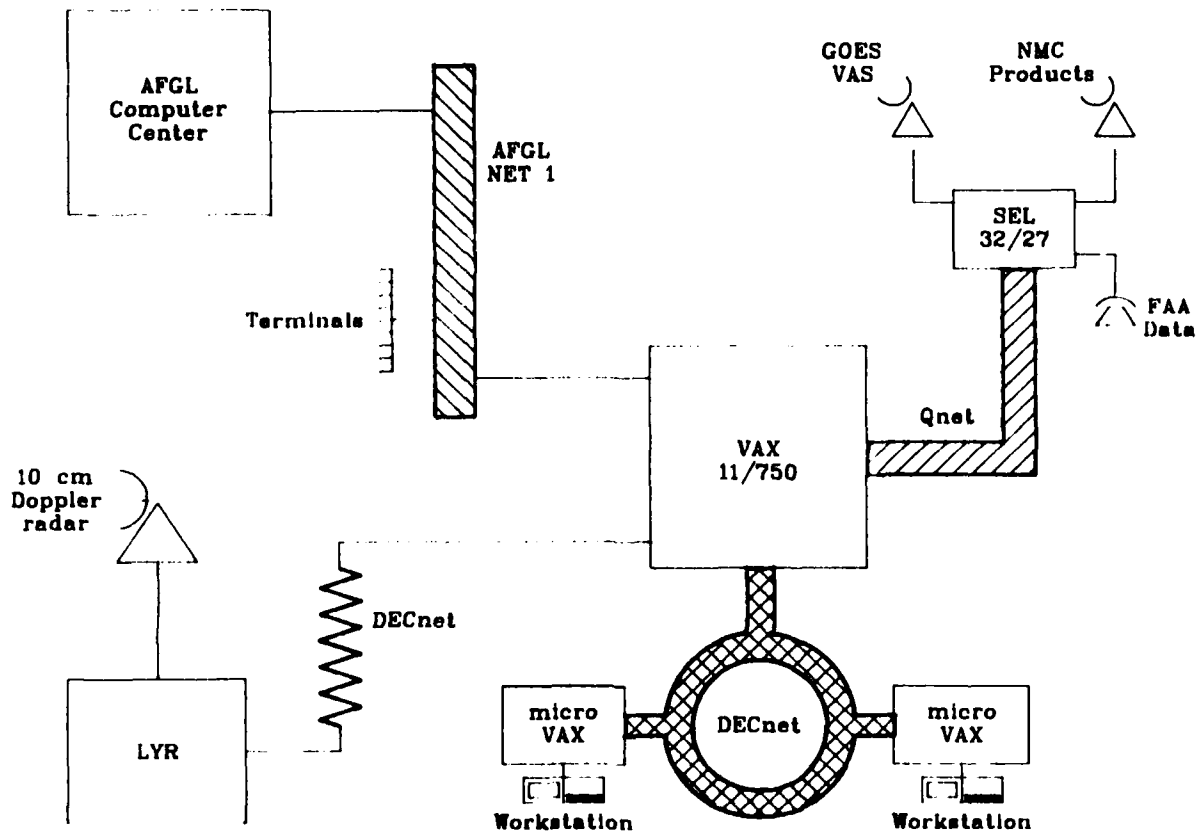


Fig. 48. Hardware Components of the ATMS

#### b. Real Time Data Ingest

Meteorological data are entered into the system in two forms, either on magnetic tape or directly via a communications link. Data received directly must be handled in real time through an interrupt driven process. Currently real time data consist of GOES VISSR mode A data received directly from the satellite in stretched format and standard meteorological observations for the U.S., Canada, and Mexico received over a telephone line. Plans call for both of these services to be upgraded in AIMS. In the latter half of 1986 GOES will change from mode A to mode AAA which will provide VAS sounding data in addition to the visible and thermal IR channels. The standard observations (e.g., surface reports and balloon soundings) for North America will be supplemented by global observations and gridded NMC forecast model products received via a satellite communications link. A Gould SEL 32/27 minicomputer will serve as the real time ingest processor.

#### c. Image Processing Workstations

Interactive satellite image processing and graphical analysis take place at two workstation configurations. Each workstation consists of a high/low resolution color monitor, a graphics terminal, and a graphics tablet. The monitors are driven by two ADAGE 3000 frame buffers with onboard bit slice processors, 32 Kbytes RAM for microcode storage, and four Mbytes of video RAM. Workstation hosts are projected to be microVAX II microcomputers with three Mbytes memory and large (> 450 Mbytes) mass storage devices.

Plans include separate high resolution graphics only workstations for interactive applications that call for graphical display without imagery. Graphics workstations would consist of stand alone units capable of a minimum of 1024 X 1024 X 4 bits display resolution, with onboard graphics processor, display list support, and VT100 emulation. In order to provide a standard graphics library for the various display devices around the system, a commercial device independent graphics software package is being investigated.

### 3. Implementation Plan

Implementation of the system design is proceeding according to the requirements of the layered software approach outlined in the design

specification (Reifenstein and Ali, 1985). Low level routines (i.e., most machine dependent) will be completely implemented before the next higher layer of software is started. From this outline, a three phase implementation plan has been developed.

Phase I consists of the development of a set of tools designed to aid in the development of software. These tools include routines to compile, link, and manage object libraries in an identical manner across all computers in the system. Additionally several libraries of software development utilities have been built for use in applications programs. These libraries include console management routines, terminal input handlers and parsing algorithms, sorting and table lookup functions, and other aids to program development.

Phase II of the implementation plan lays the foundation for all future work on the system. It consists of three tasks that are being undertaken concurrently.

- \* Task 1 consists of the development of a system wide database manager (DBM). Since data can be entered, created, modified, or deleted on any processor in the system, and since file access will be unrestricted, a coherent data manager must be developed before any processing can be attempted.
- \* Task 2 requires the specification and integration of a local area network (LAN) to provide for flow of data and commands between the various processors in the system. Obviously the DBM must be able to operate over the network; however, DBM design can take place concurrently with the LAN acquisition.
- \* Task 3 is the design of a standard user interface for control of all applications programs and system utilities. To the extent that this task is functionally distinct from Tasks 1 and 2, work can proceed without either the DBMS or LAN being fully implemented.

Phase III of the plan consists of the transfer and development of applications programs onto the new system. System integration will also take place during this phase.

Phase I has been completed and work is underway on Phase II. SASC Technologies, Inc. scientists are involved in all three tasks under Phase II and are specifically responsible for the design and implementation of the DBM and specification and integration of the LAN. Work on the user interface is a cooperative effort among all users of the system.

Another part of the AIMS, not included in the formal implementation plan but an integral part of the new system, is the capability to receive via direct transmission the new GOES mode AAA data format. To achieve this goal AFGL has undertaken to procure new ground station equipment designed to handle the expanded AAA bandwidth. SASC Technologies, Inc. is providing both hardware and software engineering support to this effort based on its experience gained in developing a mode A ground station for the Northeast Area Remote Sensing System.

#### 4. Database Manager

The database manager is designed to provide system wide control of all data files. The management function can be divided into three broad categories: 1) manage data files created by applications programs (including data ingest routines); 2) provide applications programs with data files on demand; and 3) provide data descriptors and file structure information to applications programs. In an effort to reduce the complexity of providing these functions and to insulate the applications programmer as much as possible from the details of these operations, a multilayer DBM design was produced. The layers are divided into an interface layer providing a logical path between applications and the actual data management process, a data dictionary layer that maintains information on the data currently available either on the system or in the archive, and an I/O layer that performs the actual transfer of data between the applications and the mass storage devices.

As described in Gerlach (1984) several data dictionaries are maintained that describe the characteristics and availability of all data on the system. The actual data are contained in separate "data only" files; all control and ancillary information is kept in the appropriate data dictionary files. A commercial DBM package has been purchased to manage the data dictionary files through a relational model.

The interface layer provides a logical path between the applications and other DBM layers. Standard DBM queries are translated

into commands that can be interpreted by the data dictionary manager and then passed to that layer. The query response is stored in a global buffer and analyzed; any required file management functions (e.g., file creation, deletion, logical assignments) are automatically performed. In many cases all that is returned to the application is a single status word.

The I/O layer provides a standardized method of accessing data in any file. File characteristics are received directly from the interface layer and conversion from user coordinates to file record and byte count are performed automatically. In this way the user is free to request data in the form best suited to the application, such as latitude/longitude bounds or grid coordinates, rather than in terms of file structure. I/O is optimized through the use of large internal blocking buffers, eliminating the need for the user to be concerned with system resource usage.

Situated logically above the three DBMS layers is a series of utility programs that allow interactive manipulation of the database. For example a formalized procedure for adding new types of data into the database has been implemented in a set of utility routines. Similarly casual data queries can be entered from a terminal and a report will be generated at the CRT indicating the status of the database in response to the request.

To illustrate how the various layers of the DBM interact, Figs. 49 and 50 show control flow through the layers for two common database operations accessing data and adding a data file.

For an application to access data handled by the DMB (Fig. 49) a description of the desired data (e.g., data type, valid time, location, etc.) is generated by the applications program and passed to the interface layer through a standard function call. Here the data descriptor information is inserted into a binary command string that will initiate a search of the data dictionaries (DD). The DD files have a structure that permits very fast and efficient searches on certain key fields through a process known as indexed sequential access method (ISAM). Results of the DD search are returned to the interface layer where a status message is generated indicating success or failure of the search operation. Additionally the data file is opened and the file characteristics are placed in a global common area. At this point the status message is returned to the application and actual data transfer between the database

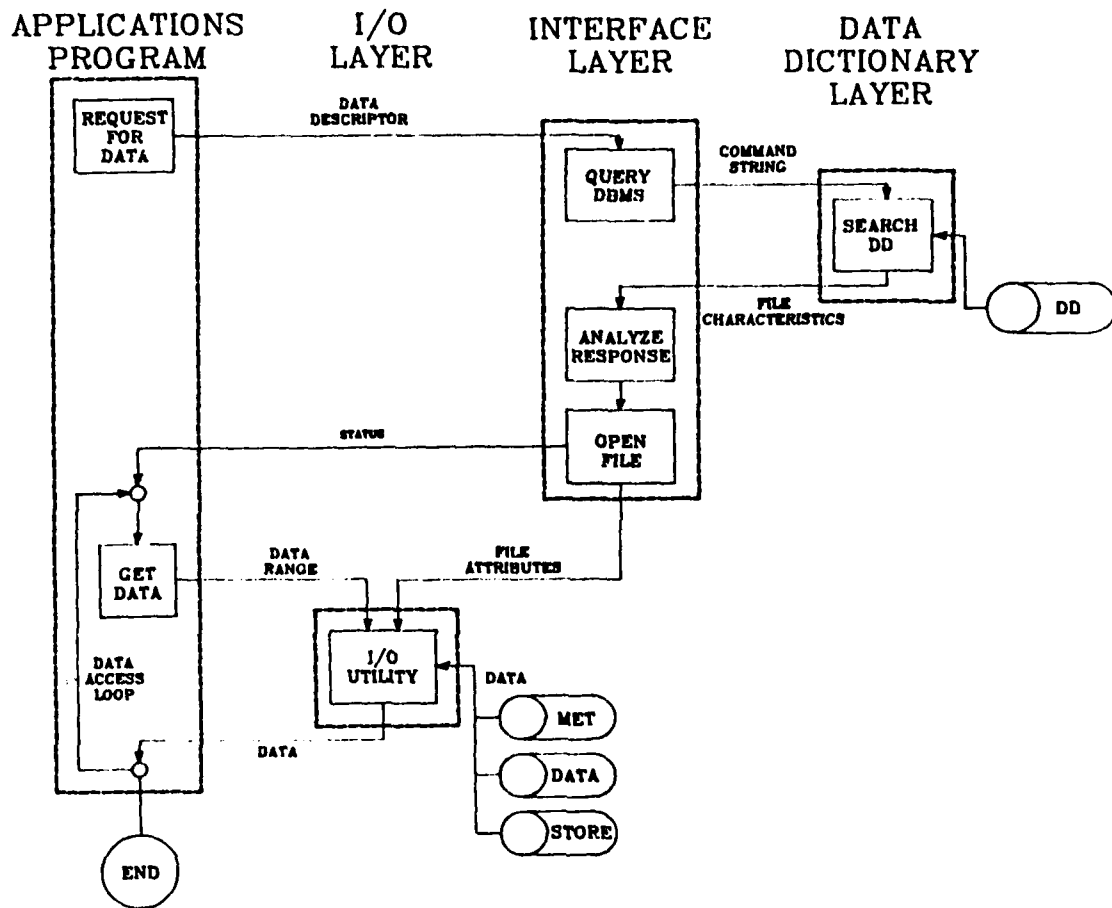


Fig. 49. Accessing Data from the Database

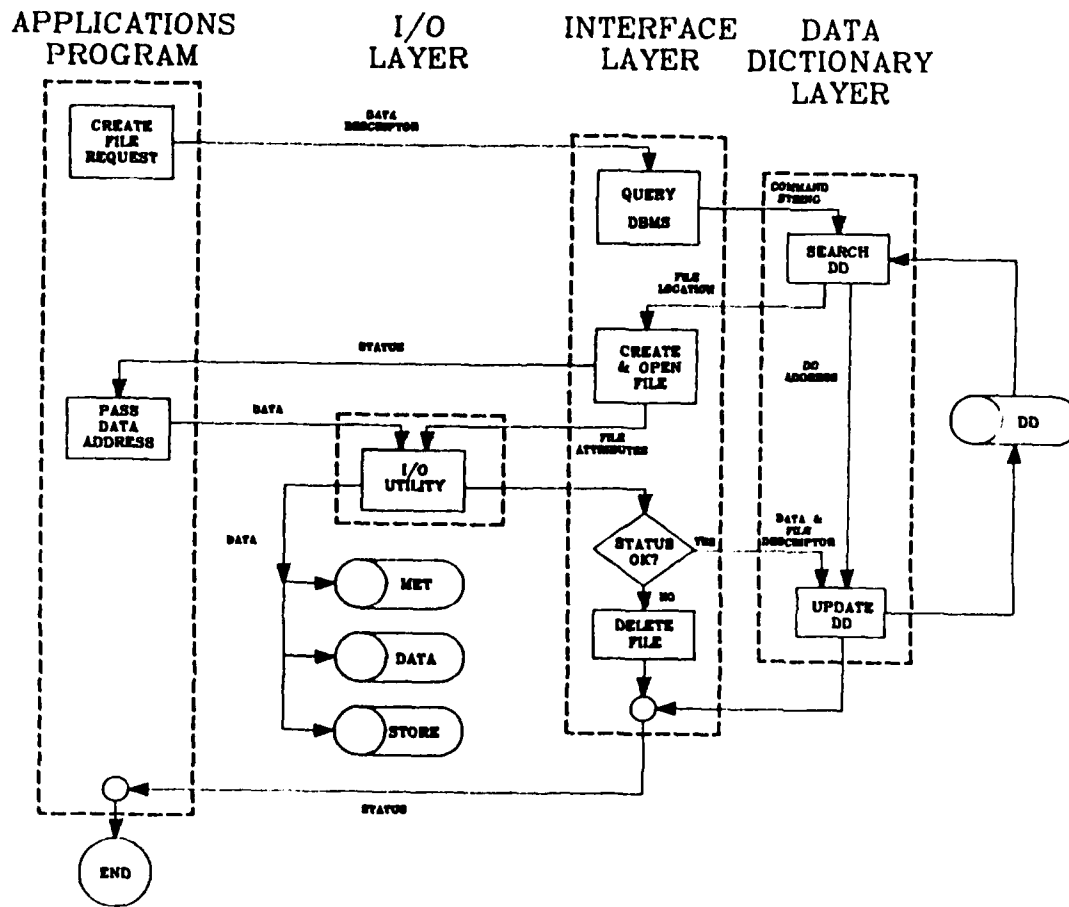


Fig. 50. Adding a Data File to the Database

and the applications program can begin. If the application requires only a segment of the data contained in the file it must pass the range limits to the I/O layer, otherwise all that is required is the address in memory of the data buffer where the data are to be placed. The I/O utilities perform any necessary conversions and return the data in the specified format.

To add a data file to the database (Fig. 50) a similar procedure is followed. The data dictionary query returns a coded file name and the location in the system where the data are to be stored. The interface layer creates the file at the specified location and returns a status message to the application. The data dictionary is not updated until the data transfer to the disk file is complete. Should the process be interrupted before the transfer is complete, the partially filled file is deleted, the data dictionary remains unchanged, and the process must be reinitiated from the beginning. This procedure insures simultaneity between the data dictionary and the data files that actually exist out on the system.

Safeguards are built into the DBMS to protect against corruption of either data files or data dictionary entries due to concurrent access of the same file by more than one user. While shared access is allowed, built-in locks force updates to occur in an orderly manner. Additionally, all database files are protected so that they cannot be created or deleted by circumventing the DBM routines. By forcing users to go through the formal DBM procedure simultaneity between the dictionaries and data files is maintained.

## 5. Local Area Network

A search of commercially available local area networks was undertaken to locate an implementation that would link the SEL 32/27 computer with the VAX 11/750 and future microVAX computers. However, after an extensive investigation no single network structure could be found that would operate on all three architectures and still fall within budget constraints. The best solution that could be found to the networking requirements discussed in Gerlach (1984) consisted of two separate links connecting the Gould and DEC machines (refer to Fig. 48). A DECnet protocol running over a token passing ring topology was selected to link the VAX and microVAX computers. The same DECnet protocol running over a dedicated synchronous serial line is providing a link to the AFGL/LYR radar



site for the exchange of digital satellite and radar data. A second protocol, known as Qnet, was selected to connect the SEL computer with the DECnet network through a direct DMA point-to-point link with the VAX 11/750. Qnet is functionally similar to DECnet but will operate under both the VAX/VMS and the SEL/MPX environments. With this configuration the VAX effectively becomes a gateway between Qnet and DECnet. The VAX was chosen as the gateway node for several reasons: the 11/750, as a batch oriented node, has few real time priorities that could interfere with network communications; the systems wide data dictionaries reside here so that update requests and queries come in from all nodes; the DECnet link to LYR terminates here; and the gateway node has to run VMS. Qnet and DECnet complement each other in that each extends its functionality to the other; that is, the SEL can interact directly with DECnet devices and has full access to files on any disk linked by DECnet. Similarly all DECnet processors have full access to the 32/27 and its devices. Therefore all peripherals such as tape drives, disk drives, and terminals become system wide resources. Thus, while two separate network protocols are involved and some additional overhead is incurred in converting between them, functionally it appears as though all processors in the system are linked to one network.

Examination of Fig. 48 shows that there exists a third network in the system, referred to as AFGL NET 1. This is a broad band network running throughout AFGL and linking all computers in the Laboratory. Currently this network is only available for terminal communications and is used to link terminals in programmers' offices to the VAX or SEL computers. A DECnet link is planned between the VAX 11/750 and the AFGL computing center's VAX 11/780 over the NET 1 link. This link will enable transfer of large data files between the two machines. At present file transfers can only take place between these machines using the relatively inefficient byte oriented Kermit protocol.

## 6. User Interface

User interface is a term used to describe the means by which a computer user makes requests known to the computer. It allows communications between the user and the computer hardware. Following the idea of device independent graphics, the user interface will provide for

varying levels of sophistication based on the Input/Output device associated with the interactive session and the preference of the user.

The user interface will consist of three primary support categories: (1) Keyboard Terminal, (2) Graphics Pull Down Menus, and (3) Graphics Tablet Icons Menu.

a. Keyboard Terminals - Command Line Interpreter

The Keyboard Terminal can be anything from a dumb teletype to a more elaborate graphics device. Any commands that generate tabular output may be executed at these types of terminals. However, in the case of a graphics terminal, such as the Tektronix 4010, the user will also be able to generate simple graphic representations of data, e.g., a plot of New England overlaid with wind flags and a temperature contour.

On the Keyboard Terminal commands are entered as ordinary VAX/VMS commands; that is, a command verb followed by various qualifiers and parameters. Qualifiers are words preceded by a slash (/) character and allow for specific options. A parameter contains information necessary for the command to function. For example, the plot referred to above would be executed with the command string:

```
PLOT NEW_ENGLAND
```

This will display a map outline of New England on the graphics terminal. To request that certain data be included on the plot, the user would enter

```
PLOT/SYMBOLS=WIND_FLAGS NEW_ENGLAND
```

and to include a contour

```
PLOT/SYMBOLS=WIND_FLAGS/CONTOUR=TEMPERATURE NEW_ENGLAND
```

This type of command is very long and verbose. However, the user interface is capable of accepting the fewest number of characters required to identify a term uniquely, as

```
PL/SY=W/CO=T NEW_E
```

The rule is that no other command, qualifier, or parameter could be confused by the given abbreviation.

The VAX/VMS operating system used by the DECnet devices supports a feature called Symbols. A symbol is defined as a command abbreviation that executes another command. The example above could be set up as

```
IA:==PLOT/SYMBOLS=WIND_FLAGS/CONTOUR=TEMPERATURE NEW_ENGLAND
```

The user need only enter the command IA to create the plot. Symbols can also provide for part of the command as

```
IA:==PLOT/SYMBOLS=WIND_FLAGS/CONTOUR=TEMPERATURE
```

Here the geographic area parameter is omitted. To use this command the user would simply enter

```
IA NEW_ENGLAND or IA NEW_E
```

The possibilities are unlimited. Using this technique AIMS could be customized to look like McIDAS.

In addition, a symbol can be defined to execute a command procedure (which is a series of VAX/VMS commands) to string many other commands together. This is also known as a macro. For example

```
MAPS:=@DRAW_MAPS.COM
```

The @ sign instructs the operating system that DRAW\_MAPS.COM be executed as a command procedure.

DRAW\_MAPS.COM contains

```
$PLOT/SYMBOLS=WIND_FLAGS/PANEL=1/CLEAR_SCREEN=ALL NEW_ENGLAND  
$PLOT/CONTOUR=TEMPERATURE/PANEL=2/NOCLEAR_SCREEN NEW_ENGLAND  
$PLOT/CONTOUR=RADAR/PANEL=3/NOCLEAR_SCREEN NEW_ENGLAND  
$PLOT/SYMBOLS=ID_STATIONS/PANEL=4/NOCLEAR_SCREEN NEW_ENGLAND
```

In this example, the command MAPS is defined to execute a command procedure. In turn, the procedure will generate four plots of New England, each with different data and displayed in a different quadrant of the screen. Note that the first plot clears the screen, but the remaining three plots specify the screen be left alone.

#### b. Keyboard Terminals - Screen Menus

For novice users of the system, a second support category for Keyboard Terminals will be implemented: Menus. The effect of these menus is to prompt the user to select the desired command verb, and then to display the available options and parameters. The end result is to generate a command as was shown in the section above.

The menu will be window oriented if the Keyboard Terminal is a VAX/VMS supported type, e.g., VT100, VT220. If not, the menu system will still function without the windowing capability. The VAX/VMS Screen Management System will handle the complex task of the window functions.

#### c. Graphics Pull Down Menus

The second major category of the user interface is Graphics Pull Down Menus. This interface will only be implemented on the image processing workstations. Pull Down Menus are activated by pressing a selected button on the Graphics Tablet Puck. A menu appears as an overlay on the graphics display. Moving the display cursor over the menu and pressing a puck button selects the options. Then the overlay is removed.

#### d. Graphics Tablet Icons Menu

The third major category of the user interface is the Graphics Tablet Icons Menu. The surface of the Graphics Tablet is divided into an array of boxes. This matrix of boxes is defined by the software to select options, vary video look-up tables (RGB), move the ADAGE graphics cursor, etc. This can also be defined to execute command procedures as explained in the Keyboard Terminal section.

### 7. GOKS Ingest

Plans are being implemented to replace certain electronic components of the AFGL ground station receive subsystem. The replacement

is required to support the operational communications format for GOES VAS data scheduled for transmission in Summer 1986. The format is known as mode AAA. The Gould 32/27 minicomputer has been identified as the node responsible for ingesting and archiving mode AAA data. The current hardware configuration on the 32/27 includes Gould's High Speed Device (HSD), a DMA device that accepts as input 32-bit parallel data, which will interface between the receive subsystem interface electronics and the 32/27 CPU. Once data are ingested, the 32/27 will also transmit selected subsets of the GOES transmission to receiving nodes on the local area network. Procurement of the receive subsystem and downlink interface electronics is underway. SASC Technologies, Inc. is participating in the software system specification and development.

Prior to software development, the required tasks must be specified. To this end an initial task outline has been generated:

- \* Main loop
- \* FORTRAN - callable system service
- \* Applications job initialization
- \* Hardware related software
- \* Imagery file management system
- \* Sounding file management system
- \* Navigation file management system
- \* Data ingest
- \* Data storage
- \* Data transmission
- \* Auto restart

With a division of the process into identifiable components, a review of required operating system features can be made. The system must be a real time operating system equipped to handle the asynchronous collection and dissemination of data and operator commands. It must accommodate multitasking to encourage the layered approach to program design and to allow concurrent processing of overlapping tasks. Since the various tasks comprising an ingest/store/transmit cycle must execute in an orderly manner and require the sharing of common data, the system must allow synchronized task processing and intertask communication through system service requests. Finally, the operating system must be flexible enough to

accommodate unanticipated system design changes or expansion. Gould's Mapped Program Executive (MPX) operating system meets all these requirements and was therefore incorporated.

Initial plans will consider a rotating archive of GOES mode AAA data. The 32/27 is currently configured with two 340 MB disks and one 160 MB disk. The system specification is expected to include support for both Multi-Spectral Imaging (MSI) and Dwell Sounding (DS), the two modes of remote sensing for VAS that will be available for broadcasts under mode AAA.

### C. McIDAS Operations and Maintenance

#### 1. McIDAS Operations

SASC is responsible for day to day operations support of the AFGL McIDAS. Routine operations performed included maintenance of the Sony satellite archive, GOES navigation ingest and quality control, scheduling use of terminal time, and maintenance and updating of the surface and upper air data archive. Real time GOES imagery ingest scheduling and production of data save tapes and hardcopy imagery were provided in response to the needs of project scientists. The condition of existing McIDAS software was monitored to ensure system integrity. System software saves were made. System regenerations from save tapes were performed when software or hardware failures warranted such action.

#### 2. McIDAS Maintenance

##### a. Resident Engineering

The following items required maintenance during the year. The end item is listed, followed by the component(s) replaced or repaired to bring the equipment back to operating condition.

- \* Video Bay #3
  - Top blower fan assembly
- \* Digital Video Storage System
  - Bottom blower fan assembly
- \* Terminal 22 Blue Enhancement Drawer
  - Memory IC P3101A
- \* Terminal 22 Digital Cursor Drawer
  - Resoldered connection on pin 5 of IC 8242 "E"

- \* **EMR PSK/PCM Demodulator Model 729**  
Q16 and Q17 (ZN2501)
- \* **Aydin 350 PCM Bit Synchronizer**  
± 15V power supply
- \* **ODIS Kennedy Tape Transport**  
Take-up arm sensor lamp
- \* **Sony Archive Recorders and Players**  
Replaced drive belts in all four units
- \* **Terminal 22 Green Enhancement Drawer**  
Repaired cold solder connection on IC  
"F" (P3101A) in the B table
- \* **ADAGE System**  
Installed two 19" color monitors
- \* **VG 2800 Sony Recorder**  
Fast-forward/reverse idler assembly
- \* **EMR Frame Synchronizer Model 822**  
Counter IC 74193

**b. Contract Engineering**

Under service contract Harris Corporation maintained the Harris 6024/5 computer system. The following equipments required repair by field service engineers.

- \* **Harris Line Printer Model 4110**  
Replaced hammer driver board and vertical  
format board
- \* **Control Data 80 MB Disk**  
Replaced disk controller board, -5 volt sense power  
supply, voice coil, and carriage head assembly
- \* **Harris Computer Model 6024/5**  
Fabricated a one shot timing circuit to correct  
erratic operation of the 120 HZ clock module caused  
by noisy AC line input
- \* **Wangco Tape Transport Model 6640**  
Replaced faulty write ring enable switch

## VI. CLIMATOLOGY

### A. An Update to the LANDSAT MSS Data Handling Configuration at AFGL

Information on the availability and data handling of LANDSAT MSS digital tapes at AFGL provided in Gerlach (1984) was updated to include seven additional LANDSAT tape volumes. Table 14 lists all LANDSAT tape volumes available and was expanded to include general area of coverage, spectral band availability, and format type. The data handling configuration originally designed for processing band interleaved (BIL) format was also updated to include additional software that permits handling of the data in band sequential (BSQ) format. Names of the updated software modules and their relative positions in the data handling configuration are shown in the shaded areas outlined in Fig. 51.

Programs LTAP21 and 22 add copying capabilities for both BSQ and BIL formatted data. FULLMX was added to handle BSQ type format to produce tapes of full sized LANDSAT scenes for display on the McIDAS imaging system. Likewise, FULLR2 was added to provide full resolution subsection scenes. Software for handling spectrally interleaved (SIL) format will be added when the need for reducing this type of data arises. Processing of digitized space shuttle photographs was also added to the data handling configuration.

It should be noted that in ordering LANDSAT data from the U.S. Geological Survey, Sioux Falls, SD some processing efficiency can be gained by requesting data in a format suitable to the investigation being performed. For example, a request for BSQ formatted data would be advantageous for supporting investigations requiring only single spectral signatures. BIL formatted data are useful in investigations requiring multispectral signatures, as are data in the less efficient SIL format.

### B. Statistical Properties of Cumulus Cloud Structures

#### 1. Introduction

Space shuttle missions include a photographic capability utilized to yield detailed cloud information from space. At AFGL, digital images are being produced from selected portions of these photographs to determine statistical properties of cumulus cloud populations.



TABLE 14. LANDSAT MSS DATA AVAILABILITY AT AFGL (Update, 1985)

IMAGE IDENT	TAPE NO.		FORMAT			BANDS	CENTER		GENERAL AREA	DATE
	ORIG.	COPY	BIL	BSQ	SIL	45678	LAT.	LONG.		
82210915051	T0001	LSAT01	X			XXXX	26.5N	79.5W	MIAMI, FL STR.	801031
	T0002	LSAT02	X			XXXX				
82214414593	T0003	LSAT03	X			XXXX	24.5N	78.0W	FL STR. ANDROS	801205
	T0004	LSAT04	X			XXXX				
82207215000	T0005	LSAT05	X			XXXX	24.5N	78.0W	FL STR. ANDROS	800924
	T0006	LSAT06	X			XXXX				
82207215003	T0007	LSAT07	X			XXXX	23.0N	78.5W	FL STR. N.CUBA	800924
	T0008	LSAT08	X			XXXX				
82207315055	T0009	LSAT09	X			XXXX	24.5N	79.5W	FL STR.	800925
	T0010	LSAT10	X			XXXX				
82205615113	T0011	LSAT11	X			XXXX	24.5N	81.0W	FL STR. KEYS	800908
	T0012	LSAT12	X			XXXX				
82214715162	T0013	LSAT13	X			XXXX	26.0N	82.0W	GULF OF MEXICO	801208
	T0014	LSAT14	X			XXXX				
82210915054	T0015	LSAT15	X			XXXX	24.5N	79.5W	FL STR.	801031
	T0016	LSAT16	X			XXXX				
82212715052	T0017	LSAT17	X			XXXX	24.5N	79.5W	FL STR.	801118
	T0018	LSAT18	X			XXXX				
82137214532	T0019	LSAT19			X	XXXX	33.0N	78.6W	COASTAL S.C.	781025
2165216030	UA06E	.....		X		XX	24.5N	95.4W	GULF OF MEXICO	790801
	UA06F	.....		X		XX				
82160015152	T0020	LSAT20		X		XX	33.0N	81.4W	S. CAROLINA	790829
	T0021	LSAT21		X		XX				
82160015154	T0022	LSAT22		X		XX	31.6N	81.9W	GEORGIA	790829
	T0023	LSAT23		X		XX				

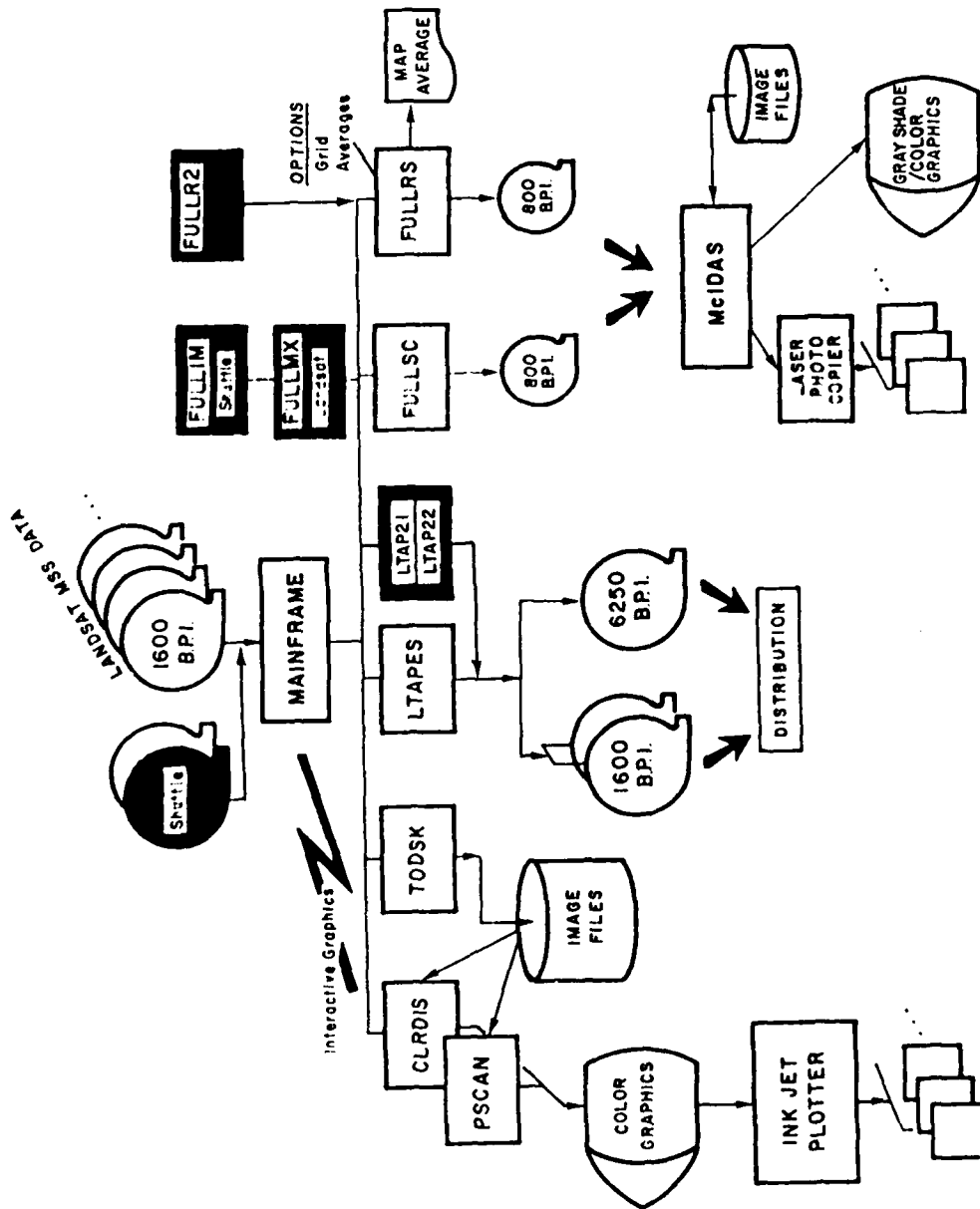


Fig. 51. Satellite High Resolution Data Handling Configuration Update (1985)

## 2. Specifications

The specifications set for the data processing activities involved in utilizing digitized space shuttle photographs and LANDSAT data are:

- \* Using digitized products of selected photographs of cumulus clouds from space shuttle missions and LANDSAT data, prepare the data in permanent storage format and determine cloud/no cloud threshold values for input to subsequent software.
- \* Display through image processing techniques the cloud/no cloud scenes pictorially for threshold verification.
- \* Develop and implement software to determine:
  - (a) statistics of clear and cloudy intervals by both row and column scanning techniques,
  - (b) spatial tetrachoric correlations of cloud scenes,
  - (c) spectrum of clear and cloudy intervals through Fourier analysis,
  - (d) distributions of center to center distances between cumulus clouds and equivalent cumulus cloud diameters.

## 3. Source Data

Space shuttle photographs were reviewed to sort out areas showing uniform cumulus cloud fields uncontaminated by cirrus or alto cumulus clouds, or sunglint scattering. Cases of highly oblique viewing angles were rejected. Areas of selected cases were marked off in sizes amenable to machine digitizing.

Several of the cases selected were digitized by hand. This was accomplished by projecting the area of interest from a negative onto graph paper of predetermined size. Each square on the grid was set equal to a code (number) that distinguished clear, partly cloudy, and cloudy squares. When completed the entire coded grid was entered into the computer.

LANDSAT data sources were also used in this study to compare resolution effects on cumulus cloud distributions different from those obtained using the shuttle data.

#### 4. Software Development

The data processing configuration developed for deriving the various statistical distributions of cumulus clouds as viewed from space is shown in Fig. 52. This and subsequent figures of data flow show how data sources combine with developed software to produce end results. The diagrams show data sources at the left, followed by the data transfer software developed to format, compress, and transfer data to permanent files for interactive processing. Names of permanent files are directed to the scientific applications software developed to accomplish what is briefly described at the right of each diagram. The backup tape numbers and tape labels (TN) also shown record where all data for each project are kept for permanent retention. Details of the data flow in Fig. 52 are discussed below.

Data from two hand digitized space shuttle photographs were entered into the mainframe computer via a Zenith PC/InterComm network system. The data were then merged and stored in a compatible format for use with subsequent software. The two cases were scenes 41D 265, just off shore of Cape Canaveral, FL (D 80), and 41D-298, over an area in the eastern Pacific (D 120). Three machine digitized space shuttle photographs on tape were also stored using program GETSAT.

Data set CALIA contained the machine digitized version of a shuttle photograph over the eastern Pacific. TASCIA and PHOTOM contained digitized photograph 41D-133, representing a case over land in the Trade Wind Islands. Program TODSK provided portions of LANDSAT digital data for three cases. LAND7D is a band 7 case over the Straits of Florida; LANDG4 is a band 4 scene over an island in the Straits of Florida, and LANDI4 a band 4 case in the Gulf of Mexico.

Horizontal dimensions of cumulus clouds near their bases are of vital concern in this study. Therefore the procedures described next and depicted in Fig. 53 are critical in determining a cloud/no cloud (CNC) threshold value that best defines the horizontal base dimensions of cumulus cloud content within each image. First, histograms of selected small areas,

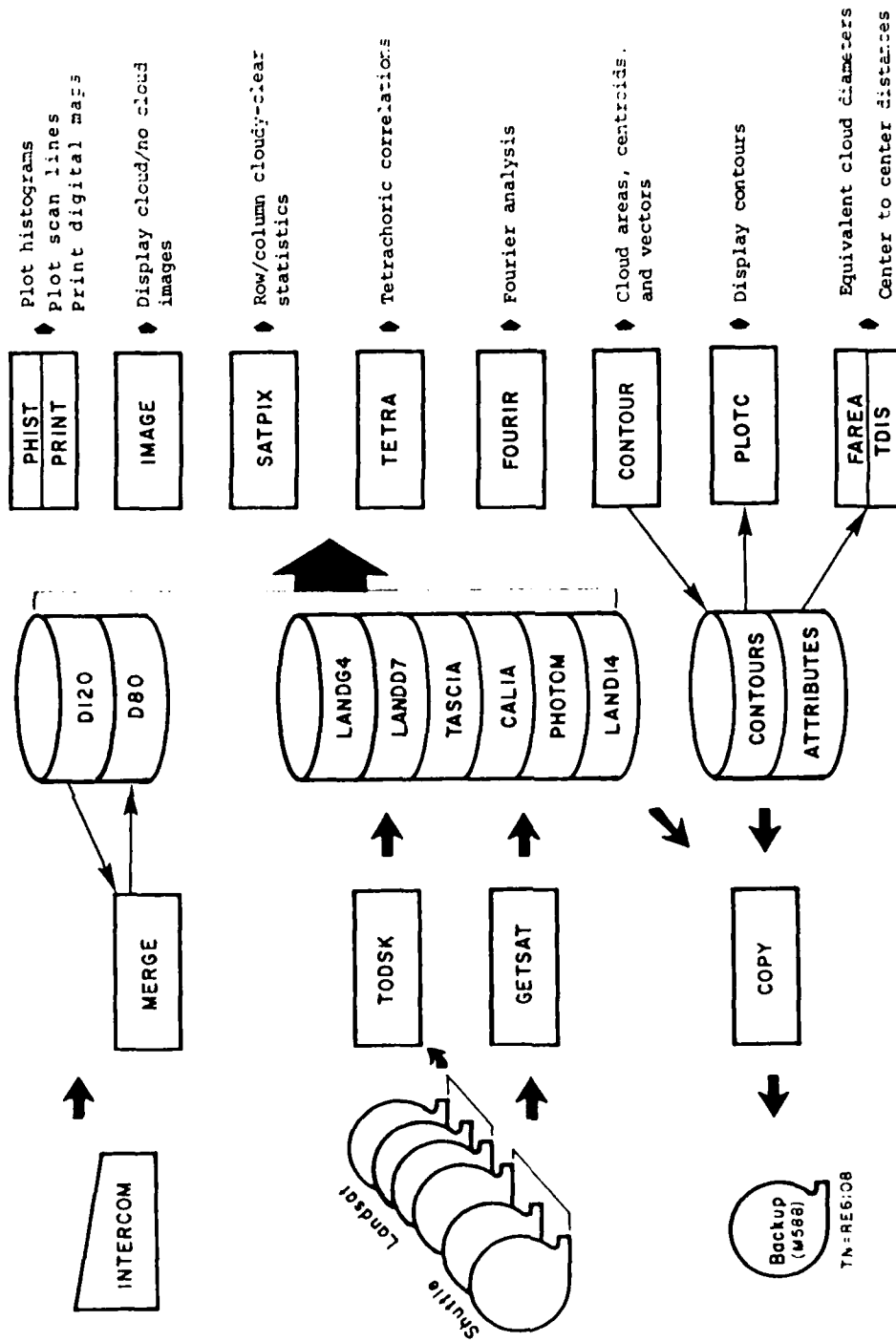


Fig. 52. Configuration for Processing Digitized Cloud Images

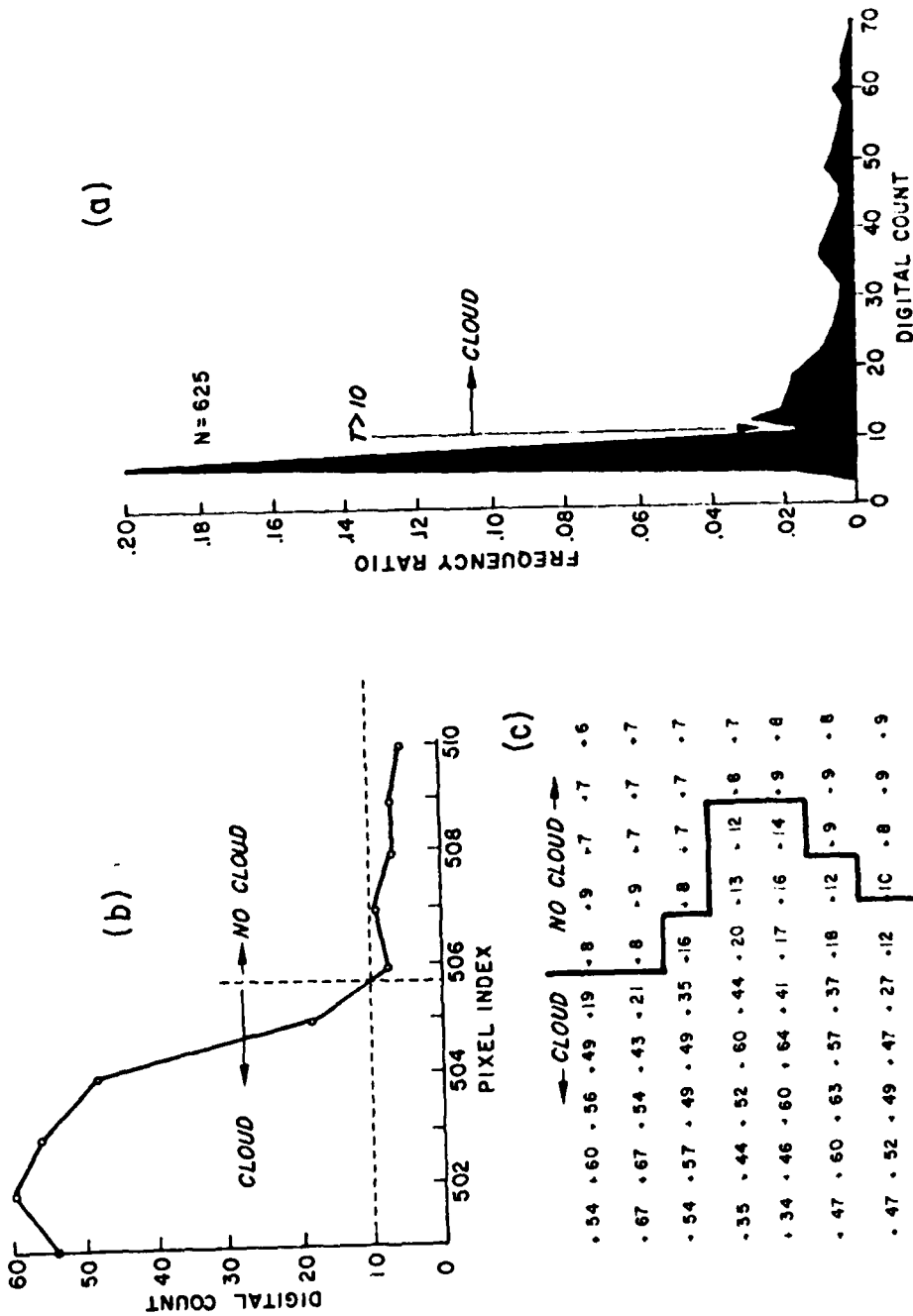


Fig. 53. Sample Three Step Method for Determining Cloud No Cloud (CNC) Thresholds

or of entire portions of stored scenes, were portrayed by program PHIST. These histograms provided quick quality checks of the digitization process and in some cases proved to be a good CNC threshold indicator. For example, in cases of bimodal distributions a CNC threshold can be estimated to be the value between the two peaks of the distribution. Hence, in Fig. 53a, T greater than digital count value 10 would signify cloud. However, distributions of this shape are rare, so as an option to the PHIST program selected scan lines were also portrayed, similar to the one shown in Fig. 53b. The vertical dashed line separating the obvious cloud on the left from the earth background on the right again suggests that 10 is a possible CNC threshold. Finally, grid print maps generated by program PRINT are printed out for selected area sizes. The maps can be contour analyzed to separate obvious areas of cloud from the more homogeneous spectral signatures of the earth background, as shown in Fig. 53c. Again it is evident that 10 is the best estimated CNC threshold for the scene being investigated. This procedure was not performed on the hand digitized scenes since the human eye was the effective CNC discriminator in those cases.

Program IMAGE was developed to display pictorially each scene as it would appear by applying the CNC threshold determined by the procedure mentioned above. A typical CNC scene generated by this program is shown in Fig. 54. It is the hand digitized photograph over the eastern Pacific. Clouds are portrayed in these types of scenes by many small dark symbols against a blank earth background.

Images of all machine digitized data products are produced on the McIDAS laser photo copier using the data handling configuration shown in Fig. 51. These images in sixteen gray shades are compared with CNC images for threshold verification. For example, the machine digitized space shuttle scene over the eastern Pacific was compressed and stored on tape by the FULLIM program in Fig. 51. Later the image on tape was displayed by the McIDAS to produce the picture in Fig. 55. The area outlined in Fig. 55 is then compared with the CNC display over the same area. If thresholds have been correctly determined statistical processing is undertaken as explained next.

Program SATPIX was developed to produce population frequency distributions of clear and cloudy intervals that appear in CNC images. The program processes the input of a CNC image one scan line at a time, but the

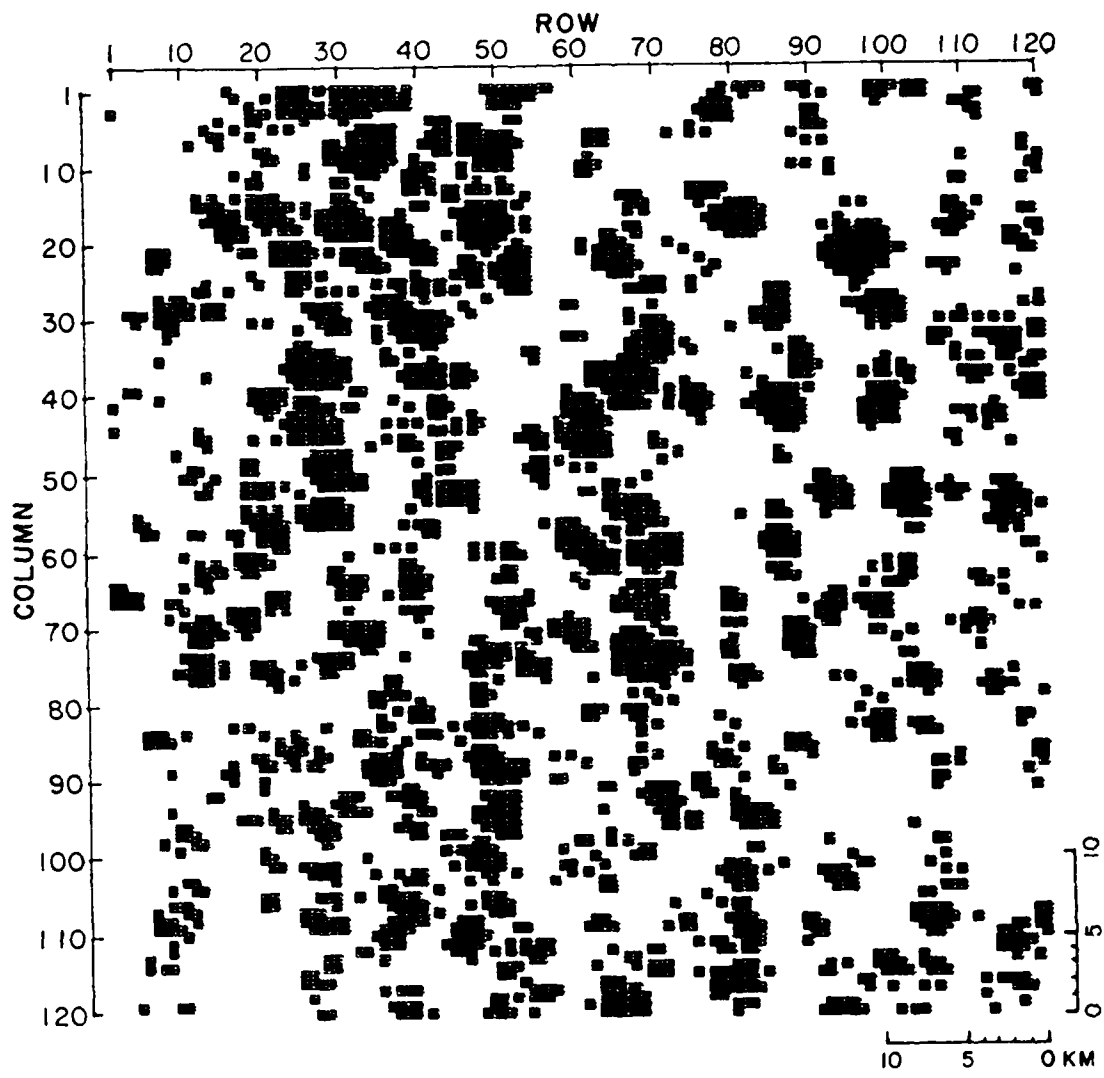


Fig. 54. Typical Cloud/No Cloud (CNC) Image

Hand digitized space shuttle photograph 41D-298 over the Eastern Pacific.



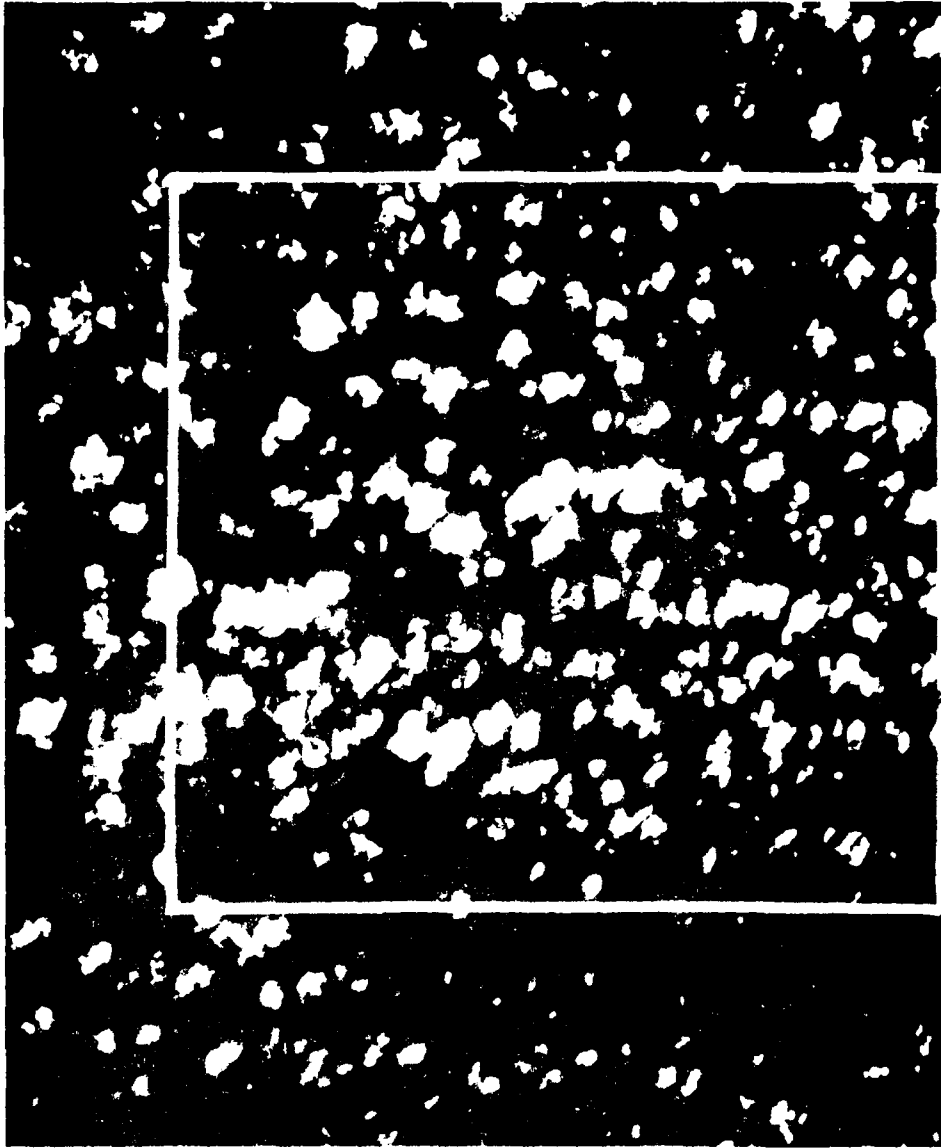


Fig. 55. Sixteen Gray Shaded Image of the Machine Digitized Space Shuttle Photograph over the Eastern Pacific

Outlined is the CNC area under investigation.

logic for deriving the statistics treats the data as one long vector of pixels starting in the upper left hand corner and ending at the bottom right side of the frame. By scanning the image in this manner, frequencies of occurrences of the lengths of uninterrupted clear and cloudy pixels are tabulated. These frequencies were fitted to hypothetical mathematical functions.

These results were presented at the Third Tri-Service Clouds Modeling Workshop,<sup>56</sup> together with displays of spatial autocorrelation functions and Fourier analysis of cumulus cloud fields.<sup>57</sup>

The spatial autocorrelation functions and Fourier transforms of cumulus cloud fields were made possible through development of programs TETRA and FOURIR. Complete documentation of program TETRA, also known as COND80, was prepared; see Appendix D. Program functions were described to compute tetrachoric correlation coefficients R from

$$R = \sin \left[ \frac{\pi}{2} \left( \frac{\sqrt{AD} - \sqrt{BC}}{\sqrt{AD} + \sqrt{BC}} \right) \right]$$

where A, B, C, and D are array elements (1,1), (1,2), (2,1), and (2,2) respectively of conditional occurrences of clear and cloudy pixels within a cloud scene.

Selected routines<sup>58</sup> were paired with image data manipulation logic in program FOURIR to perform the specified Fourier analysis of CNC images. A spectrum plot of the results from program FOURIR and a spatial autocorrelation function derived from program TETRA for the hand digitized eastern Pacific space shuttle photograph are shown in Fig. 56.

---

56. Grantham, D. D., and J. W. Snow, eds., 1985: Presentations at the Third Tri-Service Clouds Modeling Workshop. Air Force Geophysics Laboratory, Hanscom AFB, MA.

57. Snow, J. W., E. Tomlinson, and J. H. Willand, 1985: Distributions of clear and cloudy intervals, spatial correlations from space shuttle cloud photographs. In Presentations at the Third Tri-Service Clouds Modeling Workshop, Air Force Geophysics Laboratory, Hanscom AFB, MA.

58. IBM, 1968: System/360 Scientific Subroutine Package (360-GM-03X) Version III Programmers Manual. IBM Technical Publications Department, White Plains, NY.

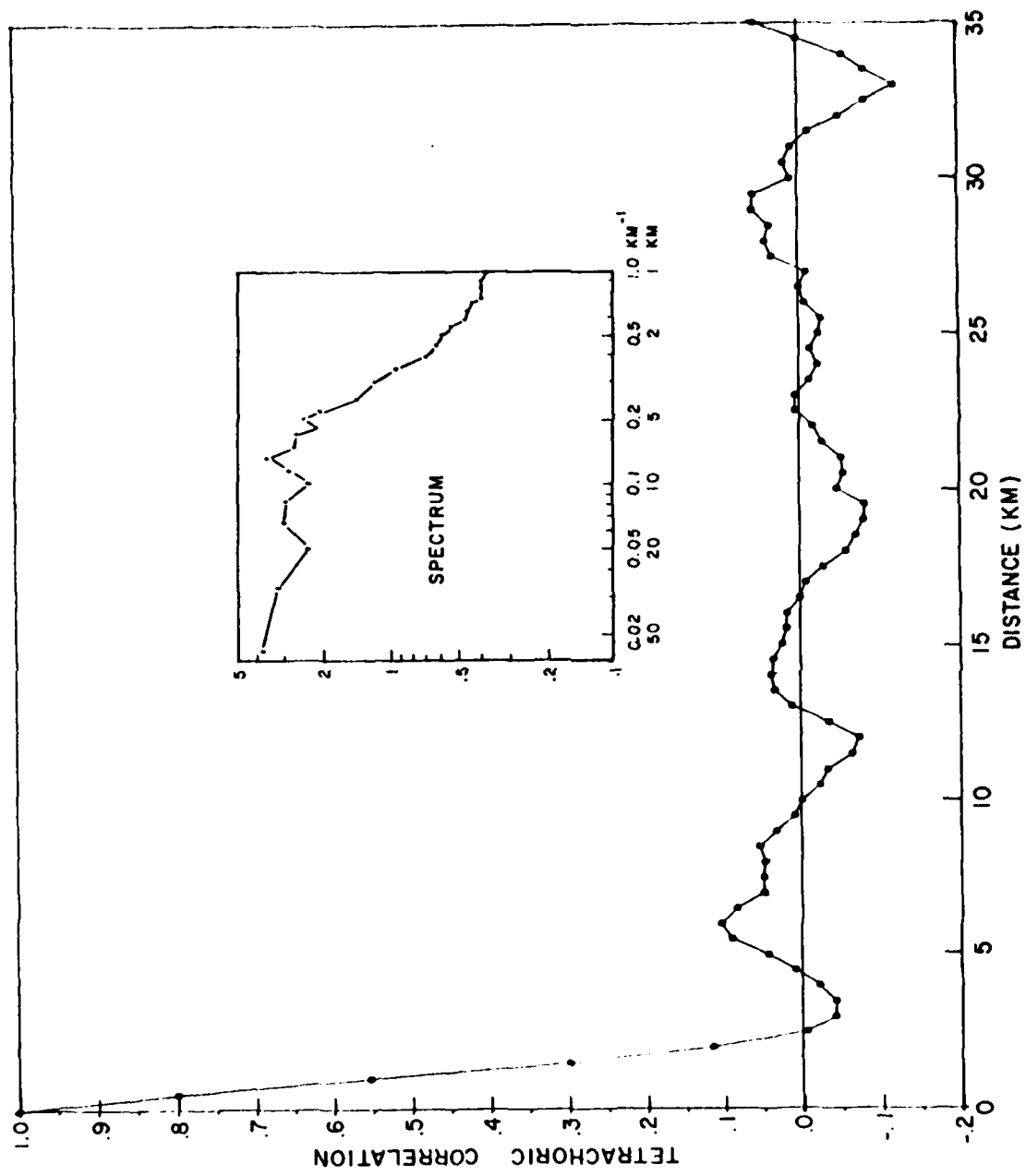


Fig. 56. Spatial Autocorrelation Function and Fourier Transform (Spectrum) of Hard Digitized Space Shuttle Photograph over the Eastern Pacific

The investigation of cumulus cloud populations is also interested in the distributions of their distances apart and equivalent diameter sizes. Program CONTOUR was initiated to provide preprocessing support in deriving these distributions. Given one or more thresholds the program will convert data stored as raster scans to x and y vectors that outline polygons (clouds). In addition, attributes of areas and centroids of the polygons being vectorized are computed. A flag attribute is attached to each polygon, distinguishing completed polygons from incompleting edge types. Moreover, percent cloud cover is computed for the entire image by dividing the sum totals of all the cloud area attributes by the total number of pixels in the image. The contours and attributes computed are stored separately for further processing.

Program PLOTG plots the stored contours at selected scales. If exact image scales are used, undistorted transparencies of the contours can be made to fit directly over an image for assistance in CNC threshold verification.

Distributions of equivalent diameters of the cumulus clouds are computed by program FAREA. Hence, assuming that the bases of cumulus clouds approximate circular shapes and given the area A of a circle to be  $.7854D^2$  where D equals diameter, then the diameter of a cumulus cloud is estimated to be

$$D_{ID} = \sqrt{A_{ID} / .7854}$$

where

$A_{ID}$  - area attribute of identified cloud ID.

Program TDIS computes the center to center distances between the clouds using the centroid attributes. Hence, from the fundamental distance formula

$$d = \sqrt{(x_2 - x_1)^2 + (y_2 - y_1)^2}$$

where

$x_1, y_1$  - pixel centroid of cloud 1

$x_2, y_2$  - pixel centroid of cloud 2

then

$d$  = distance in pixels.

Distance can now be statistically distributed and the next distance from cloud 1 to cloud 3 is determined, etc., until all distances from cloud 1 to cloud  $n$  are distributed. Cloud 1 is then eliminated and the process is repeated from cloud 2, etc., for  $n-1$  clouds in the entire scene.

Top of Fig. 57 displays the CNC contour derived from the machine digitized version of the space shuttle photograph over the eastern Pacific. Note that the resolution is eight times that of the hand digitized case. A few sample attributes in pixel units are listed at the bottom of Fig. 57. Many partial clouds were paired to form 761 actual clouds in the entire scene having a total cloud amount of 19.6 percent. Program CONTOUR and its related product have tremendous potential for further development. With very little program modification, the following could be produced:

- \* Three-dimensional cloud structures
- \* Two-dimensional elongation cloud structure factors
- \* Cloud water content, mass, and weighted centroids
- \* "Zoom in" for individual cloud investigation, shapes, etc.

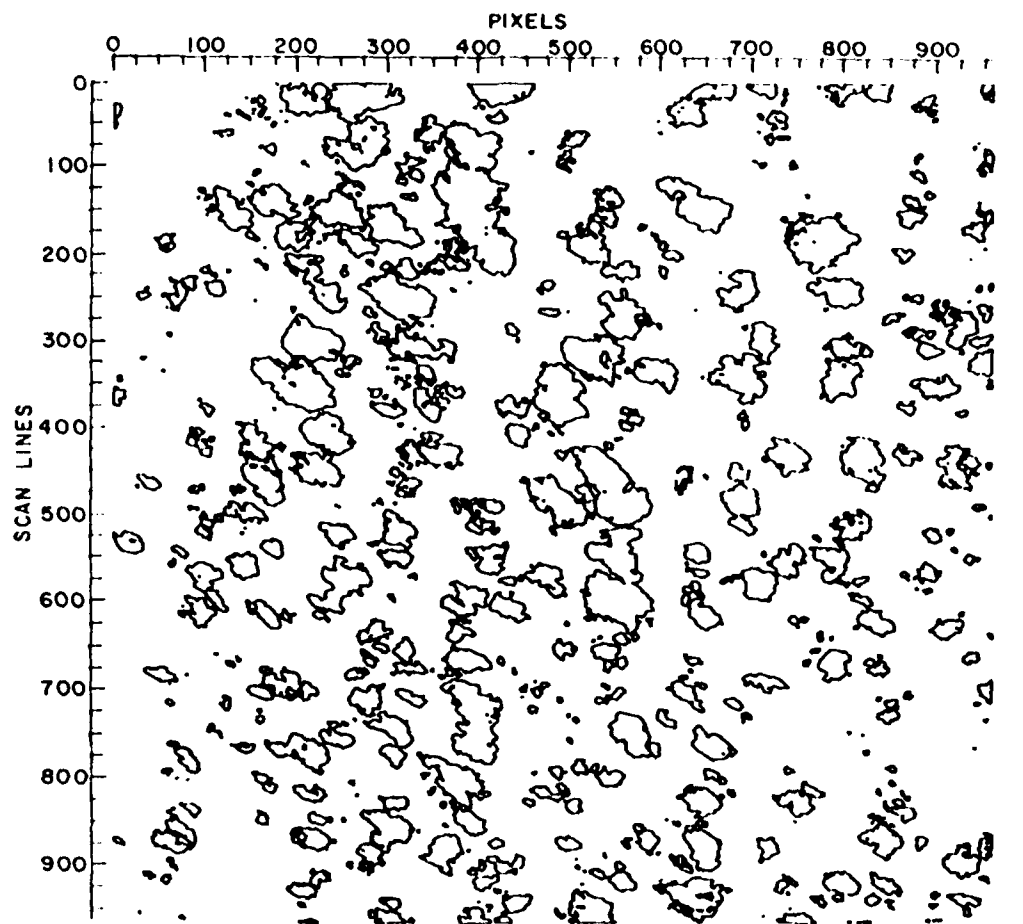
With perhaps moderate modification horizontal and vertical cloud motions could be obtained which could lead to wind direction and speed detection. Program timing and storage capacity considerations would, of course, be important in any redesign. At present the program, on a CDC850, computed and stored the attributes and contours of 761 clouds within the 960 X 960 pixel array in Fig. 57 in less than eight minutes. The plot program plotted the contours on a Tektronix CRT in less than six seconds.

Large sample sizes are necessary for development of reliable statistics. Other space shuttle photographs of cumulus cloud fields will be added to the existing sample through the data processing techniques described above.

### C. Spatial and Temporal Cloud Cover Distributions from Conventional Observations

#### 1. Introduction

Conventional surface meteorological observations from many global locations were acquired to study the spatial and temporal coherence



SAMPLE ATTRIBUTES

CNC=205

<u>ID</u>	<u><math>\bar{X}</math></u>	<u><math>\bar{Y}</math></u>	<u>AREA</u>	<u>DIAM.</u>	<u>WT.</u>
1	178.5	.5	1	1.1	205
2	193.5	.5	1	1.1	205
...	...	...	...	...	...
256	224.9	225.9	1644	45.8	337020
257	394.2	129.6	9670	111.0	1982350
...	...	...	...	...	...
1389	827.0	959.5	2	1.6	410

Fig. 57. Contour of 205 CNC Threshold for the Machine Digitized Space Shuttle Photograph over the Eastern Pacific (top); Sample Attributes; in Pixel Units; (bottom)

of cloud cover as observed from ground based stations. The data processing activities performed in support of this study are discussed in this section.

## 2. Specifications

Specifications for data processing support of this study are:

- \* From conventional meteorological observations archived on digital tapes for a limited network of stations in the U.S., extract hourly observations of cloud cover and store them in efficient format for subsequent statistical software usage.
- \* Develop and implement software that combines readily written statistical subroutine packages with input and output routines to provide spatial and temporal statistics of observed cloud amounts for January, April, July, and October mid-season months.
- \* Restrict processing of spatial cloud cover conditions to include only those observed at 00, 01, 02, 06, 07, 08, 12, 13, 14, 18, 19, 20 GMT.

## 3. Source Data

The ground observed meteorological data are contained on 77 tapes covering selected line oriented (located along a fixed directional line) stations over eastern Europe, Australia, South America, Hawaii, Alaska, and central U.S. The data, including documentation of DATSAV format (Reference Manual, 1977),<sup>59</sup> cover the period 1973-1983.

Each tape contains surface observations for a single station. Some tapes contain data archived every hour for 24 hours a day while others archive only mandatory six hourly GMT synoptic observations.

Cloud data in DATSAV format are in two basic forms, synoptic code and Airways code. Synoptic code reports the total fraction of the celestial dome covered in octas, (0 through 8 eighths; 9 meaning obscured),

---

59. Reference Manual, 1977: USAFETAC DATSAV Data Base Handbook. USAFETAC-TN-77-2, Air Force Environmental Technical Applications Center, Scott AFB, IL.

while Airways code denotes sky conditions as scattered, broken, overcast, obscured, or partially obscured. Definitions of cloud cover codes and other information are listed in Table 15 for further discussion below. These coded arrangements are critical for the derivation of cloud statistics in this study.

TABLE 15. CLOUD COVER CODING ASSIGNMENTS

DATSAV Tape Code	Data Compaction Code	Cloud Cover Conditions	Clear/Cloudy Conversion Code
<b>Synoptic</b>			
0	1	Clear	1
1	2	.1 octas	1
2	3	.2	1
3	4	.3	1
4	5	.4	1
5	6	.5	10
6	7	.6	10
7	8	.7	10
8	9	.8	10
9	10	Obscured	10
<b>Airways</b>			
* 0	1	Clear	1
-2	12	Scattered	1
-7	13	Broken	10
-8	14	Overcast	10
-9	15	Obscured	10
-10	16	Partially Obscured	1
65535	31	Missing Data	31

\*NOTE: DATSAV documentation does not define an Airways code for clear sky cover. Through data dump investigations and telephone conversations with USAFETAC, it was deduced that zero in this field signifies an Airways clear sky condition.



#### 4. Software Development

Fig. 58 shows the data handling configuration designed to process ground observed cloud observations for deriving spatial and temporal cloud cover statistics.

Program GETCOV was developed and implemented to extract from the DATSAV tapes the hourly cloud cover observations. The program converts the incoming sky cover codes to data compaction codes shown in Table 15. The largest compaction code number is 31 or 37 to the base eight which can be contained in a five bit byte. Since the mainframe computer being utilized is a 60 bit word addressable machine, 12 five bit bytes can fit in one word. Two words can then be used to store 24 five bit bytes or one day (24 hours) of cloud observations. Sixty-two words (2 X 31 days) will hold an entire month of observations. Adding two more words for station numbers and latitude-longitude locators brings the total number of words to 64, which becomes a single physical record length for one month's data. Final size of a random access data set required to store all cloud observations for a single station is 132 records (12 mos X 11 yrs). The compacted data sets are stored for further processing under file directory names such as A72529, meaning data from block 72 in the U.S.A. for station number 529, Rochester, NY.

Program GETDAT was developed to list out the entire contents of the compacted data sets for quality assurance and data availability statistics.

Subroutine POLYCR<sup>60</sup> was chosen to provide the mathematical algorithm for estimating spatial and temporal correlations of cloud cover in this study. The routine will compute accurate estimates of correlation coefficients from fourfold tables (tetrachoric correlations) as well with the addition of code described by Beardwood (1977).<sup>61</sup> Also updated and

60. Martinson, E. D., and M. A. Hamdan, 1975: Algorithm AS87: Calculation of polychoric estimate of correlation in contingency tables. Applied Statistics, 24, 272-278.

61. Beardwood, J. E., 1977: A remark on algorithm AS87: Calculation of polychoric estimate of correlation in contingency tables. Applied Statistics, 26, 121.

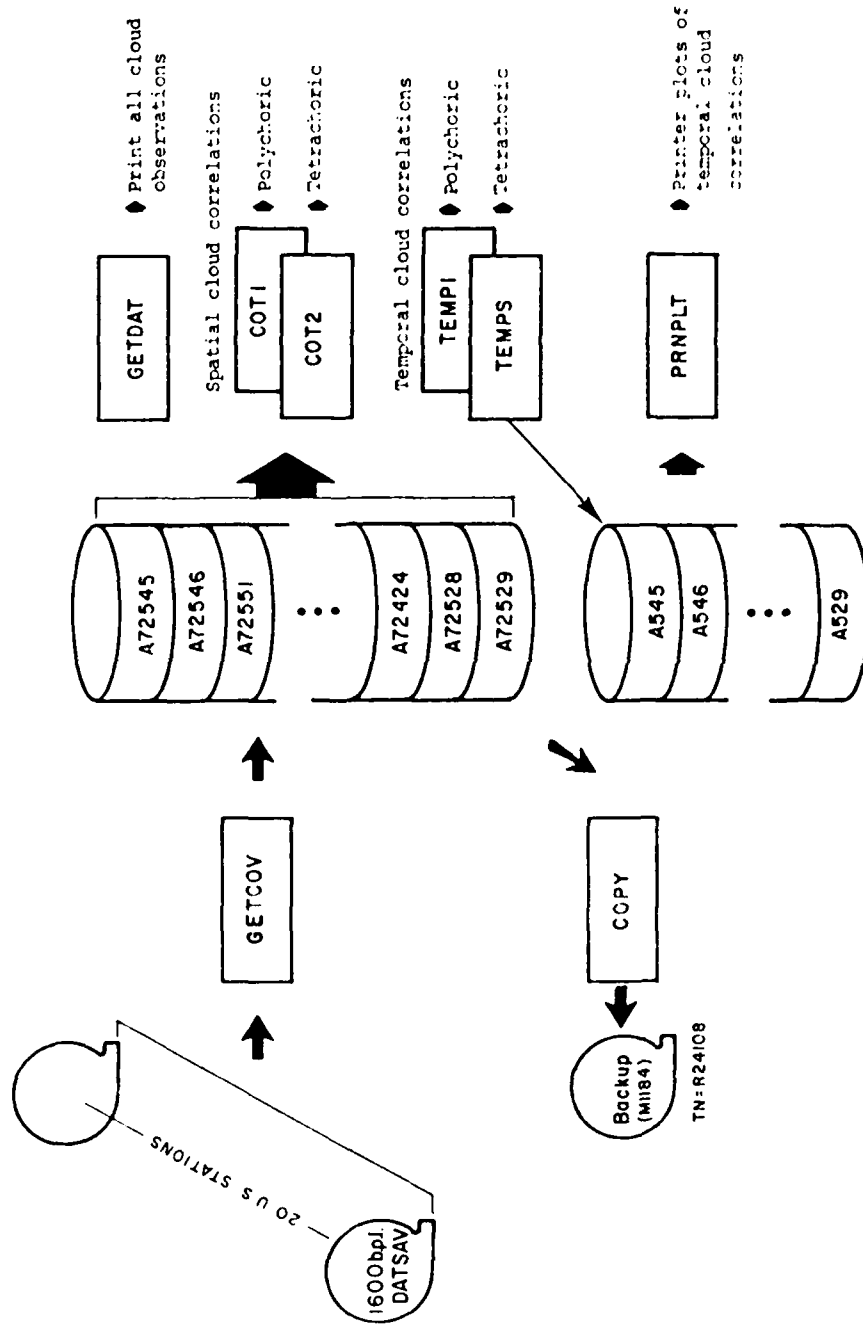


Fig. 58. Data Processing Configuration for Providing Cloud Cover Statistics from Ground Based Observations

included in the routine is an algorithm for computing the probable error of a coefficient of correlation in a fourfold table (Pearson, 1914-15).<sup>62</sup>

The only required inputs to routine POLYCR are contingency tables containing frequencies of predescribed conditions and table size parameters. It is therefore flexible enough for use in computing polychoric and tetrachoric correlations for both spatial and temporal cloud cover conditions.

Programs COT1 and COT2 provide the necessary logic for setting up contingency tables for use with routine POLYCR to compute spatial cloud correlations from the compacted data previously stored. Polychoric correlations can be obtained through the use of program COT1 which defines contingency tables large enough to handle all of the DATSAV cloud cover conditions listed in Table 15. However, polychoric correlations are not being processed at present because of major differences in specifying cloud amounts between synoptic and Airways reports.

The clear/cloudy conversion code column listed in Table 15 was specified to convert cloud amount into two unique categories. For example, cloud cover below five eighths is coded (1) and above four-eighths (10). Program COT2 converts the incoming sky condition to clear/cloudy code to set up fourfold contingency tables in routine POLYCR that are necessary for computing tetrachoric correlation coefficients and the associated probable error.

Distances between stations are computed using stored latitude-longitude locators by

$$nm = 60 \cdot \cos^{-1} [\cos(90 - LA_1) \cos(90 - LA_2) + \sin(90 - LA_1) \sin(90 - LA_2) \cos(LO_2 - LO_1)]$$

where

$LA_1$  and  $LO_1$  = latitude and longitude of station 1

$LA_2$  and  $LO_2$  = latitude and longitude of station 2

then

nm = nautical mile distance.

62. Pearson, K., 1914-15: On the probable error of a coefficient of correlation as found from a fourfold table. Biometrika, 10, 384.

Fig. 59 shows the spatial correlation function of cloud cover in January for the stations outlined in the accompanying map (Salem, OR not shown). Functions of this nature are being formulated for other time periods and mid-season months as well.

Programs TEMPI and TEMPS set up contingency tables for routine POLYCR to compute polychoric and tetrachoric correlation coefficients describing temporal cloud amount conditions. Cloud amount codes in Table 15 are utilized in the same manner discussed for the COT1 and 2 programs. Tetrachoric correlation coefficients stratified over a 48 hr period for January, April, July, and October of individual stations are computed and stored for plotting purposes.

Program PRNPLT plots the stored temporal statistics in histogram form like those shown in Fig. 60 for station 528, Buffalo, NY. These displays are useful in studying diurnal cloud effects over individual locations around the world. Fig. 61 shows the temporal correlation function over a 38 hr period as derived from the data ensemble associated with the stations shown on the map in Fig. 59.

Many more ground observing stations from other parts of the earth are being processed by the data handling software described here. Results obtained through the use of this software should lead to improved global cloud models.

#### D. Rainfall Rate Recurrence Statistics

##### 1. Introduction

Rainfall rate recurrence statistics are useful in modeling attenuation of satellite communication systems. This section discusses software developed to provide such statistics.

##### 2. Specifications

Software was to be developed and implemented to provide rainfall rate recurrence statistics responsive to these specifications:

- \* Stratify rainfall rate recurrence statistics by season.
- \* Determine maximum-minimum and average interval of times between recurrences of specified rainfall rate duration times.

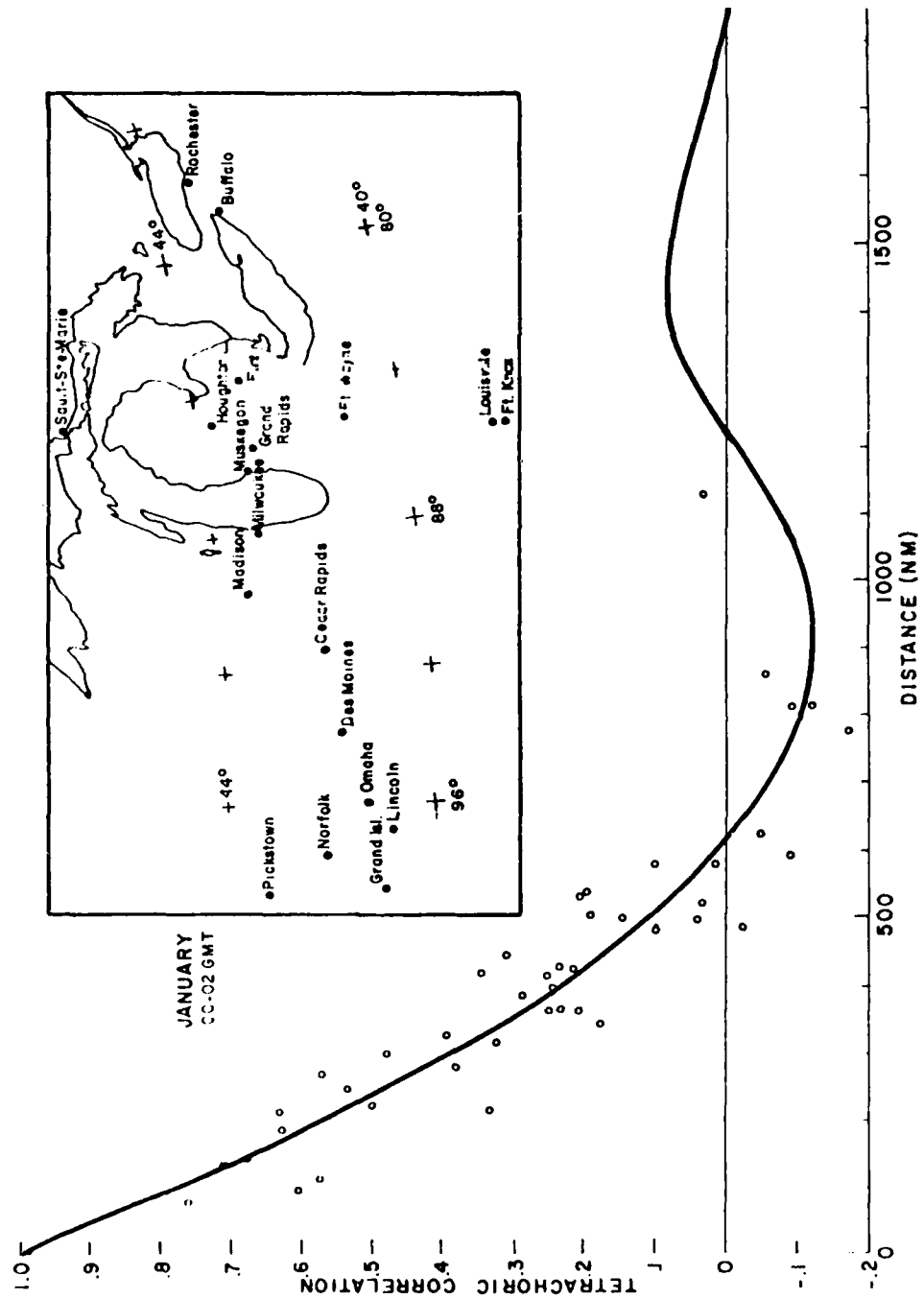


Fig. 59. Spatial Correlation Function of Cloud Cover for the Stations Shown in Map

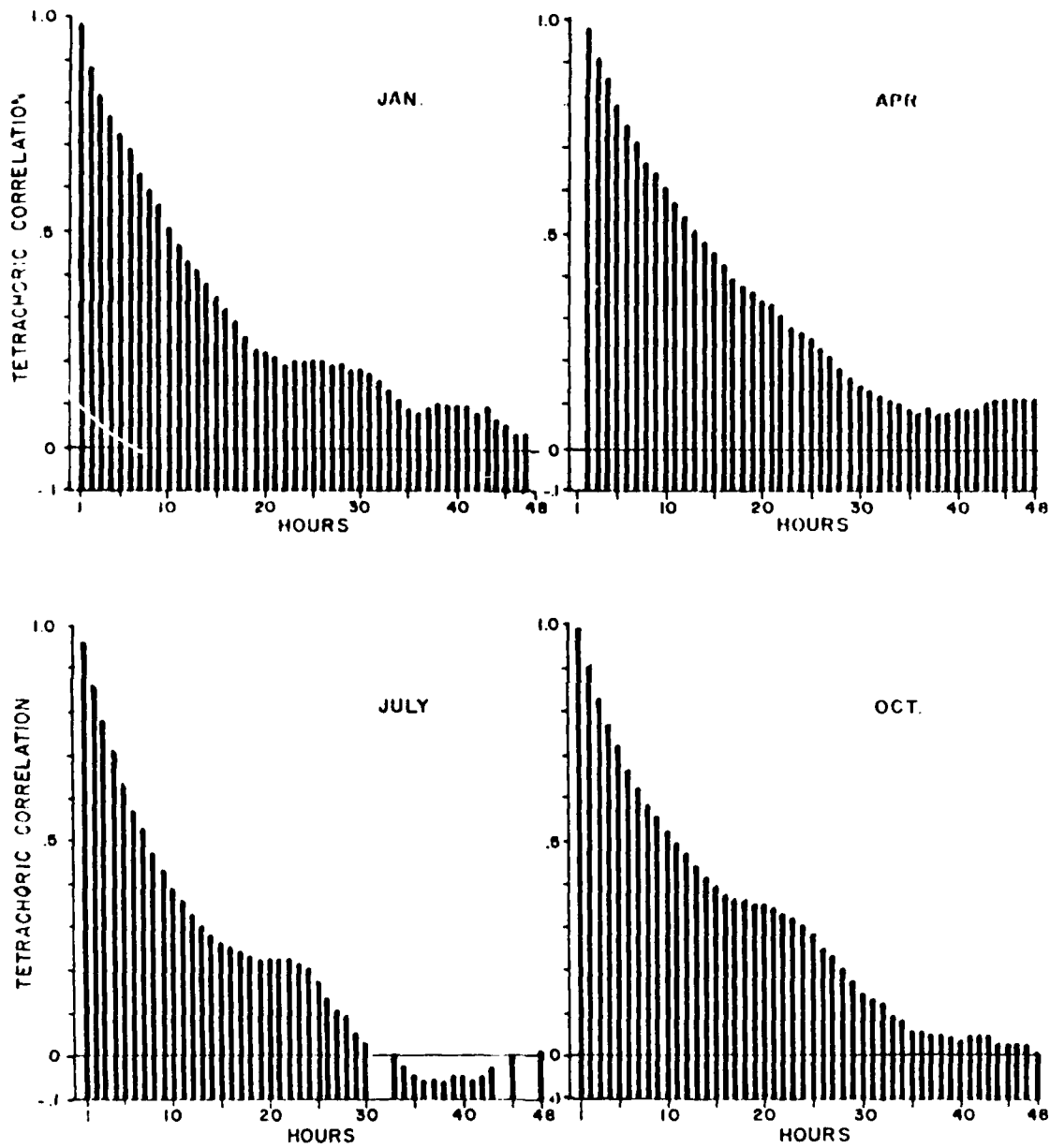


Fig. 60. Mid-Season Temporal Empirical Correlation Function: of Cloud Cover for Buffalo, NY (1973; 1983)

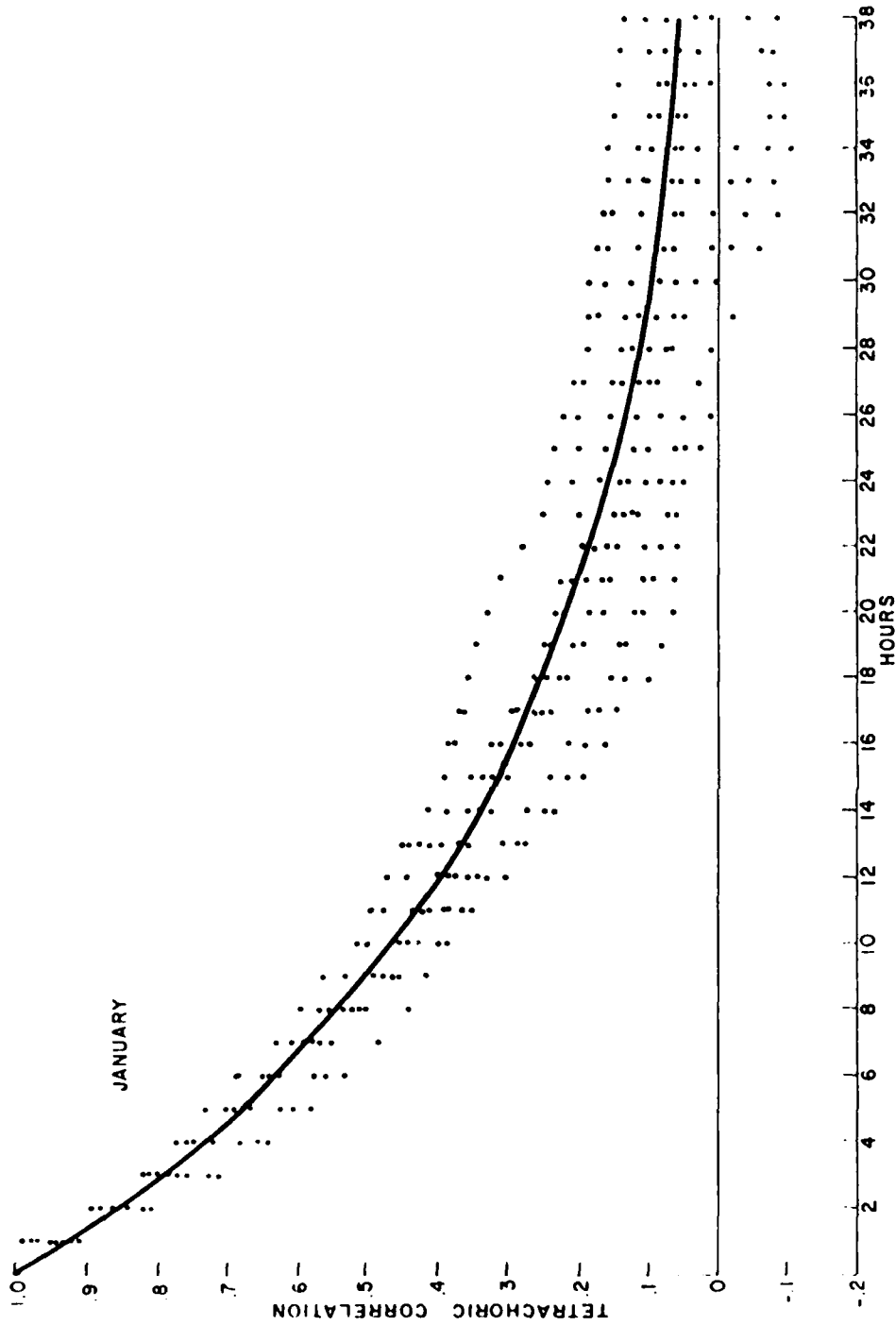


Fig. 61. Temporal Correlation Function of Cloud Cover for Stations on Fig. 59 May

- \* For each season, start interval at end of first duration and end interval at beginning of last duration even if first and last duration span into other seasons.
- \* Do all of above for rainfall rate duration times greater or equal to five and ten minutes with rain rates that exceed or equal .1, .25, .5, .75, 1.0, and 2.54 mm min<sup>-1</sup>.
- \* Display cumulative frequencies of occurrences of rainfall rates in graphical normal probability vs. logarithmic grid form.

### 3. Data Sources

Two tapes containing 1-minute rainfall rates over Urbana, IL from May 13, 1969 through August 31, 1979 and accompanying tape reference manuals<sup>63</sup> were the major data sources. One-minute rainfall rates together with relevant dates and times were stored on the tapes for rainy periods only; periods of no precipitation were ignored in the data gathering process.

### 4. Software Development

Fig. 62 depicts the overall software configuration designed to process rainfall rate data for defining rainfall rate recurrence statistics.

The first step was to get the data from tape onto permanent disk storage for interactive processing. Two separate programs were developed to accomplish the data transfer because of format differences between the two data tapes.

Program SEARC2 was developed to re-format the data on the KRAIN seven track tape (from May 13, 1969 through April 30, 1972) to make it compatible with the second tape. Results were stored in a file called KRAIN. Program SEARCH is a direct data transfer program (no format changes) written to file permanently onto the RAIN data set the record from January 1, 1972 through August 31, 1979 from the second tape, called RAIN24.

63. Tape Reference Manual: Tapes Containing 1-minute Rainfall Rates. Illinois State Water Survey, Urbana, IL.



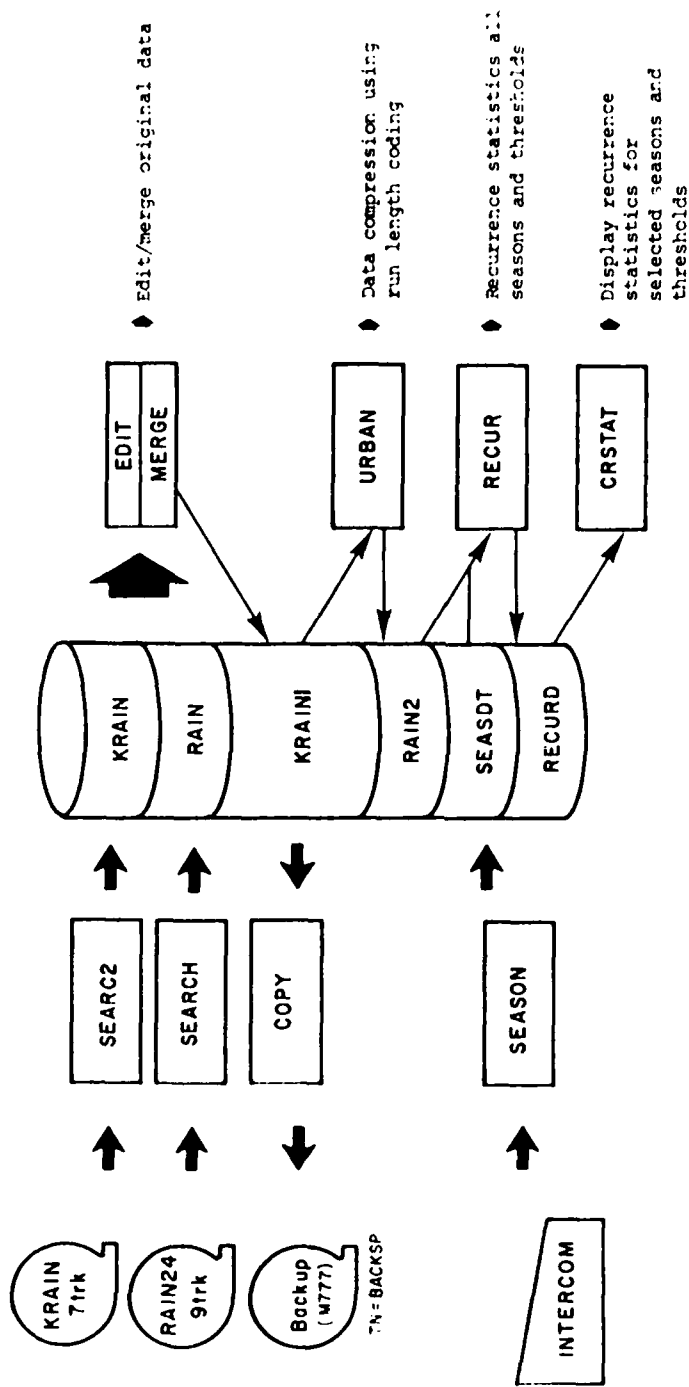


Fig. 62. Data Processing Configuration Providing Rainfall Rate Recurrence Statistics

Because of overlapping periods of record in the KRAIN and RAIN data sets and the discovery of other data anomalies, an editor (EDIT) was developed to clean up the data. The edited version on permanent file was then merged into one coherent data file called KRAIN1. Being approximately two megabytes, the merged file was spooled off onto a backup tape for permanent retention and reclaimed whenever access was warranted.

The data amount was so large that a special effort was made to compress it to manageable size for easier access.

Hence, program URBAN was implemented. It uses a run length coding algorithm to compress the rainfall rate data into manageable form. It uses a routine for keeping track of the number of minutes elapsed from 00 GMT on January 1, 1969 to any given date and time through the year 1980. Two computer words are used to store the run length codes that describe each rainfall rate duration. The first word contains the integer value of the time in minutes of the first occurrence of a rainfall rate equal to or exceeding a given threshold. The second word contains the number of minutes the occurrence lasted, together with the threshold value of concern. Compressed in this manner the entire data set was stored in RAIN2 with an approximately 80 percent reduction in storage requirement. The one drawback is that return to the original data for reprocessing is necessary if any one of the previously chosen rainfall rate thresholds is changed.

Through the use of the Zenith PC/InterComm and a program called SEASON, an additional data set SEASDT was created to provide start and stop times in minutes of the four seasons in the entire data period.

Program RECUR combines the compacted rainfall rates with the bookkeeping SEASDT data to compute the rainfall rate recurrence statistics. Maximum minimum and average minute time intervals of the recurrences between specified duration periods of rainfall rates at given thresholds are tabulated and printed. Cumulative frequencies of the occurrences of the lapse times between the various rainfall rates are stored on file RECURD for plotting purposes using program CRSTAT.

As a final step, program CRSTAT was designed to plot the cumulative frequencies of occurrences of the lapse times in normal probability vs. logarithmic graphical form.

Fig. 63 shows the summer and winter seasonal cumulative probabilities of lapse times incurred between rainfall rates equal to or

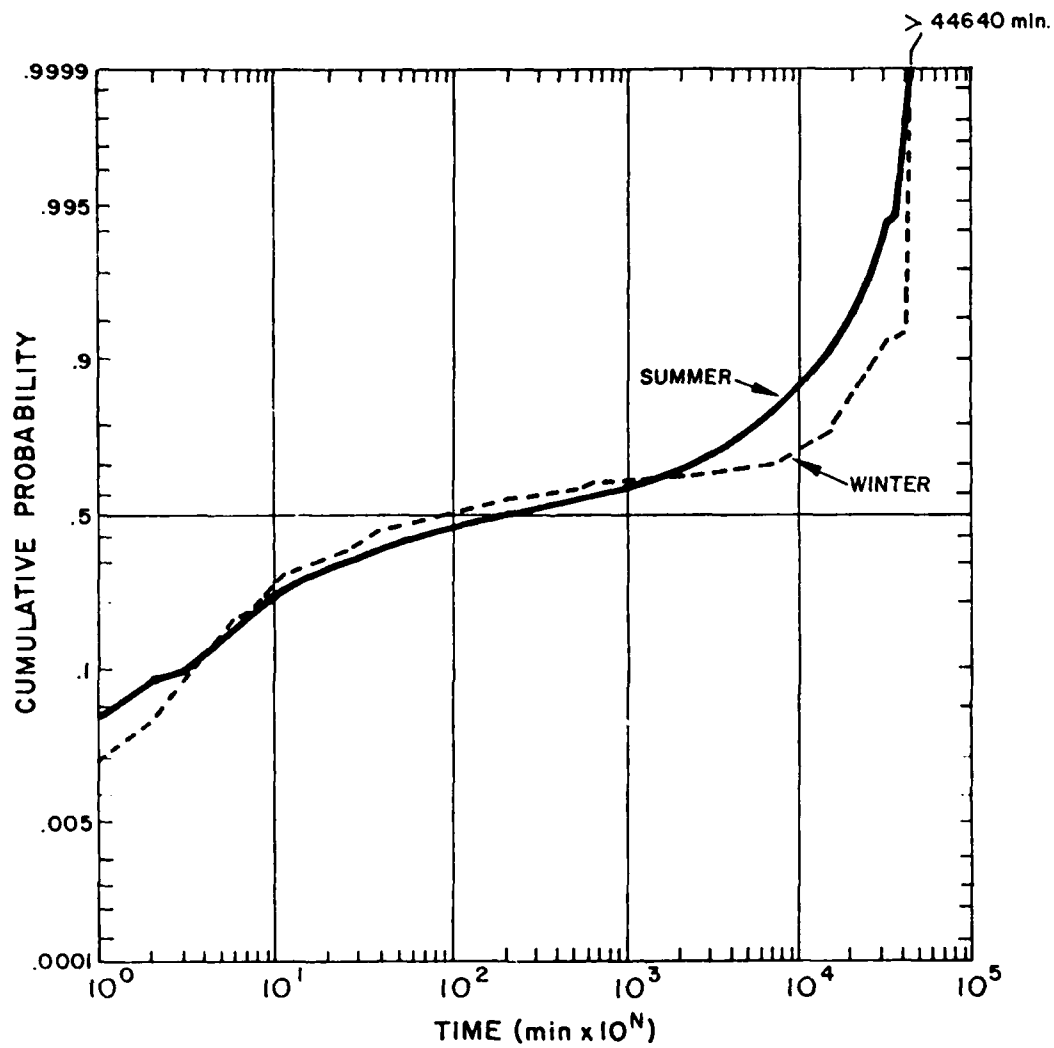


Fig. 63. Cumulative Probabilities of Recurrences of Rainfall Rates  $> 0.1$  mm/min, Urbana, IL, 1969-1979

greater than  $0.1 \text{ mm min.}^{-1}$  (Lapse times exceeding 44,640 minutes, or one month, are summed into a single group interval.) Graphs of this type were produced for all thresholds and seasons specified from the Urbana, IL data. Additional data archives of rainfall rates are being acquired.

## E. Cumulus Cloud Cover vs. Satellite Brightness Values

### 1. Introduction

Effects of small scale cumulus clouds on various sensor fields of view were investigated using LANDSAT MSS data. Much of the data processing involved was carried out by the data handling configuration shown in Fig. 51. This section describes the data processing performed beyond that point to get the data arrays into a form suitable for statistical analysis.

### 2. Specifications

Data processing specifications for determining cumulus cloud cover vs. satellite brightness values are:

- \* Produce good quality pictures of LANDSAT full resolution subsection scenes for reading percent cloud amounts in .75 nm grid squares.
- \* From the digital values, determine thresholds that give percent cloud cover the same as the eye sees.
- \* Compute average brightness and percent cloud cover over 1 X 1, 2 X 2, and 4 X 4 averaged digital subsection arrays. Include sun angle correction factors to correct digital data for sun angle effects.
- \* Provide statistical results in the form of scatter plots.

### 3. Source Data

Band interleaved (BIL) formatted LANDSAT data for bands 4 (.5 - .6  $\mu\text{m}$ ) and 7 (.8 - 1.1  $\mu\text{m}$ ) were the major data sources. Six cases depicting small cumulus clouds over ocean areas in the Straits of Florida were selected for investigation. Full resolution subsections of these cases were extracted by the data handling configuration in Fig. 51 and displayed on the McIDAS imaging system. Further software was then developed to process these six cases to meet the specifications.

#### 4. Software Development

Fig. 64 depicts the software configuration used to assemble the data images into manageable form for deducing statistics of cumulus cloud cover vs. satellite observed brightness.

Fig. 65 is a full-resolution subsection scene of case number 3. Small cumulus clouds are readily seen in the image, which is located over the Straits of Florida just west of the Grand Bahama Bank. Twenty-four by sixteen grid squares, approximately .75 nm apart, are superimposed onto each image as guides for reading cloud cover subjectively by a skilled analyst. The cloud amounts read are stepped into the computer through an intercom system and stored separately for each of the six cases as A4, B4, C4, etc. (Band 7 cases are stored as A7, B7, C7, etc.)

Program TODSK, taken from Fig. 51, is utilized to extract the full resolution digital subsections from the LANDSAT data tapes. Each section extracted is filed separately as LANDA4, LANDB4, etc., or LANDA7, LANDB7, etc., representing data from band 4 and 7, respectively.

Program DTHRES was developed to combine the cloud amount readings with the digital data to determine a threshold level best suited to the subjective cloud cover in each box. In other words, what is sought is the threshold value that minimizes

$$\frac{\sum_{1}^{N} (CC_R - CC_T)}{N}$$

where  $CC_R$  is one of the readings and  $CC_T$  is the cloud cover from the digital data in a box at threshold T. The thresholds thus found are used in subsequent software.

Before any statistical parameters were computed from the data sets it was specified that all digital arrays be corrected for sun angle effects. Program COSAV7 was therefore introduced to compute correction factors for adjusting satellite observed brightnesses to theoretical brightnesses at normal incidence angle. This was accomplished by inserting a modification of a sun angle correction algorithm originally developed by

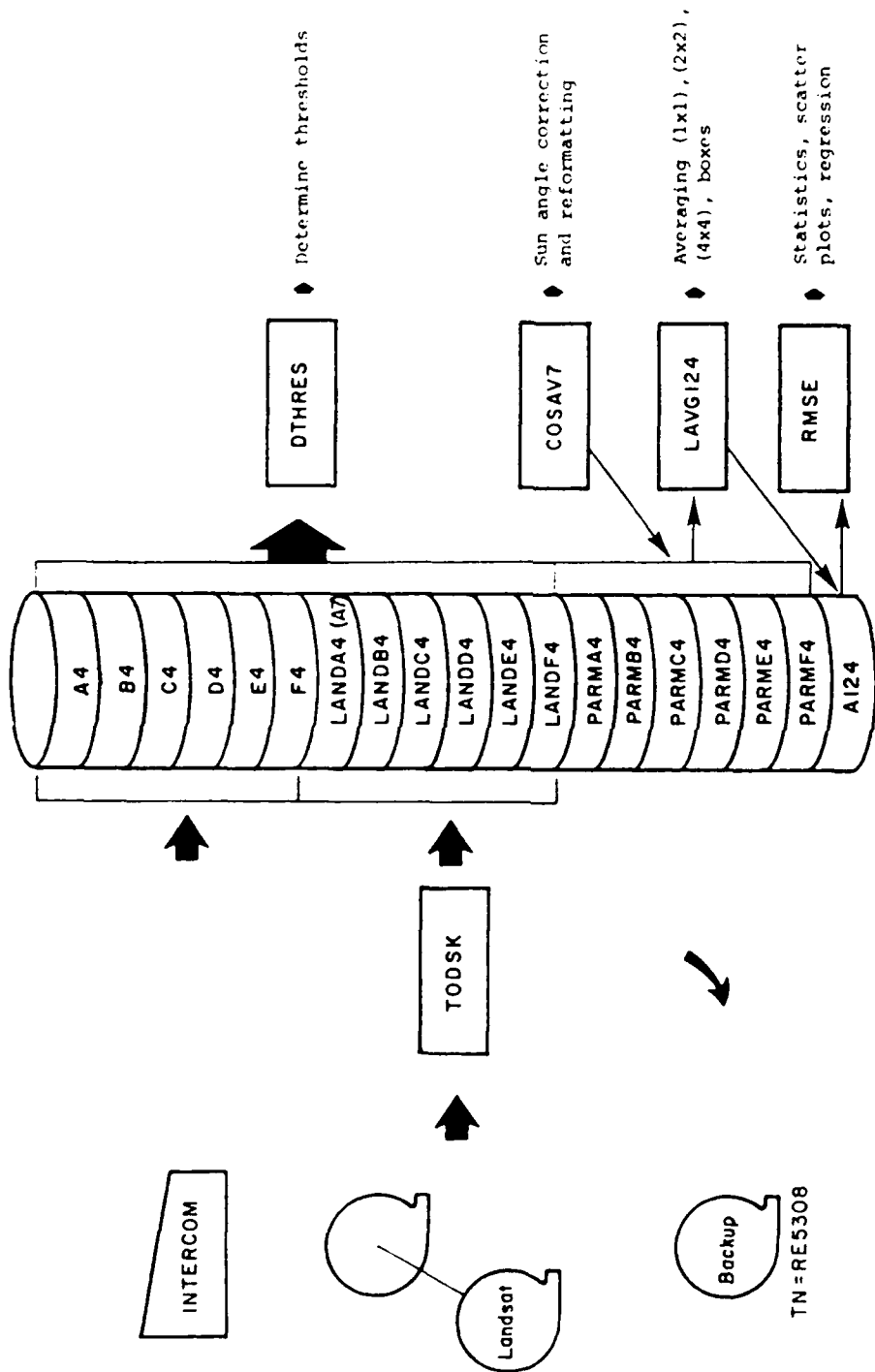


Fig. 64. Configuration for Assembling LANDSAT Data for Statistical Processing



Fig. 65. LANDSAT Full Resolution Subscene for Case 3 (LANDC4) (Band 4; September 25, 1980)  
Superimposed are 3/4 nm grid cells.

Willand.<sup>64</sup> The program also assembled all data into a single compatible format for optimum use with statistical software. These assembled data parameters were stored on files named PARMA4, PARMB4, etc.

Program LAVG124 was used to average the original data in 1 X 1 (.75 nm) boxes into 2 X 2 and 4 X 4 grid boxes to simulate 1.5 and 3 nm grid sizes. Theoretically this averaged the data into fields of view compatible with those found on conventional meteorological satellites.

Program RMSE was assembled to plot scattergrams of cloud amounts vs. average brightness counts D as shown in Fig. 66 for the 1 X 1 (.75 nm) grid resolution scenes. Also produced were statistics of data populations, means, standard deviations, variances, bias, correlation coefficients, RMSE, and best fit linear equation coefficients for each spatial resolution.

The software discussed will be further utilized when additional LANDSAT tapes are made available.

---

64. Willand, J. H., 1977: Program GEOESI (Version 1.0, Level 1/0502). Environmental Research and Technology, Inc., Concord, MA.



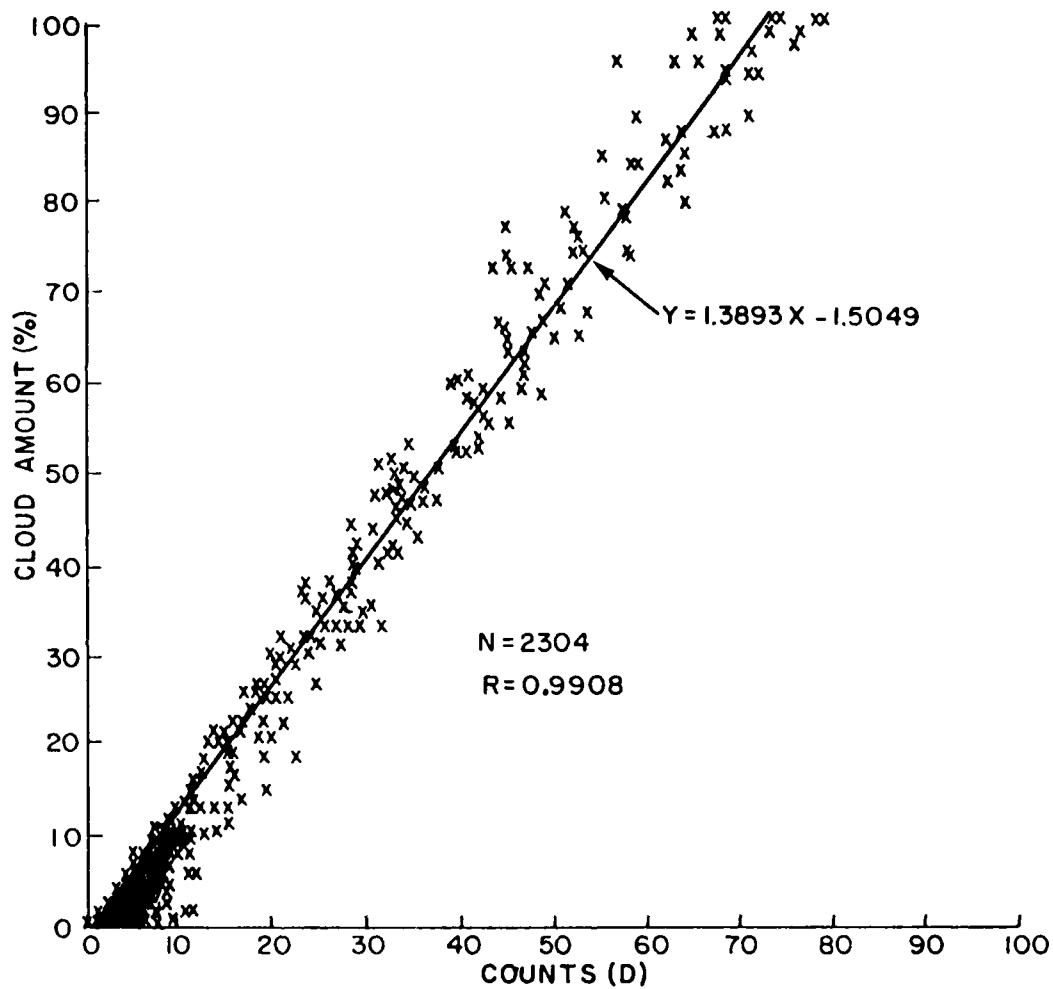


Fig. 66. Scatter Plot of 1 X 1 (.75 nm) Grid Resolution Parameters

## Appendix D. Program COND80

### PURPOSE:

Program COND80 (Version 2.0, Level 850415), written in FORTRAN V for use on the AFGL CDC Cyber interactive system, computes and tabulates unconditional and spatial conditional probability of cloud populations. It is applied to cloud photography taken on space shuttle missions.

### PROGRAM DESCRIPTION:

Table D1 provides a listing of COND80, specified for the processing of a hand digitized portion of a photograph taken from the space shuttle mission 41D just off-shore of Cape Canaveral, Florida. The digitized area is comprised of 80 pixels X 80 scans and is listed in Table D2. The program is set up to process ten chosen scan lines starting with scan line number 8 in increments of 8; a threshold value of 2 is used to determine if a pixel is cloudy or clear. These two settings are defined in the program at lines 10 and 11. Hence,

NLINES defines the scan line number within a data set where processing is to begin. Statement number 31 controls the incremental index that points to the next desired scan line to process.

ITHRES defines the cloud/clear threshold pixel value where, in this case, a pixel is assessed as cloudy if its value is greater than or equal to 2. Otherwise, it is defined to be cloud-free, i.e., clear.

### INPUT:

Refer to the details given in Table D2. The scene begins with an identification line that is followed by sequential scan lines (top to bottom) and sequential coded pixel values along each scan line oriented left to right.

### OUTPUT:

The card image data are simply read into program COND80 (Line 24) scan line by scan line to compute the statistics shown in the output example in Table D3. As shown, unconditional statistics of clear (CLR) and cloudy (CLD) pixels are tabulated followed by spatial conditional arrays organized so that the given condition is on the left followed by the observed condition

TABLE D-1. PROGRAM COND80 LISTING

```

1      PROGRAM COND80 (OUTPUT, TAPE1)
2      C *****
3      C CHECK SPATIAL CONDITIONALITY ON 80 X 80 HAND DIGITIZED
4      C SPACE SHUTTLE CLOUD SCENE.
5      C *****
6      DIMENSION IN(80), IC(3,3,79), IU(3), CN(2), CN2(2,2)
7      DIMENSION AP(2)
8      DATA PI2/1.5707963/
9      DATA AP(1)/'CL6'/, AP(2)/'CLD'/
10     DATA NLINES/8/
11     DATA LTHRES/2/
12     C =====
13     READ(1,667) (IN(I), I=1,80)
14     667 FORMAT (80A1)
15     DO 8 I=1,4
16     IU(I)=0
17     8 CONTINUE
18     DO 9 K=1,79
19     DO 9 J=1,3
20     DO 9 I=1,3
21     IC(I,J,K)=0
22     9 CONTINUE
23     NREC=C
24     1111 READ(1,668,END=995) (IN(I), I=1,80)
25     668 FORMAT (80I1)
26     NREC=NREC+1
27     IF(NREC.GT.NLINES) GO TO 998
28     IF(NREC.NE.NLINES) GO TO 1111
29     PRINT 599, NLINES
30     599 FORMAT (1H, "PROCESSING SCAN LINE", I5)
31     NLINES=NLINES+8
32     JNUM=0
33     101 JNUM=JNUM+1
34     IF(JNUM.GT.79) GO TO 20
35     NGIVEN=1
36     IF(IN(JNUM).GE.LTHRES) NGIVEN=2
37     IU(NGIVEN)=IU(NGIVEN)+1
38     IU(3)=IU(3)+1
39     INUM=JNUM+1
40     NEXT=L
41     DO 10 M=INUM,80
42     NEXT=NEXT+1
43     NCOND=1
44     IF(IN(M).GE.LTHRES) NCOND=2
45     IC(NGIVEN, NCOND, NEXT) = IC(NGIVEN, NCOND, NEXT) + 1
46     IC(NGIVEN, 3, NEXT) = IC(NGIVEN, 3, NEXT) + 1
47     10 CONTINUE
48     GO TO 101
49     20 NGIVEN=1
50     IF(IN(80).GE.LTHRES) NGIVEN=2
51     IU(NGIVEN)=IU(NGIVEN)+1
52     IU(3)=IU(3)+1
53     GO TO 1111
54     C
55     C PRINT RESULTS.

```

```

57          C
58          998 PRINT 600
59          600 FORMAT(" UNCONCITIONAL STATISTICS FOR 80 X 80 CASE")
60          PRINT 601
61          601 FORMAT(/8X,"CLK",4X,"CLD",4X,"SUM")
62          PRINT 602,(IU(I),I=1,3)
63          602 FORMAT(4X,3I7)
64          CN(1)=FLOAT(IU(1))/FLOAT(IU(3))
65          CN(2)=FLOAT(IU(2))/FLOAT(IU(3))
66          PRINT 603,CN(1),CN(2)
67          603 FORMAT(4X,2F7.3)
68          PRINT 604
69          604 FORMAT(/" SPATIAL CONDITIONALS")
70          DO 30 KK=1,79
71          DO 21 IGIVEN=1,2
72          CN2(IGIVEN,1)=0.0
73          CN2(IGIVEN,2)=0.0
74          IF (IC(IGIVEN,3,KK).LE.0)GO TO 21
75          CN2(IGIVEN,1)=FLOAT(IC(IGIVEN,1,KK))/FLOAT(IC(IGIVEN,3,KK))
76          CN2(IGIVEN,2)=FLOAT(IC(IGIVEN,2,KK))/FLOAT(IC(IGIVEN,3,KK))
77          21 CONTINUE
78          R=0.0
79          TOP=SQRT(CN2(1,1)*CN2(2,2))-SQRT(CN2(1,2)*CN2(2,1))
80          BOT=SQRT(CN2(1,1)*CN2(2,2))+SQRT(CN2(1,2)*CN2(2,1))
81          IF (BOT.EQ.0.0)GO TO 778
82          TEMP=PI2*(TOP/BOT)
83          R=SI*TEMP)
84          778 PRINT 605,KK,R
85          605 FORMAT(/8X,"CLE",,X,"CLD",4X,"SI",2X,"DIST",,14," R",F8.5)
86          DO 22 IGIVEN=1,2
87          PRINT 606,AP(IGIVEN),(IC(IGIVEN,J,KK),J=1,3)
88          606 FORMAT(1X,A3,3I7)
89          PRINT 607,(CN2(IGIVEN,J),J=1,2)
90          607 FORMAT(4X,2F7.3)
91          22 CONTINUE
92          30 CONTINUE
93          STOP
94          END

```





TABLE D-3. SAMPLE OUTPUT

PROCESSING SCAN LINE 8  
 PROCESSING SCAN LINE 16  
 PROCESSING SCAN LINE 24  
 PROCESSING SCAN LINE 32  
 PROCESSING SCAN LINE 40  
 PROCESSING SCAN LINE 48  
 PROCESSING SCAN LINE 56  
 PROCESSING SCAN LINE 64  
 PROCESSING SCAN LINE 72  
 PROCESSING SCAN LINE 80  
 UNCONDITIONAL STATISTICS FOR 80 X 80 CASE

CLR	CLD	SUM
327	473	800
.409	.591	

SPATIAL CONDITIONALS

DIST= 1 R .92186

	CLR	CLD	SUM
CLR	270	51	321
	.841	.159	
CLD	47	422	469
	.100	.900	

DIST= 2 R .82891

CLR	CLR	CLD	SUM
	240	77	317
	.757	.243	
CLD	67	396	463
	.145	.855	

DIST= 3 R .74382

CLR	CLR	CLD	SUM
	219	95	314
	.697	.303	
CLD	80	376	456
	.175	.825	

•  
•  
•

DIST= 79 R .00000

CLR	CLR	CLD	SUM
	6	4	10
	.600	.400	
CLD	0	0	0
	.000	.000	

STOP

to the right for pixel distances (DIST) away. Tetrachoric correlation coefficient (R) is also computed and printed from the elements of each conditional array using the expression

$$R = \sin \left[ \frac{\pi}{2} \left( \frac{\sqrt{AD} - \sqrt{BC}}{\sqrt{AD} + \sqrt{BC}} \right) \right]$$

where

A, B, C, and D are array elements (1,1), (1,2), (2,1), and (2,2) respectively.